

Towards Cryogenic Scalable Quantum Computing with Trapped Ions

Dissertation

zur Erlangung des Doktorgrades an der
Fakultät für Mathematik, Informatik und Physik
der Leopold-Franzens-Universität Innsbruck

vorgelegt durch

DI DI Matthias F. Brandl, BSc

durchgeführt am Institut für Experimentalphysik
unter der Leitung von
Univ.-Prof. Dr. Rainer Blatt

Innsbruck, 29. November 2016

Kurzzusammenfassung

In den letzten zwei Jahrzehnten hat sich das Feld der Quanteninformationsverarbeitung zu einem wichtigen Feld der Physik entwickelt und Systeme mit Ionenfallen sind eine der aussichtsreichsten Technologien um einen Quantencomputer zu bauen. Da Gatteroperationen an einigen wenigen Ionen bereits mit hoher Güte gezeigt wurden, liegt das Augenmerk nun auf skalierbaren Quantensystemen. Die hier präsentierte Arbeit beschreibt die Entwicklung eines skalierbaren Experiments zur Quanteninformationsverarbeitung mit $^{40}\text{Ca}^+$ und $^{88}\text{Sr}^+$ Ionen in Paulfallen. Die verwendete Ionenfalle ist eine planare, segmentierte Paulfalle, die es ermöglicht die gespeicherten Ionen in flexible Quanteninformationsregister für die Quanteninformationsverarbeitung zu unterteilen. Die Heizrate in der Falle und die Kollisionsrate der Ionen mit dem Hintergrundgas können verringert werden, indem die Falle in einer kryogenen Umgebung betrieben wird. Die Wände des Kryostaten werden als magnetische Abschirmung verwendet, indem der Skin-Effekt ausgenutzt wird. Die gemessene Dämpfung von 120 dB der Magnetfeldabschirmung von 50 Hz-Signalen verlängert die Kohärenzzeiten der Quantenbits im Vergleich zu Experimenten bei Raumtemperatur. Es wurde eine Vibrationsisolation in den Kryostaten integriert, damit sich die Position der Ionen in der Falle nicht gegenüber dem optischen Tisch ändert. Dadurch ist während eines Experiments eine wohldefinierte Phase des Lichts an der Stelle der Ionen gewährleistet. Zusätzlich zum Kryostaten wurden der optische Aufbau und die elektronische Steuerung zur Verwendung von $^{40}\text{Ca}^+$ und $^{88}\text{Sr}^+$ im Labor installiert. Dies ermöglichte eine Charakterisierung des Aufbaus unter Verwendung der Ionen. Die gemessene Kohärenzzeit von $^{40}\text{Ca}^+$ Ionen zeigte einen Gaußschen Verlauf des Ramsey-Kontrasts mit einer $1/e$ -Zeit von 18.2(8) ms. Weiter wurde eine Heizrate von 2.14(16) Phononen/s gemessen.

Abstract

Over the last two decades, the field of quantum computation has grown into a major field of physics and the trapped ion systems are one of the most promising candidates for the development of a quantum computer. As high-fidelity gate operations with few ions have already been demonstrated, the experimental challenges for quantum information processing lie in transferring these techniques onto scalable quantum systems. The presented work describes the development of a scalable experiment for trapped ion quantum computation with $^{40}\text{Ca}^+$ and $^{88}\text{Sr}^+$ ions. The incorporated ion trap is a planar, segmented Paul trap which enables reconfiguration of the stored ions in flexible quantum information registers to scale up quantum computation. In order to decrease the heating rate and the collision rate with background gas, the trap is operated in a cryogenic environment. The walls of the cryostat are used as magnetic shields by exploiting skin-effect to enhance the coherence times of the qubits. Measurements resulted in an attenuation of 120 dB for the magnetic shielding for 50 Hz signals. Vibration isolation was integrated in the design of the cryostat so that the positions of the ions in the trap are static with respect to the optical setup, resulting in a well-defined phase of the interaction field with respect to the qubit transition. In addition to the cryogenic apparatus, optical setups and electronic control systems for the operation with $^{40}\text{Ca}^+$ and $^{88}\text{Sr}^+$ ions were installed, which allowed a characterization of the entire system using trapped ions. The measurement of the coherence time of $^{40}\text{Ca}^+$ showed a Gaussian decay of the Ramsey contrast with a $1/e$ -time of 18.2(8) ms and the obtained heating rate was 2.14(16) phonons/s.

Contents

Abstract	II
1 Introduction	1
2 Quantum information processing with trapped ions	4
2.1 Quantum Bits	4
2.2 Quantum information processing with optical qubits	6
2.3 Paul traps	10
2.4 Segmented Paul traps	11
2.5 Atom-light interaction	12
2.6 Entangling gates	14
2.7 Laser cooling of trapped ions	14
2.8 Estimate the fidelity of single qubit operations	16
2.8.1 Rotation angle	17
2.8.2 Stability of the rotation axis	19
2.8.3 Spontaneous photon scattering	20
2.8.4 Summary of the required precision	21
3 Electronics: Resonator and Filter Design	22
3.1 Resonator Design	22
3.1.1 General considerations	22
3.1.1.1 Choosing the trap drive frequency	22
3.1.1.2 Matching	23
3.1.1.3 Pick up	24
3.1.2 Coil design	25
3.1.2.1 PCB Coils	25
3.1.2.2 Wire Coils	27
3.1.2.3 Spiral Coil	27
3.1.3 Matching	29
3.1.4 RF-Shield	32
3.1.5 Results of the designed resonators	33
3.2 Filter Design	34
3.2.1 Filter Noise at Secular Motion Frequencies	35
3.2.2 Shunt Trap Drive Signal on DC Lines	38
4 A cryostat for scalable quantum computation with trapped ions	41
4.1 Choosing the type of cryostat	41
4.2 Minimizing the thermal load	43
4.3 Beam geometries and trap orientation	44
4.4 Magnetic field stability	46
4.4.1 Spatial homogeneity	46
4.4.2 Magnetic shielding	49
4.5 The trap	54
4.6 Trap mount and lens systems in a cryogenic environment	55
4.7 Mechanical structure and vibrational decoupling	59
4.8 Oven mount and non-evaporative getters	61
4.9 Resonator	64
4.10 Filter design and cryostat wiring	65

4.11	Characterization	67
4.11.1	Magnetic shielding	69
4.11.2	Vibrations	71
5	Experimental setup	76
5.1	Lasers and optics	76
5.1.1	Photo-ionization lasers	76
5.1.2	Lasers driving dipole transitions	77
5.1.3	Lasers driving quadrupole transitions	79
5.1.4	Detection optics	81
5.2	Electronics	82
5.2.1	Electronics for quasi-static signals	83
5.2.2	Electronics for dynamic signals	84
5.2.3	Electronics developed during this thesis	84
5.2.3.1	Bus sequencer	84
5.2.3.2	Counter to compensate micromotion	85
6	Experimental results	87
7	Outlook - ideas for improvements and future experiments	92
7.1	Higher frequencies of secular motion	92
7.2	Stabilizing the interaction field at the position of the ion	93
7.2.1	Stabilizing the intensity of the light	93
7.2.2	Decreasing phase drifts of the light at the position of the ion	95
7.3	Reduce the time of an experimental cycle	96
7.3.1	Implement EIT cooling	96
7.3.2	Replacing the camera with multiple PMTs	97
7.3.3	Addressing	98
7.4	Work with Zeeman qubits	99
7.5	High-fidelity global RF gates	100
7.6	Measurement of the coherence time	100
7.7	Suggestions for experimental improvements in future setups	102
8	Summary	103
A	Appendix	105
A.1	Suggestions for the improvements on magnetic field stability	105
A.1.1	Low-pass filter current through coils for quantization field	105
A.1.2	Passively stabilize the magnetic field with copper	106
A.2	Shield against EM noise with a conductor around the trap	106
A.3	RF voltage stabilization	108
B	Construction manual of the cryostat	111
B.1	Assembly of the inner heat shield including the trap	111
B.2	Assembly of the vacuum chamber and outer heat shield	115
B.3	Assembly of the flow cryostat and the oven mount	118
C	Journal publications	121
	Bibliography	122
	Danksagung	134

1 Introduction

The development of computers started with simple machines for addition and subtraction [Tan05]. After the invention of integrated circuits, the computational power of computers has increased exponentially over time, which is described by Moore's law [Moo65, Moo75]. With simple processors for special purpose calculations as a starting point in the 1960s, this scaling resulted in the rapid development of desktop computers, laptops, tablets, and mobile phones which have drastically altered the every-day-life of people on this planet.

As Moore's law for the development of computers is expected to end [Wal16], the field of quantum computing has emerged to provide an alternative to classical computing. While quantum computation (QC) may not speed up universal computation, there are quantum algorithms which solve certain problems more efficiently than classical computers. Two examples of such algorithms are Shor's algorithm for efficient prime factoring [Sho97] or Grover's algorithm for efficient searching in unsorted databases [Gro97].

As the required resources of simulations of quantum mechanical systems scale exponentially with the size of the system, Richard Feynman suggested using a quantum mechanical system to simulate the behavior of another quantum mechanical system [Fey82]. For such simulations, quantum mechanical systems can be employed either as analog simulators [GKZ⁺10] or as digital simulators [LHN⁺11]. With large scale quantum simulations, one can try to find room-temperature superconductors or new efficient fertilizers.

In classical computers, the information is stored in bits which can either be 0 or 1. In quantum computers, the information is stored in quantum bits, or short qubits. A qubit is a quantum mechanical two-level system of which one state is denoted $|0\rangle$ and the other $|1\rangle$. In contrast to classical information, qubits cannot only be stored in the $|0\rangle$ or $|1\rangle$ state but also in a superposition of those states.

There are many quantum mechanical systems under investigation as possible candidates for a quantum computer [WBB⁺03, KYG⁺07, LBC⁺12, JW06, LMM⁺15, MLX⁺15]. All these systems have to fulfill the following criteria, suggested by David DiVincenzo [DI00], to successfully build a quantum computer:

1. A scalable physical system with well characterized qubits
2. The ability to initialize the state of the qubits
3. Long relevant decoherence times, much longer than the gate operation time
4. A universal set of quantum gates
5. A qubit-specific measurement capability

One of the most promising systems for the fabrication of a quantum computer, and the topic of this thesis, is trapped ions [WMI⁺98, LBMW03]. The ions are confined in chains inside Paul traps [POF58, Pau90], which enable quantum state manipulation with the aid of laser light or radio-frequency (RF) fields. External fields allow the manipulation of the motional state of an ion string in the trap as well, which combined with manipulation of the electronic state can be exploited to perform entangling gate operations [CZ95, SM99]. For these multi-qubit operations, the motion of the ion crystal acts as a data-bus to mediate interaction between qubits. Single gate operations with an infidelity of 10^{-6} in combination with a coherence time T_2^* of 50 s [HAB⁺14] have been demonstrated as well as two-qubit gate operations with an infidelity of 10^{-3} [BHL⁺16]. This high level of quantum control in trapped ion experiments

led to impressive results in quantum simulation [GKZ⁺10, RGL⁺14, JLH⁺14] and quantum computation [SBM⁺11, MNM⁺16] with trapped ions.

Scaling up quantum systems to hundreds or thousands of qubits is one of the few remaining challenges for trapped ion QC. To circumvent working with a single ion chain of hundreds or thousands of ions, the ion string can be split into substrings which can be recombined arbitrarily for quantum information processing (QIP) [KMW02]. When scaling up trapped ion QC with Paul traps, several issues have emerged which can be solved by operating the Paul traps in cryogenic environments. These issues are

- **Magnetic field fluctuations:** at low temperatures, physical phenomena like superconductivity can be employed to overcome technical problems in the design of a quantum computer. For example, superconducting magnets can be used to stabilize the magnetic fields in trapped ion experiments [WLG⁺10]. Another application is to use the extremely high conductivity of ultra-pure metals at low temperatures by exploiting skin-effect to repel alternating magnetic fields and thereby decouple the trapped ion QIP experiments from alternating magnetic field noise of the laboratory environment [BWC⁺11].
- **Motional heating rates:** electric field noise in Paul traps at the secular motion frequencies causes heating of the ion string [TKK⁺00]. Since entangling gates require the generation and annihilation of phonons in ion chains [CZ95, SM99], high heating rates limit the fidelities of entangling gates. However, heating rates can be strongly attenuated by operating Paul traps at cryogenic temperatures [LGA⁺08].
- **Vacuum pressure:** with larger and larger ion crystals in trapped ion experiments [RGL⁺14, JLH⁺14], collisions with background gas become an increasing problem. In modern vacuum chambers, one can reach vacuum pressures of about 10^{-11} mbar at room temperature that allow the operation with several tens of ions. Pressures below that can only be achieved in cryostats, where pressures of 10^{-16} mbar at 4 K have been demonstrated [DHH⁺98]. Hence, to minimize quantum information loss due to collisions, one can freeze out the background gas at cryogenic temperatures.
- **Turnaround time:** in order to reach ultra-high vacuum (UHV), vacuum chambers have to be baked for several weeks. Hence, the capability to test the performance of many different trap designs in a short period of time requires cryogenic setups, which do not need to be baked to reach UHV conditions. Turnaround times of less than 24 hours have been shown [Nie15].

In general, cryogenic setups are more complicated than room temperature setups as they require heat shields and thermal anchoring of the wiring. Furthermore, the operation of a cryostat costs much more than the operation of a room temperature setup. Nevertheless, over the years, multiple cryogenic ion trap experiments have been set up, such as experiments to implement atomic clocks [BMB⁺98a], to test new trap designs [BWC⁺11, Zie12], to investigate heating rates [LGA⁺08, ASA⁺09, VWB⁺13, Nie15], to study molecules [SVW⁺12, ELH⁺14], or to couple ions to solid-state systems [DGTH13].

The aim of this thesis was to design and build a cryogenic setup optimized for QIP with trapped ions. This dissertation is structured as follows: the theoretical framework for the description of quantum bits and the operation of Paul traps is introduced in Chapter 2. Chapter 3 provides theoretical insight on how to construct an RF resonator and the filters required for the operation of scalable traps in a cryogenic environment. Chapter 4 covers the design, fabrication, and characterization of the cryogenic setup developed during this thesis. The laser system and electronic setup required for the operation with Ca⁺ and Sr⁺ ions is described in Chapter 5. The characterization of the setup using trapped ions is presented in Chapter 6 and contains

heating rate measurements and Ramsey experiments. Suggestions for further improvements and future experiments are made in Chapter 7. Finally, Chapter 8 sums up the presented work.

2 Quantum information processing with trapped ions

This chapter will give an overview of QIP with trapped ions. It starts by explaining what quantum bits are and shows how to use them for QIP. In the following sections, the encoding of the qubit in the electronic level structure of ions is discussed. Furthermore, a brief introduction to Paul traps is given with a focus on micrometer scale Paul traps, called segmented traps. These segmented traps are required for scalable quantum computation with trapped ions. The second part of the chapter will cover atom-light interaction, and how to exploit it to perform gates with this interaction and to cool of ions in a trap. When building a quantum computer, it is mandatory to know the precision of the individual parameters of the quantum gate operations required to reach certain target fidelities of these operations. These requirements are discussed in Section 2.8.

2.1 Quantum Bits

Just like normal computers work with bits as their representation of information, quantum computers work with quantum bits [NC11], or short qubits. A classical bit can either be 0 or 1. A qubit is a quantum mechanical two-level system and in analogy to the classical bits, the states of a qubit are denoted $|0\rangle$ and $|1\rangle$. But in contrast to classical bits, general qubit states can be in superposition states of $|0\rangle$ and $|1\rangle$. Such a general state can be written as

$$|\Psi\rangle = \alpha |0\rangle + \beta |1\rangle \quad , \quad (2.1)$$

where α and β are complex numbers which fulfill $|\alpha|^2 + |\beta|^2 = 1$ for normalization. The qubit can be represented by a vector in a sphere, called Bloch sphere, as shown in Figure 2.1.

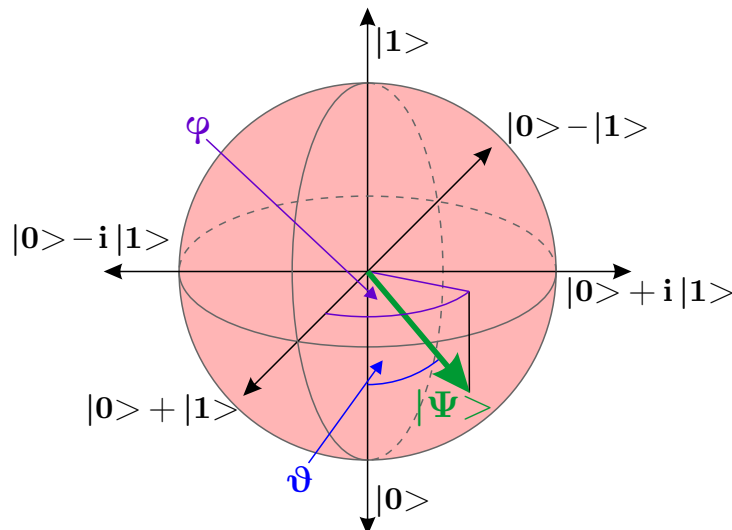


Figure 2.1.: The Bloch sphere representation of a qubit.

The computational power of quantum computers lies in the superposition. For one qubit, one needs two complex numbers to describe the state. If one uses two qubits, one will obtain a general state $|\Psi\rangle = \alpha |00\rangle + \beta |01\rangle + \gamma |10\rangle + \delta |11\rangle$ which requires four complex numbers to describe it. And generally for N qubits, one requires 2^N complex numbers to describe the state.

Hence, with 500 qubits, it is possible to store more complex numbers than there are estimated atoms in the universe [NC11].

A quantum algorithm using qubits can start with a superposition of possible states and during the computation, the probability of finding the correct states is increased, as done for example in the quantum Fourier transform (QFT) [NC11] or Shor's algorithm [Sho97]. Another feature of quantum computers is that during the computation, they make use of entanglement or "spooky action at a distance" as Albert Einstein called it [EPR35]. To understand an easy example of entanglement, one can look at the state $|\Psi\rangle = \frac{|00\rangle + |11\rangle}{\sqrt{2}}$. After the preparation of this entangled state of two qubits, one can separate the two qubits spatially without measuring their state. When the state of one qubit is measured after the separation, the state of the other qubit is defined as well. If one measured $|0\rangle$ for one qubit then the other would be $|0\rangle$. Or, if one measured $|1\rangle$ for one qubit then the other would be $|1\rangle$. This mapping of the second qubit into a well defined state happens instantly after the measurement of the first qubit and is not limited by the speed of light, thus Einstein called it "spooky action at a distance".

To build a quantum computer, the physical system has to fulfill the following criteria, suggested by David DiVincenzo [DI00].

1. A scalable physical system with well characterized qubits
2. The ability to initialize the state of the qubits
3. Long relevant decoherence times, much longer than the gate operation time
4. A universal set of quantum gates
5. A qubit-specific measurement capability

Currently, many physical systems are being investigated as suitable candidates for a quantum computer, for example trapped ions [WBB⁺03, MNM⁺16], superconducting qubits [KYG⁺07, LBC⁺12], nitrogen vacancy centers in diamond [JW06], quantum dots in silicon [VYH⁺15, LMM⁺15], ultra-cold atoms [MLX⁺15], and many more.

The subject of this thesis is QC with trapped ions. The atoms used in these experiments are mainly singly ionized elements of the group of alkaline earth metals, like Be⁺, Mg⁺, Ca⁺, Sr⁺, or Ba⁺. Other used elements are singly ionized Zn⁺, Cd⁺, Hg⁺, and Yb⁺ [Oze11]. What all these ions have in common is that when they are singly ionized, their electronic structure is very simple. The filled lower electron shells screen the nucleus and what remains is a hydrogen-like system with a single valence electron and a positive core.

In the field of trapped ions, three different types of qubits have emerged, the optical qubit [NBE⁺98, Rie05], the spin or Zeeman qubit [Oze11, Zie12], and the hyperfine qubit [BLMW04, Bla10]. Their encoding in the level structure of the ions is shown in Figure 2.2.

For an optical qubit, the ion must have a stable or meta-stable state separated by an optical transition from the ground state. Of the elements stated above, Ca⁺, Sr⁺, Ba⁺, and Hg⁺ are possible optical qubit candidates [Jam98]. In these elements, the D-state is lower in energy than the P-state. This type of qubit is called optical qubit because the energy difference between the S-state and the D-state corresponds to a frequency in the optical domain, typically hundreds of THz, and the qubit is encoded in these two energy levels. Since the transition from the S-ground state to the D-state is a dipole-forbidden transition, the D-state is metastable with lifetimes ranging from several milliseconds to tens of seconds. This is long compared to the gate time which is typically on the order of 10 μ s and thus one can perform QIP with an optical qubit [MSB⁺11, SBM⁺11, NMM⁺14].

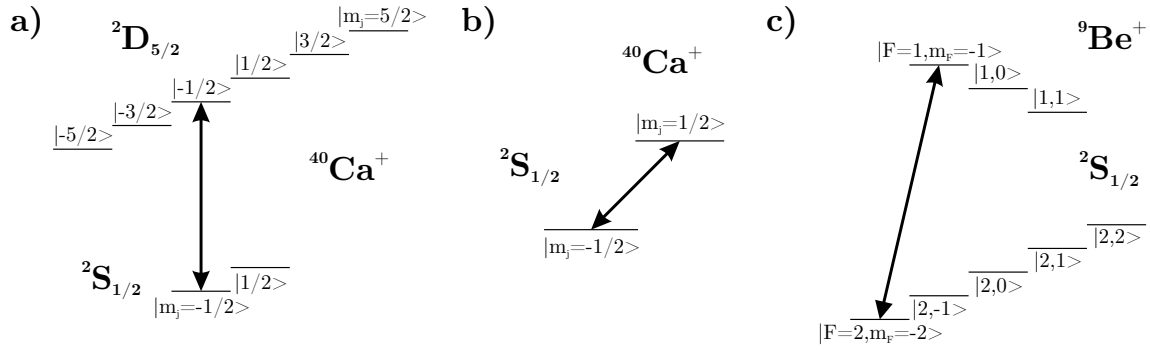


Figure 2.2.: Types of trapped ion qubits. Panel **a** shows an optical qubit with $^{40}\text{Ca}^+$, panel **b** a spin or Zeeman qubit in the ground state of $^{40}\text{Ca}^+$, and panel **c** a hyperfine qubit in the ground state of $^9\text{Be}^+$.

To avoid decoherence due to spontaneous decay from the D-state to the S-state, one can encode a qubit in the ground state of the ion. If the ion has no nuclear spin, the level splitting is only due to Zeeman shifts (Figure 2.2 b). Thus, this type of qubit is called Zeeman, or spin, qubit and for example fast ion movement [WZR⁺12] and fast ion splitting [RWK⁺14] have been demonstrated with Zeeman qubits. The transition frequencies of Zeeman qubits are typically in the low MHz regime but depend on the magnetic field used in the experiment. If the ion species has a nuclear spin, the ground state splits into two hyperfine manifolds which each experience Zeeman splitting, see Figure 2.2 c. Due to the different sign in the magnetic field sensitivity of the two hyperfine manifolds, one can find magnetic fields for which certain transitions show no linear dependence on magnetic fields but only second order dependence [BHI⁺91, Har13]. These transitions are typically called clock transitions, and these qubits are known as hyperfine qubits.

The work during this thesis was centered on optical qubits with $^{40}\text{Ca}^+$ and $^{88}\text{Sr}^+$. Hence, the following chapters will explain these in more detail.

2.2 Quantum information processing with optical qubits

Table 2.1.: Transition frequencies of $^{40}\text{Ca}^+$ and $^{88}\text{Sr}^+$ which were observed in the lab. For details on the exact frequency shifts, please refer to Chapter 5.1.

Ion species	Transition	Appr. wavelength	Exact transition freq. (THz)
$^{40}\text{Ca}^+$	$^2\text{S}_{1/2} \rightarrow ^2\text{P}_{1/2}$	397 nm = 794 nm / 2	$2 \cdot 377.6114^1$
	$^2\text{S}_{1/2} \rightarrow ^2\text{D}_{5/2}$	729 nm	411.0413
	$^2\text{D}_{3/2} \rightarrow ^2\text{P}_{1/2}$	866 nm	345.9999
	$^2\text{D}_{5/2} \rightarrow ^2\text{P}_{3/2}$	854 nm	350.8626
$^{88}\text{Sr}^+$	$^2\text{S}_{1/2} \rightarrow ^2\text{P}_{1/2}$	422 nm	710.9623
	$^2\text{S}_{1/2} \rightarrow ^2\text{D}_{5/2}$	674 nm	444.7790 [MHB ⁺ 03]
	$^2\text{D}_{3/2} \rightarrow ^2\text{P}_{1/2}$	1092 nm	274.5890
	$^2\text{D}_{5/2} \rightarrow ^2\text{P}_{3/2}$	1033 nm	290.2125

The two ion species used during this thesis were $^{40}\text{Ca}^+$ and $^{88}\text{Sr}^+$ and their level schemes can be seen in Figure 2.3. Both species have a D-level between the S-ground state and the P-excited state. Both P- and D- states have fine splitting and split into $^2\text{P}_{1/2}$ and $^2\text{P}_{3/2}$ as well as $^2\text{D}_{3/2}$

¹The 397 nm laser is a frequency-doubled laser and of which the fundamental, 794 nm, is locked. Hence, the correct frequency is twice the frequency to which the laser is locked.

and $^2D_{5/2}$. The frequencies of the optically driven transitions as observed in the lab are shown in Table 2.1. The laser frequencies were measured with a WS/6-200 wavemeter from *High Finesse*² and the laser light was frequency shifted on the order of 100 MHz by acousto optic modulators (AOMs). For details on the exact frequency shifts, please refer to Chapter 5.1.

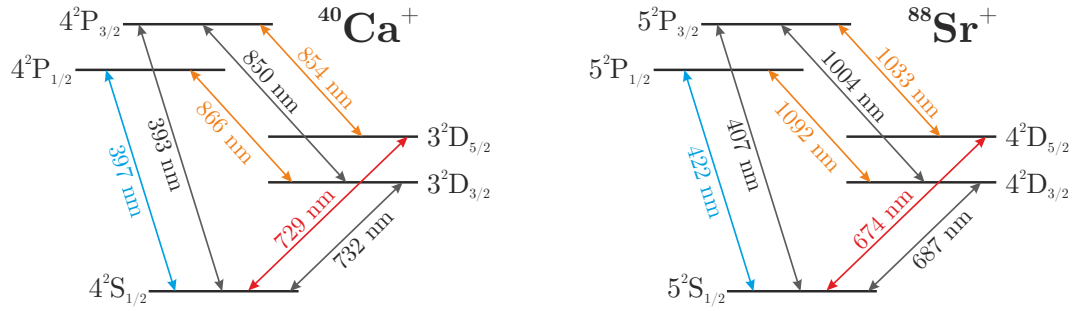


Figure 2.3.: The level schemes of $^{40}\text{Ca}^+$ and $^{88}\text{Sr}^+$.

In the following, the DiVincenzo criteria [DI00] will be discussed for an optical qubit.

I. A scalable physical system with well characterized qubits

Ions suitable as optical qubits have been introduced in the previous text, and trapping of ions is discussed in Chapter 2.3. A brief introduction to scalable trapped ion QC is given in Chapter 2.4.

II. The ability to initialize the state of the qubits

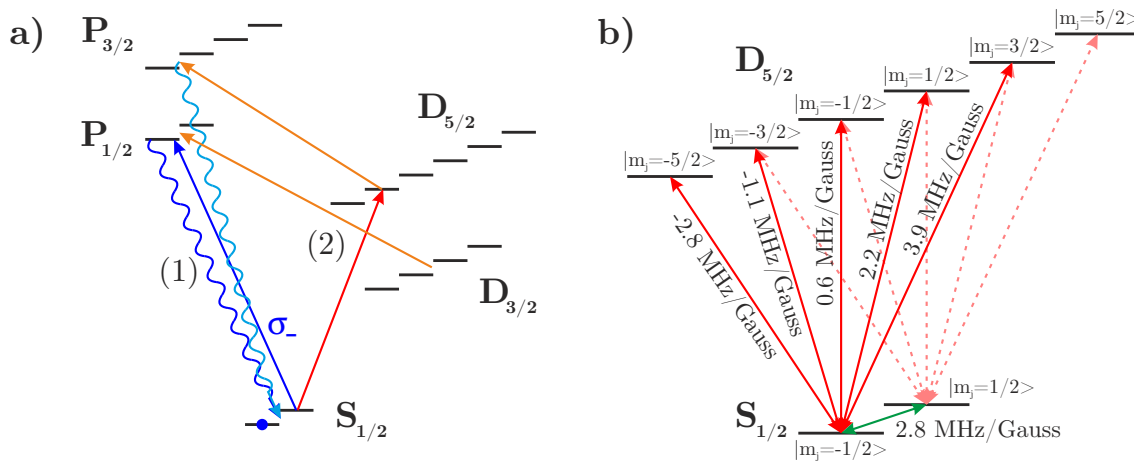


Figure 2.4.: Panel **a** shows two ways how to initialize the qubit into one ground state. Panel **b** illustrates the possible optical qubits and the Zeeman qubit with their magnetic field sensitivities.

To initialize an optical (or a Zeeman qubit), one has to transfer the whole population into one of the two ground states. In particular, optical pumping of the $|m_j = +1/2\rangle$ state into the $|m_j = -1/2\rangle$ state initializes electron population in the $|m_j = -1/2\rangle$. Figure 2.4 a shows two possible ways of such optical pumping. For option (1) in Figure 2.4 a, σ_- -polarized light couples the $|m_j = +1/2\rangle$ state of the $^2S_{1/2}$ state manifold with the $|m_j = -1/2\rangle$ state of the $^2P_{1/2}$ state manifold. The population in $|m_j = -1/2\rangle$ ground state does not couple to this transition and thus stays unaffected. The spontaneous decay from the $^2P_{1/2}$ level allows a transition into both states of the ground state manifold. If the electron ends up in the $|m_j = +1/2\rangle$ state, it will be

²HighFinesse GmbH, Auf der Morgenstelle 14, 72076 Tübingen, Germany

reexcited by the σ_- -polarized light. If it decays into the $|m_j = -1/2\rangle$ state, it is initialized and will not interact with the light field anymore.

Since this pumping technique depends on how accurate one can generate σ -polarized light, the initialization fidelity may not be high enough for successful quantum computation. Another optical pumping scheme, that does not rely on polarization but is frequency selective, is depicted in (2) of Figure 2.4 a. There, one transfers the population of $|m_j = +1/2\rangle$ state of the $^2S_{1/2}$ ground state manifold to the $|m_j = -3/2\rangle$ state of the $^2D_{5/2}$ state manifold with a resonant laser. Another laser transfers this population into the $^2P_{3/2}$ manifold from where it decays into one of the two ground states. This process is repeated until the desired fidelity of the initialization into the $|S, m_j = -1/2\rangle$ state is reached.

III. Long relevant decoherence times, much longer than the gate operation time

Typical gate times for optical qubits are between 1 and 100 μs [BKRB08, SNM⁺13]. Hence, in order to execute a quantum algorithm with about 1000 gate operation, one will require a coherence time of about 100 ms. To achieve that one has to keep in mind that ion qubits are subject to decoherence and have to be decoupled from their environment. Sources of decoherence are magnetic field noise, electric field noise, fluctuations of the intensity of the interaction field, phase fluctuations between the ion and the interaction fields, frequency offsets between the ion transitions and the interaction fields, off-resonant excitations, and electrical quadrupole shifts of the D-levels in the Paul trap.

For coherence times of several milliseconds, the biggest limiting factor is the Zeeman shift of the qubit transition [SNM⁺13]. For an arbitrary transition, the Zeeman shift [CTDL99] is given by

$$\Delta f = \frac{\mu_B}{\hbar} (g(\text{State1}) m_1 - g(\text{State2}) m_2) B \quad (2.2)$$

where μ_B is the Bohr magneton, g is the Landé factor of the level, m_i are the magnetic quantum numbers of the states, and B is the applied magnetic field. The factor μ_B/\hbar corresponds to a magnetic sensitivity of about 1.4 MHz/Gauss. The g-factors of the S- and the D-state are ≈ 2 and ≈ 1.2 respectively [TPR⁺03, BHK⁺15, Chw09]. Therefore, the magnetic sensitivity depends on the exact qubit encoding in the Zeeman sublevels and can be seen in Figure 2.4 b for different qubits.

The frequencies of motion of Paul traps (see Chapter 2.3) are typically between 10 kHz and 10 MHz. Electric field noise at a frequency of motion in a Paul trap excites motion and, thus, causes motional heating [TKK⁺00]. This heating process leads to motional decoherence, and therefore, electrical noise at the frequencies of motion in a Paul trap has to be suppressed with external circuits (see Chapter 3.2).

To suppress other decoherence sources, high precision of the intensity, frequency, and phase of the interaction field and a high control over the position of the ion in the trap are required. This required precision is discussed in Chapter 2.8 in more detail. To highlight the required stability, one can have a look at the qubit transition frequencies of Table 2.1 which are on order of $4 \cdot 10^{14}$ Hz. Hence, in order to achieve a coherence time of 250 ms, one requires a relative frequency stability of 10^{-14} . Experimentally, coherence times of tens of milliseconds have been shown [SNM⁺13].

IV. A universal set of quantum gates

For a universal set of quantum gates, one needs to be able to perform single qubit operations and multi-qubit operations [Oze11, NC11]. All gate operations are unitary and thus reversible. Although quantum computation with N ion is performed in a 2^N dimensional Hilbert space,

it has been shown that one does not require $2^N - 1$ independent unitary operations but it is possible to concatenate a small number of operations to compute in the whole Hilbert space [Deu89, BBC⁺95]. The capability to perform single qubit operations and controlled-not (CNOT) gate-operations is sufficient. CNOT gate-operations are gates for which one qubit is flipped if and only if the other qubit is in state $|1\rangle$.

One can depict single qubit operations as rotations of the state vector on the Bloch sphere [NC11]. The rotations by an angle ϑ around the three axes of the Cartesian coordinate system are then

$$R_x(\vartheta) = e^{-i\frac{\vartheta}{2}\mathbf{X}} = \cos\frac{\vartheta}{2}\mathbf{I} - i\sin\frac{\vartheta}{2}\mathbf{X} = \begin{pmatrix} \cos\frac{\vartheta}{2} & -i\sin\frac{\vartheta}{2} \\ -i\sin\frac{\vartheta}{2} & \cos\frac{\vartheta}{2} \end{pmatrix} \quad (2.3)$$

$$R_y(\vartheta) = e^{-i\frac{\vartheta}{2}\mathbf{Y}} = \cos\frac{\vartheta}{2}\mathbf{I} - i\sin\frac{\vartheta}{2}\mathbf{Y} = \begin{pmatrix} \cos\frac{\vartheta}{2} & -\sin\frac{\vartheta}{2} \\ \sin\frac{\vartheta}{2} & \cos\frac{\vartheta}{2} \end{pmatrix} \quad (2.4)$$

$$R_z(\vartheta) = e^{-i\frac{\vartheta}{2}\mathbf{Z}} = \cos\frac{\vartheta}{2}\mathbf{I} - i\sin\frac{\vartheta}{2}\mathbf{Z} = \begin{pmatrix} e^{-i\vartheta/2} & 0 \\ 0 & e^{i\vartheta/2} \end{pmatrix} \quad (2.5)$$

with the Pauli matrices

$$\mathbf{X} = \begin{pmatrix} 0 & 1 \\ 1 & 0 \end{pmatrix} \quad ; \quad \mathbf{Y} = \begin{pmatrix} 0 & -i \\ i & 0 \end{pmatrix} \quad ; \quad \mathbf{Z} = \begin{pmatrix} 1 & 0 \\ 0 & -1 \end{pmatrix} \quad (2.6)$$

and the identity matrix

$$\mathbf{I} = \begin{pmatrix} 1 & 0 \\ 0 & 1 \end{pmatrix} \quad . \quad (2.7)$$

One can generalize these rotations to rotations by an angle ϑ around a (normalized) vector $\hat{n} = (n_x, n_y, n_z)$ and obtains

$$R_{\hat{n}}(\vartheta) = e^{-i\frac{\vartheta}{2}\hat{n}\vec{\sigma}} = \cos\frac{\vartheta}{2}\mathbf{I} - i\sin\frac{\vartheta}{2}(n_x\mathbf{X} + n_y\mathbf{Y} + n_z\mathbf{Z}) \quad , \quad (2.8)$$

where $\vec{\sigma}$ denotes the three component vector (\mathbf{X} , \mathbf{Y} , \mathbf{Z}) of Pauli matrices. Other important rotation matrices, which can be performed by general rotation of the form of Eq. 2.8, are the Hadamard gate \mathbf{H} , the phase gate \mathbf{S} , and the $\pi/8$ gate \mathbf{T} :

$$\mathbf{H} = \frac{1}{\sqrt{2}} \begin{pmatrix} 1 & 1 \\ 1 & -1 \end{pmatrix} \quad ; \quad \mathbf{S} = \begin{pmatrix} 1 & 0 \\ 0 & i \end{pmatrix} \quad ; \quad \mathbf{T} = \begin{pmatrix} 1 & 0 \\ 0 & e^{i\pi/4} \end{pmatrix} \quad . \quad (2.9)$$

The physical description of single qubits gate-operations in trapped ion systems is discussed in Chapter 2.5 in more detail.

Multi-qubit gate-operations are gates whose unitary transformation cannot be decomposed into individual single qubit rotations but require interaction between at least two qubits. These gates are called entangling or controlled quantum gates and generate entanglement. One or more qubit(s) act(s) as control qubit(s) which control an interaction with target qubit(s). One example for an entangling gate is the mentioned CNOT gate, or controlled X gate. The Hilbert space for two qubits is four dimensional. Hence, a matrix representation of controlled gates between two qubits has to be a four by four matrix. For the CNOT gate, this would be

$$\mathbf{U}_{\text{CNOT}} = \begin{pmatrix} 1 & 0 & 0 & 0 \\ 0 & 1 & 0 & 0 \\ 0 & 0 & 0 & 1 \\ 0 & 0 & 1 & 0 \end{pmatrix} \quad . \quad (2.10)$$

The often used controlled Z gate, or controlled phase gate, can be described by the matrix

$$\mathbf{U}_\phi = \begin{pmatrix} 1 & 0 & 0 & 0 \\ 0 & 1 & 0 & 0 \\ 0 & 0 & 1 & 0 \\ 0 & 0 & 0 & -1 \end{pmatrix}. \quad (2.11)$$

The physical description of controlled gates in trapped ion systems is discussed in Chapter 2.6 in more detail.

V. A qubit-specific measurement capability

The detection of the optical qubit state is performed via state-dependent fluorescence [Oze11]. If the electron is in the S state manifold and light resonant with the ${}^2S_{1/2} \rightarrow {}^2P_{1/2}$ transition (Figure 2.3) is sent to the ion, the ion will start to fluoresce at this transition frequency. This fluorescence can then be detected with photo-detectors. If the electron is in the ${}^2D_{5/2}$ state manifold, the light resonant with the S-to-P transition will not interact with the ion, the ion will stay dark, and no signal will be detected on the photo-detector. For the Zeeman qubit, one has to perform an electron shelving pulse, which transfers the population of one of the Zeeman states in the ground state manifold into the D-state manifold, before one can detect with state-dependent fluorescence.

2.3 Paul traps

The Earnshaw theorem states that one cannot have an electrostatic potential minimum in all three space dimensions which would allow storage of ions [Ear42]. In at least one direction, one must have an anti-trapping potential. To circumvent this problem for trapping ions, one can either use a strong magnetic field and a direct current (DC) voltage in a Penning trap (Figure 2.5 a) [Pen36, Pie54] or a radio frequency (RF) in a Paul trap (Figure 2.5 b) [Pau90, POF58]. The latter is used in this thesis and will be described in the following.

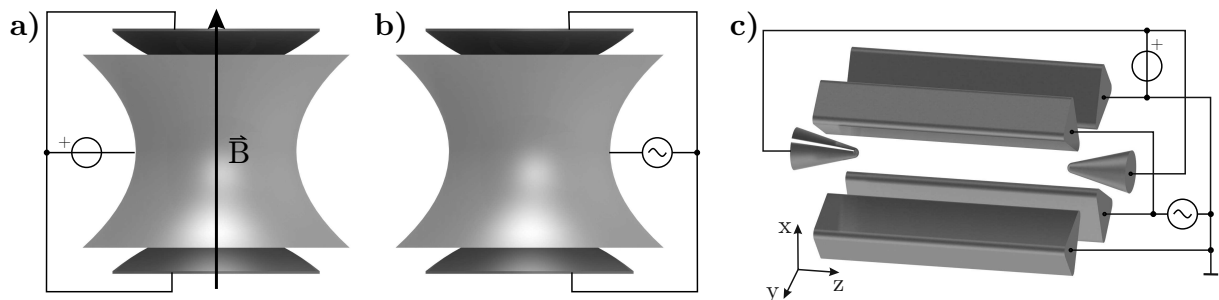


Figure 2.5.: Types of ion traps. Panel a shows a Penning trap, panel b a Paul trap, and panel c a linear Paul trap.

Due to the time-varying voltage in a Paul trap, a quadrupole field is formed in whose saddle point a charged particle can be trapped. The time-varying voltage changes the direction of confinement and anti-confinement in the trap's center, resulting in a time-averaged restoring force in all directions [MGW05]. Modern traps for QIP are linear Paul traps (Figure 2.5 c), which allow confinement of ions along a linear string. Without an additional DC voltage, the saddle potential in the XY-plane of the trap can be described as

$$\phi(\vec{r}, t) = \frac{x^2 - y^2}{r_0} V_0 \cos(\Omega t) \quad (2.12)$$

where V_0 is the applied time-varying voltage, Ω its frequency, and r_0 the minimum distance from the trap center to the electrodes. This equation holds true close to the center of the trap even if the electrodes are not hyperbolically shaped [MGW05]. The time-varying voltage generates an RF-null in the center and causes confinement in the XY-plane. For confinement along the trap axis of a linear Paul trap, the Z-direction, one can use DC voltages applied to end cap electrodes.

The conditions for stable confinement are given by the equations of motion. In the case of a linear Paul trap, one obtains equations of Mathieu type in the XY-plane [WMI+98].

$$\frac{d^2 r_i}{dt^2} - 2q r_i \cos(\Omega t) = 0 \quad \forall r_i = x, y \quad (2.13)$$

with the substitution for the trap stability parameter q

$$q = \frac{2QV_0}{mr_0^2\Omega^2} \quad (2.14)$$

where Q is the charge of the particle and m its mass. The solution of the Mathieu equations consists of two distinct frequencies, the slow *secular motion* with a radial frequencies $\omega_x = \omega_y = \frac{q\Omega}{2\sqrt{2}}$ and the superimposed fast *micromotion* at the frequency of the trap drive Ω . The secular motion frequencies in all three directions of a specific ion species depend on the applied voltages and the geometry of the trap. With additional DC-voltages, stable trapping requires a trap stability parameter q between 0 and 0.908. Due to the non-hyperbolic shape of linear Paul traps, anharmonicities of the motion of the stored ions appear when the sum of integer multiples of the secular motion frequencies add up to the trap drive frequency [GSW97]. To avoid these anharmonicities, one has to operate the trap with $q < 0.3$.

For N ions to stay in a linear string, the axial secular motion frequency ω_z and the radial secular motion frequency $\omega_r = \omega_x = \omega_y$ have to fulfill the following condition [Sch93, ESG+00]

$$\left(\frac{\omega_r}{\omega_z}\right)^2 \geq \frac{N^{1.73}}{2.53} \quad (2.15)$$

For $N = 8$, one obtains $\omega_r \geq 3.80\omega_z$. Through Eq. 2.15 and the condition $q < 0.3$, the number of ions and the desired secular motion frequencies set a lower bound for the trap drive frequency Ω , required for the choice of the trap drive frequency in Chapter 3.1.1.1.

2.4 Segmented Paul traps

Eq. 2.15 shows that when loading more and more ions into a linear Paul trap, one would have to decrease the axial confinement while increasing the radial confinement. Hence, large scale QC in a single linear Paul trap is challenging.

To solve this problem, one can use miniaturized, segmented linear Paul traps [SCR+06, WGM09]. To understand how they work, one can look at the cross-section of a normal linear Paul trap, as depicted in Figure 2.6 a. By splitting the central top ground electrode into two ground electrodes, one can fold this structure of the radial plane into a single line as shown in Figure 2.6 b. As required for trapping in a Paul trap, such a geometry results in a quadrupole potential above the central electrode, assuming that the potential opposite to the trap is ground for RF. This condition is referred to as far-field ground. The outer segments are divided along the trap axis into multiple segments, as illustrated in Figure 2.6 c. As in the case of linear Paul traps, the confinement in the axial direction in segmented traps is realized by a static potential. To

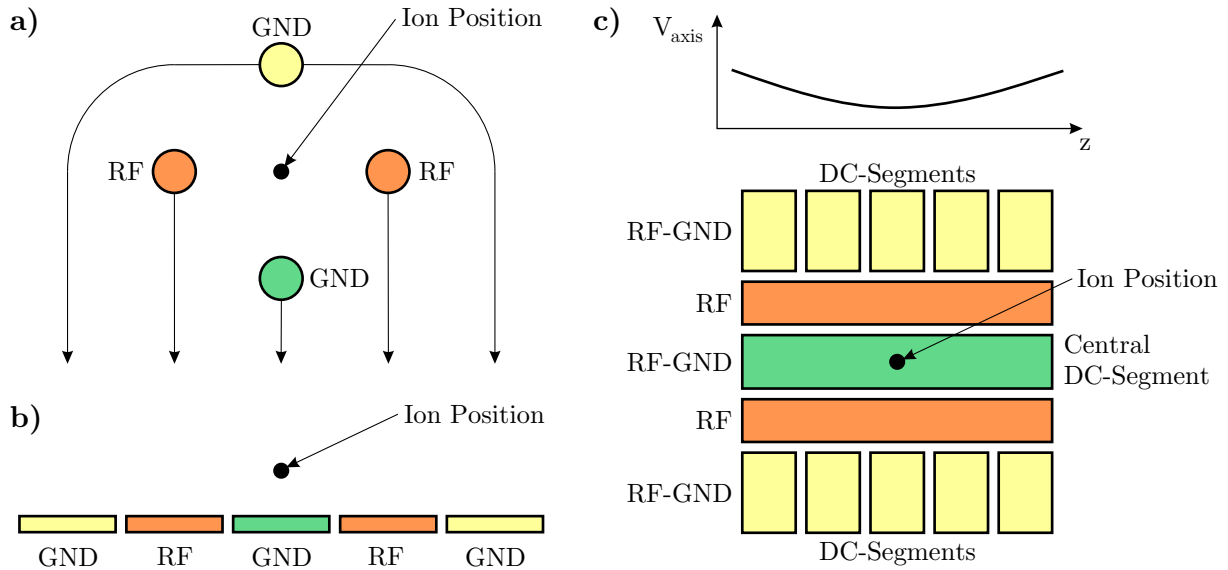


Figure 2.6.: Panel **a** shows a linear Paul trap in the radial plane. In order to get to a two-dimensional structure, one splits the top ground electrode and projects the result onto a plane, as shown in panel **b**. The outer segments, whose RF potential is ground, can then be structured along the horizontal trap axis of panel **c**. With different DC voltages on the individual segments, confinement in the axial direction is obtained.

generate a confining potential along the trap axis, one can apply static voltages to the individual segments.

If one uses a trap with many segment pairs, one can move ions chains on the chip by changing the static voltages of the segments such that the minimum of the axial potential changes position. This idea of shuttling ions resulted in a design for a scalable trapped ion QC architecture [WMI⁺98, KMW02]. In this architecture, one has loading, storing, and processing zones which consist of such segmented traps. These individual regions are connected via straight connections, X-junctions, and Y-junctions and besides movement of whole strings, it is possible to split ion chains and recombine them. Hence, it is possible to interact only with a few ions at a time while maintaining the capability to manipulate arbitrarily many ions. Experimentally, fast shuttling over hundreds of μm in less than $10 \mu\text{s}$ has been shown [WZR⁺12, BGL⁺12]. Furthermore, movements through an X-junction [BOV⁺11], a Y-junction [MHS⁺11] and splitting of ion strings [RWK⁺14] have been demonstrated.

2.5 Atom-light interaction

To describe how an atom interacts with light, one can reduce the atom with a complex level structure to the simple two-level system that is used as the qubit. The Hamiltonian of the ion without the presence of the light [Lou00, WGM09] consists of the harmonic confinement in the Paul trap and the electronic two-level system, and it is given by:

$$H_{\text{ion}} = H_{\text{motion}} + H_{\text{2level}} = \frac{\hat{p}^2}{2m} + \frac{m\omega_{\text{motion}}^2}{2}\hat{x}^2 + \frac{\hbar\omega_0}{2}\sigma_z \quad (2.16)$$

where m is the mass of the atom, \hat{p} the momentum operator, ω_{motion} the (angular) frequency of motion in the harmonic oscillator, \hat{x} the position operator, $\hbar\omega_0$ the energy splitting of the two-level system, and σ_z the z-Pauli matrix. With the creation operator $a^\dagger = (2m\hbar\omega_{\text{motion}})^{-1/2}(m\omega_{\text{motion}}\hat{q} - i\hat{p})$ and the annihilation operator

$a = (2m\hbar\omega_{\text{motion}})^{-1/2} (m\omega_{\text{motion}}\hat{q} + i\hat{p})$, the Hamiltonian for the motion in the harmonic Paul trap can be written as

$$H_{\text{motion}} = \hbar\omega_{\text{motion}} \left(a^\dagger a + \frac{1}{2} \right) \quad (2.17)$$

in its quantized form. For the interaction, one assumes a planar wave with frequency ω_{light} and phase ϕ traveling along the direction of the motion in the harmonic oscillator ($\vec{k} = k\vec{e}_x$). The interaction Hamiltonian [WGM09] is then given by

$$H_{\text{int}} = \frac{\hbar\Omega}{2} (\sigma_+ + \sigma_-) \left(e^{i(k\hat{x} - \omega_{\text{light}}t + \phi)} + e^{-i(k\hat{x} - \omega_{\text{light}}t + \phi)} \right) \quad (2.18)$$

where σ_+ and σ_- are the Pauli spin matrices, and Ω is the transition matrix element of the two-level system which is usually referred to as Rabi-frequency. The Lamb-Dicke parameter, which is defined by

$$\eta = k\sqrt{\frac{\hbar}{2m\omega_{\text{motion}}}} \quad (2.19)$$

allows a substitution $k\hat{x} = \eta(a^\dagger + a)$. Thus, the interaction Hamiltonian can be written as

$$H_{\text{int}} = \frac{\hbar\Omega}{2} \left(e^{i\eta(a^\dagger + a)} \sigma_+ e^{-i(\omega_{\text{light}}t + \phi)} + e^{-i\eta(a^\dagger + a)} \sigma_- e^{i(\omega_{\text{light}}t + \phi)} \right) \quad (2.20)$$

After changing into the interaction picture and applying the rotating wave approximation [LBMW03, WGM09], the obtained interaction Hamiltonian takes the form

$$H_{\text{int}}(t) = \frac{\hbar\Omega}{2} \left(\sigma_+ e^{i\eta(a^\dagger e^{i\omega_{\text{motion}}t} + a e^{-i\omega_{\text{motion}}t})} e^{i(\phi - \delta t)} + h.c. \right) \quad (2.21)$$

where the detuning $\delta = \omega_{\text{light}} - \omega_0$. In the Lamb-Dicke regime ($\eta^2(2n+1) \ll 1$ with n being the number of phonons in the ion crystal), the wave packet of the ion in the trap is much smaller than the wavelength of the interacting light and one can perform an expansion retaining the lowest order in η obtaining

$$H_{\text{int,LD}}(t) = \frac{\hbar\Omega}{2} \left(\sigma_+ \left(1 + i\eta \left(a^\dagger e^{i\omega_{\text{motion}}t} + a e^{-i\omega_{\text{motion}}t} \right) \right) e^{i(\phi - \delta t)} + h.c. \right) \quad (2.22)$$

From this, it follows that it is possible to influence both the internal levels of the ion as well as the motion of the ion with external laser fields. If the detuning $\delta = -\omega_{\text{motion}}$, a phonon is removed from the system when the two-level system is excited. In this case, one speaks of the red sideband and the obtained Rabi frequency is

$$\Omega_{\text{red}} = \Omega_{n,n-1} = \sqrt{n} \eta \Omega \quad (2.23)$$

If the detuning $\delta = \omega_{\text{motion}}$, a phonon is created in the system when the two-level system is excited. In this case, one speaks of the blue sideband and the resulting Rabi frequency is

$$\Omega_{\text{blue}} = \Omega_{n,n+1} = \sqrt{n+1} \eta \Omega \quad (2.24)$$

For the case $\delta = 0$, one couples the two states $|0, n\rangle$ and $|1, n\rangle$ with the same number of phonons. This is called a carrier transition and results in a Rabi frequency

$$\Omega_{\text{carrier}} = \Omega_{n,n} = \Omega(1 - \eta^2 n) \quad (2.25)$$

where the term $-\eta^2 n$ is a higher order correction term. The time evolution [NC11, Ben08] is then a rotation on the Bloch sphere and is given by

$$U(t) = \begin{pmatrix} \cos(\Omega t) & -ie^{i\phi} \sin(\Omega t) \\ -ie^{i\phi} \sin(\Omega t) & \cos(\Omega t) \end{pmatrix} = R(\theta = \pi/2, \phi) \quad , \quad (2.26)$$

where θ is the vertical Euler angle. Since $\theta = \pi/2$, the rotation axis lies in the equatorial plane and is given by $\cos(\phi) \vec{e}_x + \sin(\phi) \vec{e}_y$. In the experiment, the phase of the first rotation defines the coordinate system of the Bloch sphere and phases of all following rotations have to be adjusted with respect to the phase of the first rotation.

2.6 Entangling gates

In the previous chapter, it was shown that with precise control over the Rabi frequency, the timing, the frequency and phase of the interaction light, it is possible to perform single qubit rotations on the Bloch sphere. But when the field of quantum computation emerged, it was unclear how multiple isolated two-level systems could interact to perform entangling gates. In 1995, Cirac and Zoller suggested to use Coulomb interaction between ions, thus the phonons in an ion crystal, for the interaction between multiple ions [CZ95]. Their original idea still had the disadvantage that it required the ion strings to stay in the ground state of the motion in the trap which proved difficult to achieve in experiments [BKRB15]. In 1999, Mølmer and Sørensen [SM99] proposed a gate which allows quantum computation in the presence of thermal motion.

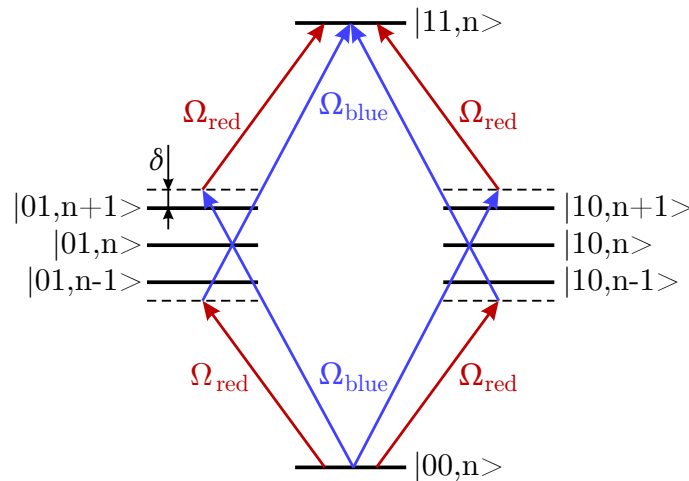


Figure 2.7.: The level scheme and the transitions involved in a Mølmer-Sørensen gate.

Figure 2.7 shows the scheme of the Mølmer-Sørensen gate [BKRB08]. The gate itself is realized with a two-photon process with a detuning δ coupling the two levels $|00, n\rangle$ and $|11, n\rangle$ via phononic sidebands. This two-photon process is performed with two laser frequencies. Quantum mechanically, there are four different energy levels responsible for the coupling. These four paths interfere destructively if $\delta/(2\pi) = 1/T$, where T is the gate time. After a full population transfer, one ends up with a state $|00, n\rangle + e^{i\phi} |11, n\rangle$. This obtained state is an entangled state and thus the Mølmer-Sørensen gate can be used for quantum computation [MSB⁺11, SBM⁺11, MNM⁺16].

2.7 Laser cooling of trapped ions

The higher order correction term $-\eta^2 n$ in Eq. 2.25 causes a dependence of the Rabi frequency of a carrier transition on the phonon number in the ion crystal. To perform gate operations with

a well-defined Rabi frequency, and thus with high fidelity, the ions have to be cooled near the ground state of motion in the trap. In the following, several laser cooling schemes are discussed.

Doppler cooling

In the semi-classical description of Doppler cooling of ions in a trap [MGW05, Roo00], light close to resonance with two energy levels in the ion interacts with the ion. The absorption of a photon of the light field transfers the momentum $\hbar\vec{k}_{\text{light}}$ onto the ion. The following emission of a photon causes another recoil. Because of isotropic emission, the average momentum transfer over many emission processes is zero. Thus, if the detuning δ of the laser is chosen such that it is lower than the frequency of the two-level system ($\delta = \omega_{\text{light}} - \omega_{\text{2level}} < 0$), the momentum from the motion of the ion is required for absorption. On average, no momentum is generated during emission. Therefore, this leads to an effective cooling of the ion in the trap. For $\delta = -\Gamma/2$, where Γ is the linewidth of the cooling transition, one can reach the lowest motional energy $k_{\text{B}}T = \hbar\Gamma/2$. Expressed as a minimum mean phonon number, this yields $\bar{n}_{\text{min}} = \Gamma/2\omega_{\text{motion}}$.

Optical sideband cooling

Optical sideband cooling can be used to cool ions to the ground state of motion [RZR⁺99], but it is only possible in the Lamb-Dicke regime where the individual motional sidebands in a frequency spectrum are resolved. In this regime, it is possible to drive red sideband transitions from the $|S, n\rangle$ state to the $|D, n-1\rangle$ state. This process removes one phonon from the ion crystal. To get the ion into the $|S, n-1\rangle$ state, spontaneous decay from the $|D, n-1\rangle$ state is too slow because of the long life time of the excited state. Hence, light resonant with the $D_{5/2}$ and $P_{3/2}$ transition excites the electron to the $P_{3/2}$ level from where it will decay back to the $|S, n-1\rangle$ state with a low probability to generate a phonon (Lamb-Dicke condition). Thus, one cooling cycle removes one phonon from the system. The process can be repeated until the ground state of motion is reached as illustrated in Figure 2.8 a.

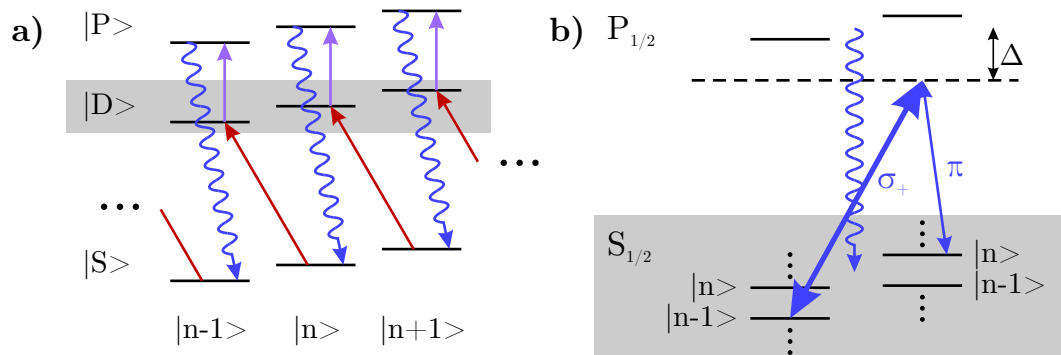


Figure 2.8.: The schemes of sideband cooling **a** and Raman cooling **b**.

Raman cooling

With sideband cooling, it is possible to reach the zero phonon state with very high probability. This comes at the price that it requires a dipole-forbidden transition and is, thus, slow. Another way to cool ion crystals to the ground state of motion is to use Raman cooling [MMK⁺95]. A detailed explanation of Raman cooling can be found in the PhD thesis of Daniel Nigg [Nig16]. A brief explanation is as follows: as depicted in Figure 2.8 b, the cooling process is a Raman process in which σ_{+} - and π -polarized light couple the two Zeeman levels of the $S_{1/2}$ ground state. The detuning Δ from the $P_{1/2}$ state is typically several GHz. The frequencies of the Raman beams are chosen such that the states $|m_j = -1/2, n-1\rangle$ and $|m_j = 1/2, n\rangle$ are coupled. The σ_{+} -polarized light is much higher in intensity than π -polarized light and thus the probability to off-resonantly excite the $|m_j = -1/2, n-1\rangle$ state to the $P_{1/2}$ level is much higher than for

the $|m_j = 1/2, n\rangle$ state. The decay back to the $|S\rangle$ state has high probability to not change the phonon number in the system. If the electron decays to the $|m_j = 1/2, n - 1\rangle$ state, a cooling cycle is completed. Since Raman cooling uses a dipole transition, it is faster than sideband cooling but the resulting average phonon number after cooling is higher and limited by the detuning and the light intensities. The fast speed of Raman cooling makes it useful for in-sequence recooling of ion strings.

EIT cooling

Both sideband and Raman cooling only cool one vibrational mode. Hence, if one wants to cool all vibrational modes of a long ion string, cooling can take up most of the time of one measurement cycle. The solution to this is multimode cooling, for example with electromagnetically induced transparency (EIT) cooling [MEK00, RLM+00]. A detailed explanation of EIT cooling can be found in the PhD thesis of Regina Lechner [Lec16]. A brief explanation is as follows: For EIT cooling, one requires a Λ -level scheme similar to the one used in Raman cooling (Figure 2.8 b) with a ground state $|g\rangle$, an excited state $|e\rangle$, and another stable or metastable state $|r\rangle$. One transition is driven hard which cancels the absorption on another transition. Therefore, EIT is also often called dark resonance as it is a quantum mechanical interference phenomenon in three-level systems. With the right choice of detunings and intensities, it is possible to suppress the absorption of the $|g, n\rangle \rightarrow |e, n\rangle$ transition (where n is the phonon number) and reduce the absorption on the $|g, n\rangle \rightarrow |e, n + 1\rangle$ transition while enhancing the absorption on the $|g, n\rangle \rightarrow |e, n - 1\rangle$ transition. This leads to strong cooling while suppressing the carrier. EIT cooling uses dipole transitions for fast cooling and is multimode. Thus, it is the most efficient cooling method presented here.

2.8 Estimate the fidelity of single qubit operations

When building a quantum computer, it is mandatory to know how technical imperfections affect the operation of the quantum computer. Different error correction schemes require different fidelities [NC11, CS96, Ste96, SBM+11, NMM+14]. Thus, it is useful to look at what precision of operation results in what fidelity, or error rate (infidelity), as thresholds for error correction procedures assume an infidelity of each gate operation. In the following, only single qubit rotations and their required precision will be investigated. This is performed by looking at the effect of imperfect control parameters onto gate operations, such as the light intensity or the gate time for a specific implementation of this operation.

In the mathematical analysis, each gate operation is treated separately in dependence of a control parameter p_i , where i represents the index of the gate operation, and each algorithm is repeated many times. Assuming only fluctuations in the control parameters in the following, the result of each quantum algorithm is a pure state, the ensemble of all copies is a mixed state $\rho_{\text{exp}} = \sum_j |\psi_j\rangle \langle \psi_j|$, where $|\psi_j\rangle$ is the resulting experimental state after iteration j . The fidelity of this mixed state is given by

$$\mathcal{F} = \text{Tr}(\rho_{\text{ideal}}\rho_{\text{exp}}) = \sum_j \text{Tr}(\rho_{\text{ideal}} |\psi_j\rangle \langle \psi_j|) \quad (2.27)$$

with ρ_{ideal} being the density matrix of the ideal algorithm execution. The term $\rho_{\text{ideal}} |\psi_j\rangle \langle \psi_j|$ represents the fidelity of a pure state and, thus, can be written as

$$\mathcal{F}_{\text{pure},j} = |\langle \varphi | \psi_j \rangle|^2 \quad (2.28)$$

where $|\varphi\rangle$ is the resulting ideal state. The expected process fidelity is the mean of $\mathcal{F}_{\text{pure},j}$ averaged over all input states j . $\mathcal{F}_{\text{pure},j}$ is given by the mean fidelity for input state j over the fluctuating control parameter p_i .

The fidelity of one interaction $\mathcal{F}_{\text{pure},j}$ is the product of the fidelities of the individual operations $\mathcal{F}_{\text{pure},i}$ which depend on the control parameter p_i . Hence, if the distribution of p_i is known, one can calculate the fidelities $\mathcal{F}_{\text{pure},i} = |\langle \varphi_i | \psi_i \rangle|^2$ of the individual gate operations, and thus $\mathcal{F}_{\text{pure},j}$ and \mathcal{F} . The infidelity is defined as $\mathcal{I} = 1 - \mathcal{F}$.

Real quantum gates will suffer from infidelities of many sources. However, to simplify the treatment in the following, a single noise source is picked while assuming that all other parameters are ideal. These parameters of single qubit gates, which are discussed here, are rotation angle and rotation axis on the Bloch sphere, and spontaneous photon scattering.

2.8.1 Rotation angle

The rotation angle on the Bloch sphere due to a resonant light pulse is Ωt , where Ω is the Rabi frequency as defined Eq. 2.26 for carrier rotations and t is the time. Because of the assumption that this is the only source of infidelity, the Bloch sphere can be simplified to a circle, for example in the XZ-plane, as depicted in Figure 2.9 a. The overlap between the ideal state $|\varphi\rangle$ and the imperfect state $|\psi\rangle$ is proportional to $\cos(\Omega t - \Omega_0 t_0)$, where Ωt is the real rotation angle and $\Omega_0 t_0$ is the ideal rotation angle. The infidelity of a single gate operation due to rotation is therefore

$$\mathcal{I} = 1 - \cos^2(\Omega t - \Omega_0 t_0) = \sin^2(\Omega t - \Omega_0 t_0) \quad . \quad (2.29)$$

The biggest rotation angle required for quantum computation is π , because any bigger angle can be reached by rotating in the opposite direction with an angle smaller than π . Such rotations will therefore have the highest absolute error for a given relative error. In the following, let us assume an average rotation³ where $\Omega_0 t_0 = \pi/2$ and assume that perfect timing can be achieved. Thus, $t = t_0$ and one can write

$$\mathcal{I} = \sin^2\left(\frac{\pi}{2}\left(\frac{\Omega}{\Omega_0} - 1\right)\right) = \sin^2\left(\frac{\pi}{2}\Omega'\right) \quad (2.30)$$

where $\Omega' = \frac{\Omega}{\Omega_0} - 1$ is the relative error in Rabi frequencies. The Rabi frequency depends on the quantum mechanical transition matrix element and the applied electric field [Lou00, Ben08]. Hence, the Rabi frequency is proportional to the square root of the intensity of the interaction field ($\Omega \propto E \propto \sqrt{I}$).

$$\mathcal{I} = \sin^2\left(\frac{\pi}{2}\left(\sqrt{\frac{I}{I_0}} - 1\right)\right) = \sin^2\left(\frac{\pi}{2}\delta\right) \quad (2.31)$$

where $\delta = \sqrt{I/I_0} - 1$ is the relative error of the intensity of the interaction field, which is an electric field. After a binomial expansion of the relative intensity fluctuations $\Delta I = I/I_0 - 1$, one obtains $\mathcal{I} \approx \sin^2(\pi/4 \Delta I) \approx (\pi/4 \Delta I)^2$ for small ΔI . The dependence of the gate infidelity on relative intensity fluctuations during a $\pi/2$ -gate operation is depicted in Figure 2.9 b, where $x_0 = I_0$ for the ideal intensity and $x = I$ for intensity during the real gate operation.

For these fidelity estimates, the intensity of the interaction field at the position of the ion matters. Hence, experimentally, one has to make sure that the intensity of the interaction field is not influenced by environmental conditions, like beam pointing instabilities of the laser beam due to turbulence in air.

With the same assumptions as for the Rabi frequency, timing errors can be treated. For $\Omega_0 t_0 =$

³Although, a worst-case rotation would be a π rotation which would cause an error that is up to a factor $2^2 = 4$ higher.

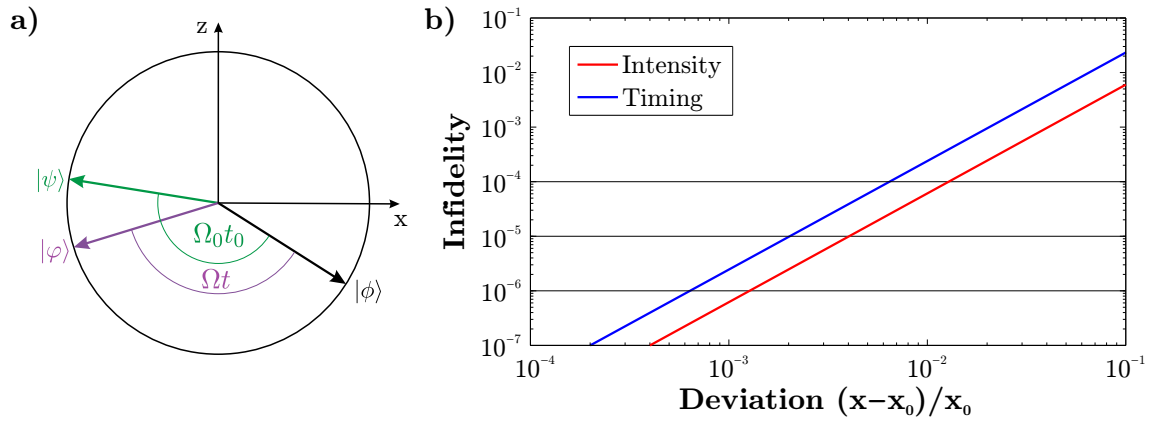


Figure 2.9.: Panel **a** illustrates two rotations in the XZ-plane of a Bloch sphere, where $|\phi\rangle$ is the initial state, $|\varphi\rangle$ the resulting state after an imperfect rotation, and $|\psi\rangle$ the resulting state after a perfect rotation. Panel **b** depicts the infidelity of a $\pi/2$ -gate operation for imperfect rotations due to intensity fluctuations and timing jitter, where the relative deviation of the corresponding control parameter is given as $(x - x_0)/x_0$.

$\pi/2$ and $\Omega = \Omega_0$, one obtains for its dependence

$$\mathcal{I} = \sin^2 \left(\frac{\pi}{2} \left(\frac{t}{t_0} - 1 \right) \right) = \sin^2 \left(\frac{\pi}{2} t' \right) \quad (2.32)$$

where t' is the relative error in timing. The dependence of the gate infidelity on the timing is depicted in Figure 2.9 b, where $x_0 = t_0$ for the ideal gate time and $x = t$ for gate time during the real gate operation.

Timing errors originate in a jitter in the involved components. Typically, one should assume timing jitters higher than 100 ps⁴ suggesting a minimum gate time of about 100 ns to 1 μ s to achieve 10^{-6} infidelity. Gates driven by laser light are mainly performed with AOMs. There, an acoustic wave has to pass through a crystal and acoustic processes have typically higher jitter, usually on the order of several ns. As shown in Figure 2.9 b, a gate infidelity of 10^{-6} or better requires a relative timing deviation of less than 10^{-3} . Therefore, the minimum gate time to achieve 10^{-6} infidelity will be on the order of about 10 μ s. To reduce jitter when switching light beams on and off, one can work with electro-optic modulators (EOMs).

Another aspect that changes the rotation angle in the Bloch sphere is the phonon number. Eq. 2.25 contains the higher order correction term $-\eta^2 n$ which depends on the phonon number n and the Lamb-Dicke parameter η . In the case of optical qubits, the Lamb-Dicke parameter η is typically on the order of 10 %. If an ion string is in a thermal state after cooling, the thermal distribution of motional states will result in different Rabi frequencies due to a different phonon population after each cooling. Since the Rabi frequency in the experiment is optimized for a mean phonon number, the thermal occupation of the state of motion in the trap will alter the fidelity of the gate operations. Besides the thermal distribution, heating also affects the Rabi frequency. If one assumes for example $\eta = 5$ % and one assumes further that the experiment starts in the ground state of motion, heating of 3 phonons during the execution of a quantum algorithm will result in $n = 3$, after which the infidelities for each gate operation are higher than 10^{-4} .

⁴One can engineer electrical circuits to only have about 10 ps jitter, but typical experiments are not optimized for low jitter. In general, it is not possible to state that a certain amount of jitter will occur in the experiment. For such a statement, one has to look in the datasheets of all involved electrical components and calculate the resulting jitter. The stated value of higher than 100 ps is only an estimate for typical conditions.

2.8.2 Stability of the rotation axis

Coherence [Gla63] is a term adapted from optics which is also crucial for QC. The basic idea is that the phase of two frequency sources must not drift apart to still be able to see interference fringes. In QC, the frequency of one source is given by the energy splitting of the two-level system, whereas the other source is the frequency of the driving field which has to be synchronous to the energy splitting. The phase of the interaction field defines the rotation axis in the XY-plane of the Bloch sphere, as described in Chapter 2.5, and phase drifts between the phase in the two-level system and the phase in the interaction field will alter the rotation axis and, thus, decrease the fidelity of the operation. These phase errors can originate from the following sources:

- **Frequency instability:** for optical qubits, the transition frequency is about 400 THz and lasers typically used as qubit lasers have a linewidth of about 1 Hz [Pos15]. This 1 Hz uncertainty will lead to a phase uncertainty of $2\pi \cdot 10^{-3}$ after 1 ms. In order to determine the phase with $2\pi \cdot 10^{-3}$ precision after 1 s, one would need a relative frequency stability of about $2.5 \cdot 10^{-18}$. For hyperfine qubits, coherence times of 50 s have been demonstrated with $^{43}\text{Ca}^+$ [HAB⁺14] which has a transition frequency of 3.2 GHz. If one wants to measure the phase of such a qubit with $2\pi \cdot 10^{-3}$ precision after 50 s idle time, one will require a frequency source with $6.25 \cdot 10^{-15}$ relative stability.
- **Zeeman shifts:** trapped ion qubits are sensitive to Zeeman shifts which alter the energy difference between the qubit states. Hence, the magnetic field has to be stabilized so that the phase error during one experiment is minimized. For example, a Zeeman qubit has a magnetic field sensitivity of 2.8 MHz/Gauss [TPR⁺03, CTDL99]. Therefore, a magnetic field offset of only 360 nGauss will cause a frequency offset of 1 Hz.
- **AC-Stark shifts:** near-resonant interaction fields can couple to the two-level system. This coupling is called AC-Stark shift and alters the energy difference between the two states. Thus, the phase of the qubit will drift with respect to the external frequency source. This effect can be desired and one can use it to perform gates [Mon11] with AC-Stark shifts as they represent rotations around the z-axis of the Bloch sphere. But when driving resonant fields during quantum gates, undesired AC-Stark shifts arise from nearby spectator levels. Their effect must be determined to account for the unknown but constant phase evolution during quantum computation.
- **Spatial position:** even if the frequencies of the interaction field and the two-level system are equal, phase offsets can occur due to a change of the distance between the ion and the frequency source. This length change can be caused by movement of the ion inside the trap or it can be caused by a phase offset in the electrical cables or in optical fibers. Especially for optical qubits, suppressing the length fluctuations can be challenging. For example, the optical qubit transition of $^{40}\text{Ca}^+$ is 729 nm. Hence, optical path length changes between the laser source and the trapping position of about 0.7 nm result in a phase error of $2\pi \cdot 10^{-3}$.
- **Electrical quadrupole shifts:** similar to Zeeman shifts, electrical quadrupole shifts cause frequency shifts of the two-level system. They occur in optical qubits when the D-level interacts with the quadrupole potential of the Paul trap [Ita00]. Hence, the ions have to be placed in the RF-null as well as possible to minimize these shifts. In ion chains with more than 10 ions in linear Paul traps, these shifts are on the order of 10 Hz.

For the fidelity estimate due to phase drifts, the rotation angle Ωt is assumed to be constant. In the following, the rotation angle is set to $\pi/2$. For such gates, the error depends on the initial state of the qubit. To perform a worst case estimation, the initial state is chosen as one of the poles of the Bloch sphere. In this case, the rotation ends in the equatorial plane. Figure 2.10 a

depicts two of such rotations in the Bloch sphere with a phase mismatch $\Delta\varphi$. The resulting infidelity of a single gate operation is given by

$$\mathcal{I} = 1 - \cos^2(\Delta\varphi) = \sin^2(\Delta\varphi) \quad (2.33)$$

and illustrated for a varying phase mismatch $\Delta\varphi$ in Figure 2.10 b. In this worst case fidelity estimation, a phase mismatch of $2\pi \cdot 10^{-3}$ corresponds to an infidelity of about $4 \cdot 10^{-5}$.

In the field of experimental QC, it is usual to state a decay time of a used coherence measure to compare the coherence of different systems. But the restriction to the phase mismatch shows that it is not very useful to perform long quantum algorithms when the phase of the two-level system is not accurately known. Hence, one has to keep in mind that high-fidelity quantum computation can only be performed in a certain fraction of the stated decay time.

2.8.3 Spontaneous photon scattering

For QIP, ions are usually treated as two-level system. But as seen in sideband and Raman cooling (Figure 2.8), the electronic level structure contains many energy levels. Although transitions to energy levels which should stay unpopulated are not directly driven, off-resonant excitations into such an energy level are possible and have to be avoided, as the subsequent spontaneous decay is an incoherent process.

The rate of off-resonant excitation γ [VW94, Stu12] can be approximated by

$$\gamma \approx \left(\frac{\Omega}{2\Delta}\right)^2 \Gamma \quad (2.34)$$

for large detunings ($\Delta \gg \Omega$), where Ω is the driven Rabi frequency, Δ is the detuning, and Γ is the scatter rate of the transition. A good example for desired off-resonant excitation is Raman cooling, displayed in Figure 2.8 b. There, a Raman process between the two Zeeman ground state levels is driven via the P-level of the ion. The cooling cycle can only be completed when the σ_+ -polarized light off-resonantly excites a P-state and decays back down to the ground state.

As the spontaneous decay following an off-resonant excitation is an incoherent process, the detuning and Rabi frequency have to be chosen such that these processes happen so rarely that

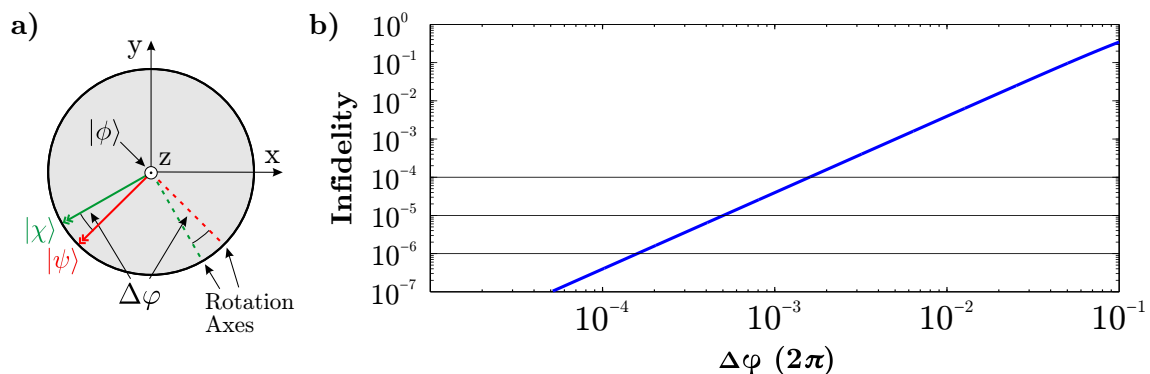


Figure 2.10.: Panel a) shows the top view of the Bloch sphere with two $\pi/2$ -rotations from the pole to the equatorial plane, where $|\phi\rangle$ is the initial state, $|\chi\rangle$ the resulting state after an imperfect rotation, and $|\psi\rangle$ the resulting state after a perfect rotation. The phase mismatch between the two-level system and the interaction field is $\Delta\varphi$. The resulting infidelity of $\pi/2$ -rotations as a function of the angle offset is shown in Panel b).

the target fidelity can be achieved [OIB⁺07]. If there are multiple energy levels which might be subject to off-resonant excitations, the sum of all rates has to stay below the threshold for the error model. For example, a Rabi frequency of 1 MHz with a detuning of 1 GHz on a dipole transition with a scatter rate of 10 MHz results in a rate of off-resonant excitation of 2.5 Hz. If it is possible to drive on average 25000 gates per second using these parameters, about 1 in 10000 gates will result in decoherence due to off-resonant excitation.

2.8.4 Summary of the required precision

Table 2.2.: A summary of the required precision for individual parameters of a trapped ion experiment to achieve a certain infidelity of single qubit operations. ΔI corresponds to relative fluctuations in the light intensity, Δt to relative timing uncertainty, $\Delta\varphi$ to phase uncertainty, and P_{raman} is the required laser power for a Raman transition in $^{43}\text{Ca}^+$ as derived in reference [OIB⁺07] for Gaussian beams with $w_0 = 20 \mu\text{m}$ and a detuning of -442 GHz.

Infidelity	ΔI	Δt	$\Delta\varphi (2\pi)$	P_{raman}
10^{-4}	1.2 %	$6.4 \cdot 10^{-3}$	$1.6 \cdot 10^{-3}$	1.7 mW
10^{-5}	$4.0 \cdot 10^{-3}$	$2.0 \cdot 10^{-3}$	$5.0 \cdot 10^{-4}$	17 mW ⁵
10^{-6}	$1.2 \cdot 10^{-3}$	$6.4 \cdot 10^{-4}$	$1.6 \cdot 10^{-4}$	170 mW ⁵

The presented formalism relates the fidelity to fluctuations of control parameters, like light intensity fluctuations or time jitter. Table 2.2 sums up the required precision for the different parameters, as discussed in the previous chapters.

⁵ Value extrapolated from calculations in reference [OIB⁺07].

3 Electronics: Resonator and Filter Design

This chapter covers the design and fabrication of electronics which have to be placed inside the vacuum chamber, or even the inner heat shield of a cryostat, because they must be operated close to the trap to function properly. The electronics, used in the cryostat built during the course of this thesis, are described in detail in Chapter 4. Chapter 3.1 is a study on the design and fabrication of radio-frequency (RF) resonators to generate the high RF voltages required for operation of Paul traps. This part mainly follows the publication "Cryogenic resonator design for trapped ion experiments in Paul traps" [BSMB16] but is more detailed on certain topics than the journal publication. In Chapter 3.2, the design of filter electronics is described, which is used to filter unwanted frequencies on the DC lines of segmented Paul traps.

3.1 Resonator Design

The operation of Paul traps requires high RF voltages, which are usually generated with the aid of the voltage gain present in RF resonators. For this purpose, helical resonators are typically used in the frequency regime up to 50 MHz, whereas for experiments requiring higher drive frequencies coaxial resonators have been used as well [MS59, SSWH12, JMBW95]. In cryogenic experiments, the resonator needs to fulfill different criteria than in room temperature experiments where the resonator can be placed outside the vacuum vessel. In particular, the connections in a cryostat need to have low thermal conductivity to limit the thermal load. Following the Wiedemann-Franz law [FW53], this results in a low electrical conductivity between room-temperature and the cryogenic parts of the experiment. Thus, the resonators have to be operated at the cold-stage. Moreover, space constraints are stricter in cryogenic systems which make helical resonators undesirable as they are generally bulky¹. To minimize the volume of the resonator, an RLC-series-resonator can be used [GNK⁺12].

3.1.1 General considerations

In this chapter, general considerations in resonator design are discussed which are not limited to a specific resonator type.

3.1.1.1 Choosing the trap drive frequency

In any resonator design, but especially in a cryogenic resonator design, it is important to consider the losses and its scaling with frequency. From the solution of the equation of motion of a trapped ion in a Paul trap (Mathieu equation) in Chapter 2.3, one obtains the trap voltages with the stability parameter $q \propto \frac{V}{\Omega^2}$ (Eq. 2.14) where V is the amplitude of the RF-voltage at the trap and Ω is the trap drive (angular) frequency. Hence, for constant q the loss power scales as

$$P \propto V^2 \propto \Omega^4 \quad . \quad (3.1)$$

A low trap drive frequency will reduce the losses. However, for the operation of ion trap experiments, the secular motion frequencies are of utter importance. When designing an RF resonator for a trapped ion experiment, the secular motion frequencies are chosen as follows.

¹Helical resonators have been used in cryogenic systems [PBIW96].

- The gate operations in trapped ion experiments are performed with light pulses. The spectral width of narrow linewidth light pulses is given by the Fourier transform of its pulse shape over time. Undesired excitations limit the gate speeds. Thus, higher secular frequencies will allow for faster gates.
- The distances between ions decrease with increasing axial secular frequency and increasing number of ions [Jam98]. A full set of quantum gate operations requires single ion addressing. Hence, the available numerical aperture for single ion addressing sets a limit on the highest axial motion frequency. However, it is possible to decrease the axial confinement to address ions.
- The ions should usually stay in a string and not transition into a zigzag-configuration during the quantum gates. To avoid this, the secular frequencies have to fulfill Eq. 2.15. For a string of 8 ions, this yields $\omega_r \geq 3.80 \omega_z$.
- The heating rate of an ion trap decreases with increasing frequency of the secular motion [BKRB15], suggesting higher frequencies of secular motion for lower heating rates.
- Locked lasers have servo bumps [Pos15, Ger15]. In order to avoid excitations on the carrier due to the servo bumps when driving a motional sideband, one has to make sure that the frequencies of secular motion are higher than the highest frequency of a servo bump, which is typically on the order of 1 MHz.
- The Lamb-Dicke parameter η scales as $\frac{1}{\sqrt{\omega_{\text{secular}}}}$ (Eq. 2.19). Hence, higher frequencies of secular motion require higher light intensities for the same gate times.

As mentioned in Chapter 2.3, traps have to be operated with a stability parameter $q < 0.3$ to avoid anharmonicities due to the non-hyperbolic shape of the electrodes in modern Paul traps. In the following, q should be around 0.25, and the axial frequency of secular motion should be 1 MHz. Therefore, one can write for a string of 8 ions that the radial frequency of secular motion has to be greater than 3.8 MHz. Since $\omega_r = \frac{q\Omega}{2\sqrt{2}}$, one obtains a trap drive frequency around 43 MHz, and simulations of the trap for this resonator show that a drive voltage of about $170V_{\text{rms}}$ is required to reach the desired frequencies of secular motion. In order to limit the thermal load onto the cryostat from dissipated power in the resonator, this voltage should be reached with less than 100mW of RF input power. This power corresponds to a consumption of about 1/7 liters of liquid helium per hour when operating a wet cryostat at 4.2 K [Eki06].

3.1.1.2 Matching

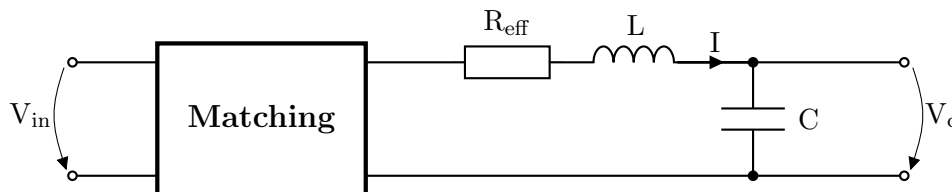


Figure 3.1.: An RLC-series-resonator with a matching network used to generate high RF-voltages at the trap

Figure 3.1 shows an RLC-series-resonator driven through a matching network. In the following, we will assume perfect impedance matching with a loss-free matching network and that the losses in the connecting cable do not influence the resonator circuit. Thus, one can set the input power equal to the loss power in the resonator $P_{\text{input}} = P_{\text{loss,resonator}}$, where $P_{\text{input}} = V_{\text{in}}^2/R_{\text{wave}}$

with V_{in} being the input voltage supplied to the circuit and R_{wave} the wave impedance of the connecting cable, commonly 50Ω . One can further write

$$P_{\text{loss,resonator}} = |I|^2 \cdot R_{\text{eff}} = \left| \frac{V_c}{\frac{1}{i\Omega C}} \right|^2 \cdot R_{\text{eff}} \quad , \quad (3.2)$$

where I is the current in the resonator, R_{eff} its effective loss resistance of the resonator, Ω its frequency, V_c the voltage at the capacitor, and C the capacitor representing the trap. Thus, one obtains

$$\frac{V_{\text{in}}^2}{R_{\text{wave}}} = |\Omega C V_{\text{in}} G_V|^2 \cdot R_{\text{eff}} \quad (3.3)$$

where G_V is the voltage gain of the circuit, defined as $G_V = \frac{V_c}{V_{\text{in}}}$.

The quality factor Q of a resonator is defined as the resonance frequency f_0 divided by the bandwidth Δf

$$Q = \frac{f_0}{\Delta f} \quad . \quad (3.4)$$

In trapped ion experiments, one is usually not interested in a small bandwidth around Ω but rather in a large voltage gain at the trap drive frequency. It should be noted that the voltage gain and bandwidth are qualitatively but not necessary quantitatively the same for different types of resonators. The quantity that is of direct interest for trapped ion experiments is the voltage gain, which can be derived from Eq. 3.3 as

$$G_V = \frac{1}{\Omega \cdot C} \cdot \frac{1}{\sqrt{R_{\text{wave}} \cdot R_{\text{eff}}}} = \sqrt{\frac{Q}{R_{\text{wave}} \cdot \Omega \cdot C}} \quad (3.5)$$

with the quality factor of an ideal RLC-resonator $Q = \frac{1}{R_{\text{eff}} \cdot \Omega \cdot C}$. This indicates that both, the capacitive load and the effective resistance of the resonator should be minimized.

3.1.1.3 Pick up

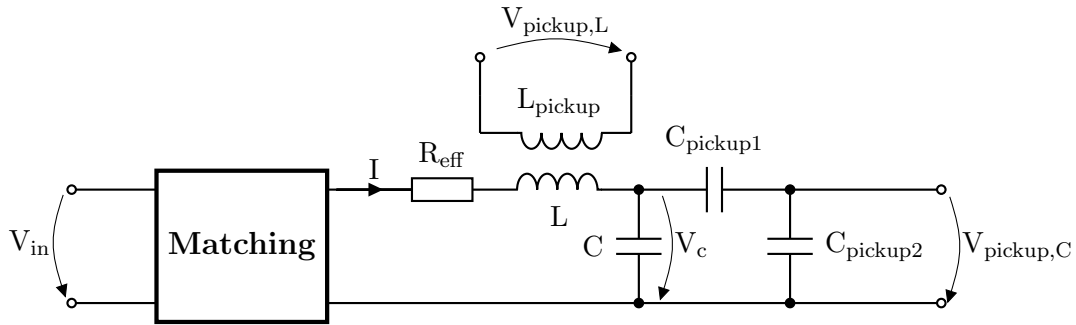


Figure 3.2.: The circuit of an RLC-series-resonator with an inductive and a capacitive pick up.

Voltage pick ups are not required for the operation of the trap, but are useful to measure the voltage on the trap and are required to actively stabilize the RF voltage on the trap. In this chapter, both inductive and capacitive pick ups are discussed, which are shown in Figure 3.2.

A capacitive pick up consists of a voltage divider parallel to the trap, where $C_{\text{pickup2}} \gg C_{\text{pickup1}}$, which leads to the pick up voltage

$$V_{\text{pickup,C}} = \frac{C_{\text{pickup1}}}{C_{\text{pickup1}} + C_{\text{pickup2}}} \cdot V_c \quad . \quad (3.6)$$

C_{pickup1} has to be small compared to the trap capacitance C or the capacitive load of the RLC-resonator will increase significantly, reducing G_V as shown in eq. 3.5. Typical values for C_{pickup2} are several hundred times the value of C_{pickup1} .

In an ideal RLC-series-resonator, the voltage on the coil is the same as the voltage at the capacitor but with a 180° phase shift. Thus, one can monitor the voltage at the coil as a signal proportional to the voltage at the trap. Here, L and L_{pickup} are coupled, and the pick up voltage can be estimated following the derivations from reference [SSWH12].

In order to maintain low losses, the pick up should not add significant losses in the resonator. If one uses a coaxial cable with a wave impedance R_{wave} to monitor the pick up signal, a resistor R_{wave} is used as a termination to avoid reflections. The losses are then $V_{\text{pickup}}^2/R_{\text{wave}}$ which need to be small compared to the losses in the resonator P .

In general, one should use an inductive pick up, because it does not increase the capacitive load, which would reduce the voltage gain. However for experiments, which frequently test different traps, a capacitive pick up may be preferable since the more accurate ratio between pick up and applied voltage facilitates estimating trapping parameters.

3.1.2 Coil design

Surface traps for cryogenic environments typically use a high-quality dielectric carrier material and thus the losses in the resonator are usually dominated by the coil. In the following, the design and production of compact and low-loss coils are shown to satisfy the conditions stated in Chapter 3.1.1.1. Coils produced with machines are desirable because the production process is reproducible. Furthermore, toroid coils are preferred as they guide the magnetic field in their center, making them less sensitive to their environment. In the trapped ion experiments, ferromagnetic core materials are undesirable, because they would induce spatial inhomogeneities of the magnetic field near the trap. A typical load capacitance of the resonator can be estimated around 10 pF, which at a given resonance frequency of 43 MHz yields a required inductance of $1.4 \mu\text{H}$.

3.1.2.1 PCB Coils

Kamby and coworkers [KKA12] demonstrated the integration of toroidal RF-inductors into printed circuit boards (PCB). These coils can be fully produced by machines and will be referred to as PCB coils in this work.

Kamby et al. [KKA12] provide formulas for the inductance

$$L = \frac{N^2 h \mu}{2\pi} \ln\left(\frac{r_o}{r_i}\right) + \frac{r_i + r_o}{2} \mu \left(\ln\left(8 \frac{r_o + r_i}{r_o - r_i}\right) - 2 \right), \quad (3.7)$$

the resistance of one segment

$$R_{\text{seg}} = \frac{\rho N}{2\pi \delta} \ln\left(\frac{2\pi r_o - \alpha N}{2\pi r_i - \alpha N}\right) \quad \forall 2\pi r_i > \alpha N, \quad (3.8)$$

and the resistance of one via

$$R_{\text{via}} = \frac{2h\rho}{(2\hat{r} - \delta)\pi\delta}, \quad (3.9)$$

where N is the number of windings, h is the thickness of the PCB material, μ its permeability, r_o is the outer radius of the coil, r_i is the inner radius of the coil, ρ is the resistivity of the

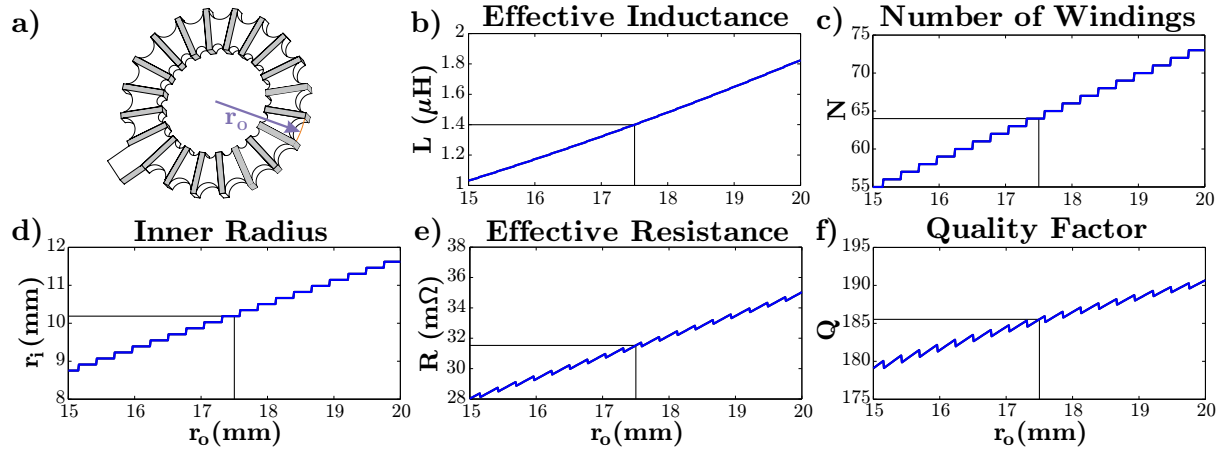


Figure 3.3.: Panel a) shows a sketch of a PCB coil. The white areas represent the traces and the gray areas the insulation between the traces. The other graphs are results of simulations where the outer radius of the ring r_o was varied to determine the resulting inductance **b**, the number of windings **c**, the smallest possible inner radius **d**, the effective resistance **e**, and the resulting quality factor **f**.

conductor material, α is the distance between two segments, \hat{r} is the radius of the via, and δ is the skin depth in the conductor due to skin effect.

In order to minimize the losses of the coil, it is sufficient to minimize the resistance of one winding while maintaining a constant cross-section to keep the inductance constant. The resistance of one winding is defined by

$$\begin{aligned} 2R_{\text{seg}} + 2R_{\text{via}} &= 2\frac{R_{\text{seg}}}{r_o - r_i} (r_o - r_i) + 2\frac{R_{\text{via}}}{h} h = \\ &= 2R'_{\text{seg}} (r_o - r_i) + 2R'_{\text{via}} h \quad , \end{aligned} \quad (3.10)$$

where R'_{seg} and R'_{via} are the average length-dependent resistances of a segment and a via. R'_{seg} and R'_{via} depend on the exact geometry, but usually vias have similar cross-sections as segments, making their length-dependent resistances approximately equal. That means, in order to minimize Eq. 3.10 while keeping the cross section of the coil constant, $(r_o - r_i)$ and h should be similar in size.

Rogers 4350B was chosen as the substrate material, because it has a small loss tangent, a similar thermal expansion coefficient as copper, and is UHV compatible. The thickest available Rogers 4350B had 3.1 mm thickness, which is unfortunately too thin to minimize the resistance for a given cross-section of a coil with an inductance of 1.4 μH .

The PCB coils were produced in-house² with dimensions obtained from simulations with the formulas from reference [KKA12]. During multiple iterations, the size and the number of vias were varied. Thin vias with a diameter below 0.4 mm could not be produced with the in-house processes. And the lowest losses were obtained with the design depicted in Figure 3.3 a). The circuit board is milled in a way that the PCB coil is a ring with a terminal for the connections. The vias are semicircles whose diameter is the same as the width of the segment at the point of the vias, similar to a sidewall plating of circuit boards.

Eqs. 3.7-3.9 were used to perform simulations for which the outer radius was varied, the distance between the segments α was set to 0.3 mm, and semicircle diameters of the inner ring and the outer ring were 0.7 mm and 1.4 mm respectively. The predicted inductances can be seen in

²Gerhard Hendl from the Institute of Quantum Optics and Quantum Information of the Austrian Academy produced the coils described here.

Figure 3.3 b, the highest number of windings in Figure 3.3 c, the smallest inner radius of the ring in Figure 3.3 d, the effective resistance in Figure 3.3 e, and the simulated quality factor of coil in Figure 3.3 f.

To get an inductance of $1.4 \mu\text{H}$, one can deduce from these simulations that a minimum outer radius of the ring of 17.5 mm with 64 windings, and an inner radius of 10.2 mm are required. With these values, one should obtain a copper coil with an effective resistance of $26.5 \text{ m}\Omega$ and a quality factor of about 185. - These simulations were performed with copper at room temperature as the conductor. When cooling down to cryogenic temperatures, the losses will drop, which allows fulfilling the criteria stated in Chapter 3.1.1.1.

A manufactured PCB coil with these dimensions is shown in Figure 3.4 a. One winding, which is galvanically isolated from the rest of the coil, was added acting as a reproducible inductive pick up.

3.1.2.2 Wire Coils

For the second type of coils, wire coils, a single wire was wound around a rigid structure leading to a similar geometry as the PCB coils. Such a coil is less reproducible than a PCB coil since the wire length will vary for each coil. Hence, its inductance and its resistance will vary as well. A coil with the same geometry as for the PCB coils above, made out of silver-plated copper on a Rogers 4350B substrate, is shown in Figure 3.4 b.

In wire coils, the cross-section of the core of a wire coil is bigger than that of a PCB coil, because the wire bends are less sharp. Hence, one expects the inductance of a wire coil to be higher than the one of a PCB coil with the same nominal geometry. The 0.4 mm thick silver-plated copper wire, which was used for the wire coil, had a cross-section similar to the average cross-section of a PCB coil. Therefore, the losses are expected to be similar in both types of coils with the same geometries. These considerations allow characterizing the production processes of the PCB coils by comparing the two types of coils. Higher losses in the PCB coils would be an indication that the production of the PCB coils could be improved.

Since traces are not required on the substrate, it is possible to use any machinable material with a low loss tangent. For example, Teflon has a lower loss tangent and a lower dielectric constant than Rogers 4350B. Thus, the losses of a coil with a Teflon coil will be less affected by the core material and the self-resonance frequency of the coil will be higher. Another option to minimize the losses in the coil can be to use a superconducting wire to reduce the ohmic losses of the resonator.

3.1.2.3 Spiral Coil

The quality factors of the presented coils are limited by the ohmic resistances of the conductors. Thus, a coil based on a superconductor is expected to result in lower losses in the resonator. Furthermore, it could be advantageous to operate the experiment at temperatures above 15 K to reduce the liquid helium consumption. At these temperatures, a superconductor with a high critical temperature, such as a high-temperature superconductor (HTS), is required. However, a coil made from readily available HTS material needs to be a two-dimensional (2D) structure due to manufacturing constraints. Therefore, a spiral geometry was chosen as shown in Figure 3.4 c.

PCB coils and wire coils are both toroid coils and most of their generated magnetic field will be inside the core material. In contrast, spiral coils are 2D structures and have magnetic fields that only pass through this 2D plane. Their magnetic fields are mainly in the space surrounding the

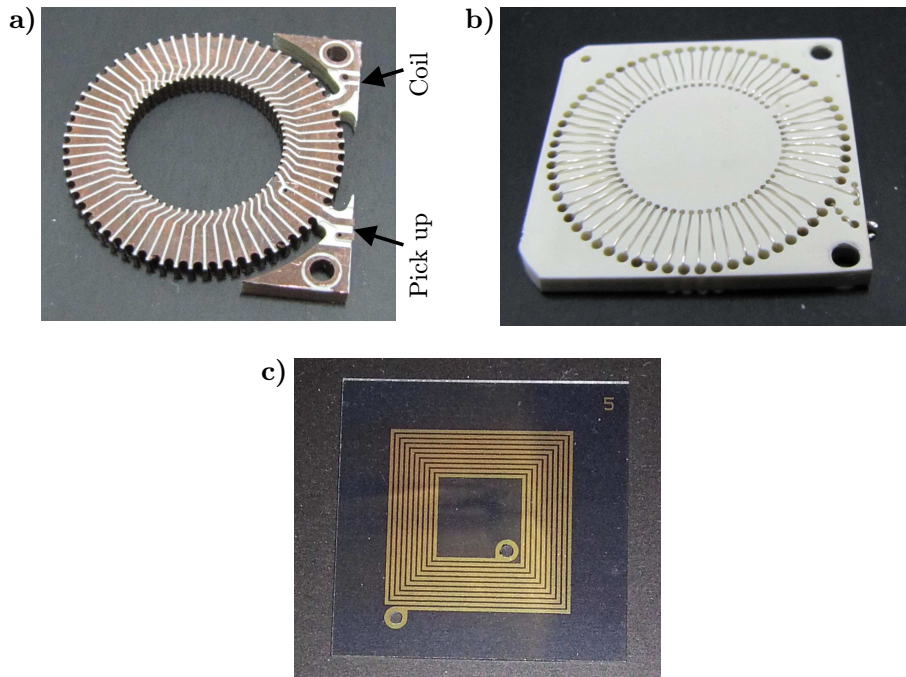


Figure 3.4.: Panel **a** shows a PCB coil produced in copper with a diameter of 35 mm, 64 windings, and inductive pick up. Panel **b** exhibits a wire coil made out of 0.4 mm thick silver-plated copper wire on a 3.1 mm thick Rogers 4350B core. Panel **c** displays a spiral coil made out of a gold plated high temperature superconductor.

coils. Hence, RF shields containing these magnetic fields will influence the magnetic flux and thereby affect the inductance of the coil.

Since such coils require only 2D structuring, they can be manufactured in a very accurate and reproducible way. For the demonstrated spiral coil, a HTS was produced by *Ceraco Ceramic Coating*³. These coils were made out of an yttrium barium copper oxide (YBCO) film of 330 nm thickness on a sapphire wafer. To facilitate soldered connections, a 200 nm film of gold was placed on top of the superconductor. This film is thinner than the skin depth around the expected 43 MHz and thus should not dominate the losses in the resonator. The critical temperature of this YBCO film is above 87 K, and its critical current density is higher than $2 \cdot 10^6$ A/cm² at 77 K. One can derive the peak current in the coil from Chapter 3.1.1.1 to be 0.64 A. Hence, traces with a width of more than 100 μ m are required to stay below the critical current density.

For these square spiral coils, a trace width of 300 μ m, a trace gap of 150 μ m, and 10 windings were chosen. 9 different coils were designed with a varying outer diameter between 14 and 20 mm. Eq. 4.1 of reference [Moh99] gives an estimate for the inductances, which result in target inductances between 1.2 μ H and 1.6 μ H for these coils. This design should allow for coils with very high quality factors already at temperatures accessible with liquid nitrogen instead of liquid helium.

It should be noted here that superconductors are perfect diamagnets, which are spatial inhomogeneities for magnetic fields. One can align the 2D plane of the spiral coil with the spatially homogeneous magnetic field of the experiment to minimize this effect, but one should always keep this in mind.

³Ceraco Ceramic Coating GmbH, Rote-Kreuz-Str. 8, D-85737 Ismaning, Germany

3.1.3 Matching

The resonator is connected to the source through a cable with a given wave resistance R_{wave} , typically 50Ω . The complex voltage reflection coefficient \underline{r}_v at the transition from the cable to the resonator [Poz11] is then

$$\underline{r}_v = \frac{V_{\text{reflection}}}{V_{\text{input}}} = \frac{\underline{Z}_{\text{res}} - R_{\text{wave}}}{\underline{Z}_{\text{res}} + R_{\text{wave}}}, \quad (3.11)$$

where $\underline{V}_{\text{reflection}}$ is the complex reflected voltage, $\underline{V}_{\text{input}}$ is the complex incoming voltage, and $\underline{Z}_{\text{res}}$ is the complex impedance of the resonator⁴. The reflected power coefficient R_p is then just $R_p = |\underline{r}_v|^2$. Since RLC-series resonators have very low impedance on resonance ($\underline{Z}_{\text{res}} = R_{\text{eff}}$), the transition from a 50Ω -cable to the resonator on resonance will reflect almost all the inserted power. In order to minimize the reflection, a properly designed impedance matching network is required. The most commonly used matching network is the L -network as it is the simplest, consisting only of two circuit elements.

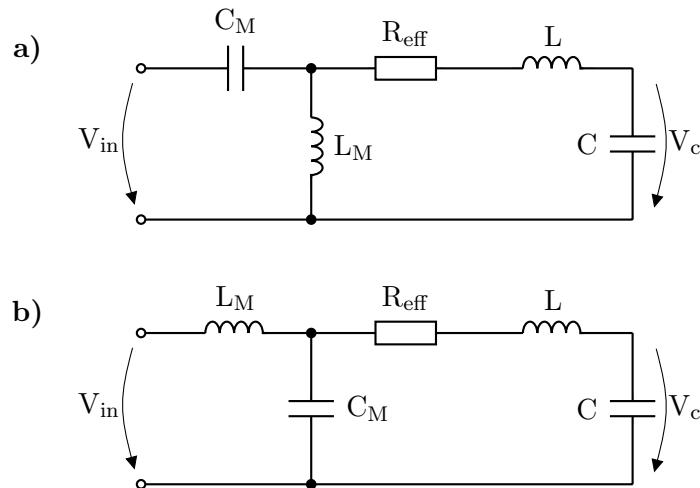


Figure 3.5.: Two possible matching networks. In panel **a**), the matching capacitor C_M is in series and the matching coil L_M parallel to the RLC-series resonator. In panel **b**), the matching coil L_M is in series and the matching capacitor C_M parallel to the RLC-series resonator.

Figure 3.5 shows the two possible L -networks where the reactance parallel to the resonator transforms the real part of the impedance to be R_{wave} . The resulting imaginary term is small compared to R_{wave} (for low loss resonators) and can be compensated with the series reactance.

With the matching network of Figure 3.5 a), the effective inductance of the resonator will be $L_{\text{eff}} = L_M + L$. Hence, the resonance frequency will drop depending on L_M . With the matching network of Figure 3.5 b), the effective capacitance of the resonator will be $C_{\text{eff}} = \frac{C_M C}{C_M + C}$. Hence, the resonance frequency will rise depending on C_M .

The resonator's quality factor from Eq. 3.4 can be written as

$$Q_{\text{coil}} = \frac{\Omega L}{R_{\text{eff}}} \quad (3.12)$$

for an RLC-series resonator. Figure 3.6 shows the required values for the matching capacitor C_M and inductance L_M as a function of the quality factor of the coil with inductance of $1.4 \mu\text{H}$. For quality factors around 1000, the required inductance L_M is in the range of 10 nH . Thin

⁴The underline denotes a complex quantity.

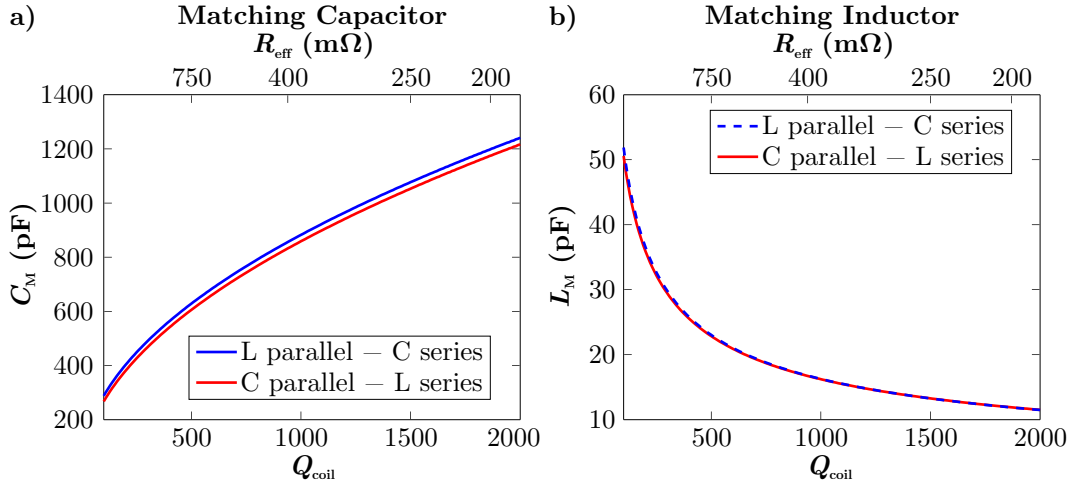


Figure 3.6.: Calculated values of the matching capacitor C_M **a** and matching coil L_M **b** for the matching networks of Figure 3.5 over a varying quality factor of the coil. The matching is calculated for a $50\ \Omega$ -cable, an inductor of $1.4\ \mu\text{H}$, and a capacitor of $10\ \text{pF}$.

traces on a PCB have approximately a length-dependent inductance of $1\ \text{nH}/\text{mm}$. Therefore, small deviations in the trace length will lead to inefficient matching. The strong dependence of the matching on the reactance parallel to the resonator makes the matching network from Figure 3.5 b more favorable, because capacitances of several hundred pF can be adjusted with more precision than inductances of about $10\ \text{nH}$. One can incorporate the inductance L_M into the trace on the PCB from the coaxial connector to the matching capacitance, by setting this distance between 1 and 2 cm. Hence, one can expect a power reflection of 1% or less even without adding an additional inductor.

RF transformers or balanced-unbalanced couplers, short baluns, on the RF input side are commonly used to avoid ground loops between the RF source and the experiment. When using the circuit from Figure 3.5 b in combination with a transformer, the DC potential of the trap electrodes is not defined. One can mitigate this by adding an RF-choke parallel to the matching capacitor, where $\Omega L_{\text{choke}} \gg \frac{1}{\Omega C_M}$, as depicted in Figure 3.7.

In a cryostat, it is impractical to adjust the matching capacitance C_M during or after a cool down. Tunable capacitors, like varactor diodes, that operate at cryogenic temperatures typically have only $10\ \text{pF}$ capacitance, and it would require more than 100 varactor diode to match a low-loss resonator. Hence, one has to find an efficient way of choosing the best value for C_M with a minimum number of temperature cycles. For this, one can simulate the matching circuit for varying and also for a constant value of C_M . Figure 3.8 shows results of simulations for which the fixed capacitor value was chosen for a match at $Q_{\text{coil}} = 1200$. Figure 3.8 a depicts an increase of the optimum C_M with increasing Q_{coil} . Figure 3.8 b illustrates the dependence of the matched

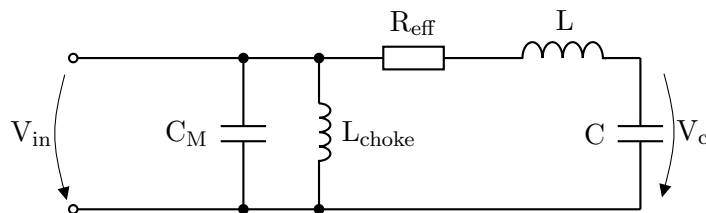


Figure 3.7.: Chosen matching network with only a matching capacitor C_M parallel to the RLC-series resonator. Additionally, one can put an RF-choke parallel to C_M to avoid a possible charging up of C .

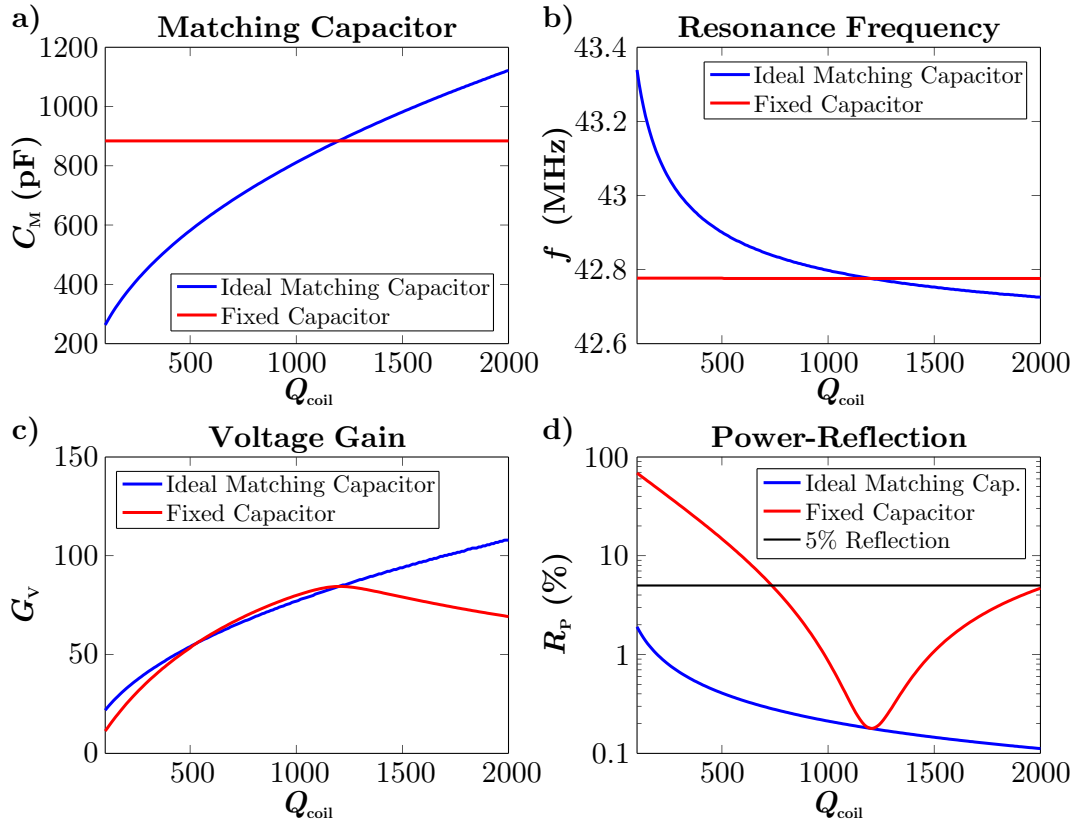


Figure 3.8.: The matching of these plots is calculated for a 50Ω -cable, an inductor of $1.4 \mu\text{H}$, and a capacitor of 10 pF , thus a resonance frequency of 43 MHz . The black lines show the values for a fixed capacitance C_M chosen for an ideal matching of $Q_{\text{coil}} = 1200$. In panel **a**, one can see the required matching capacitor as a function of the quality factor of the coil Q_{coil} . Panel **b** shows the change in resonance frequency of an ideal match. In panel **c**, the voltage gain is plotted over Q_{coil} . Panel **d** shows the reflection coefficient of the matching network.

resonance frequency on Q_{coil} . In Figure 3.8 c, the simulations confirm the dependence of the voltage gain on Q_{coil} , following from Eq. 3.5. If the physical value for Q_{coil} is smaller than the expected value, used to chose the fixed matching capacitor, the voltage gain is about the same than for an ideal match. But if the actual quality factor Q_{coil} is higher than the expected value, the voltage gain will be lower than with an ideal match. Hence, underestimating the quality factor of the coil should be avoided since it would result in a significantly lower voltage gain.

Figure 3.8 d shows the reflection coefficient as a function of Q_{coil} . The effect of L_M is small and thus it was omitted for these simulations. One can see that even without L_M , but with an ideally matched C_M , a low reflection coefficient can be achieved. If one chooses a constant value for C_M at a match for $Q_{\text{coil}} = 1200$, the reflected power will stay below 5% even if Q_{coil} varies between 800 and 2000.

The parameters for exact impedance matching can be estimated with one additional cooling cycle. For the first cycle, one has to guess the value for Q_{coil} and adjust C_M according to simulations following the approach outlined in Figure 3.8 a. When the resonator is cold, the reflection coefficient is measured and compared with the simulations in Figure 3.8 d. The measured reflection coefficient can then only correspond to two values for Q_{coil} . If the reflection coefficient passed a minimum during cool-down, one should choose the higher value, if not, the lower value of Q_{coil} . With this new value for Q_{coil} , one can calculate the correct matching capacitor value C_M . Experience shows that this method will yield a power reflection coefficient

of less than 2% for the second cool down.

3.1.4 RF-Shield

RF resonators emit electromagnetic radiation, which needs to be shielded to minimize unwanted interference in other parts of the experiment. The RF shield is a grounded enclosure which generates an additional capacitance between the resonator and ground. This capacitance has to be minimized as suggested in Eq. 3.5. Minimizing it will increase the size of the shield, and thus, one has to find a trade-off between the size of the shield and the capacitance added by it.

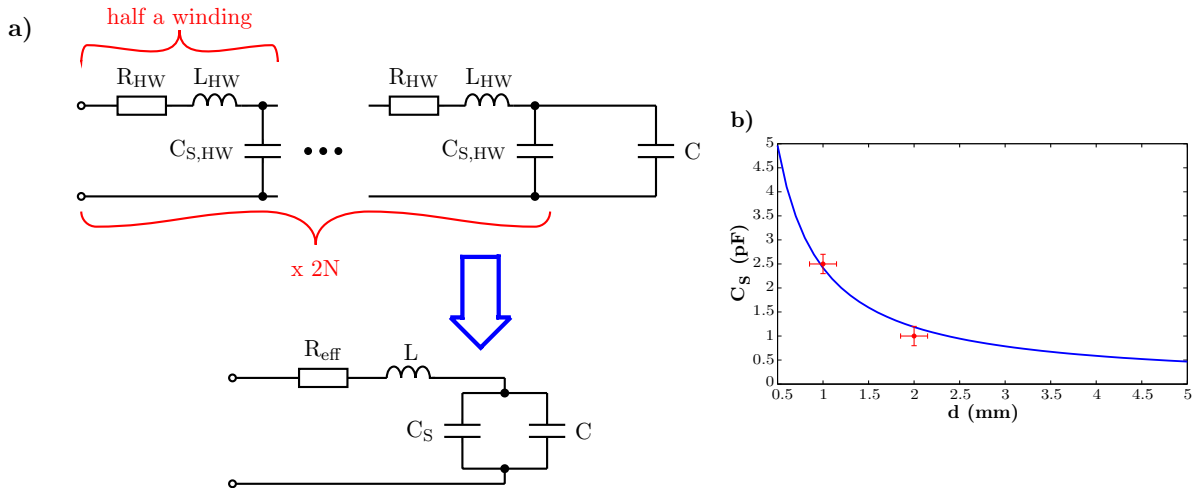


Figure 3.9.: Panel a shows the model for the capacitance of the RF shield. From the resistance R_{HW} , the inductance L_{HW} , and the capacitance to the shield $C_{S,HW}$ of half a winding, one can calculate the total impedance of the circuit, which allows one to derive the total capacitance C_S caused by the shield. Panel b depicts simulations with this model of the total capacitance caused by the shield.

Figure 3.9 a depicts a model shield capacitance C_S where the coil is divided in $2N$ half windings. Each has an ohmic resistance of R_{HW} , an inductance $L_{HW} = L/(2N)$, and a capacitance to the shield $C_{S,HW}$. One can estimate $C_{S,HW}$ with the standard formula for a parallel-plate capacitor. From the calculations of the impedance of the entire circuit, one can extract the effective capacitance C_S that is added due to the presence of the shield.

The results of these simulations for the PCB coils with an outer radius of 17.5 mm and an inner radius of 10.2 mm are shown in Figure 3.9 b. It can be seen that a distance of about 2 mm is sufficient to keep the additional capacitive load below 1 pF. Adapted simulations for the wire coils yield results similar to the ones for the PCB coils. Hence, one can use the same shield for both types of coils.

The capacitance caused by the shield for the spiral coils will be even smaller, because its surface is smaller. Additionally, if the spiral coil is placed in the center of the same shield, the distance to the shield will be 1.55 mm bigger than for the other coils. Hence, the capacitance to ground will decrease further. One should keep in mind that the shield influences the field lines of the coil's magnet field, and thus, also affects the losses and the inductance of the coil.

At room temperature, the skin depth (skin effect) in copper at frequencies around 40 MHz is about 10 μm . Thus, any mechanically stable shield, of a couple of 1/10 mm thickness, should yield a suitable attenuation. Figure 3.10 shows a resonator encased in a silver-plated copper shield. The dimensions of this resonator are 57 mm x 40 mm x 10.2 mm. On the left side of the

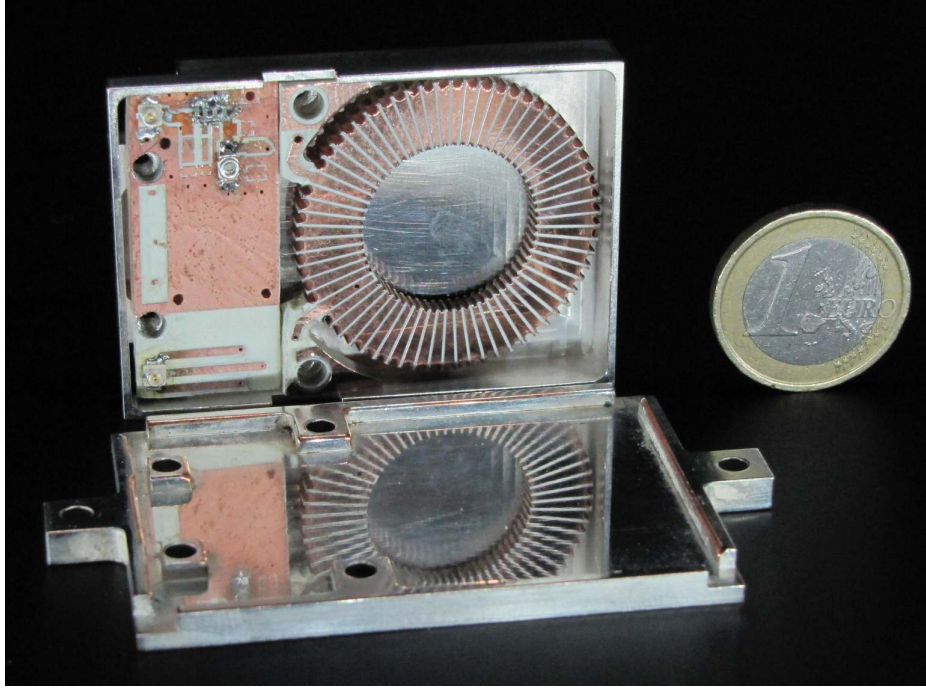


Figure 3.10.: The RLC-resonator built with a PCB coil (right) and the matching network (left) in a silver-plated copper shield. The dimensions of the shielded resonator are 57 mm x 40 mm x 10.2 mm.

resonator, one can see a PCB with the matching network at the top and the SMT-connector for the inductive pick up at the bottom. On the right side is the PCB coil, and the two PCBs are connected together by soldered joints.

3.1.5 Results of the designed resonators

In the resonator test setup, a capacitive pick up was used to measure the voltage at the trap. With the known ratio of this capacitive voltage divider, one could directly measure the voltage at the trap and calibrate the inductive pick up of the coil. All measurements were performed with a test trap as the load capacitance.

Table 3.1 shows the measurement results. The PCB coils had an inductance very close to the desired value. Unfortunately, the expected quality factor could not be reached. The wire coils were designed to have losses similar to the PCB coils, but the PCB coils showed higher losses than the wire coils. The assumption is that this is due to an imperfect production process that could not be improved further with the in-house techniques.

Additionally to the PCB coils in copper, some of these coils were silver plated. The inductances were similar, but the losses in the silver coils were even higher. This was unexpected as silver is a better conductor than copper. The silver coils needed to be reworked after fabrication to remove shorts between the segments. During this process, the silver coating might have been scratched, resulting in higher losses. To reduce the losses of the silver PCB coils in the future, one could silver plate after structuring instead of before.

The voltage gain of about 60 of the wire coil would require 160 mW RF input power to get to the desired $170 V_{\text{rms}}$ at the trap. If one adjusts the voltage to keep the stability parameter $q = 0.25$, only 100 mW RF input power are required at the modified resonance frequency. With a thicker wire, it will be possible to reduce the losses in the resonator even further.

Table 3.1.: Measured resonance frequencies, voltage gains, and quality factors of the tested coils. The measurement uncertainties were dominated by the uncertainty in the ratio of this capacitive voltage divider, about 10 %.

Name	T	f_{res}	G_V	Q_{coil}
PCB coil	295 K	42.4 MHz	19(2)	60(13)
PCB coil	~ 80 K	42.8 MHz	27(3)	115(27)
PCB coil	~ 10 K	42.9 MHz	41(4)	208(43)
Wire Coil	295 K	36.8 MHz	25(2)	89(15)
Wire Coil	~ 80 K	37.2 MHz	36(3)	184(32)
Wire Coil	~ 10 K	37.9 MHz	58(6)	624(136)
HTS Coil	< 88 K	44.3 MHz	92(9)	1172(241)
Ref. [PBIW96]	4.2 K	13 MHz	237	3000
Ref. [GNK ⁺ 12]	5.7 K	7.43 MHz	101(6)	700(30)
Ref. [Wan12]	77 K	33-40 MHz	20	-

Furthermore, a resonator with superconducting wire coil was tested as well. Unfortunately, the observed voltage gain of this resonator with a lead-plated wire did not increase. Either the critical temperature of lead was not reached in the test setup, or the lead was not pure enough to become superconducting.

The HTS spiral coil showed the highest voltage gain, although the shield influences the magnetic field generated by the coil. A change of the resonance frequency of a couple of percent was observed when cooling down from liquid nitrogen temperatures to liquid helium temperatures, which was attributed to the shield surrounding the coil. During this cool down, the losses in the resonator dropped by about 20 % confirming that the resonator is not limited by skin-effect in the gold layer on top of the HTS coil but most likely by ohmic resistances in the resonator (e.g. in the bond wires of the trap). With a voltage gain of 92, one would need about 70mW of RF input power to get $170V_{\text{rms}}$. With a stability parameter $q = 0.25$ at the higher resonance frequency, it would be 82mW.

These resonators can be compared to devices used in other experiments [PBIW96, GNK⁺12, Wan12]. Although the voltage gain there seems comparable, one needs to keep in mind that due to Eq. 3.5, the voltage gain is inversely proportional to the frequency and the capacitive load. Taking this into consideration, the resonator with the HTS coils outperforms all other resonators listed in Table 3.1. But such comparison neglects that helical resonators [PBIW96, Wan12]⁵ typically require more volume than RLC-resonators.

3.2 Filter Design

Filter design for the DC lines of segmented Paul traps is a crucial part in the design of a segmented ion trap design, but often not given the right weight in the design process. Poor filter design can lead to high heating rates, axial micromotion, or can prevent shuttling of ions during one measurement cycle. With these filters, one wants to attenuate noise signals at the secular motion frequencies, while at the same time, limit the slew rate at the DC segments for ion shuttling as little as possible. Therefore, one has to find a trade-off between the attenuation and shuttling speed, as discussed in Chapter 3.2.1. Furthermore, the filters have to reduce the RF pick up on the DC signals, which is covered in Chapter 3.2.2.

⁵The exact load capacitances were not mentioned in these publications but were assumed to be similar to the 10 pF used in this design.

3.2.1 Filter Noise at Secular Motion Frequencies

The movement of ions in a segmented Paul trap during a measurement cycle should happen as fast as possible. To avoid motional heating from these rapid voltage changes caused by ion shuttling, the voltages at the segments are usually low-pass filtered. There, the highest frequencies applied on the DC lines of the trap should not exceed a certain fraction of the lowest secular motion frequency, typically about a tenth of the lowest secular motion frequency. In the following, the filter design will be discussed for the case of $^{40}\text{Ca}^+$ ions, in which typical axial secular motion frequencies are about 1 MHz, and typical radial secular motion frequencies are on the order of 3 to 4 MHz. Hence, one needs to design low-pass filters with a cut-off frequency between 100 kHz and 1 MHz for a trapped ion experiment with $^{40}\text{Ca}^+$ ions.

At first, one has to decide what type of low-pass filter to use. As will be shown in Chapter 3.2.2, these filters have to be placed very close to the trap, thus in the vacuum chamber. A reliable operation is required to prevent frequent opening and closing of the vacuum chamber. Active filters are less reliable than passive filters and the noise of the active components of the filter is not attenuated. Furthermore, the filters need to work in cryogenic environments. This places additional restrictions on the choice of active electronics. Therefore, passive filters are typically the preferred type of filters for segmented Paul traps.

Filter design is not trivial and it is recommended to look into more detailed literature [Che98]. But the actual design parameters will always depend on the specific application. In some experiments, it is best to have a steep roll-off⁶ to reduce the ratio of lowest motional frequency and the maximum frequency used for ion movement. This can be achieved with Chebyshev filters. In other experiments, one may try to apply frequencies above the cut-off frequency. By overshooting the voltages for higher frequencies, one can move ions even faster. For this application of ion movement, a flat transfer function in amplitude and phase facilitates waveform design and, thus, Butterworth filters are a good choice because Butterworth filters are optimized for such a flat transfer function. In the following, the fundamentals for a typical filter design of an experiment with trapped $^{40}\text{Ca}^+$ ions will be discussed.

Figure 3.11 shows different types of filters that are used in trapped ion quantum computing experiments and their transfer functions. For simplicity, all filters have their cut-off frequency set to 300 kHz. The single stage RC and LC filters, depicted in Figure 3.11 a and c, have a flat roll-off, displayed in Figure 3.11 e. This results in weak filtering at the secular motion frequencies, and thus one has to use multi-stage filters for a steeper roll-off.

The multi-stage RC and LC filters are depicted in Figure 3.11 b and d. The fourth-order RC filter does not show an overshoot in the amplitude of the transfer function (Figure 3.11 e). But it causes phase shifts for frequencies higher than about 10 kHz (Figure 3.11 f), which will require an individual calibration of each segment for voltage changes faster than 10 kHz as the phase evolution from segment to segment might vary. The two stage LC filter has an overshoot in the amplitude below the critical frequency. The height of overshoot and the exact phase of the transfer function depend on the quality factor of LC filter stage, usually dominated by the internal resistance of the inductor. The simulations of Figure 3.11 were done for a quality factor of about 1 for the coils. In cryogenic environments, the quality factor can be significantly higher, resulting in a higher overshoot and a sharper phase shift around the critical frequency.

The choice whether to use RC or LC filters depends on the application. When changing the voltage at a segment, a current will flow. If one places the filter boards as close as possible to the trap, these currents might produce magnetic fields, which may be unwanted close to the experiment. Hence, RC filters are a good choice in such cases. In cryogenic setups, coils have high quality factors resulting in sharp phase shifts around the critical frequencies, which could

⁶<https://en.wikipedia.org/wiki/Roll-off>

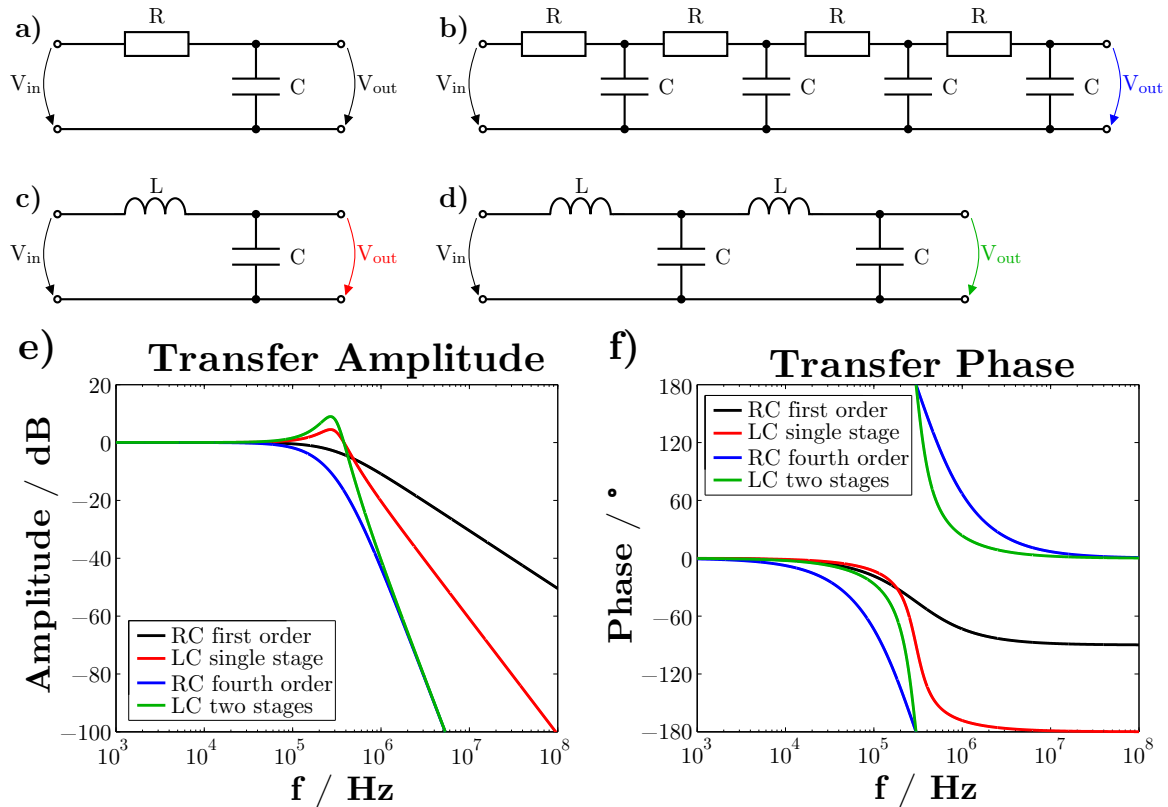


Figure 3.11.: Different types of filters: a first order RC low-pass filter **a**, a fourth order RC low-pass filter **b**, a single stage LC low-pass filter **c**, a two stage LC low-pass filter **d**. Panels **e** and **f** depict the transfer functions for these filters (see legend for lines).

be desirable for fast shuttling of ions. Further, space is precious in most cryogenic setups and LC filters require only half as many components as RC filters of the same order, which becomes more important with increasing number of connected DC segments. The magnetic field produced by the coils can be filtered by the walls of the inner heat shield by placing the filters in the outer heat shield. Hence, in the case of cryogenic systems, LC filters are a good choice.

The voltage noise is originating predominantly from three different sources: (i) Technical noise. It is produced by the generation of the voltages for the segment, for example in a digital-to-analog converter (DAC). One cannot prevent it, but with clever circuit design one can minimize it or shift it to frequencies which do not cause problems in the experiment [WZR⁺12]. (ii) Pick up of electromagnetic noise. It can be reduced by using short, shielded cables from the voltage sources to the trap and by avoiding ground loops. It is important to not perform experiments with motional frequencies close to an RF source in the lab, such as switching power supplies or unshielded DC-to-DC converters, as this will lead to motional heating in the experiment. (iii) Johnson noise. Each resistor with resistance R , in particular one used to build a filter, produces a voltage noise $V_{R,\text{rms}}$, defined over its spectral density

$$\frac{dV_{R,\text{rms}}^2}{df} = 4k_B T R \quad (3.13)$$

with k_B being the Boltzmann constant, and T being the temperature of the resistor. Johnson noise is white, and thus, will always have spectral components at the secular motion frequencies. In order to minimize Johnson noise, one can cool down the resistor as done in a cryostat, and one should always use resistors with resistances as low as possible.

Figure 3.12 shows a typical circuit for one segment of an ion trap. A voltage source V_{source} ,

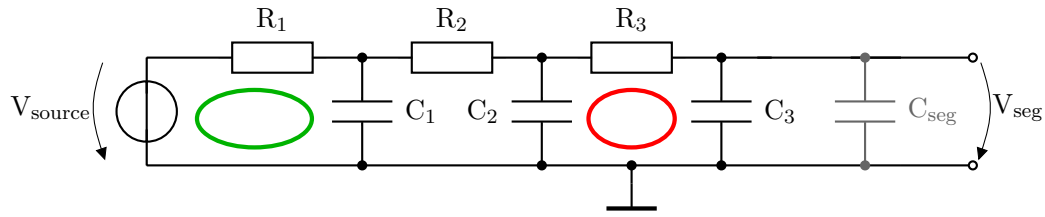


Figure 3.12.: A third order RC low-pass filter, used to filter the input voltage applied at one segment.

containing the technical noise from generation and pick up, supplies a voltage to the segment, depicted as the capacitance C_{seg} to ground, through a third order RC low-pass filter. Typically, C_{seg} is only a fraction of 1 pF and C_3 is in the nF regime. Hence for the simulations of the filter, C_{seg} is negligible, and one only considers C_3 for the calculation of V_{seg} .

In Figure 3.12, the Johnson noise of R_1 originates in the same loop of the circuit as V_{source} , denoted by the green ellipse. Therefore, it is filtered by the third order low-pass filter just like the technical noise of V_{source} . The Johnson noise of R_3 originates in the loop containing R_3 , denoted by the red ellipse, and is only filtered by a first order RC low-pass filter consisting of R_3 and C_3 in series with C_2 ⁷. This low-pass filter has a higher cut-off frequency than a low-pass filter consisting only of R_3 and C_3 , which filters noise at the secular frequencies even less.

With this knowledge, one can state the following rules for the filter design to reduce Johnson noise on segments of the ion traps.

1. If one chooses to use the same resistance for the different filter stages, the resistance should be as low as possible while still maintaining the desired cut-off frequency. This will result in high capacitance values, and one has to keep in mind that the voltage source might have to supply a high current during voltage switching.
2. If one chooses to use different resistances for the different filter stages, the resistance value should be lower the closer the resistor is placed to the trap. The reason for this is the lower order filtering closer to the trap. There, the Johnson noise cannot be attenuated as much and it has to be lower intrinsically.
3. If one chooses to use different cut-off frequencies for the different filter stages, the cut-off frequency should be lower the closer the filter stage is placed to the trap. This means that one tries to filter stronger closer to the trap.
4. LC filters usually have lower ohmic resistances than RC filters of the same filter order, which makes them more attractive for such filters from a Johnson noise point of view. But the coils used in LC filters will produce magnetic fields when the voltages are switched and a current is flowing through them. This could make magnetic shielding necessary, which is often hard to implement inside the vacuum chamber.

In most experiments, it may be hard to fulfill all rules and one might have to find a trade-off between restrictions dictated by the vacuum chamber design and these rules.

⁷For the frequency regime of interest to us, $f > f_c$, $R_2 > \frac{1}{\omega C_2}$. Hence, one can neglect the circuit parallel (left of) C_2 .

3.2.2 Shunt Trap Drive Signal on DC Lines

In the ideal operation principle of a segmented Paul trap, the DC segments are grounded for the RF trap drive. At the same time, they must provide axial confinement and hold DC voltages. Therefore in reality, the DC segments have to be shunted to ground for the trap drive, while being unaffected for the axially confining voltages. These signals usually have spectral components below the cut-off of the filters.

Before designing the shunt network, one has to understand its purpose. From an ion trapping point of view, it is not necessary that the DC segments need to have RF ground potential. A residual RF on the segments will influence the confinement and the ion height, which could be desired e.g. to change the ion height at a fixed geometry. But usually, traps are designed to have no residual RF on the DC segments. Hence, one tries to minimize the voltage on the DC segments by shunting the trap drive to ground. Thereby, axial micromotion is avoided which facilitates the trap operation.

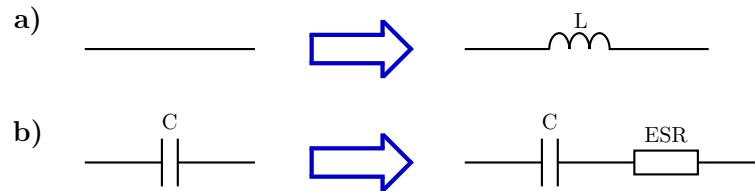


Figure 3.13.: Circuit representation of a circuit trace as an inductor **a**, and a capacitor with its equivalent series resistance (ESR) **b**.

For accurate circuit analysis at frequencies of tens of MHz, typically used as trap drive frequencies, one has to consider high frequency phenomena. For example, each connection like a wire or a trace on a PCB has an inductance depending on the considered geometry. This inductance is typically on the order of 10 nH and can thus only be seen at high frequencies. But at these frequencies, one has to replace each connection with an inductor for thorough treatment of the circuit, as depicted in Figure 3.13 a.

A good approximation for a bond wire is an inductance of about 1 nH per mm length, which is a common problem in packaging of high frequency integrated circuits [AMRS01]. And one can minimize the inductance of bond wires by using ribbon bonds which have lower inductances than normal bond wires. PCB traces are usually modeled as microstrip lines [Poz11], and for thin traces, for which the length is much greater than the width, one obtains similar inductance values as for normal bond wires.

Another phenomenon that one has to consider when designing circuits at these frequencies is the self-resonance frequency of coils. It has to be significantly higher than the highest frequency considered in the design or it cannot be treated as a simple coil, because coils will show a capacitive behavior above their self-resonance frequencies.

Furthermore when shunting with capacitors, it is imperative to take the equivalent series resistance (ESR) into account, see Figure 3.13 b. The ESR is a way to describe how fast the charge of the capacitor can be depleted. Capacitors with low ESRs are mica and ceramic capacitors. But for ceramic capacitors, the ESR is still very temperature and frequency dependent [TP10] and can easily reach the k Ω - or even M Ω -regime with the wrong choice of capacitor, where typical values are below 1 Ω . Thus, the choice of high quality capacitors is of utter importance for efficient shunting of RF signals. (Non-magnetic) mica capacitors and negative-positive 0 ppm/ $^{\circ}$ C (NP0) ceramic capacitors are typically used to shunt RF signals in trapped ion experiments. They are also favored for cryogenic applications as they do not change their capacitance values over the whole temperature range of the cryostat.

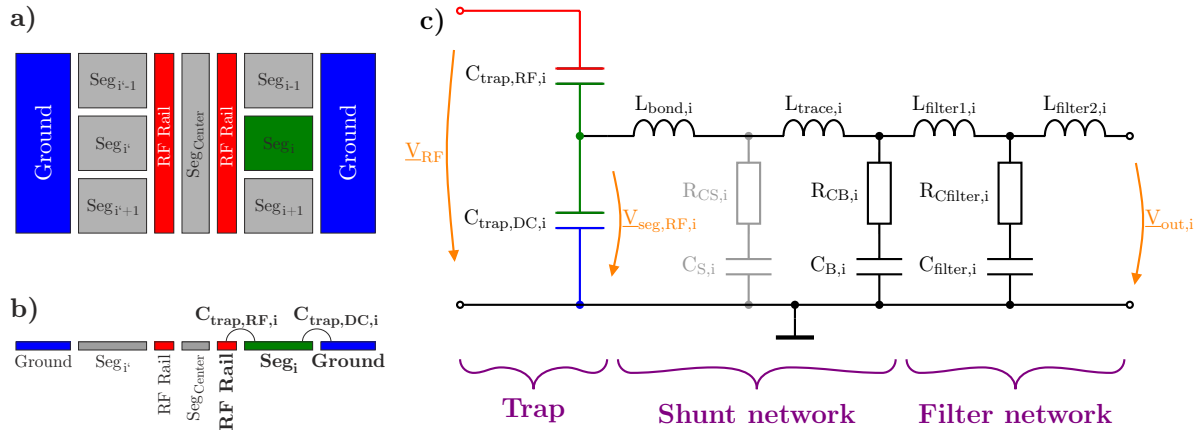


Figure 3.14.: Panel **a** shows a cut-out of 3 DC segment pairs of a segmented trap with 10 DC segment pairs. Panel **b** represents a cut through this trap along segment i and $i + 10$. Panel **c** depicts the circuit representation of the RF on DC segment i of this segmented Paul trap.

Resistors typically cause no problems at RF signals of several tens of MHz. Hence, one only needs to use (non-magnetic) ones whose resistances do not change between room temperature and the desired temperature regime.

Figure 3.14 a depicts a cut-out of 3 DC segment pairs of a segmented Paul trap. Figure 3.14 b displays the cut through this trap along segments i and i' , highlighting the relevant capacitances for the circuit analysis, which are the capacitance of segment i to the RF line $C_{\text{trap,RF},i}$ and the capacitance of segment i to ground $C_{\text{trap,DC},i}$.

The circuit representation of segment i can be seen in Figure 3.14 c. In order to minimize the voltage at the segment, a shunt network shorts RF signals to ground. Further filtering of the output of the shunt network prevents the trap drive from being radiated into the lab by the connecting DC line.

In this circuit diagram, the *trap* is represented by a capacitive voltage divider consisting of the capacitors $C_{\text{trap,RF},i}$ and $C_{\text{trap,DC},i}$. Both capacitances depend on the trap geometry and can vary from segment to segment. Without a *shunt network*, this voltage divider sets the voltage at the DC segment $\underline{V}_{\text{seg,RF},i}$.

In the circuit of Figure 3.14 c, the *shunt network* consists of the bond wire with an inductance $L_{\text{bond},i}$, the trace on the PCB with an inductance $L_{\text{trace},i}$, and a capacitor $C_{B,i}$ with its ESR $R_{CB,i}$. In special cases which will be explained later, it could be advantageous to add a capacitance $C_{S,i}$ with its ESR $R_{CS,i}$ right next to the bond pad, where $C_{S,i} < C_{B,i}$. The goal is to minimize $\underline{V}_{\text{seg,RF},i}$, and thus, one tries to reduce the reactance of the whole *shunt network*. Hence, one designs the setup to have as-short-as-possible bond wires and as-short-as-possible traces at the PCB, which end at as-big-as-possible capacitors.

The *filter network* in Figure 3.14 c does not shunt the trap drive signal further, but stops residual RF from leaving the vacuum chamber, as $L_{\text{filter1},i}$ and $C_{\text{filter},i}$ represent an LC low-pass filter. The circuit in Figure 3.14 c seen from right to left represents a two stage LC input noise filter with the coils $L_{\text{filter1},i}$ and $L_{\text{filter2},i}$, and the capacitors $C_{\text{filter},i}$ and $C_{B,i}$, which is described in Chapter 3.2.1.

If the values for $C_{\text{trap,RF},i}$ and $C_{\text{trap,DC},i}$ are not well known, it is best to perform a worst case simulation by overestimating $C_{\text{trap,RF},i}$ and underestimating the ratio $\frac{C_{\text{trap,DC},i}}{C_{\text{trap,RF},i}}$, as this will lead to an increased $\underline{V}_{\text{seg,RF},i}$. Such a simulation was performed for the plots of Figure 3.15, where

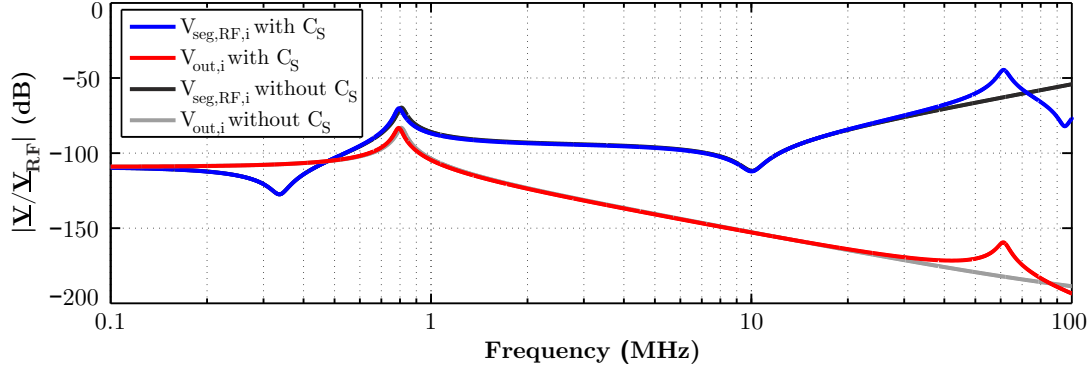


Figure 3.15.: Simulated amplitudes of $\underline{V}_{\text{seg,RF},i}$ and $\underline{V}_{\text{out},i}$ of the circuit of Figure 3.14 c with and without $C_{S,i}$.

the attenuation of the RF voltage at the segment i $\underline{V}_{\text{seg,RF},i}$ and the attenuation of the output of the *filter network* $\underline{V}_{\text{out},i}$ of the *filter network* were simulated with and without the presence of $C_{S,i}$. The following values were chosen for the components in the simulation. $C_{\text{trap,RF},i} = 0.2$ pF, $C_{\text{trap,DC},i} = 0.6$ pF, $L_{\text{bond},i} = 10$ nH, $C_{S,i} = 47$ pF, $R_{C_{S,i}} = 0.2$ Ω , $L_{\text{trace},i} = 15$ nH, $C_{B,i} = 4.7$ nF, $R_{C_{B,i}} = 0.2$ Ω , $L_{\text{filter}1,i} = 4.7$ μH , $C_{\text{filter},i} = 47$ pF, $R_{C_{\text{filter},i}} = 0.2$ Ω , $L_{\text{filter}2,i} = 4.7$ μH

Figure 3.15 shows that for trap drive frequencies below 20 MHz, the simulations with and without $C_{S,i}$ yield similar results, and the suppression of the RF voltage on the segment is larger than -80 dB for most frequencies. For frequencies above 10 MHz, $\underline{V}_{\text{seg,RF},i}$ increases with increasing frequency. In a frequency regime between 30 and 60 MHz, the small capacitor $C_{S,i}$ causes a resonance, which elevates the RF voltage at the segment $\underline{V}_{\text{seg,RF},i}$. But above 60 MHz, $\underline{V}_{\text{seg,RF},i}$ is reduced by the presence of $C_{S,i}$. These worst case simulations display that the RF voltage at the segment $\underline{V}_{\text{seg,RF},i}$ should be attenuated by more than 60 dB, meaning that the RF on a DC segment is less than 1/1000 of the total voltage on the RF segment.

In the filters for incoming noise, the outgoing trap drive is more strongly attenuated than the incoming noise at the secular motion frequencies, as depicted in Figure 3.15. For typical trap drive frequencies above 10 MHz, the ratio $\left| \frac{\underline{V}_{\text{out},i}}{\underline{V}_{\text{RF}}} \right|$ is well below -150 dB, which prevents radiating the trap drive into the lab.

4 A cryostat for scalable quantum computation with trapped ions

This chapter covers the design and characterization of a cryostat. During the design process, the setup was optimized for QIP with trapped ions. Especially, scalability should be demonstrated with this setup.

The design starts with the choice of the cryostat and the beam geometries required for the operation of a trapped ion quantum computer. Furthermore, the magnetic field at the position of the Paul trap was optimized for high spatial homogeneity and low temporal fluctuations. The trap, the resonator of the segmented Paul trap, filters for the DC segments, and a lens system are integrated in the heat shield of the cryostat. The whole setup is designed for low vibrations. After the cryostat was assembled, the movement of the inner heat shield with respect to its surroundings and the magnetic shielding were measured. A brief overview of this design can be found in the publication [BvMP⁺16].

4.1 Choosing the type of cryostat

When designing a cryogenic trapped ion experiment, the first consideration has to be what type of cryostat one uses. There are numerous different types of cryostats [Pob92, WAW88, Eki06]. The ones most commonly used in modern cryostats are

- Dilution Refrigerator
- Gifford-McMahon Cryocooler
- Pulse Tube Cryocooler
- (Continuous) Flow Cryostat
- Bath Cryostat

A **dilution refrigerator** [Pob92] is a cryostat with a mixture of ^3He and ^4He , which undergoes a phase transition at temperatures below 1 K. This phase transition allows cooling to absolute zero, and its reachable end temperature is then only limited by the thermal load on the cryostat. So far, it has not been necessary to cool ion traps to less than 1 K, and there are no ion trap experiments in dilution refrigerators. However, one experiment with a dilution refrigerator to couple ions and superconducting qubits is currently being designed [DMGR⁺16].

Gifford-McMahon cryocoolers [WAW88, Eki06] and **Pulse Tube cryocoolers** [Eki06] are closed systems, which do not require a constant supply of a cryogenic coolant, such as liquid nitrogen or liquid helium, and can be switched on when cooling is needed. This convenience results in higher acquisition costs than for other cryostats with end temperatures above 1 K. The closed-cycle cryostats introduce additional engineering challenges such as unwanted magnetic fields during the experiments¹, and acoustic noise in the lab. Most modern designs offer a spatial separation between the loud compressor and the cold head of the cryostat. But the acoustic vibrations from the transfer lines between the compressor and the cold head cannot easily be separated from the experiment. Furthermore, the cold head itself vibrates due to the

¹The option of putting a magnetic shield around these cryostats exists, but it can only attenuate and not cancel these generated magnetic fields. Furthermore, such a magnetic shield corresponds to a spatial inhomogeneity for the constant magnetic field in the experiments, which influences the homogeneity of the field in the trap.



Figure 4.1.: The UHV-compatible flow cryostat from *Janis*.

operation of the cryostat. The resulting vibrations are usually on the order of several tens of μm , and have to be decoupled in the experiment². When working with an optical qubit for which the absolute phase of visible light during one experiment matters, vibrations can lead to fast decoherence, see Chapter 4.11.2.

(Continuous) flow cryostats [WAW88, Eki06] and bath cryostats [WAW88, Eki06] are wet cryostats, which require a supply of liquid coolant, such as liquid nitrogen or liquid helium. They cool by evaporating the coolant and their disadvantage is that a constant supply of the coolant must be ensured. Therefore, the desired operating temperature defines what liquid coolant to use, its consumption, and the operating costs. With flow cryostats, one has additional control over the coolant flux to tune the temperature of the cold finger, which is not possible with bath cryostats. With the evaporated gas from the cryostat operation, one can cool a second heat shield at higher temperatures. Thereby, the thermal load on the inner shield attached to the tip of the cold finger is reduced to minimize the overall coolant consumption. The vibrations due to the boiling liquid are typically on the order of $1 \mu\text{m}$, which is about the size of the wavelength of an optical qubit. Thus, phase coherent state manipulation of optical qubits with a well-defined phase requires vibration isolation. For the sake of completeness, one should mention here that liquid helium becomes superfluid under vacuum conditions. Hence, if one pumps the exhaust side of the cryostat with a vacuum pump, liquid helium cannot create vibrations. However, that way, it is not possible to cool a second heat shield and thereby reduce the coolant consumption. Thus, it was not pursued further.

Since there was no need from an ion trapping point of view to cool below 4 K, a dilution refrigerator was not considered as a possible cryostat for this work. High acquisition costs combined with generated magnetic fields and acoustic noise ruled out closed-cycle cryocoolers. Hence, the decision for the work in this thesis was between a bath and a flow cryostat. Both wet cryostat types allow operation with any liquid coolant, like liquid nitrogen or liquid helium, and require a supply of that liquid coolant. Furthermore, both wet cryostats will require vibrational decoupling to allow QIP with an optical qubit.

This setup is intended to run continuously for a week or more. In the case of a bath cryostat, this would require a big tank of up to 100 l, whereas for a flow cryostat, the coolant is always supplied from a reservoir in a dewar, in which one can store several 100 l of the coolant. Since UHV-compatible bath cryostats with such big tanks are more expensive and do not allow tuning the coolant consumption, a continuous flow cryostat Model ST-400-1 from *Janis*³ was acquired, which is illustrated in Figure 4.1.

²The exact values for vibration strongly depend on how the cryostat is mounted. Since this is something that the manufacturers cannot influence, they are usually reluctant to give accurate numbers on how big the vibrations of their cryostats really are.

³Janis, 225 Wildwood Avenue, Woburn, MA 01801-2025, USA

4.2 Minimizing the thermal load

Heat transfer between two parts of the cryostat is due to convection in gases or liquids, through conduction in solids, and through black-body radiation [Eki06]. Trapped ion experiments require UHV conditions. Hence, one can neglect heat transfer through convection in the background gas. In order to limit heat transfer through solids along regions with a temperature gradient, one needs to choose materials with low thermal conductivity, and use as little of that material as necessary for mechanical stability.

Radiative heat transfer causes a significant heat load on the cryostat because of big temperature differences of more than 200 K. This can be minimized by radiation shields between surfaces with such big temperature differences. In this design, an outer shield is placed between the cold inner shield and the warm vacuum chamber as shown in Figure 4.2 a. The radiative heat flux \dot{q}_{rad} can be calculated with the Stefan-Boltzmann equation $\dot{q}_{\text{rad}} = \sigma \epsilon A T^4$, where σ is the Stefan-Boltzmann constant ($5.67 \cdot 10^{-8} \text{ W}/(\text{m}^2 \cdot \text{K}^4)$), A is the interacting surface area, and T is the temperature of the surface. The emissivity ϵ of a body strongly depends on the surface. It can be close to 1 for highly oxidized surfaces, and close to 0 for polished, metallic surfaces. From this equation, one can calculate the heat exchange between two surfaces with

$$P_{\text{rad}} = \Delta \dot{q}_{\text{rad}} = \sigma E A (T_2^4 - T_1^4) \quad (4.1)$$

where T_1 and T_2 are the temperatures of the two surfaces, and E a factor between 0 and 1, involving the emissivities of both surfaces. Typical values of E for specular (mirror-like) reflection can be obtained with the formula $E = \epsilon_1 \epsilon_2 / (\epsilon_1 + \epsilon_2 - \epsilon_1 \epsilon_2)$ [Eki06].

Eq. 4.1 shows that one can drastically decrease the radiative heat load on the coldest heat stage by adding an actively cooled outer heat shield at an intermediate temperature. In a flow cryostat, used in this work, one can clamp the outer heat shield onto the cold finger of the cryostat, as displayed in Figure 4.2 a. The liquid coolant evaporates at the bottom of the cold finger close to the inner shield. The evaporated cold gas will then be pushed upwards towards the exhaust at the top of the cryostat. By clamping the outer shield to the cold finger, heat from the outer heat shield is transferred into the passing, cold gas, thereby actively cooling the outer heat shield. The exact cooling power depends on the position of the clamp along the cold finger, the length of the clamp, and the flux of the gas.

Another way to decrease the radiative load on the cryostat is to use an isolated, passive layer between a hot and a cold surface, as depicted in Figure 4.2 b. The hot surface emits back-body

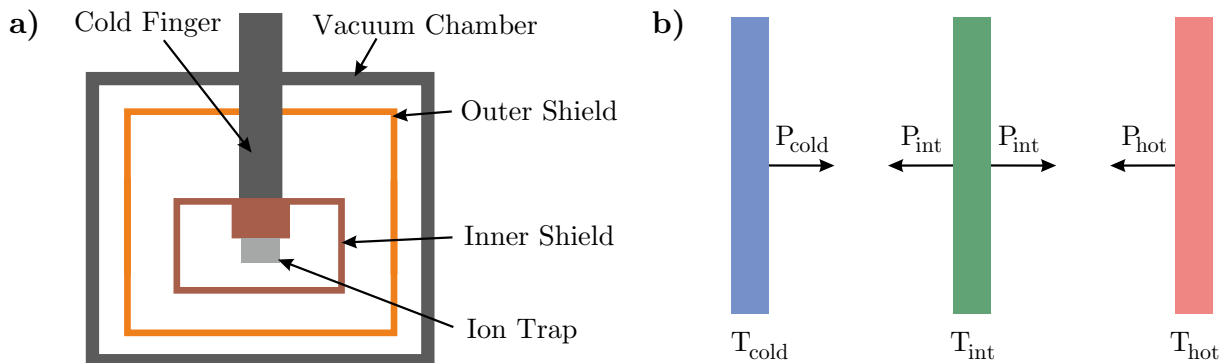


Figure 4.2.: Panel a) shows the principle, how to decrease the radiative load on a cold inner shield with an actively cooled outer shield at an intermediate temperature. Panel b) depicts the idea how to decrease the thermal load with an isolated, passive layer between a hot and a cold surface.

radiation of power P_{hot} , and the cold surface P_{cold} . The intermediate layer emits P_{int} towards both the hot and the cold surface. Hence, in a thermal equilibrium $2P_{\text{int}} = P_{\text{hot}} + P_{\text{cold}}$. If one assumes $P_{\text{hot}} \gg P_{\text{cold}}$, then one obtains for the thermally radiated power towards the cold surface $P_{\text{int}} \approx P_{\text{hot}}/2$. Or in general, one can state that with N isolated layers between a hot and a cold surface, the power of black-body radiation is decreased by a factor $1/(1+N)$ [Eki06].

This effect is used in superinsulation, typically used in dewars. There, many layers of aluminized Mylar are placed between the hot and the cold walls of the dewar. In high vacuum, the thermal conductivity between layers of Mylar can become as low as 10^{-5} W/(m·K), which effectively isolates the different aluminum layers. At the beginning of this thesis, no UHV-compatible superinsulation was available, and hence, it was not included in the design of the cryostat. In recent years, UHV-compatible superinsulation became available and in future designs, one could make use of superinsulation to thermally decouple cryostats from their environment in a passive way.

4.3 Beam geometries and trap orientation

An important constraint for the design of the experimental setup is how to align the laser beams and the trap in the chamber. In cryogenic environments, lasers beams can only illuminate an ion in the Paul trap through designated holes in the heat shields.

The most crucial design constraints on the optical setup near the trap are added by the beam used for addressing single ions in an ion string, which requires a certain numerical aperture (NA) to generate the small spot size of the qubit laser light required for high-fidelity addressing. From reference [Jam98], one can determine the ion distances along the trap axis, which depend on the number of ions, the ion mass, the ion charge, and the axial confinement potential. A typical value for ion to ion spacing would be 4 to 5 μm for a few $^{40}\text{Ca}^+$ at an axial motion frequency of about 1 MHz. And for a few $^{88}\text{Sr}^+$ at similar axial motion frequencies, the ion-to-ion distance would be 4 μm or less.

The Abbe diffraction limit states that light with wavelength λ focused onto a spot under an angle θ in a medium with refractive index n will produce a spot of radius

$$d = \frac{\lambda}{2n \sin \theta} = \frac{\lambda}{2 \text{NA}} \quad (4.2)$$

where $\text{NA} = n \sin \theta$ is the numerical aperture (NA). The qubit laser transitions for both $^{40}\text{Ca}^+$ and $^{88}\text{Sr}^+$ are around 700 nm. Single ion addressing with high fidelity should produce a spot radius which is at maximum half that distance between two neighboring ions. This means that one should use an NA of at least 0.2 for high-fidelity addressing with ion distances of about 4 μm .

Ion heights in planar Paul traps can vary between 30 μm and several hundred μm . A typical value for traps used in QIP is about 100 μm . The required $\text{NA} = 0.2$ corresponds to an aperture angle of $\theta = 11.5^\circ$, which is too big for high-fidelity addressing when the ions are only 100 μm above the surface and the trap has a width of several mm, as depicted in Figure 4.3 a. From a manufacturing point of view, it is difficult to increase the NA for a beam grazing over the surface of the trap, but traps with a slot in the center are not hard to produce. Such traps, shown in Figure 4.3 b, allow addressing through this slot with an NA of up to 0.25. When using two lenses for quantum state detection, one in the front and one in the back, the high NA in both lenses enables high photon collection efficiencies, which are required for high-fidelity detection.

The considerations for the beam geometries, shown in Figure 4.3 c and d, are as follows: the addressing beams are parallel to the optical table and perpendicular to the trap surface, as

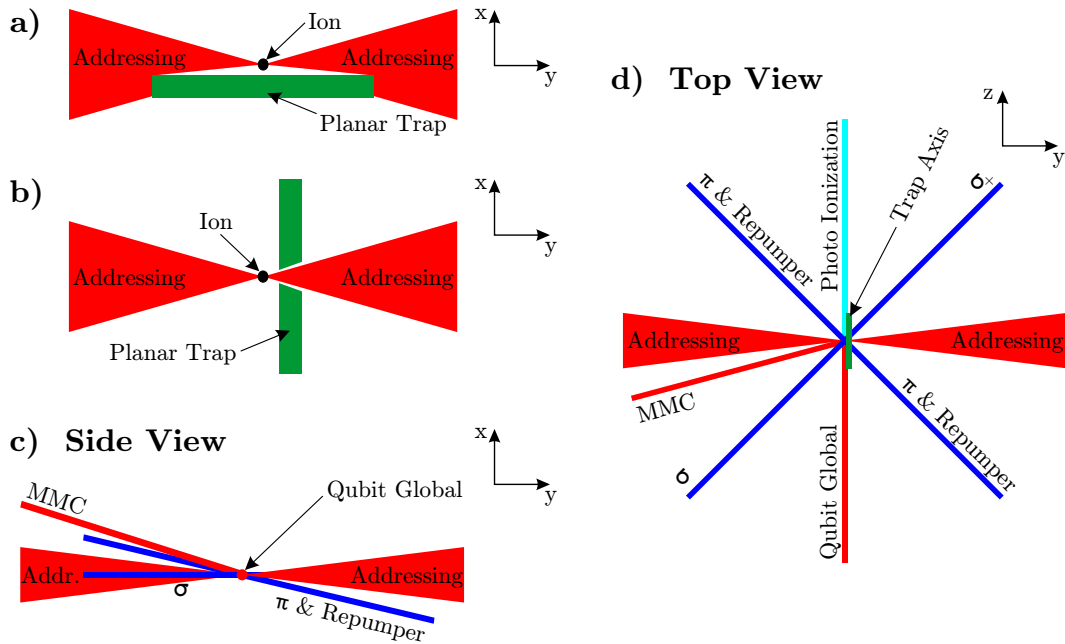


Figure 4.3.: Panel **a** shows addressing from the side of the trap, and panel **b** addressing through a slot in the trap. Panel **c** depicts the side view of the final beam geometries, and panel **d** their top view.

depicted in Figure 4.3 b. The global qubit beams and the trap axis are horizontal too, but perpendicular to the addressing beams. The magnetic field axis is in the same horizontal plane but 45° to both qubit beams, which enables using all allowed quadrupole transitions with the qubit laser light of both qubit beams⁴. The magnetic field axis in Figure 4.3 d runs parallel to the σ_+ - and σ_- -polarized beams. The light used for Doppler cooling and state detection is π -polarized light and thus perpendicular to the magnetic field axis. The repump laser beams, which couple the P- and D-states, are copropagating to the Doppler cooling and state detection beams. The σ_- and π -polarized light will later enable multi-mode cooling with EIT, see Chapter 2.7 for more details.

During the course of this thesis, two cryostats were built. In the first version, the beams of the π -polarized light were in the same horizontal plane as the qubit lasers. But even anti-reflection (AR) coated viewports reflect a fraction of the light passing through them. This means that a fraction of each beam (which is tightly focused at the position of the trap) will be reflected back towards the trap and illuminate the whole trap, which will increase the dark count rate during quantum state detection. To circumvent this in the second version, the beams of the π -polarized light are tilted by 4° out of the plane of the other beams, as shown in Figure 4.3 c. To facilitate loading, the photo ionization lasers are aligned counter-propagating to the global qubit lasers along the trap axis. So far, in this beam geometry there is no projection of qubit laser light perpendicular to the plane spanned by the addressing and global laser beams. But micromotion compensation (MMC) with the qubit laser will require such a projection [Roo00, BMB⁺98b]. Hence, a MMC beam was added, which is 15° rotated to the addressing beam horizontally and 21° up. These angles were fixed due to constraints given by the optical access in the used vacuum chamber, a *Kimball Physics* Spherical Square Chamber with additional 16CF ports.

⁴Selection rules dictate which transitions in the ion are allowed and which not. If the qubit beams are not parallel or perpendicular to the magnetic quantization axis, all quadrupole transitions will be accessible.

4.4 Magnetic field stability

This setup was optimized for operation with $^{40}\text{Ca}^+$ and $^{88}\text{Sr}^+$ ions. The qubit transitions in both species are encoded in the $^2\text{S}_{1/2} \leftrightarrow ^2\text{D}_{5/2}$ transitions (optical qubit) or in the Zeeman manifold of the $^2\text{S}_{1/2}$ ground state (Zeeman qubit), as described in Chapter 2.2. Both types of qubits have magnetic field dependences of up to 3.9 MHz/Gauss [TPR⁺03, BHK⁺15]. The ultimate limit for the frequency stability of the optical qubit is the natural linewidth of the transition in which it is encoded. For $^{40}\text{Ca}^+$, that is 140 mHz [BDL⁺00, CBK⁺09], and for $^{88}\text{Sr}^+$, it is 400 mHz [LWGS05, MHB⁺03]. To avoid being limited by magnetic field fluctuations when working with an optical qubit, the magnetic field perturbations must not exceed $\frac{140 \text{ mHz}}{3.9 \text{ MHz/Gauss}} = 36 \text{ nGauss}$. In typical experiments with $^{40}\text{Ca}^+$ and $^{88}\text{Sr}^+$ ions, the typical quantization field strength is about 3 Gauss. Therefore, it is desirable that the relative magnetic field deviation is than about $1.2 \cdot 10^{-8}$ both spatially and temporally.

4.4.1 Spatial homogeneity

(Ferro-)magnetic materials near the trap will generate high local magnetic field gradients in the quantization field, which cause an inhomogeneity at the position of the ion in the trap and the frequency of the qubit transition will vary with the position of the ion in the trap. When using the global qubit beam along the trap axis defined in Chapter 4.3, all ions in the trap will be addressed by the qubit laser and the homogeneous region has to cover the length of the trap axis in which ions interact with the qubit light. The spatial homogeneity must be guaranteed over the whole length of the addressed ion chain.

To avoid spatial inhomogeneity, one must not use (ferro-)magnetic materials near trapped ion experiments. A list of materials with low magnetic susceptibility, typically used when constructing a cryogenic experiment, is shown in Table 4.1. Austenitic stainless steels are paramagnetic, but can become ferromagnetic when welded or cyclically cooled. The only steel that does not become ferromagnetic is 316 LN⁵.

Table 4.1.: Magnetic susceptibilities of various materials over temperature typically used to construct a cryostat. These values were taken from reference [Eki06].

Material	χ at 293 K	χ at 77 K	χ at 4.2 K
Quartz	$-1.03 \cdot 10^{-6}$		$-9.27 \cdot 10^{-6}$
Phosphor bronze	$-5.86 \cdot 10^{-6}$		$-5.56 \cdot 10^{-5}$
Copper	$-9.34 \cdot 10^{-6}$	$-9.18 \cdot 10^{-6}$	$-8.67 \cdot 10^{-5}$
Aluminum	$2.07 \cdot 10^{-5}$		$2.52 \cdot 10^{-5}$
Titanium	$1.78 \cdot 10^{-4}$		
Stainless steel 304	$2.7 \cdot 10^{-3}$	$5.5 \cdot 10^{-3}$	
Stainless steel 316	$3.0 \cdot 10^{-3}$	$7.7 \cdot 10^{-3}$	$1.6 \cdot 10^{-2}$
Stainless steel 316 LN	$3.5 \cdot 10^{-3}$	$7.2 \cdot 10^{-3}$	$1.1 \cdot 10^{-2}$
Brass	$1.12 \cdot 10^{-2}$		$-1.4 \cdot 10^{-2}$

To generate homogeneous magnetic fields, one can use Helmholtz coils which are two coils of same radius on the same coil axis and the distance between the coils has to be the radius of the coils. To minimize noise on the current through the coils, they are usually wired in series to one another. Due to space constraints in the vacuum chamber, the coils could not be placed inside the vacuum chamber. Since the magnetic field axis was chosen horizontally, the size of the

⁵X6CrNi would be another exception that does not become ferromagnetic, but it is less commonly used than 316 LN stainless steel.

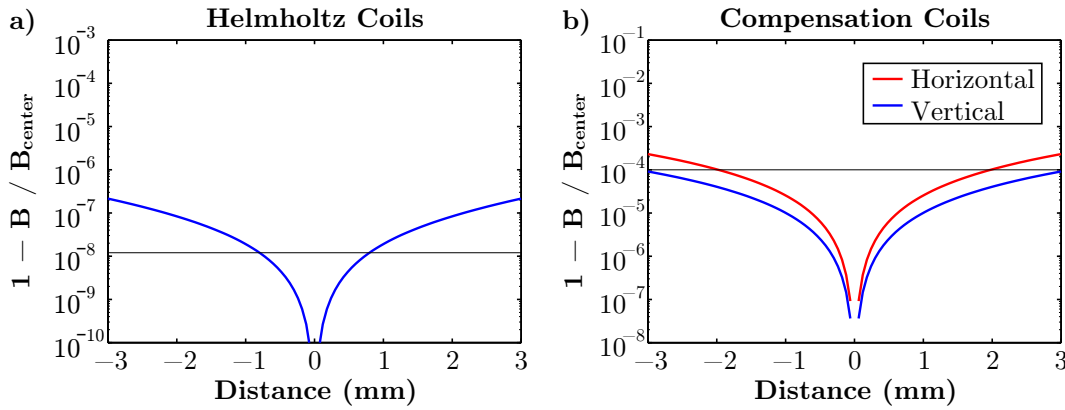


Figure 4.4.: The homogeneity of the magnetic field in the center of the apparatus for the Helmholtz coils **a** and the compensation coils **b**.

chosen vacuum vessel required a minimum coil-to-coil distance bigger than the outer diameter of a 160CF flange. Thus, the average radius⁶ of the Helmholtz coils was chosen to be 19.5 cm. The 238 windings of these coils are separated into 17 horizontal layers of 14 windings with a spacing of 1.2 mm from one winding to the next, given by the wire diameter. This results in a magnetic field of 11 Gauss per Ampere in the center of the coils. From the considerations for the beam geometries, the trap has to be placed under an angle of 45° to the magnetic field axis. Simulations of the magnetic field homogeneity of this configuration can be seen in Figure 4.4 a. The required spatial stability of $1.2 \cdot 10^{-8}$ is reached over a distance of more than 1.5 mm along the trap axis which allows simultaneous interaction with ions stored in this length along the trap axis.

The limitations on the homogeneity perpendicular to the magnetic field axis are much less restrictive. The Zeeman splitting in the ions is only dependent on the absolute value of the magnetic field and can be written as $\sqrt{B_{\text{axis}}^2 + B_{\text{perp.}}^2}$, where B_{axis} is the field along the axis and $B_{\text{perp.}}$ is the absolute value of the field perpendicular to the axis. $B_{\text{perp.}}$ has to be canceled in the region of interest to only have a magnetic field along the field axis. The binomial expansion of the absolute value of the magnetic field can then be written as

$$B_{\text{axis}} \sqrt{1 + \left(\frac{B_{\text{perp.}}}{B_{\text{axis}}}\right)^2} = B_{\text{axis}} \left(1 + \frac{1}{2} \left(\frac{B_{\text{perp.}}}{B_{\text{axis}}}\right)^2 - \frac{1}{8} \left(\frac{B_{\text{perp.}}}{B_{\text{axis}}}\right)^4 - \dots\right). \quad (4.3)$$

Thus, the required stability considered laterally for $B_{\text{perp.}} \ll B_{\text{axis}}$ is only $\sqrt{2 \cdot 1.2 \cdot 10^{-8}} \approx 10^{-4}$ and it is sufficient to have compensation coils for which the distance between the two coils is bigger than the coil radius. Thus, the horizontal coils each have 112 windings with an average radius of 6.7 cm and an average distance between the coils of 26.4 cm, which results in a magnetic field sensitivity of 1.96 Gauss/A. The vertical coils each have 56 windings with an average radius of 11 cm and an average distance between the coils of 19 cm, which results in a magnetic field sensitivity of 2.77 Gauss/A. The resulting spatial homogeneities of the compensation coils are displayed in Figure 4.4 b. The required spatial homogeneity of better than 10^{-4} is reached over several millimeters for both the vertical and horizontal coils. To incorporate the coils in the setup, they are mounted onto the flanges of the *Kimball Physics* chamber, as displayed in Figure 4.5.

⁶For coils with several hundred windings, the dimensions of the coil start playing a role. Therefore, the average radius is the radius in the middle of the windings.

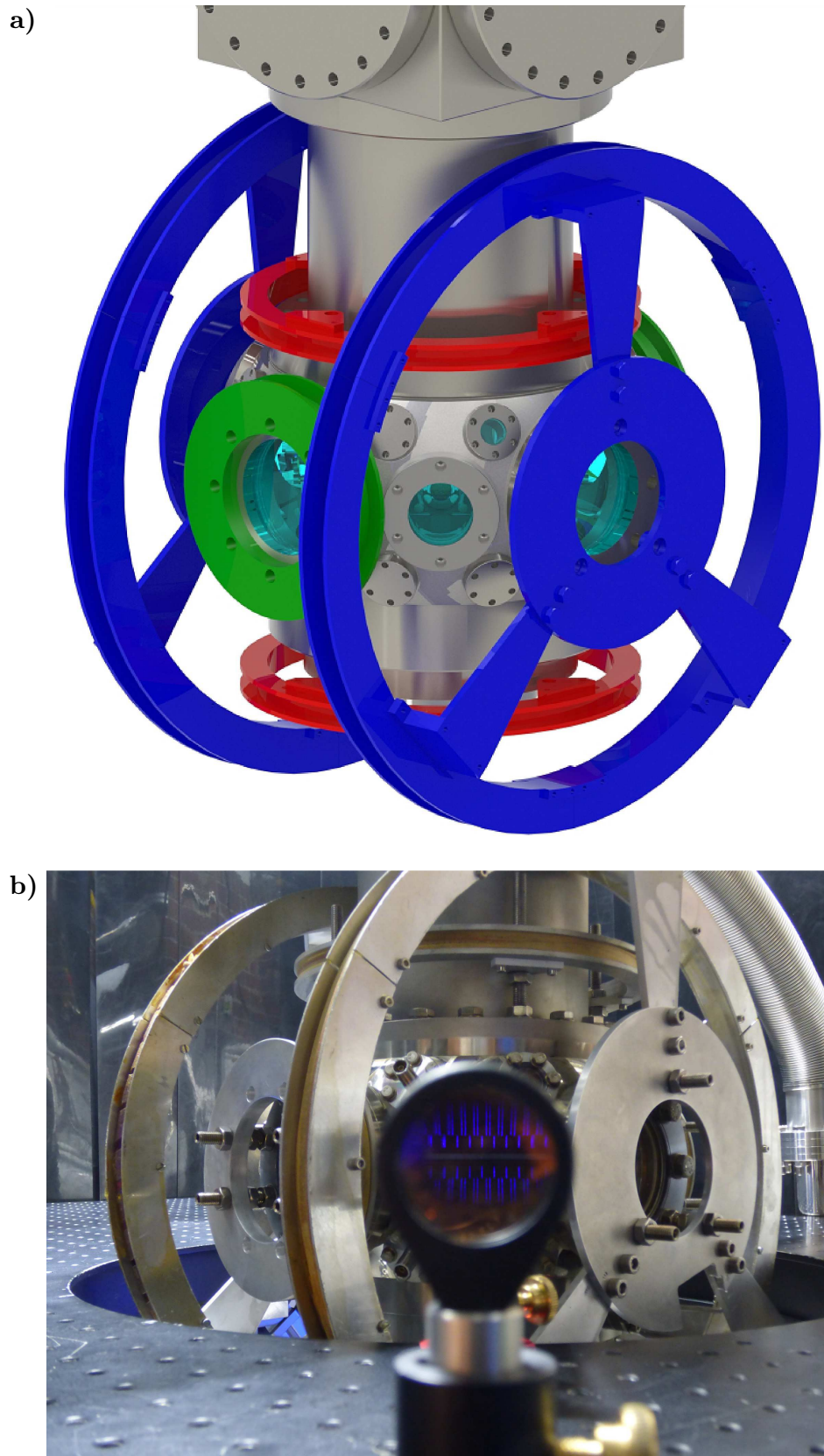


Figure 4.5.: Panel a depicts a drawing of the vacuum chamber with the surrounding coils. Blue are the Helmholtz coils, red the vertical compensation coils, and green the horizontal ones. Panel b shows a picture of the coils around the chamber in the lab. In the center, the trap is illuminated by blue laser light and magnified by lenses.

4.4.2 Magnetic shielding

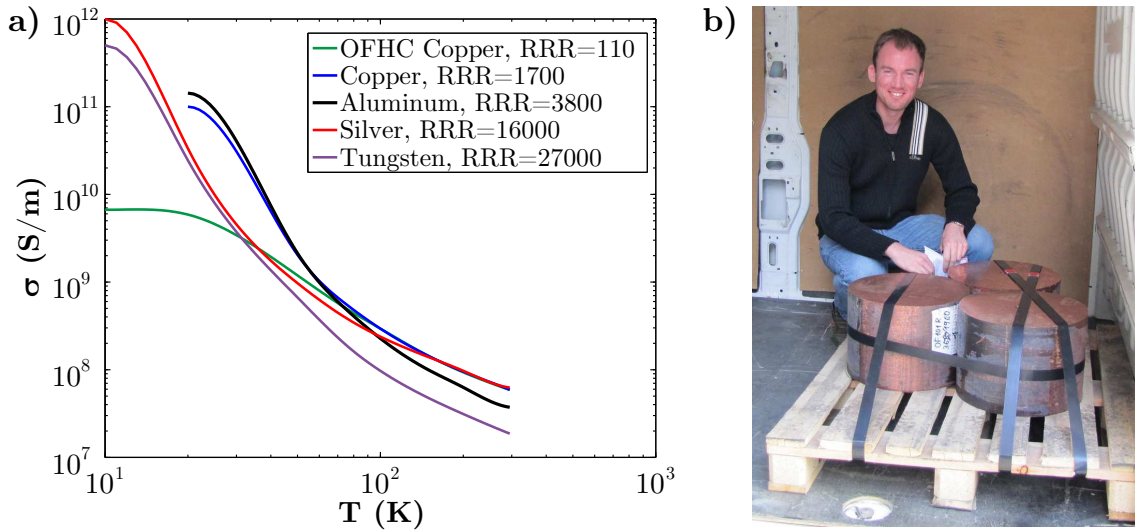


Figure 4.6.: Panel **a** shows the electrical conductivities of several materials over temperature with values from reference [Eki06]. Panel **b** displays a photo of the 770 kg of copper that were bought directly from a copper mill.

Besides the spatial homogeneity, the magnetic field has to be held stable over time. It is challenging to achieve the required stability of $1.2 \cdot 10^{-8}$ with active electronics. One way of generating, constant magnetic field is with superconducting coils. But since superconducting Helmholtz coils would have to be small to fit in the inner shield reducing the spatial homogeneity, this was not considered. Another option is to low-pass filter magnetic field noise. This low-pass filtering can be utilized by employing the skin-effect of a highly conducting enclosure of the trap, as described in reference [BWC⁺11].

In trapped ion QC experiments, a typical measurement cycle consisting of cooling, the quantum algorithm and detection takes about 20 ms of which the quantum algorithm only requires about 1 ms, see Figure 6.3. At low temperatures, the skin effect in ultra-pure metals can slow down magnetic field changes by so much that the magnetic field stays constant, meaning that the relative change is smaller than $1.2 \cdot 10^{-8}$, over time scales of up to several seconds. This way, it is possible to achieve the desired stability over multiple experiment cycles. Slow magnetic field drifts, like offset drifts of the current in the coils or changes in earth's magnetic field [Jac91], will still affect the qubits in the inner shield. Additional calibration measurements between quantum information experiments can be introduced to infer the qubit transition frequencies. If future experiments last longer than the time scale on which the magnetic field is constant, dynamical decoupling sequences [VL98] can be employed to decouple the experiments from low frequency magnetic field drifts.

The basic idea behind the damping of alternating magnetic fields with highly conducting metals is that skin effect prevents alternating magnetic fields from entering a conductor. A good attenuation is achieved if the conductor is much thicker than the skin depth δ , which is defined as

$$\delta = \sqrt{\frac{2}{\omega\sigma\mu}} \quad (4.4)$$

with ω being the (angular) frequency of the magnetic field, σ being the electrical conductivity of the material, and μ being its permeability. At low temperatures, the conductivity increases exponentially, as shown in Figure 4.6 a, so that skin effect rejects even magnetic fields of as low as a couple of Hertz over typical lengths in the mm or cm range.

To analyze the shielding potential with ultra-pure metals, one can look at the expected shielding with oxygen-free high conductivity (OFHC) copper. Experience has shown that the main spectral components of magnetic field fluctuations in trapped ion QC experiments are synchronous to the power line frequency. Therefore, magnetic field attenuation is most important at a frequency of 50 Hz and low harmonics. At room temperature, the skin depth of 50 Hz magnetic fields is about 9.2 mm in copper. When cooling with liquid helium, one can expect that the conductivity of the copper increases by a factor of 100 to 1000 compared to room temperature (residual resistivity ratio⁷ (RRR) = 100 - 1000). Therefore, the skin depth for 50 Hz signals in copper will decrease to 0.92 mm or even 0.29 mm. If one assumes that the walls of the inner shield were 20 mm thick, the magnetic shielding would increase to -188 dB or even -600 dB for 50 Hz fields. Hence, cold, thick walls of an ultra-pure metal are excellent magnetic shields for frequencies of 50 Hz and higher. The main imperfections in these magnetic shields arise from holes in the shields, which are required for optical access, and the physical barriers for eddy currents repelling the alternating magnetic fields. In the latter case, contact resistances between the two parts of the shield are typically limiting the magnetic shielding.

Because of the proximity to a copper mill⁸, ultra-pure copper (Figure 4.6 b) with an RRR value of bigger than 300 after casting could be obtained. In order to increase the RRR value of the cryostat material, the copper was thermally annealed at 450°C in a nitrogen atmosphere for 5 hours⁹. The tempering to repair surface damage after milling was performed in the vacuum chamber at 150°C (for several days). This should ensure an RRR value higher than 1000.

Due to the exponential increase in conductivity at low temperatures, it is sufficient to design only the inner heat shield as a magnetic shield. The walls of the constructed inner shield have a thickness of more than 20 mm. To maximize the shielding against alternating magnetic fields, the only through holes in the shield were for the laser beams, atomic oven beams and wiring, as displayed in Figure 4.7 and Figure 4.8. The through holes resemble hollow conducting cylinders and the magnetic field along the axis of such cylinders [CM99] is

$$H \propto \exp\left(-\alpha \frac{z}{r}\right) \quad (4.5)$$

where α is a prefactor, z is the length of the cylinder and r its radius. Hence for best shielding, it is important to have through holes with a small diameter in a thick wall.

The inner shield consists of two pieces as depicted in Figure 4.9. The green arrow symbolizes the quantization axis, and the blue arrows symbolize the two axes perpendicular to it. In order to repel alternating magnetic fields, eddy currents are induced in the inner shield. These currents are depicted by the red arrows for the three axes. Eddy currents caused by magnetic field fluctuations along the quantization axis flow parallel to the contact surface. Hence, they do not experience the contact resistance between the two pieces. But eddy currents caused by magnetic field fluctuations perpendicular to the quantization axis flow from one piece to the other and thus experience contact resistance between the two pieces.

At room temperature, the contact resistance is typically negligible to the bulk resistance. But the high conductivity at low temperatures causes the contact resistance to dominate the resistance for the eddy currents. Following the considerations of Eq. 4.3, it is most important to have the best shielding along the quantization axis. Hence, the geometry was chosen so that the surface between the two pieces of the inner shield is perpendicular to the magnetic field axis such that the eddy currents induced along this axis do not experience the contact resistance. In order

⁷The residual resistivity ratio is the ratio of the conductivity at cryogenic temperature divided by the conductivity at room temperature and is one way of describing how pure a material is.

⁸Montanwerke Brixlegg AG, Werkstraße 1, 6230 Brixlegg, Austria

⁹Private communications with Stefan Konetschnik from METTOP GmbH (Peter-Tunner-Straße 4, A-8700 Leoben, Austria)

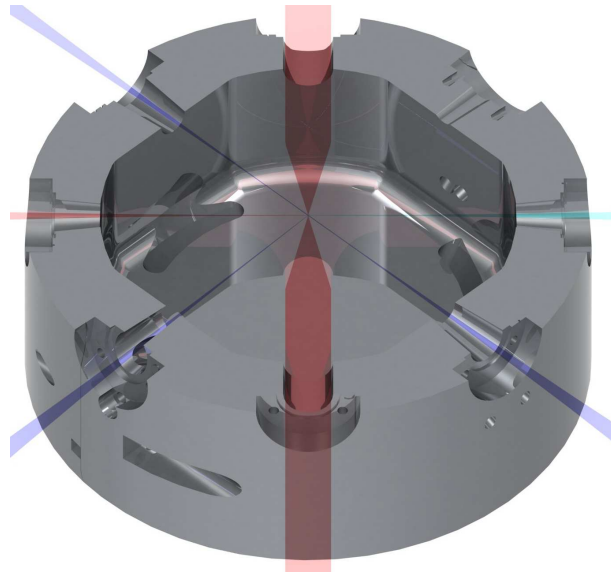


Figure 4.7.: A cut of a drawing of the inner shield with the laser beams.

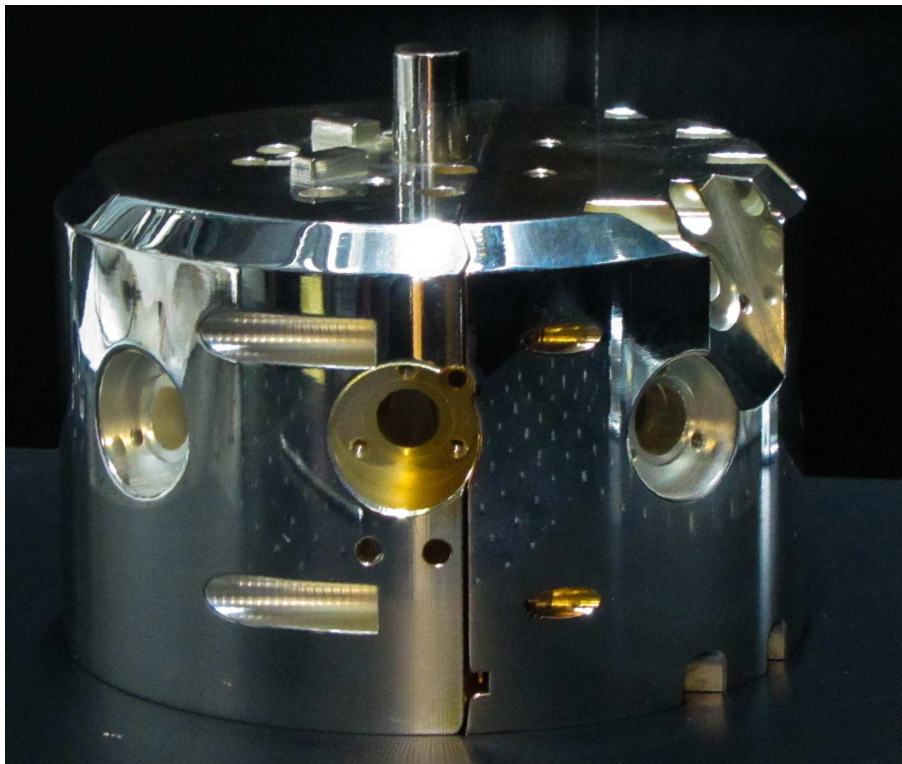


Figure 4.8.: A picture of the inner shield with its small holes.

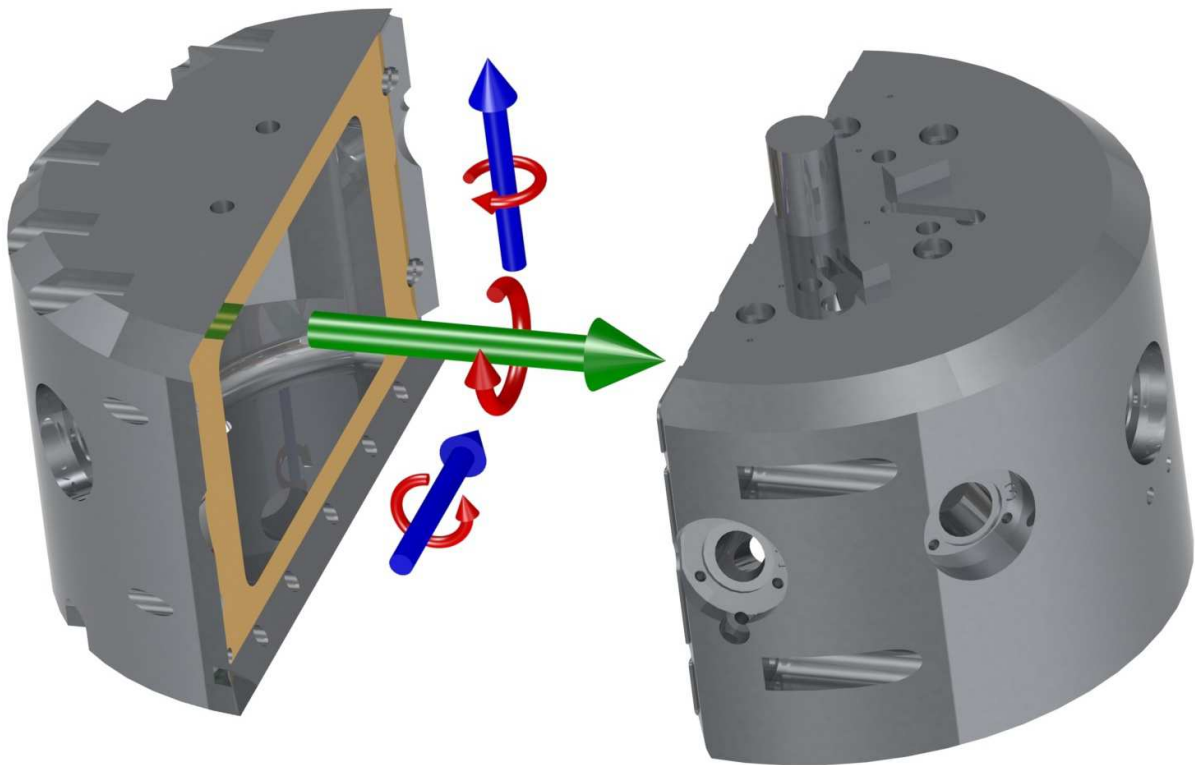


Figure 4.9.: The drawing of the two halves of the inner shield with the three main axes and the resulting eddy currents along the axes in red. The green arrow symbolizes the quantization axis. The blue arrows depict the other two axes.

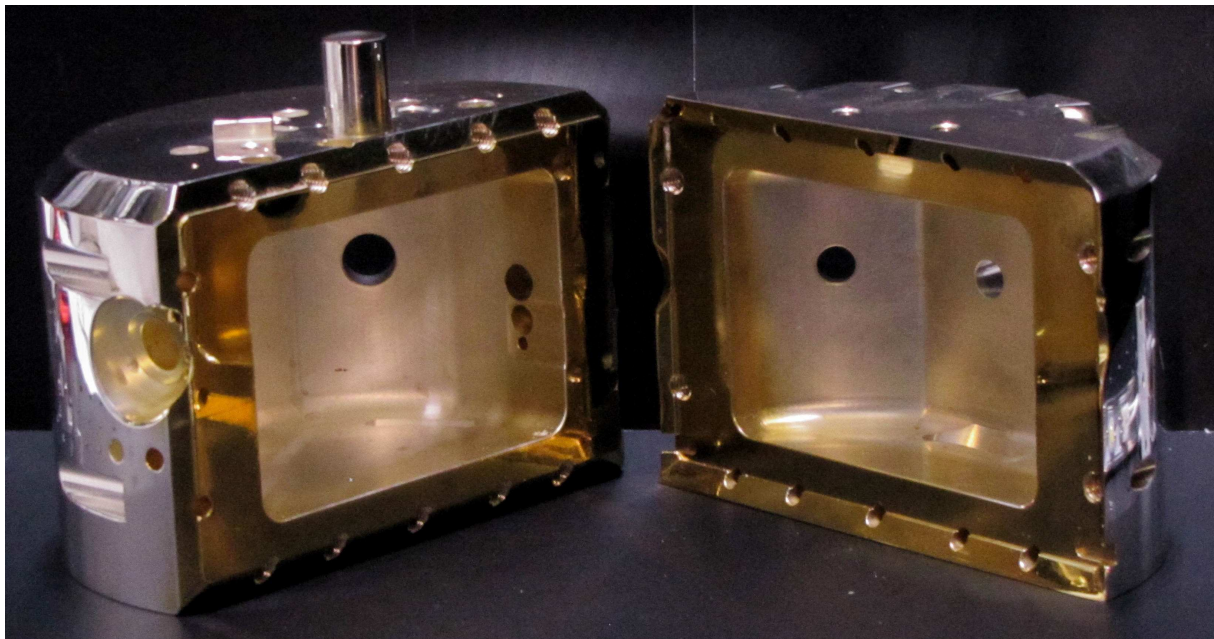


Figure 4.10.: A picture of the two halves of the inner shield folded apart. To reduce the contact resistance between them, the contact surfaces were gold-plated.

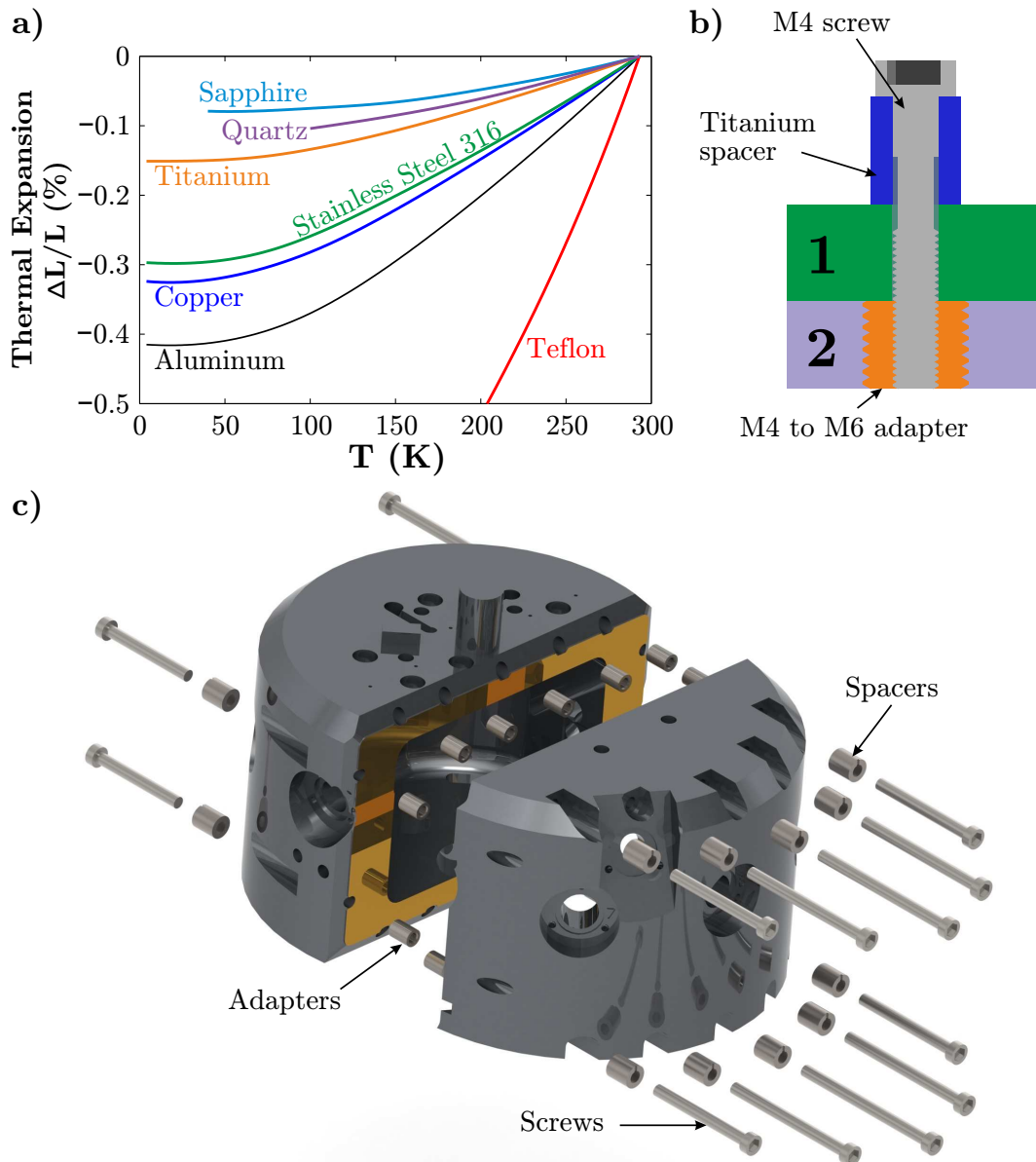


Figure 4.11.: Panel **a** shows a diagram of the thermal expansion over temperature for various materials. The values for the plot were taken from reference [Eki06]. Panel **b** illustrates how to join two copper parts 1 and 2 with a titanium spacer, a M4 screw and an adapter for M4 to M6. Panel **c** displays a 3D drawing of the inner shield and the halves are joined with high contact pressure at low temperatures.

to minimize the contact resistance, thus maximize the shielding for fluctuations perpendicular to the quantization axis, the contact surfaces were polished and gold plated, as displayed in Figure 4.10.

The contact resistance between two surfaces decreases with higher contact pressure [BSF⁺01]. Hence, it is important to tighten screws well so that they do not get loose during the cool down. Most of our cryogenic components are made of copper and copper has a high thermal expansion coefficient for a metal [Eki06], see Figure 4.11 a. The screws should be made of a material with a higher expansion coefficient. But all metals with higher thermal expansion than copper are soft materials like aluminum or tin [Eki06] and not suited as reliable screws. Thus, a different solution had to be employed in this cryostat design. During cool down, the stainless steel (316LN) M4 screws shrink about as much as the (silver-plated) copper that should be

clamped. But titanium spacers between the copper and the screw heads, see Figure 4.11 b for illustration, shrink less. Therefore, the screws will tighten with decreasing temperature and a reliable joint connection will be established.

A disadvantage of using copper as the bulk material is that it is a soft material and one has to make sure not to damage the threads when frequently unscrewing and tightly rescrewing. The solution in this cryostat design was to use adapters made out of a robust material like titanium or 316LN stainless steel. Such an adapter is a headless M6 screw with an additional M4 thread in the center. When using these adapters, they are first screwed into the M6 holes in the copper bulk before M4 screws are used to join the two copper pieces via the adapters, as displayed in Figure 4.11 b. If the M6 thread gets stuck in the soft copper, the M4 thread will not be damaged and it will be possible to open the connection between the robust adapter and the screw. Figure 4.11 c illustrates how this scheme is incorporated to join the two copper pieces of the inner heat shield.

For the sake of completeness, one should mention that it is possible to shield against alternating magnetic fields with a superconductor. If one covers the heat shield with a superconductor, the Meissner effect will prevent any external magnetic fields to enter this heat shield. This idea was not pursued however. The reason for this is that the whole superconducting heat shield does not enter the superconducting phase uniformly over time. Hence during the transition to the superconducting phase, local magnetic fields will be frozen into the superconductor which has three consequences. First, the magnetic field direction will vary for every cool down because the temperature distribution in the heat shield will vary slightly for every cool down. A varying magnetic field direction prevents one from using σ -polarized laser light as σ -polarized light has to coincide with the magnetic field direction. It is not possible to have arbitrary laser beam directions in a cryostat since the holes in the heat shield restrict the possible beam directions. Second, the magnetic field strength will vary for every cool down. In personal communications, Frank Wiekhorst from the Physikalisch-Technische Bundesanstalt (PTB) in Berlin told me that in their experiments the magnetic field strength can vary by more than the initially applied magnetic field¹⁰. Therefore, it is impossible to set a desired magnetic field strength accurately in a superconducting heat shield. Third, the superconductor deteriorates the spatial homogeneity of the magnetic field.

4.5 The trap

The trap used in this thesis is from the group of Harmut Häffner at University of California Berkeley (UCB). In order to incorporate the beam geometries discussed in the previous chapter, a few alterations had to be made. A slot with a width of $100\ \mu\text{m}$ was added in the middle of the central electrode of the trap. According to simulations at UCB, this changed the ion height above the surface plane of the trap from $120\ \mu\text{m}$ to $100\ \mu\text{m}$. The slot has a vertical depth of $100\ \mu\text{m}$ and widens towards the backside of the trap. Therefore, the slot allows a maximum NA of 0.24 and the trap has no restrictions on the optical access from the front side. A photo of the trap under a microscope is shown in Figure 4.12 a, a three-dimensional (3D) drawing of the trap with the discussed beam geometry is illustrated in Figure 4.12 b, and a cut through the trap with the slot in Figure 4.12 c.

The DC segments have a width of $200\ \mu\text{m}$ near the trapping region. The trap consists of a fused silica die which was structured by *Translume*¹¹ and covered in gold by in-house evaporation. In order to avoid charge generation due to the light sent through the slot [HBHB10], the evaporation of the slot was performed from four different angles ensuring that the slot would be fully covered

¹⁰In their setup in Berlin, the resulting magnetic field is even 100 times stronger than the initial field.

¹¹Translume Inc., 655 Phoenix Dr, Ann Arbor, MI 48108, USA

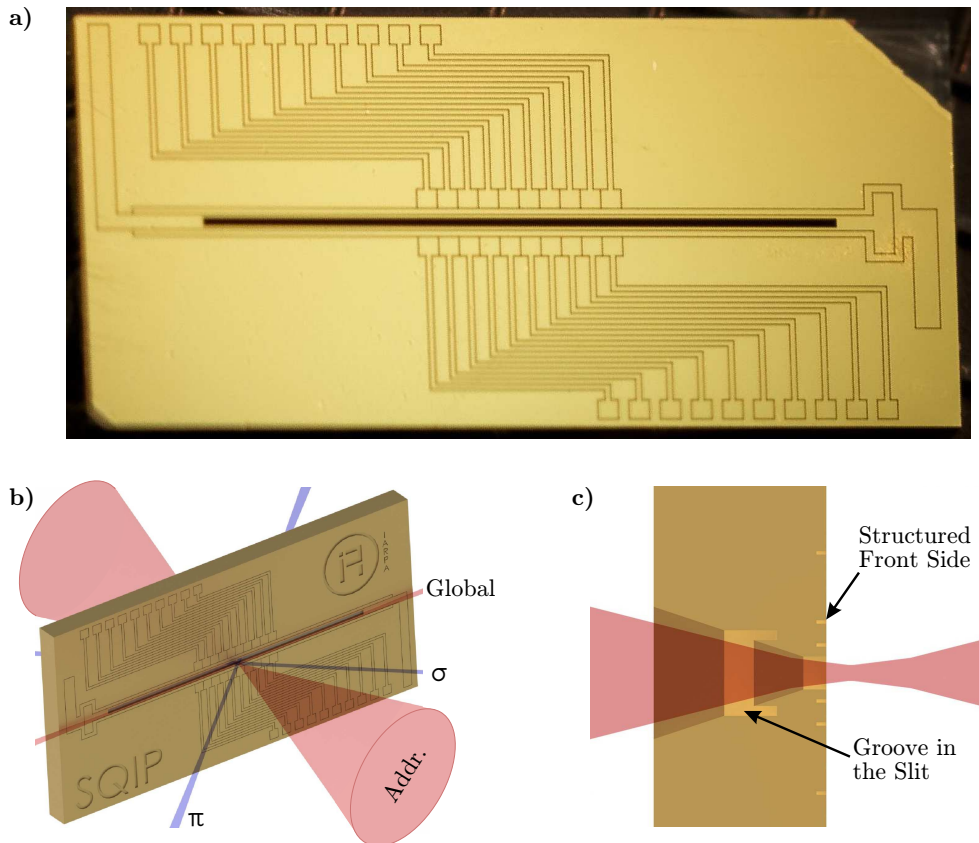


Figure 4.12.: Panel **a** shows a microscope picture of the trap (image courtesy of M. R. Knabl from the Institute for Quantum Optics and Quantum Information). Panel **b** depicts a 3D drawing of the trap with laser beams. Panel **c** displays a cut of the center of the trap with the addressing beam through the slot.

with gold. Additionally, grooves were introduced into the slot to prevent shorting the central electrodes to the grounded backside of the trap, as depicted in Figure 4.12 c.

4.6 Trap mount and lens systems in a cryogenic environment

It has been shown that the heating rates caused by surface effects decrease with decreasing temperature [LGA⁺08]. Hence, one should thermally anchor the trap as well as possible to suppress motional heating. Gluing a trap to a copper mount that has higher thermal expansion than the fused silica die can generate undesired mechanical stress. Thus, the trap in this setup was only glued on one of its corners to the copper mount with EPO-TEKTM H74.

In order to shunt the trap drive RF to ground for the DC segments (see Chapter 3.2.2), one requires capacitors close to the trap which are mounted on a PCB. The trap was elevated from the plane of the PCB to maintain optical access parallel to the surface of the trap, as illustrated in Figure 4.13 and Figure 4.14.

For the operation of planar surface Paul traps, one usually assumes an ideal far field ground opposite to the traps surface. This holds true for an operation in a cryostat as the trap is surrounded by a grounded heat shield. But on dielectrics surfaces, like the PCB, lenses and other pieces of glass, charges can accumulate and alter the DC potential in the trap. If the amount of these charges varies over time, for example because laser light is sent through a dielectric lens which generates new charges on its surface, these charges alter the voltages in

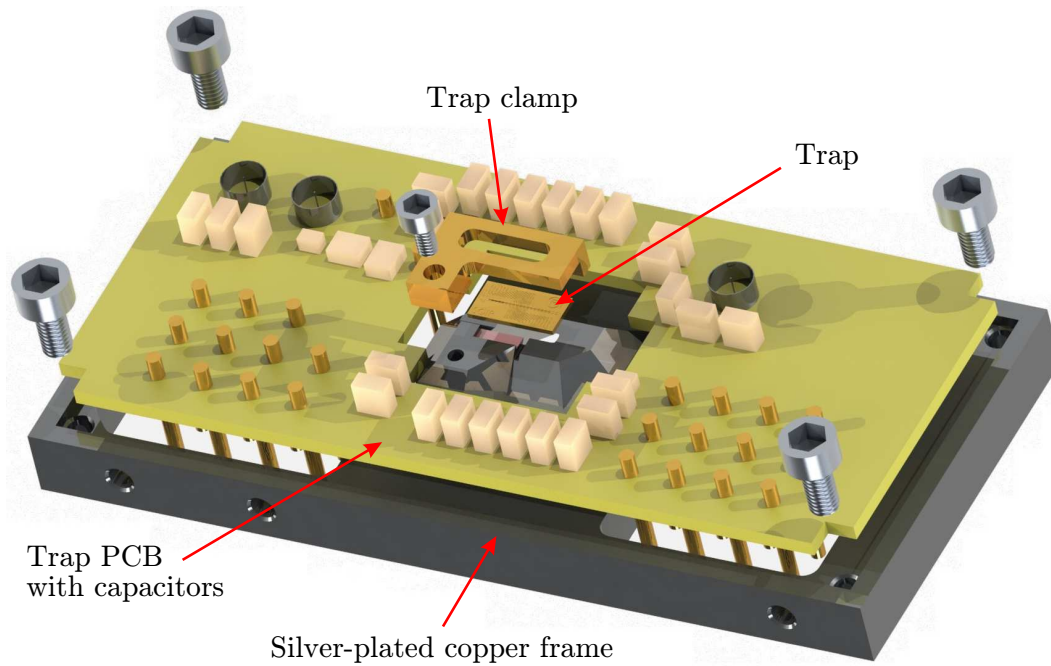


Figure 4.13.: An explosion view of the trap mount.

the Paul trap and thereby affect ion trapping. To circumvent this, a grounded metallic clamp was placed 1.5 mm above the trap surface. This clamp shields against the electric fields from charges near the trap. The required hole in the center of the clamp is just big enough to not limit optical access. The polished and gold-plated clamp above the trap is shown in Figure 4.13 and Figure 4.14.

An NA bigger than 0.2 will be required for high-fidelity single ion addressing as stated in Chapter 4.3. If the addressing optics were placed entirely outside the heat shields of the cryostat, such an NA would require holes of large diameter in the heat shield, which would reduce the magnetic shielding, see Eq. 4.5. Therefore, lenses had to be placed inside the inner heat shield to focus a collimated addressing beam entering the inner shield onto the ions. When placing a lens in a cryogenic environment, mechanical stress, caused by different thermal expansion of

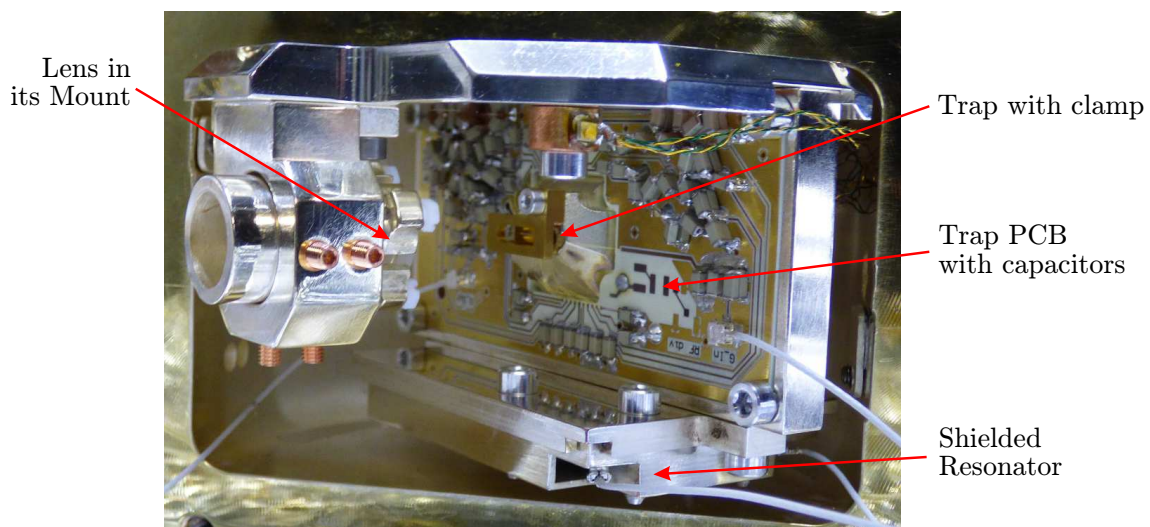


Figure 4.14.: A photo of the trap in the inner heat shield.

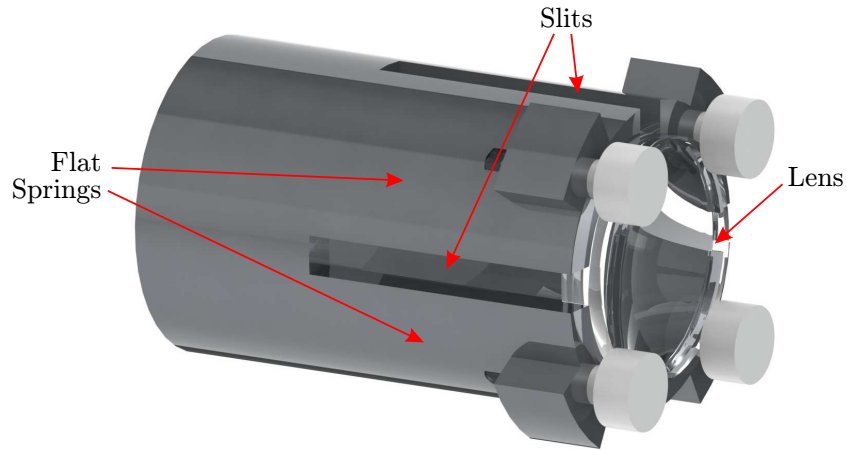


Figure 4.15.: A drawing of the lens mount which prevents birefringence in the lens due to flat springs in the mount.

the lens and its holder, results in undesired birefringence in the lens. Therefore, a lens mount needs to have a spring-like component to reduce mechanical stress while still being rigid enough so that the lens cannot move. The designed lens mount is of cylindrical shape with four long grooves, shown in Figure 4.15. These cut-outs provide a spring behavior and four additional Teflon screws prevent the lens from falling out of the lens mount.

The used aspherical lenses with half-inch diameter (*Thorlabs* AL-1225) have a focal length of 25 mm and an NA of 0.23. Their custom anti-reflection-coating allows using the lenses for single

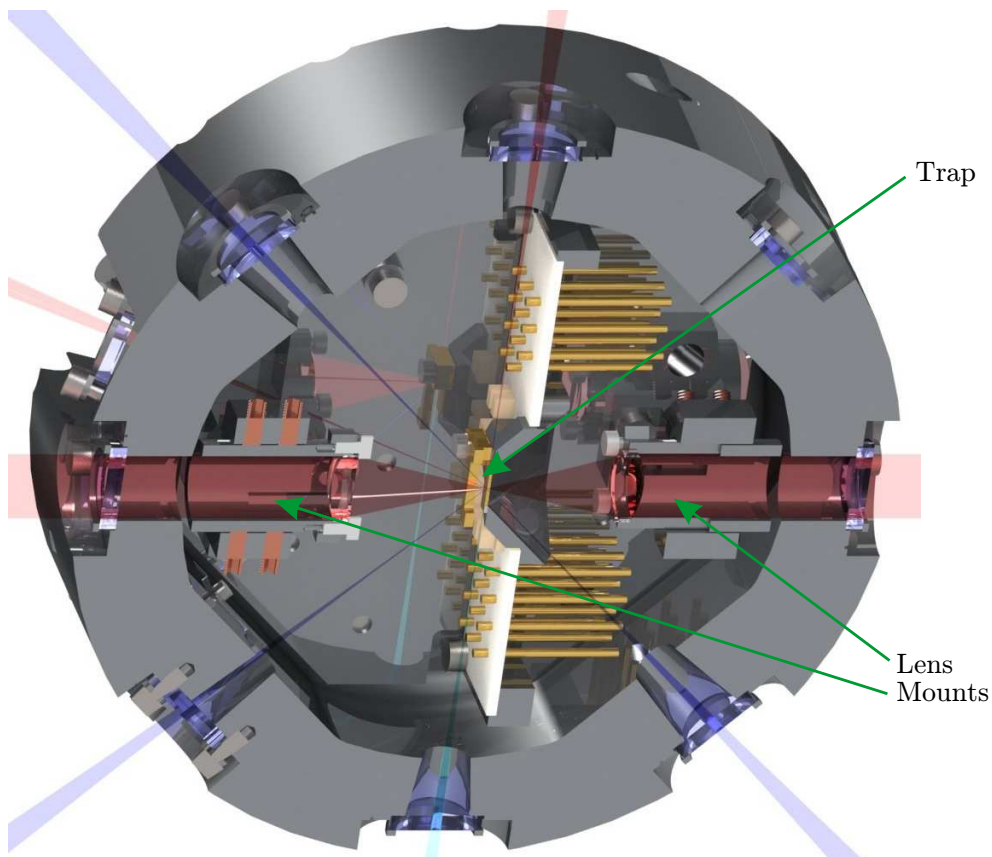


Figure 4.16.: A cut of the inner shield with the trap, the two lens mounts, and all laser beams.

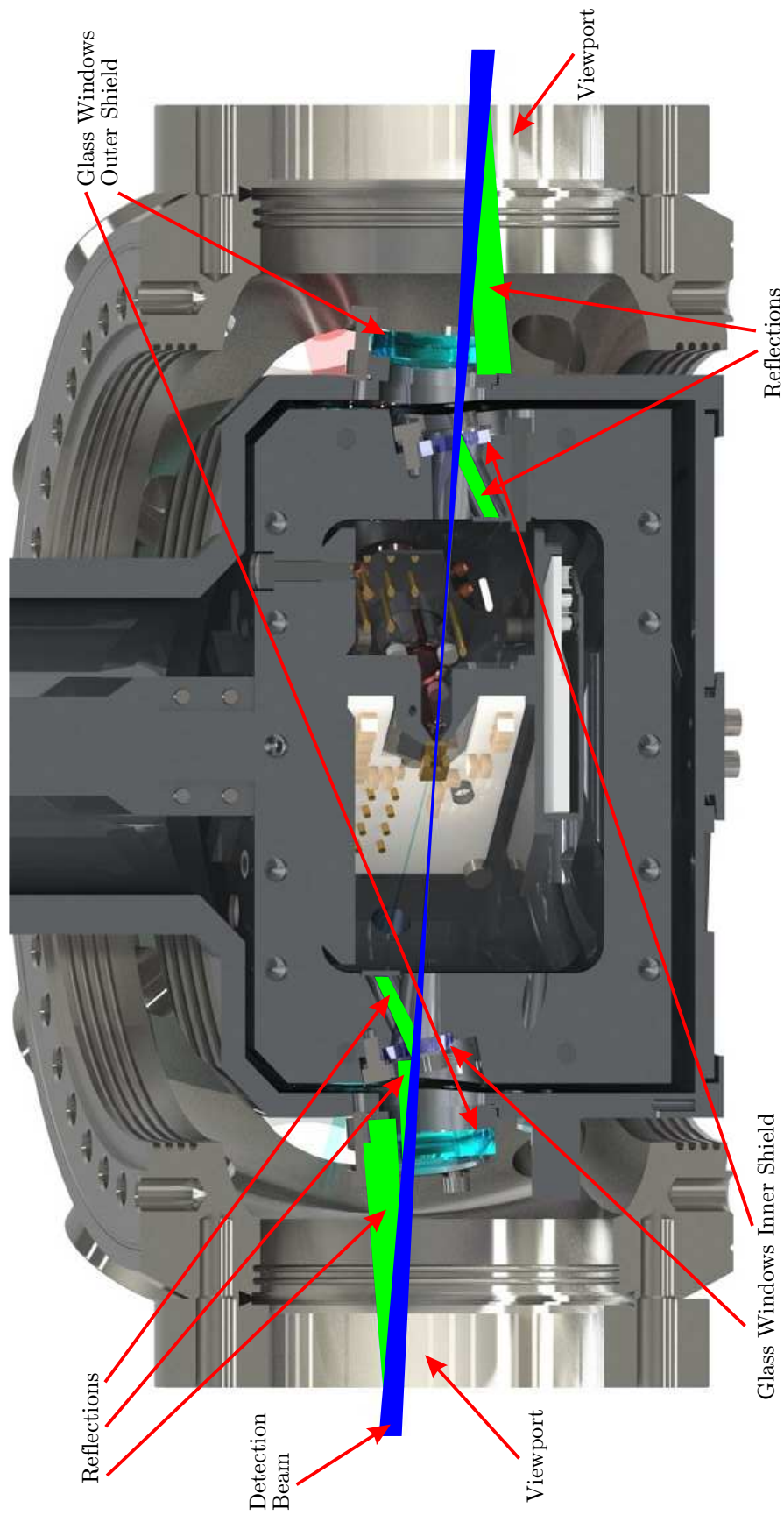


Figure 4.17.: A drawing of a cut of the vacuum chamber along the detection beams. The reflections of the beams on each glass surface are shown for beams entering the vacuum chamber from both sides. None of these reflections can hit the trap, which reduces the dark counts during detection.

ion addressing with the qubit lasers around 700 nm as well as for detection of the quantum states around 400 nm. To increase the collection efficiency, two lenses, one at the front and one at the back of the trap, were placed inside the inner shield, as depicted in Figure 4.16.

Since there was not enough space in the inner shield to mount lenses on piezo stages, the lenses had to be aligned before placing them inside the inner shield. Optics simulations showed that the aberrations for the used aspherical lenses would be tolerable if the lenses were aligned with a precision of $\pm 100 \mu\text{m}$ around the ideal position. To accomplish this, both lens mounts and the trap mount were placed on a rigid structure for alignment. This allows alignment of the lenses outside the inner shield and documentation on the alignment procedure can be found in the Master's thesis of Anton Nolf [Nol16]. After the alignment, the board with the lenses, the trap, and the resonator was mounted as one piece inside the inner shield.

As described in Chapter 4.3, the detection beam is tilted by 4° with respect to the horizontal plane in which the other laser beams are aligned. If the beam was horizontal, the backreflections of the glass windows in the vacuum chamber would illuminate the whole trap and cause a high dark count rate during detection. To prevent this, all glass pieces in the vacuum chamber (inner and outer shield¹², viewport) are aligned so that no light can be reflected back towards the trap, as drawn in Figure 4.17. The 4° tilt prevents the reflections of the viewport to enter the outer heat shield. The glass windows in the outer heat shield are tilted sideways so that their reflections cannot enter the inner heat shield. And in the inner heat shield, the reflections of the windows are directed towards beam blocks covered with *Acktar*¹³ Spectral Black foil which absorbs most of the light.

4.7 Mechanical structure and vibrational decoupling

As mentioned in Chapter 4.1, the peak-to-peak vibrations at the tip of the cold finger of a flow cryostat are about $1 \mu\text{m}$. When working with optical qubits with a transition wavelength around 700 nm, the vibration amplitude should not exceed a small fraction of these 700 nm. This requires vibration isolation of the trap with respect to the cold finger. The incorporated vibration decoupling scheme [TSH⁺05] is depicted in Figure 4.18 a. A membrane bellow reduces the mechanical coupling between the cold finger and the vacuum chamber. The inner shield, containing the ion trap, is mounted through rigid mounts with low thermal conductivity to the outer shield and the vacuum chamber. As part of the mechanical decoupling at cryogenic temperatures, the cold finger and the heat shields are connected through thin OFHC copper wires to reduce the transmitted vibrations while maintaining good thermal contact.

Due to the choice of a vacuum chamber with DN160CF dimensions and the size of the inner shield, defined by the thick walls and the required in vacuum optics, there was not enough space to construct the rigid mount horizontally while maintaining low thermal contact. Thus, it had to be built vertically. Heavy-Duty Groove Grabbers from *Kimball Physics* were used to fix a stainless steel (316LN) ring to the chamber. For the mount between the different heat stages, one requires a mount with low thermal conductivity to limit the thermal load on the cryostat, as well as a very rigid mount to prevent movement as required by the vibration isolation scheme. A hexapod structure made out of 316LN stainless steel with high rigidity at a small cross-section was incorporated between the vacuum chamber and the outer shield, as shown in Figure 4.18 b. Due to space constraints, a hexapod structure could not be used between the outer and the inner heat shield. Therefore, a stainless steel cylinder with a (0.5 mm) thin wall was designed. Finite

¹²To reduce black-body radiation inside the heat shields, all holes for optical access are covered with glass windows. This also improves the vacuum inside the heat shield as background gas cannot directly pass through the heat shields.

¹³Acktar Ltd., 1 Leshem St, Entrance A, P.O.B. 8643, Kiryat-Gat, 8258401, Israel

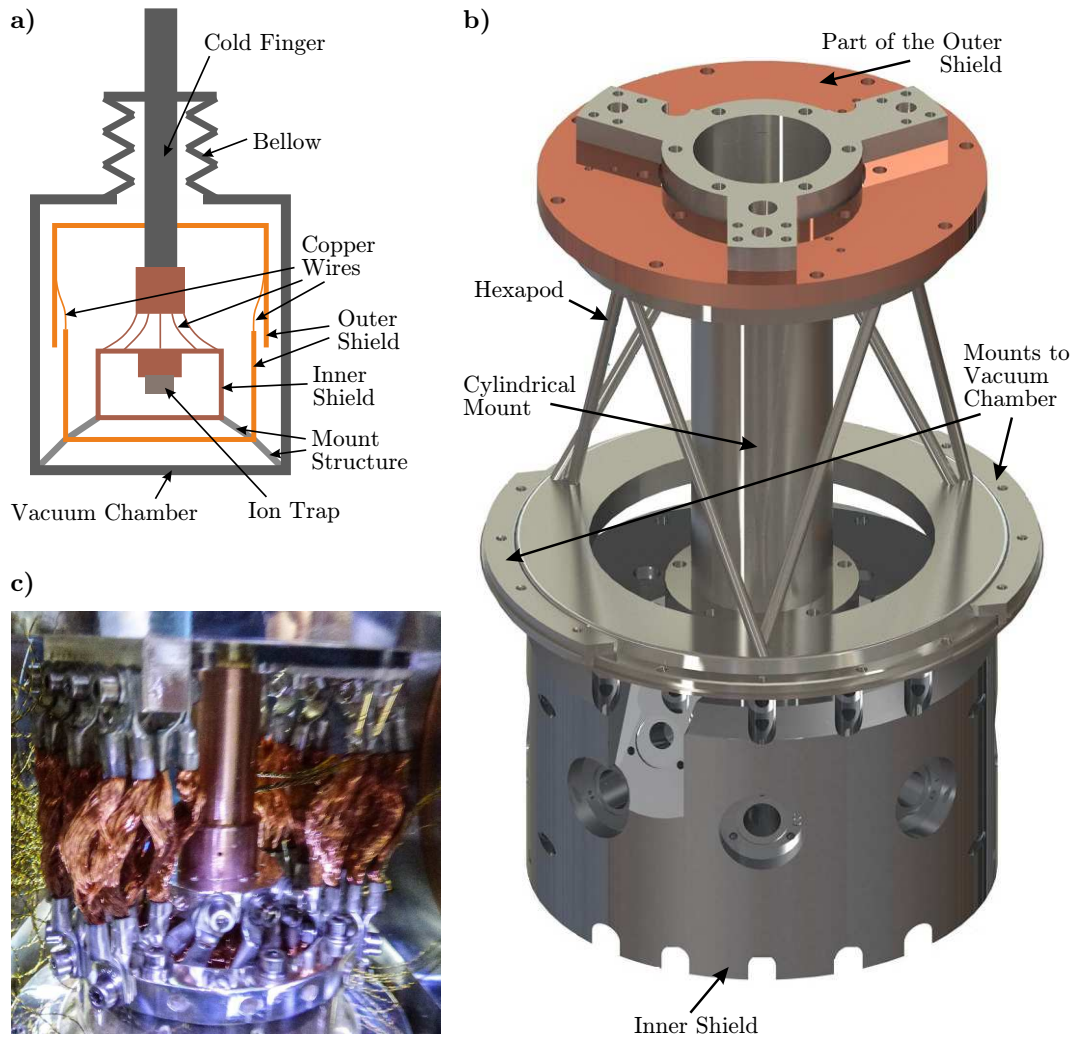


Figure 4.18.: Panel **a** shows a depiction of the vibration isolation scheme. Panel **b** displays a 3D drawing of the rigid mount used in this scheme. Panel **c** illustrates a photo of the wires used for vibration isolation at cryogenic temperatures.

element simulations of the whole mount structure were performed to find a trade-off between thermal load and rigidity. To not perturb the magnetic field homogeneity near the trap, the stainless steel mount structure was thermally annealed in vacuum at 1050°C for 15-20 min after machining.

When designing the vibration isolation stages at cryogenic temperatures with OFHC copper wires, one has to keep in mind that many thin wires result in better mechanical decoupling than one thick wire with the cross-section equal to the sum of the cross-sections of all thin wires. Hence, each single OFHC wire should have a small diameter and the total required cross-section (the number of wires) has to be estimated from simulations and verified during the first cool down by temperature and vibration measurements. In the first version of the cryostat, the wires were initially clamped between two copper pieces at the cold finger and at the rigidly mounted part of the cryostat. This did not work because some wires got loose. The resulting low contact pressure would have resulted in a high thermal contact resistance between the cold finger and the heat shields. The solution was to crimp the wires with cable lugs on both sides and thereby form strands of wires. To form a flexible, but thermally conducting connection, one cable lug of a strand was screwed to the cold finger and the other cable lug to the heat shield, as illustrated in Figure 4.18 c.

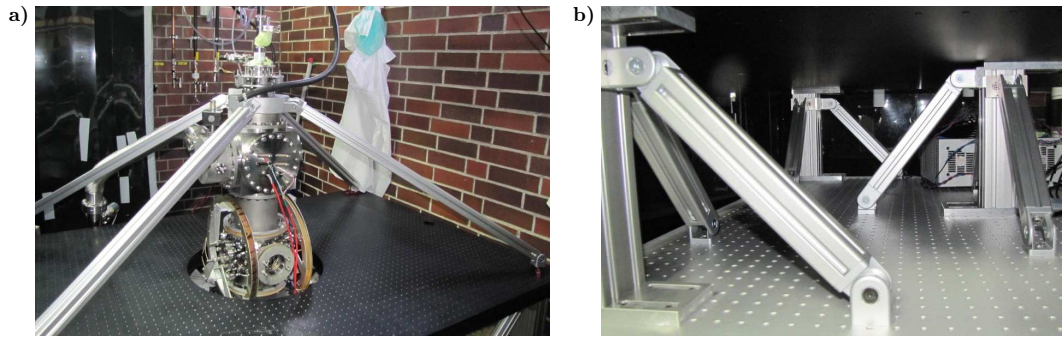


Figure 4.19.: Panel **a** shows a picture of the experiment table with the vacuum chamber in its center. To prevent wobbling, four aluminum cross bars were installed on the black bread board. Panel **b** illustrates that the black bread board was mounted on the optical table through big aluminum post with additional cross bars.

In order to avoid magnetic inhomogeneity due to placing the experiment on an optical table which is not fully non-magnetic, an aluminum optical table from *Thorlabs* was installed in the lab. To simplify optical alignment around the chamber, an aluminum bread board with a hole for the chamber was placed above the optical table. The vacuum chamber is mounted in the hole of the bread board in such a way that the beam height of the optics on the breadboard of 65 mm corresponds to the beam height required for the experiment in the cryostat. In this design, the incorporated vibration isolation scheme resulted in a tall vacuum chamber which could oscillate on the optical table and thereby cause decoherence of the optical qubit. To prevent this, four aluminum cross bars connect the four corners of the bread board to the upper part of the vacuum vessel, as shown in Figure 4.19 a. To prevent movement of the bread board with respect to the optical table below, the bread board and the optical table were joined with in total eight aluminum bars which each have crossbars to suppress lateral movement, as depicted in Figure 4.19 b.

When joining two pieces of a cryostat with a temporal joint [Eki06], one can use grease or indium foil to reduce the thermal contact resistance. The grease mainly used for this purpose in cryostats is Apiezon N, which has a low dropping point¹⁴ and is not UHV compatible at room temperature. Therefore, Apiezon N was not an option. Milling causes crystal damage near the surface of the milled material. In order to fix this crystal damage in the milled copper¹⁵ heat shields, the copper had to be heated to more than 150 °C. The melting point of indium is 156.6 °C above which the copper parts would be soldered together by the indium. Hence, indium foil could not be used either. To reduce the thermal contact resistances, the polished surfaces of the copper parts of the heat shields were solely joined by high contact pressure caused by the titanium spacers, see Figure 4.11 b for illustration.

4.8 Oven mount and non-evaporative getters

In order to load ions into the trap, an oven is heated until it emits a beam of neutral atoms at a temperature of several hundred degrees Celsius. The atoms are ionized in the trap with photoionization, see Chapter 5.1.1. The incorporated ovens are two commercial ovens (one for calcium and one for strontium) from *Alvatec*¹⁶. To minimize the heat transfer from the oven to the cryostat, the ovens have been positioned outside the outer heat shield without thermal contact. Small holes illustrated in Figure 4.20 a allow the ovens' atom beams to pass through

¹⁴https://en.wikipedia.org/wiki/Dropping_point

¹⁵Tempering of copper is performed between 150 °C and 250 °C, ideally under vacuum conditions.

¹⁶Alvatec, Gewerbestrasse 3, 9112 Griffen, Austria

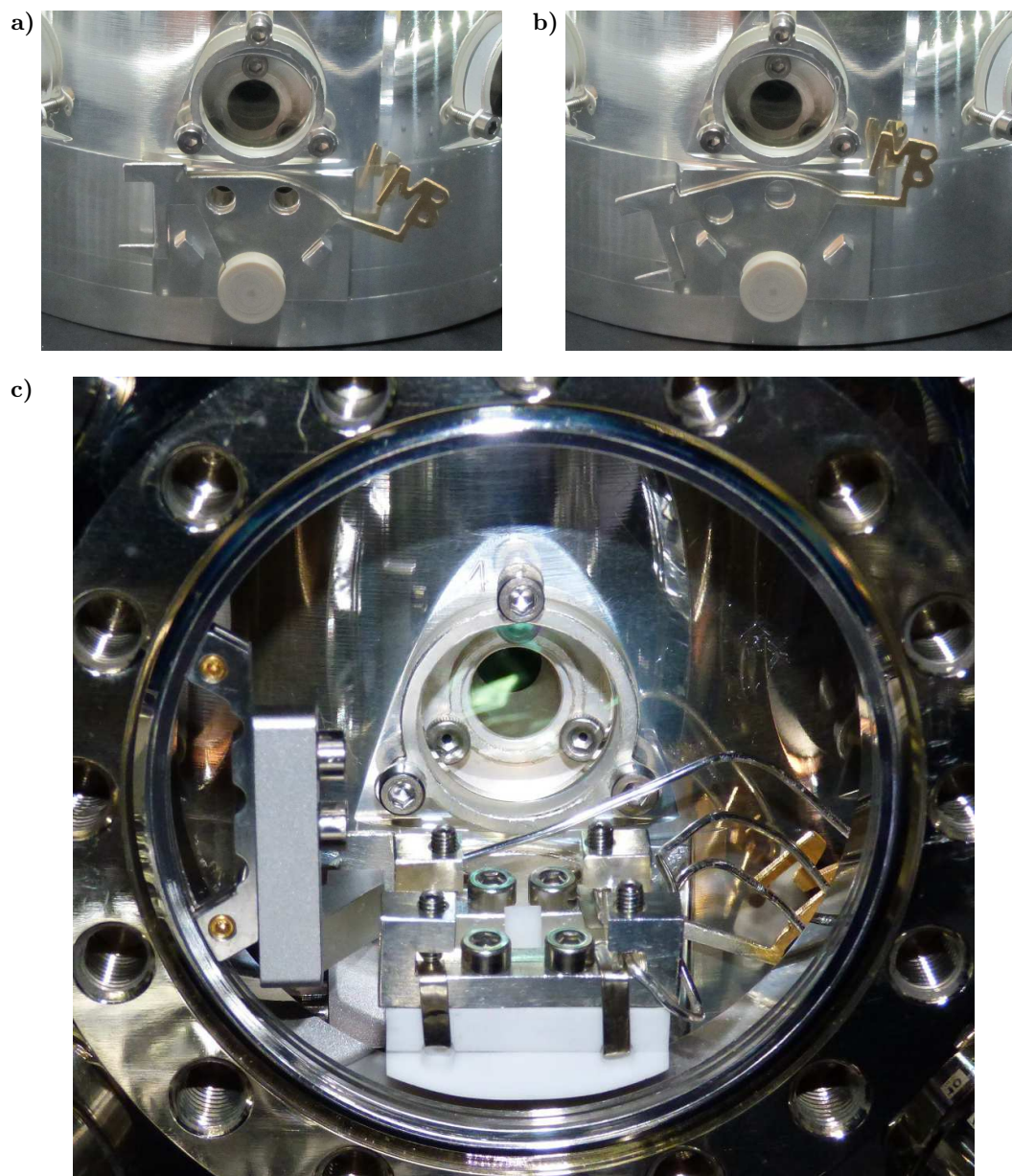


Figure 4.20.: The mechanical oven shutter is shown in its opened state **a** and its closed state **b**. The whole oven mount in the chamber can be seen in Panel **c**. The ovens are placed between the Macor pieces at the bottom. One can see only two electrical connections coming out of the white Macor pieces.

the heat shields to the loading zone of the trap. A mechanical shutter can block the beams' access to the holes, as shown in Figure 4.20 b. Manipulation of the shutter position from outside vacuum is ensured by a wobble stick in one of the DN16CF flanges of the *Kimball Physics* vacuum chamber. The oven beams have to pass through the slot of the trap before reaching the trapping zone which prevents surface contamination of the trap electrodes on the front side. Due to space constraints, the ovens had to be placed inside one of the DN63CF flanges of the vacuum chamber, as illustrated in Figure 4.20 c. Therefore the oven beams hit the trap under an angle of 45° sideways and 15° with respect to the horizontal plane, to maintain optical access through this viewport.

Bad vacuum before cool-down of the cryostat can lead to surface contamination because background gas freezes on the trap's surface. It is not clear if and how this affects the motional

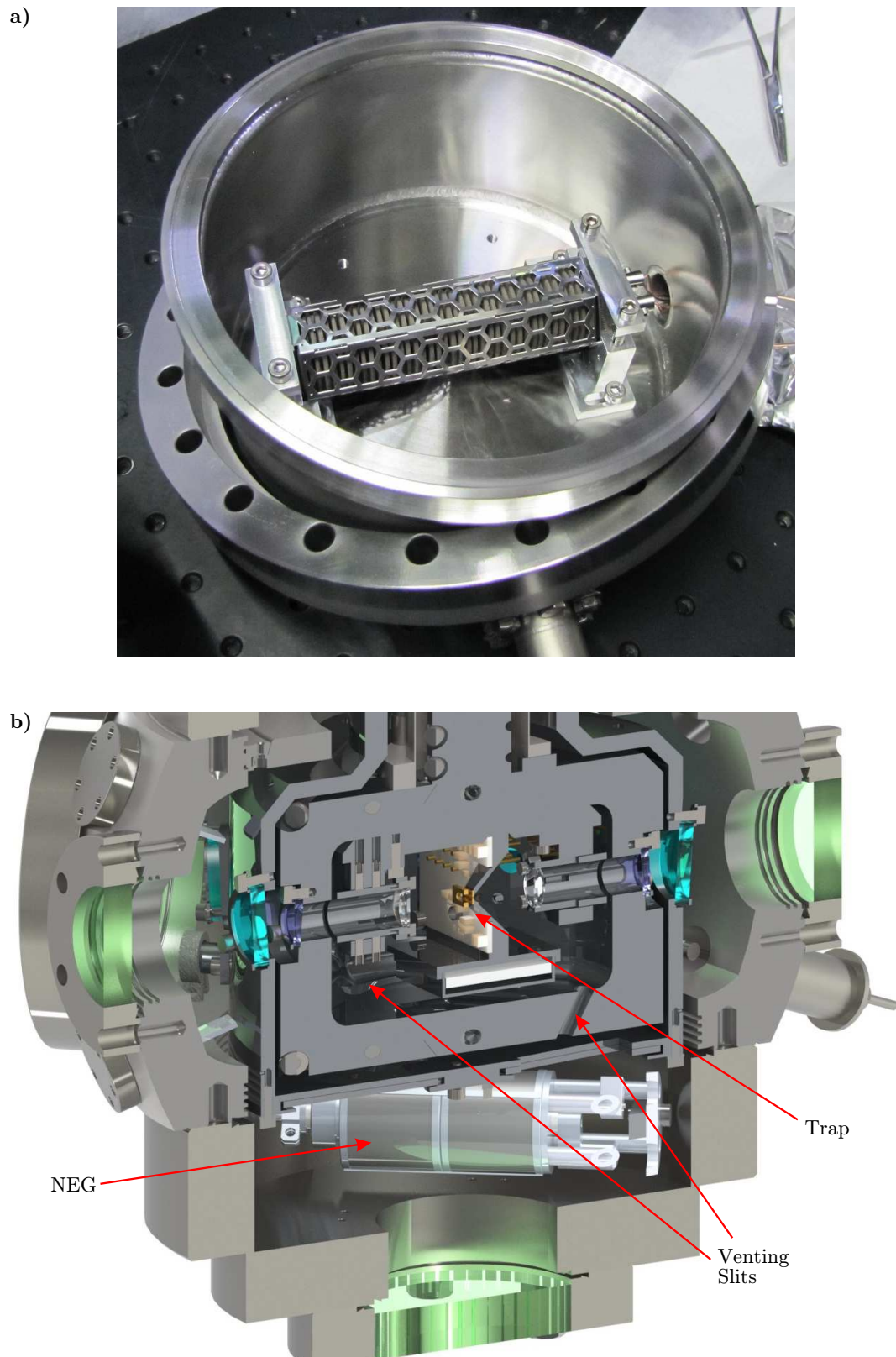


Figure 4.21.: Panel **a** shows a C400 NEG from *SAES Getters* mounted on a flange with electrical feedthroughs for activation of the NEG. Panel **b** depicts a cut through the bottom part of the vacuum chamber. The C50 is directly below the venting slits of the inner shield, which optimizes pumping for the inner shield.

heating rate of the trap [BKRB15]. To avoid frozen background gas on the trap, the goal was to achieve UHV pressures before starting the cool-down. To achieve the best vacuum, one tries to maximize the pump cross-sections. However, the cryostat in the vacuum chamber decreases the available cross-sections making UHV in cryogenic setups at room temperature challenging. To improve the vacuum pump capabilities, two non-evaporative getters (NEGs) from *SAES Getters*¹⁷ (Models C50 and C400) were placed inside the vacuum vessel. The NEG with higher pump speed (C400), depicted in Figure 4.21 a, was mounted on a flange at the top near the OFHC wires for vibration isolation. Since NEGs cannot pump noble gases, a 2 l/s *Agilent* ion getter pump was added close to the C400 NEG. For sensitive experiments, its magnet can be removed to maintain the spatial homogeneity of the magnetic field in the trap.

The inner shield has venting slits at the bottom, which allow for vacuum pumping but only minimally influence the magnetic shielding because they are small and under an outward pointing angle, as shown in Figure 4.21 b. The outer shield has openings right below these venting slits. The second NEG is placed underneath these openings to maximize the vacuum pumping for the inner shield. In order to minimize the thermal load on the inner shield when it is cold, the openings can be opened and closed with a wobble stick feedthrough on a DN16CF flange.

4.9 Resonator



Figure 4.22.: Photo of the resonator in its RF shield used in the setup. The outer dimensions of the RF shield are 57 mm × 40 mm × 10.2 mm.

The resonator used in this work is described in Chapter 3.1. Figure 4.22 shows a photo of the resonator in its shield with the visible coaxial surface-mount technology (SMT) connectors for the RF input and the pickup. The resonator is mounted below the trap attached to the trap mount, shown in Figure 4.14. The aim was to have a resonance frequency higher than 45 MHz, where typical values for trap drive frequencies are about 30 MHz. The higher trap drive frequency will result in higher secular motion frequencies at the same trap stability parameter q . The higher secular motion frequency will allow faster gates or gates with higher fidelities because of a bigger frequency spacing between the modes of secular motion.

¹⁷SAES Getters S.p.A., Viale Italia, 77, 20020 Lainate MI, Italy

At first, we used a planar HTS coil with an inductance of $1.6 \mu\text{H}$ and got a resonance frequency of 49.9 MHz, which corresponds to a capacitive load of 6.4 pF. With less than 100 mW, we could load ions and operate the trap.

After several months of operation, the superconducting coil broke and it was not possible to get back into a superconducting regime. It is unclear what caused this and, thus, the HTS coil was replaced with a wire coil with 0.4 mm silver-plated copper wire. The new resonance frequency was 45.4 MHz.

4.10 Filter design and cryostat wiring

A two-stage LC low-pass filter, depicted in Figure 4.23 a, is incorporated for each DC segment to filter noise at the secular motion frequency. Due to the space constraints in the inner heat shield, the components for the filter are distributed over two PCBs. The first PCB includes the first filter stage as well as the inductances for the second stage and is mounted at the outer heat shield. The second board incorporates the capacitor of the second stage and is inside the inner heat shield. This short distance to the trap electrodes allows for an efficient shunting of the trap drive RF voltages. The inductances of the filter are $4.7 \mu\text{H}$ surface-mount device (SMD)-inductors (*Murata* LQW2UAS4R7J00L), and the capacitances are a non-magnetic 4.7 nF CP0 capacitors. The filters of Figure 4.23 a results in an attenuation of 0.1 dB for 100 kHz signals, 41.8 dB for 1 MHz signals, 79.9 dB for 3 MHz signals, and 89.9 dB for 4 MHz signals. These values emphasize that fast ion movement with voltage changes at the segments with frequencies of up to 100 kHz are feasible. At the same time, the higher order filters strongly attenuate noise at the secular motion frequencies between 1 and 4 MHz.

Three filter PCBs with circuits for all DC channels are located above the trap in a separate part of the outer shield, as shown in Figure 4.23 b. The outer shield is already an excellent shield against RF noise from the outside. Hence, pickup of RF noise is limited to the trap drive, as it is the only RF signal sent into the cryostat. Since the inductors are in the outer shield, the magnetic fields produced by filtering noise or due to current through them when switching voltages will be attenuated by skin-effect in the inner shield.

Phosphor bronze twisted-pair cables were used inside vacuum to electrically connect the 10 DC segment pairs and the central segment. For each DC line, there are two separate connections. One of them is employed to apply the DC voltages, the other one is used to monitor the applied voltage on another feedthrough of the vacuum chamber. UHV compatible Sub-D 25 connectors from *Accu-Glass Products Inc.* connect the wires from the filter boards to the feedthrough. Next to the filter boards in the top of the outer shield, there are more Sub-D 25 connectors to separate the inner shield connections from the filter boards, as illustrated in Figure 4.23 b and c. For thermal anchoring between inner and outer shield, the wires are (non-inductively) wound around a copper post and clamped with Teflon rings. For thermal anchoring between outer shield and room temperature, the wires are guided in grooves along the circumference of the outer shield.

The coaxial cables to supply the RF to the resonator and to pick up RF from the resonator are 50Ω -cables with SMT connectors. Two additional SMT cables are added to apply RF signals to the central electrode for driving the ground state qubit directly with an RF field. One of these cables is the RF input and the other one is the RF output, which is required for the termination of the RF signal outside the cryostat. This minimizes the thermal load on the cryostat. For the coaxial feedthroughs, four of the DN16CF flanges of the *Kimball Physics* vacuum chamber were employed. But in DN16CF flanges, it is not possible to include isolated SMA feedthroughs to avoid ground loops. Hence, the two central contacts of a triax feedthrough are used as a 50Ω -feedthrough instead of an isolated SMA feedthrough. A small adapter PCB in vacuum connects

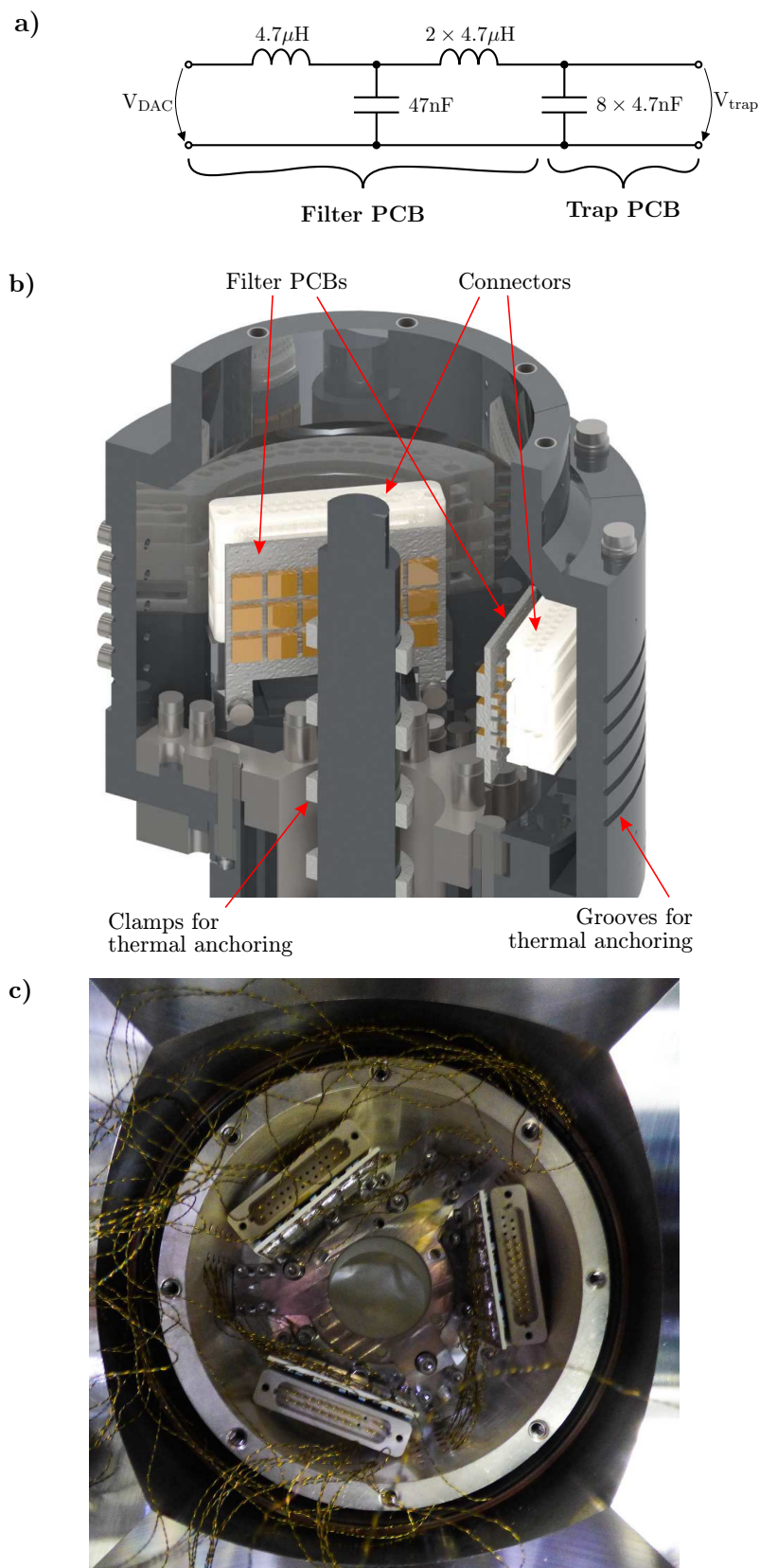


Figure 4.23.: Panel a depicts the filter circuit used for each DC segment. Panel b illustrates a cut through the outer heat shield with the filter boards and the connectors connecting the filter boards with the wires to the trap. Panel c shows a photo of the connectors and the filter boards seen from the top in the vacuum chamber.

each SMT connector with the triax feedthrough. Due to space constraints, the SMT cables could only be thermally anchored on the outer shield. In order to improve thermal decoupling of the RF connections in the inner shield and at the feedthroughs, capacitors are placed in series with the signal lines. These capacitors interrupt a continuous metallic connection from room temperature to cryogenic temperatures, and heat has to be transferred through them, resulting in a higher thermal resistance. But for RF signals with frequencies of 10 MHz and higher, the capacitors act like shorts. There are two capacitors (4.7 nF CP0) on each adapter PCBs near the feedthroughs and another two between the SMT connector at the input of the resonator and the resonator itself.

4.11 Characterization

A cut through the whole chamber can be seen in Figure 4.24. Before performing the characterization, the copper parts had to be heated up to more than 150°C¹⁸ to repair the crystal damage due to the machining. After baking the cryogenic parts for several days, the vacuum pressure was below 10⁻⁸ mbar at room temperature, which is a typical pressure that is achieved after a normal bake at 100-120°C for several days.

In order to save liquid helium, the cryostat is first precooled with liquid nitrogen. This is typically done for 24 to 48 hours, as shown after a gentle bake at 350 K in Figure 4.25 a. When cooling with a flux of liquid nitrogen that is too high for steady-state operation, one can already achieve these temperatures in the outer shield. Hence, no additional energy from the outer shield has to be removed by the helium when cooling down to liquid helium temperatures.

The cool-down with liquid helium can be as fast as a couple of hours but is usually performed in about half a day to reduce the liquid helium consumption (Figure 4.25 b). In a continuous flow cryostat, the coolant consumption depends on the operation temperature. Typically, the experiment is performed at temperatures below 20 K for which hydrogen from the background gas condensates. The steady-state temperature of the outer heat shield when cooling the inner shield to about 20 K is between 100 K and 120 K. At these temperatures of the cryostat, the liquid helium consumption of the whole cryogenic system is about 1/2 liter per hour. The helium dewar in the experiment is from *Cryo Anlagenbau*¹⁹ and can hold up to 230 l of liquid helium. In order to avoid warming up the dewar, it is typically refilled after two weeks of constant operation. The liquid helium consumption rate solely due to storage in the dewar is about 0.09 l/h. It is estimated that the transfer line causes even higher helium consumption than the dewar and thus the designed cryostat itself requires only about a 1/4 l/h liquid helium to maintain a steady-state temperature of about 20 K. When the coolant flux is turned off and the cryostat warms up starting at a temperature of 20 K, it will take about 5 days for the inner shield to reach room temperature. This time highlights how well the cryostat is thermally isolated from the vacuum chamber.

The temperature distribution during the warm up process suggests that the thermal losses due to thermal conduction in the cold finger of the flow cryostat are even higher than the losses due to thermal conduction in the rigid mount designed in Chapter 4.7. When the cryostat was acquired from *Janis*, the choice was a short flow cryostat so that the vacuum chamber would fit into the lab. In the incorporated flow cryostat, the distance from the DN40CF flange to the tip of the cold finger is only about 30 cm. This short length increases the thermal losses in the cryostat, but it also does not allow for a lot of interaction of the cold evaporated gas with the cold finger's walls to actively cool the outer shield. During this thesis, several different copper

¹⁸Private communications with Stefan Konetschnik from METTOP GmbH (Peter-Tunner-Straße 4, A-8700 Leoben, Austria)

¹⁹Cryo Anlagenbau GmbH, Bochumer Str. 6A, 57234 Wilnsdorf, Germany

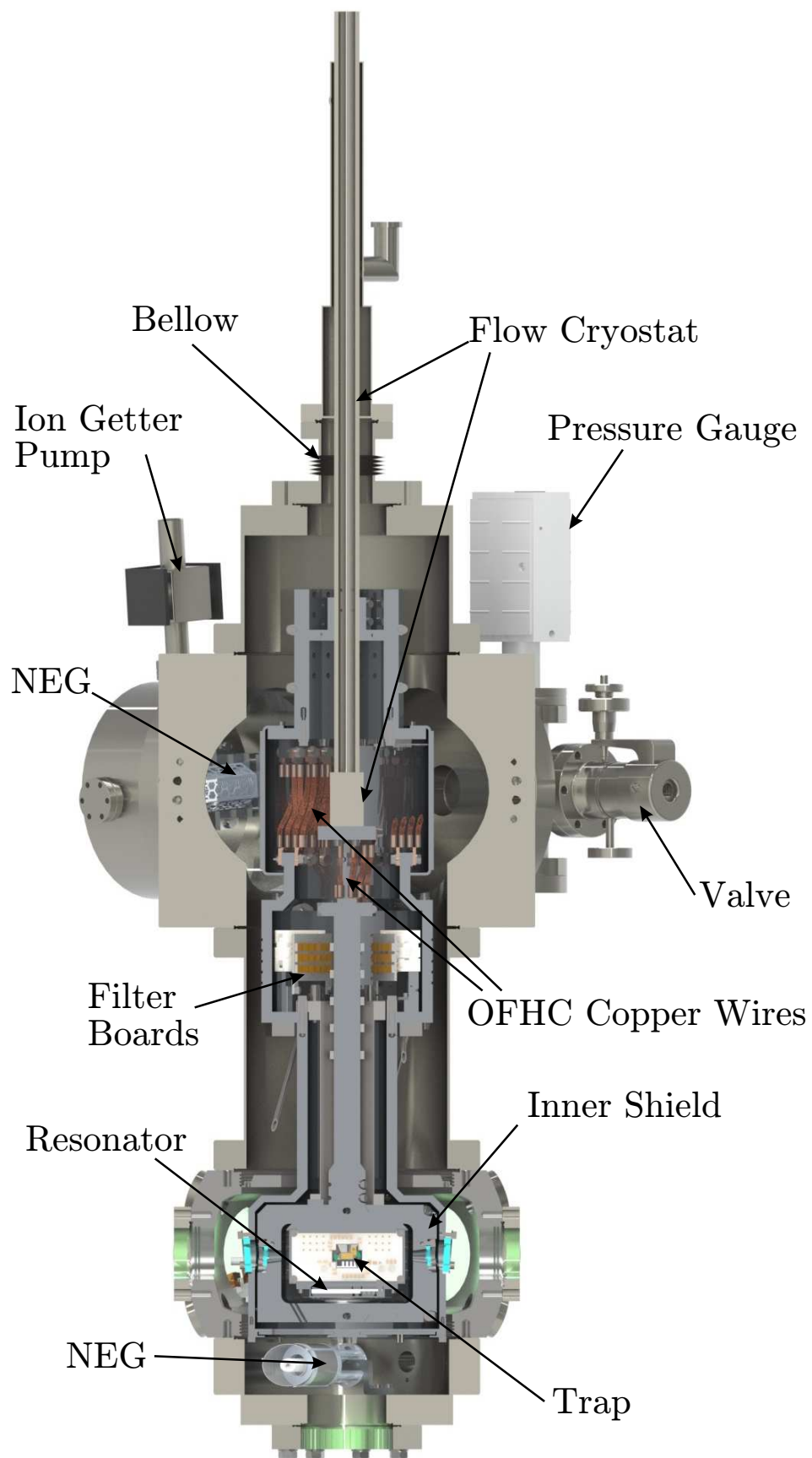


Figure 4.24.: Cut through the vacuum chamber

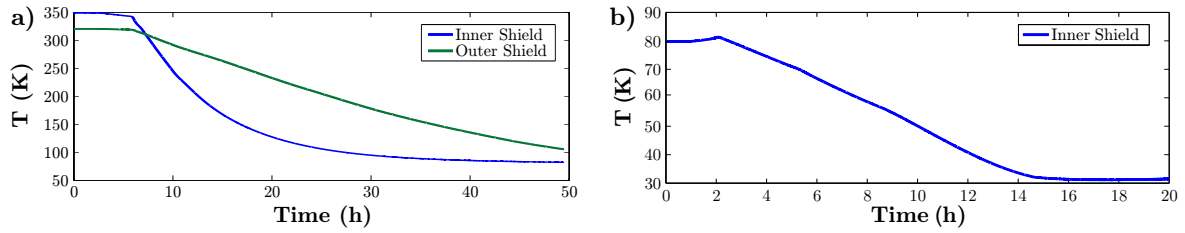


Figure 4.25.: The temperature over time during a cool-down with liquid nitrogen **a** and liquid helium **b**.

parts were clamped on different positions along the cold finger to change the cooling power and thereby the temperature of the outer shield. The lowest achieved steady-state temperature with an inner shield temperature of 20 K was 100 K. With more available length, the cooling power of the outer heat shield could have been higher by using more of the available cooling power from the evaporated gas.

The flow cryostat contains an internal heater with which one can warm up the cold finger and thereby the inner shield. To efficiently heat the outer shield for bake-outs, two ceramic heaters from *Bach Resistor Ceramics*²⁰ (Model FLE100155) were installed in the outer shield above the vibration isolation. Since the exhaust of the cryostat froze during cryostat operation, a non-magnetic heater (Raychem WinterGard FS-B-2X) was wound around the exhaust tube and hose. This heater is self-regulating in temperature and works with 230 V from the power lines in the lab. It prevents accumulation of ice above the experimental setup but will also contribute to 50 Hz noise in the lab.

4.11.1 Magnetic shielding

In order to verify the magnetic shielding, magnetic magneto-resistive sensors (*Honeywell* HMC1001 and HMC1002) were placed inside the inner shield. The sensitivity of the sensor for the current temperature was calibrated by applying a step signal to the coils.

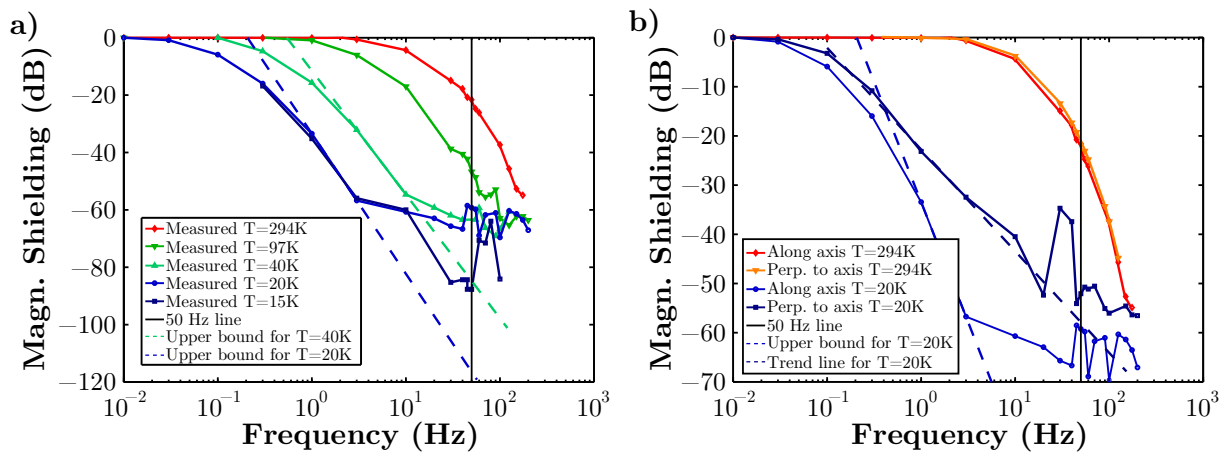


Figure 4.26.: The magnetic shielding over frequency for various temperatures of the inner shield along the quantization axis **a**, and a comparison between the attenuation along and perpendicular to the quantization axis **b**.

For the magnetic shielding measurements, a sinusoidal magnetic field with varying frequency was generated by the field coils and the response signal of the magnetic sensor was measured.

²⁰Bach Resistor Ceramics GmbH, Buchenweg 2, 16356 Werneuchen, Germany

Table 4.2.: Table of the magnetic shielding of 50 Hz fields at various temperatures. Extrapolated values are displayed in italic font.

Temperature	294 K	97 K	40 K	20 K
Attenuation	-21 dB	-46 dB	< <i>-85 dB</i>	< <i>-120 dB</i>

Employing the obtained calibration of the sensitivity, one obtains the attenuation for a specific frequency. The measurement results corresponding to the direction of the quantization axis for various temperatures of the inner shield can be seen in Figure 4.26 a. The measurement limit of the setup was between -60 and -55 dB due to pick-up in the wiring. The magnetic shielding substantially improves with decreasing temperature. Below 20 K, the attenuation saturates, which suggests that the electrical conductivity of the used copper becomes constant around 20 K. This means that it is sufficient to operate the cryostat at a temperature of the inner shield slightly below 20 K. Lower temperatures do not reduce the vacuum pressure, as hydrogen, the main constituent element of background gas, condensates at 20 K. However, lower operating temperatures would result in unnecessarily high coolant consumption.

Table 4.2 summarizes the measured attenuations of magnetic fields at 50 Hz and the estimated upper bounds. For temperatures below the boiling point of liquid nitrogen, the attenuation for 50 Hz magnetic fields exceeds the measurement capabilities. However, an upper bound for the attenuation can be determined. The attenuation due to skin effect along a direction x scales as $\exp(-x/\delta)$ with the skin depth δ from Eq. 4.4. Hence, the gradient of the attenuation becomes greater with increasing frequency, if the attenuation is limited by skin-effect. Extrapolating the last two data points above the noise floor of the measurement, an upper bound can be obtained, as displayed in Figure 4.26 a with the dashed lines for the measurements for 20 K and 40 K. For 20 K, the upper bound for the attenuation of 50 Hz magnetic fields is about -120 dB. With this attenuation, the trapped ion qubits are effectively decoupled from alternating magnetic fields which are typically in the low milli-Gauss regime in trapped ion QC labs. However, low frequency magnetic field fluctuations, such as offset drifts of the current in the coils or changes in earth's magnetic field, can still penetrate the inner shield. Dynamical decoupling sequences [VL98] can be employed to decouple the experiments from these low frequency magnetic field drifts. Additional calibration measurements between quantum information experiments can be introduced to infer the qubit transition frequencies [Chw09].

The comparison of the magnetic shielding along the quantization axis and perpendicular to it is depicted in Figure 4.26 b. At room temperature, the contact resistance is not the limiting factor, and there is no significant difference between the magnetic shielding along and perpendicular to this magnetic field axis. By contrast, at low temperatures, the conductivity of the copper increases sharply, and the contact resistance becomes the limiting factor. Hence, the magnetic shielding perpendicular to the axis will be worse than along the axis. Since the contact resistance is not frequency dependent, magnetic shielding limited by contact resistance will have a constant gradient in a double logarithmic plot. As shown in Figure 4.26 b, the shielding of magnetic fields of 50 Hz perpendicular to the quantization axis is about -60 dB, whereas along the axis the upper bound is -120 dB.

The magnetic shield performed better than expected allowing for new physics to be measured in this setup. This high attenuation limits Zeeman shifts and making the execution of quantum algorithms of several milliseconds length possible with high fidelity.

4.11.2 Vibrations

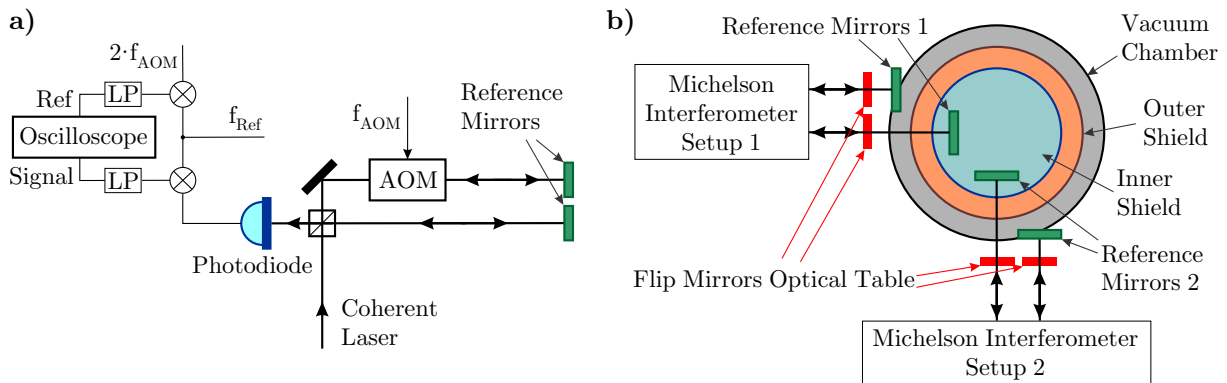


Figure 4.27.: Panel **a** depicts the interferometric measurement scheme used to measure a differential movement between two reference mirrors. Panel **b** shows the employed setup used to measure vibrations in the cryogenic setup along two axes simultaneously. LP ... low-pass filter

An interferometric distance measurement scheme with a Michelson interferometer was employed to measure the vibrations of the cryostat, as illustrated in Figure 4.27 a. In this scheme, the differential length change in the two interferometer arms is measured. In order to not limit the maximum detectable length change to half the wavelength of the coherent laser, an AOM is used for a frequency offset in the laser beams of the two interferometer arms. Without movement in the interferometer arms, the detected frequency at the photodiode will be two times the AOM frequency f_{AOM} . The distance information is encoded in the phase of the detected signal. Since the differential length changes are caused by mechanical movements of heavy copper heat shields with a total weight of about 23 kg, the phase shifts are expected to be below 1 kHz in frequency. Hence, it is sufficient to mix the detected frequency down to a beat frequency of several kHz, low-pass filter the sum frequency and record the phase evolution of the difference frequency on an oscilloscope. In the following measurements, the beat frequency was set to 5 kHz, the sampling rate of the oscilloscope was set to 100 kHz, and the signal was recorded for several seconds.

It proved useful to have a reference beat signal. For its generation, a signal with two times the AOM frequency is generated with the same reference RF signal used to mix down the interferometer signal. To obtain the distance information, the phase difference of the detected signals (reference and main signal) is calculated in post-processing and scaled so that a 2π phase shift corresponds to half the wavelength of the laser, 337 nm for the used 674nm laser.

The hexapod mount structure, see Chapter 4.7, is designed to withstand force in the vertical direction, because it has to support the weight of heavy copper shields, about 23 kg. Along the two horizontal directions, the mount resembles a double pendulum which is mechanically less rigid horizontally than vertically. Hence, it is sufficient to only investigate the vibrations in the horizontal plane, and regard the vibrations in vertical direction as much smaller than the ones in the horizontal plane. In order to obtain position information, mirrors were placed in the inner shield and glued to the vacuum chamber, as depicted in Figure 4.27 b. This allowed for a differential movement measurement between the inner shield and the vacuum chamber. Two perpendicular Michelson interferometers were installed and both beat signals were recorded simultaneously. To gather more information of the movement of the individual parts in the system, two flip mirrors were placed in the beam paths of the interferometer arms on the optical table. This enabled three more differential movement recordings between the inner shield and the optical table, between the vacuum chamber and the optical table, and vibrations on the optical table.

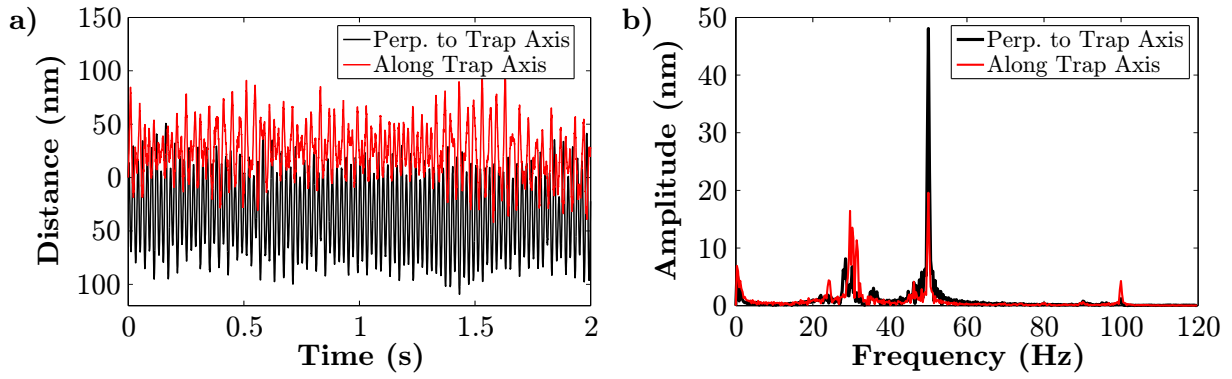


Figure 4.28.: The vibrations of the inner shield with respect to the optical table over time **a** and over frequency **b** with the cryostat at room temperature, the beam path covered, the fan filter unit off, and the optical table floating.

Figure 4.28 illustrates the vibrations when the cryostat is at room temperature. The vibrations over 2 s stay well below ± 100 nm under the best environmental condition for which the optical table is floating, the beam path is covered to avoid air turbulence, and there was no noise in the lab. In the Fourier analysis, there are peaks around 30, 50, and 100 Hz which are investigated in the following.

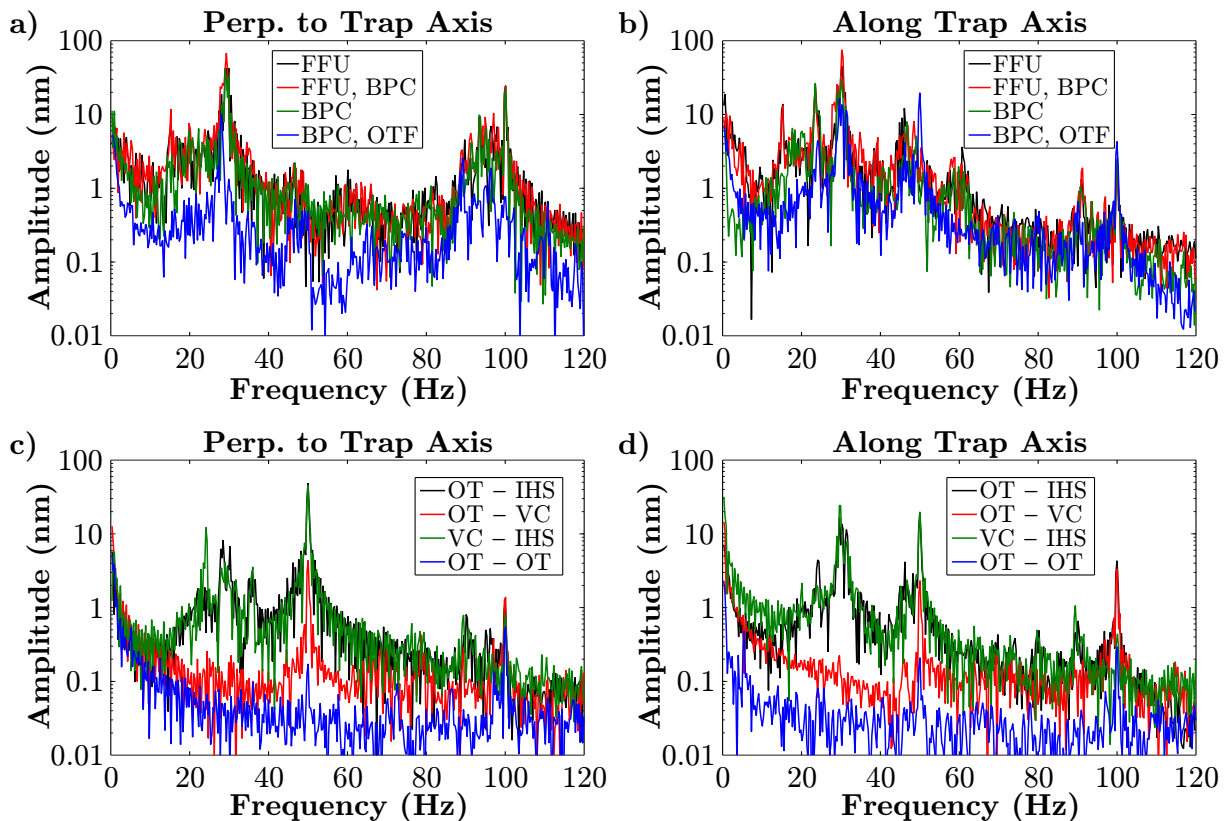


Figure 4.29.: The vibrations of the inner shield with respect to the optical table over frequency with the cryostat at room temperature. For the measurements in panels **a** and **b**, the environmental conditions were changed and the measurements of panels **c** and **d** investigate the vibrations of all four different interferometers to localize the origin of the vibration frequencies. FFU: fan filter unit switched on, BPC: beam path covered, OTF: optical table floating, OT: optical table, IHS: inner heat shield, VC: vacuum chamber

For the measurements of Figure 4.29 a and b, the environment was changed to determine the vibration amplitudes under different conditions. At first, measurements were performed without air-damping the optical table and with the fan filter unit (FFU) above the vacuum chamber switched on. The FFU created both acoustic noise and air turbulence in the optical beam path. This resulted in high vibration amplitudes of more than 100 nm. For the next measurement, the optical beam path was covered with aluminum foil to avoid air turbulence. This reduced the vibration amplitudes only by a small amount. But when the FFU was switched off to reduce the acoustic noise in the lab, the vibration amplitudes drop drastically, especially along the trap axis as shown in Figure 4.29 b. When the optical table was floated for the last environment measurement, the vibrations drop even further with the exception of the peak at 50 Hz. This peak corresponds to a mechanical resonance of unknown origin in the setup that got excited.

The environmental measurements of Figure 4.29 a and b show that acoustic noise and air turbulence cause high vibration amplitudes resulting in decoherence of an optical qubit. Even a person walking by on the hallway next to the lab caused vibrations comparable to acoustic noise because of the vibrations in the floor. Hence, it is mandatory that experiments which are sensitive to the phase of the light are performed in a quiet lab in which (ideally) nobody is physically present.

For the measurements of Figure 4.29 c and d, all four different interferometer configurations were employed. By looking at the differential vibration measurement between the optical table and the vacuum chamber, one can deduce that frequencies around 30 and 50 Hz are excited in the cryostat, as they are absent in these spectra. Furthermore, the small peaks in the spectra between 90 and 100 Hz correspond to the eigenfrequencies of the vacuum chamber on the optical table because they appear in every spectrum except for the reference measurements on the optical table.

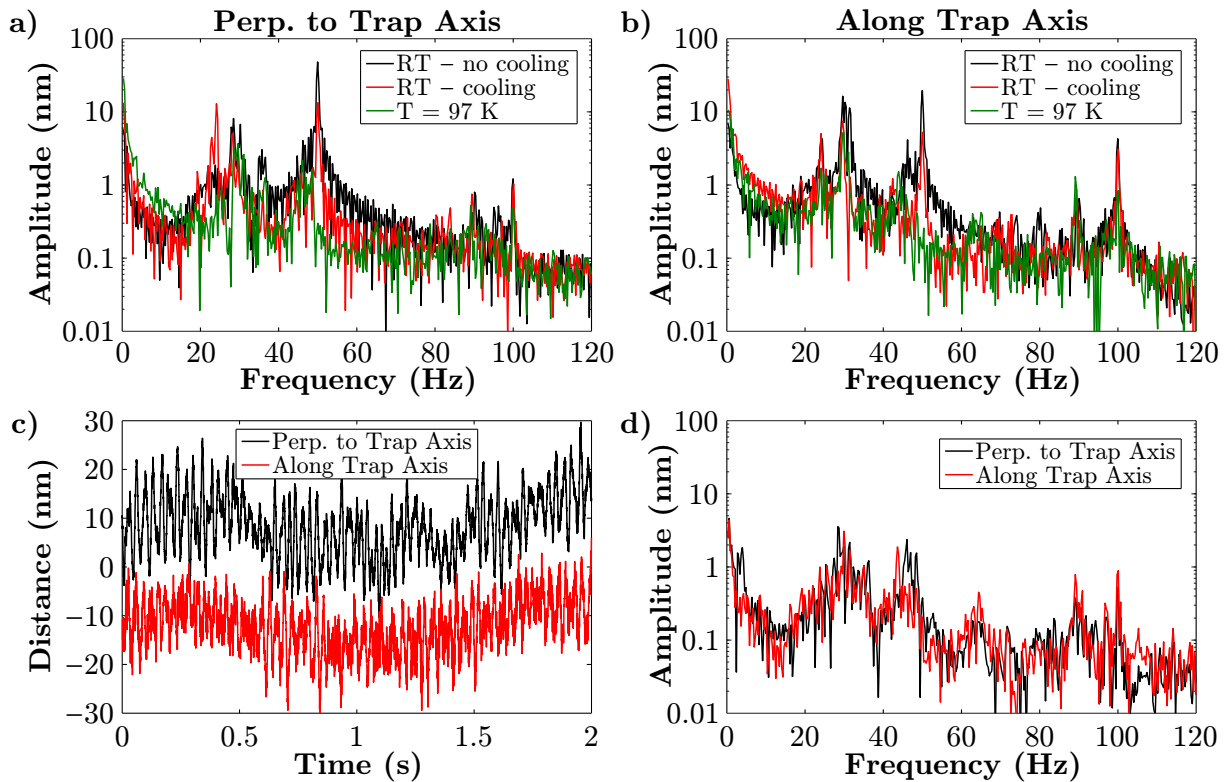


Figure 4.30.: The vibrations of the inner shield with respect to the optical table over frequency of the cryostat with the beam path covered, the FFU off, and the optical table floating. The dependence on varying temperature is shown perpendicular **a** and along **b** the trap axis. The vibrations of the cold cryostat ($T = 97$ K) are depicted over time **c** and frequency **d**.

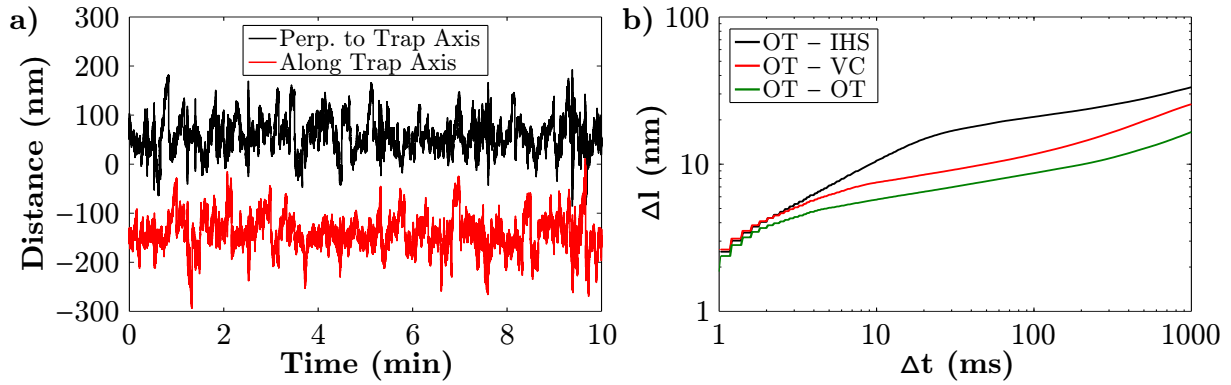


Figure 4.31.: Panel **a** shows the drift of the inner shield with respect to the optical table over 10 min. Panel **b** illustrates the mean vibrations in dependence of the time interval. OT: optical table, IHS: inner heat shield, VC: vacuum chamber

When the cooling of the cryostat was switched on, the vibration amplitudes start to decrease, as depicted in Figure 4.30 a and b. At an inner shield temperature of 97 K, the peak in the vibration spectrum at 50 Hz vanishes which points towards a loose joint in the cryostat that tightened during cool-down. The detailed analysis of the vibrations at 97 K is shown in Figure 4.30 c and d. The vibrations at this temperature stay well below ± 20 nm over 2 s. The Fourier analysis shows that the vibration amplitudes drop below 5 nm for all frequencies. The peaks below 10 Hz are slow drifts, and the peaks around 30 and 45 Hz are the mechanical resonances of the cryostat. The peaks between 90 and 100 Hz are again the eigenfrequencies of the vacuum chamber on the optical table. Unfortunately, when cooling to lower temperatures than 97 K with liquid helium, one of the two mirrors fell off and it was no longer possible to measure perpendicular to the trap axis. However, the thermal expansion is very low below 100 K as shown in Figure 4.11 a and the vibration amplitudes decreased with decreasing temperature. Therefore, it is safe to assume that the vibrations at liquid helium temperatures are similar or smaller than at 97 K.

A drift measurement over 10 min was performed at an inner shield temperature of 105 K. The vibrations stay between ± 150 nm, as depicted in Figure 4.31 a. On the time scale of tens of seconds, there are slow drifts which are likely caused by the air-damped optical table. The controllers of the air pressure in the table legs keep the optical table level. But imperfections in this stabilization cause slow tilts of the optical table, which likely cause the observed slow drifts of the inner heat shield.

To estimate the vibrations that will occur during one measurement cycle, one can look at the mean vibration amplitudes in dependence of a time interval corresponding to the duration of the experiment, as illustrated in Figure 4.31 b. For short time intervals below 5 ms, the observed vibration amplitudes of the cryostat are about equal to the one of the reference measurement on the optical table. At these time scales, acoustic noise couples to the system and the experiment is limited by the vibrations in the setup on the optical table. For increasing time intervals, the vibrations of the vacuum chamber and the inner shield increase more than the vibrations on the optical table and measurements over longer time intervals (> 10 ms) are limited by the cryostat.

The 3-5 nm average vibration amplitudes during the first milliseconds correspond to about 0.5 % of the wavelength of an optical qubit, which is about 700 nm. When applying this on the phase restrictions on QC from Chapter 2.8.2, this means that one can expect that during the execution of a quantum algorithm of a couple of milliseconds length, some gates will be performed with an infidelity of 10^{-3} . If one considers that the optical beam path of the qubit laser is about a factor of 10 longer than the short interferometer used for the vibration measurements, one will have to expect even higher infidelities of single qubit operations in such experiments. Hence, high-fidelity quantum operations over milliseconds with an optical qubit are only possible in

experiments which actively stabilize the phase of the light at the position of the ion. Such stabilization is very challenging given that the light in the experiment is pulsed.

The vibration isolation is very satisfying and performed better than expected. The vibrations are so low that experiments with optical qubits of up to 5 ms length can be performed with 99 % fidelity or higher. On that time scale, they are not limited by the movement of the cryostat but acoustics coupling to the optical setup.

5 Experimental setup

This chapter describes the experimental setup consisting of lasers and electronics. A brief overview of the setup can be found in reference [BvMP⁺16].

5.1 Lasers and optics

In this section, the laser setups required for photo-ionization and the lasers that drive dipole transitions are discussed. Furthermore, the optical setups of the qubit lasers with linewidths smaller than 10 Hz are covered at the end of this section.

5.1.1 Photo-ionization lasers

As described in Chapter 4.8, to load ions into the trap, an oven is heated until it emits a beam of neutral atoms. These atoms can pass through the cryostat and the slit of the trap to the loading zone, where they are ionized by photo-ionization [GRB⁺01, BLW⁺07]. Figure 5.1 shows the relevant energy levels for photo-ionization of calcium and strontium.

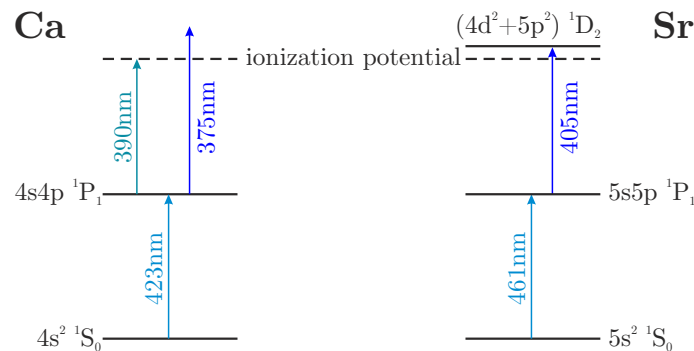


Figure 5.1.: Energy level diagrams of Ca and Sr with relevant wavelengths for photo-ionization.

Calcium can be ionized by a resonantly enhanced two-photon process in which a 423 nm laser first excites from the $4s^2 \ ^1S_0$ ground state to the $4s4p \ ^1P_1$ excited state. This is an isotope-sensitive transition [LRH⁺04] and the closest neighboring transition of another isotope is shifted by about 400 MHz from the ^{40}Ca transition, which is sufficient for isotope-selective loading of ^{40}Ca . The $4s4p \ ^1P_1$ state can then be excited to the continuum with light at a wavelength smaller than 390 nm. The laser in this setup has a wavelength of 375 nm.

Similarly in the photo-ionization of strontium, a 461 nm laser excites from the $5s^2 \ ^1S_0$ ground state to the $5s5p \ ^1P_1$ excited state. This is an isotope-sensitive transition as well, but the resulting isotope shift between ^{87}Sr and ^{88}Sr is only about 56 MHz [BLW⁺07]. Doppler broadening of the transition in the hot atom beam does not allow for isotope-selective ion loading. For the last step of the ionization, the population in the $5s5p \ ^1P_1$ state is excited to the auto-ionizing $(4d^2+5p^2) \ ^1D_2$ state through a transition near 405 nm. There exists an alternative ionization scheme [BC97] that allows isotope-selective loading of ^{88}Sr but it requires three lasers instead of two. However, using an isotope enriched ^{88}Sr source enables loading ^{88}Sr with just two lasers.

Table 5.1 shows the photo-ionization frequencies observed with the beam geometries described in Chapter 4.3. For laser excitations from the $s^2 \ ^1S_0$ to the $sp \ ^1P_1$ states for both species, external

Table 5.1.: The observed photo-ionization frequencies of ^{40}Ca and ^{88}Sr .

Species	Transition	Approximate wavelength	Transition freq.
^{40}Ca	$4s^2\ ^1S_0 \rightarrow 4s4p\ ^1P_1$	423 nm	709.0788 THz
	$4s4p\ ^1P_1 \rightarrow \text{continuum}$	375 nm	795 - 799 THz
^{88}Sr	$5s^2\ ^1S_0 \rightarrow 5s5p\ ^1P_1$	461 nm	650.5038 THz
	$5s5p\ ^1P_1 \rightarrow (4d^2+5p^2)\ ^1D_2$	405 nm	738 - 740 THz

cavity diode lasers (ECDL) (*Toptica*¹ DL pro) were employed. For the second transition, it was sufficient to use broadband light sources with enough intensity in the required wavelength range. The two photo-ionization lasers of each species are overlapped on the optical table and coupled to the same fiber, whose output is directed at the experiment.

5.1.2 Lasers driving dipole transitions

The linewidths of the dipole transitions in both ion species are on the order of about 10 MHz [Jam98]. In order to provide efficient Doppler cooling and state detection, the linewidths of the lasers driving these transitions have to be narrower than the respective transitions. When working with dark resonances like in EIT cooling (Chapter 2.7), one will require even more accurate tuning to the desired spectral part of the transition. Therefore, it is desirable to have lasers with a linewidth of a fraction of the transition linewidth. In the experiment, linewidths between 100 kHz and 1 MHz have been achieved.

In order to achieve these linewidths, one needs to stabilize the laser frequencies to stable references. There is no usable atomic reference, such as a transition in another element, suitable for stabilization of a transition in $^{40}\text{Ca}^+$ and $^{88}\text{Sr}^+$. (The only exception is the $^2S_{1/2} \leftrightarrow ^2P_{1/2}$ transition in $^{88}\text{Sr}^+$, which is close to an Rb-line near 422 nm [SMDB07].) Therefore, all lasers are locked with the Pound-Drever-Hall (PDH) scheme [DHK⁺83] to Fabry-Pérot reference cavities. As illustrated in Figure 5.2 a, one of the two mirrors of each cavity is mounted on piezos which allows precise tuning of the frequency by changing the length of the cavity. Hence, it is possible to tune each laser to an arbitrary frequency around the corresponding dipole transition of the ion. In order to minimize thermal drifts, the spacer is made out of ultra-low expansion (ULE) glass. The setup used for both the calcium laser system and the strontium laser system was designed by Muir Kumph [Kum15] and is depicted in Figure 5.2 b. The ULE spacer is placed inside a heat shield in a vacuum vessel. The aluminum box containing the whole vacuum chamber is thermally stabilized with Peltier elements and is thermally isolated from the lab by styrofoam in a plastic cover. The typical finesses of the cavities for lasers driving dipole transitions are between 500 and 1000, and the free spectral range (FSR) set by the length of the ULE spacer is about 1.5 GHz. This results in typical linewidths on the order of 100 kHz for these lasers. To minimize the effect of residual voltage ripple from the high-voltage amplifiers, driving the piezos, on the cavity length and, thus, the frequency of the laser, fifth-order RC-low-pass filters with a cut-off frequency of 10 Hz are placed in series to the piezos which tune the cavity length.

All the dipole lasers are ECDLs (*Toptica* DL pro), which are directly locked to reference cavities, with the exception of the 397 nm laser (*Toptica* TA SHG pro) which is a frequency-doubled laser and its fundamental, 794 nm light, is locked to a cavity.

The optical setup is almost identical for each ion species and, therefore, the lasers are labeled with the transition that they drive in Figure 5.3. For the Doppler cooling and detection laser,

¹Toptica Photonics AG, Lochhamer Schlag 19, 82166 Gräfelfing, Germany

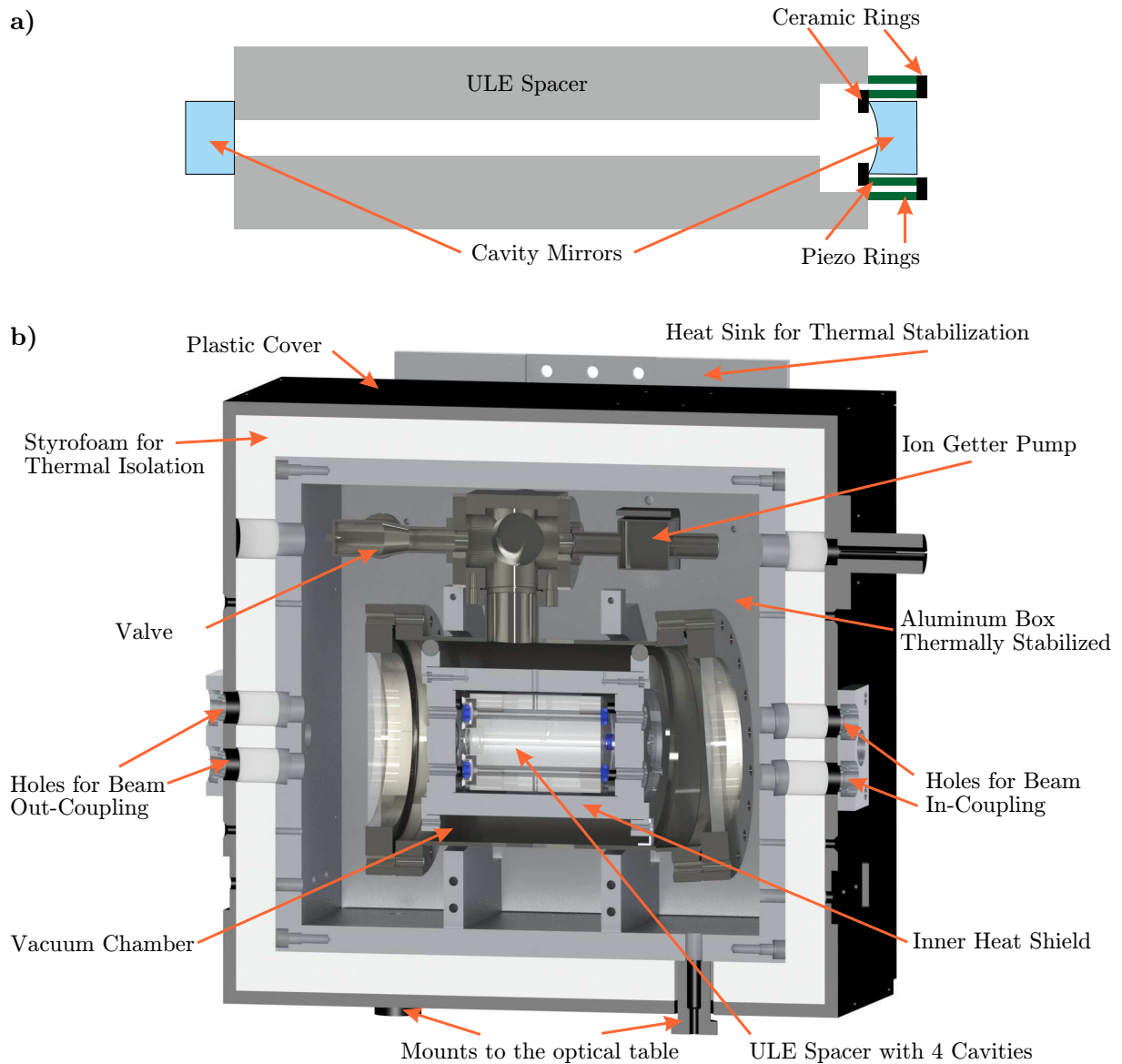


Figure 5.2.: Panel **a** shows the schematic depiction of an optical cavity on a ULE spacer with a tunable length. Panel **b** illustrates a cutaway view of the thermally stabilized setup with up to four cavities.

driving the ${}^2S_{1/2} \rightarrow {}^2P_{1/2}$ transition, the setup consists of three AOMs (*Brimrose*² QZF-80-40-397 and TEM-80-10-422) each in double pass configuration. The first double pass shifts the laser frequency by +160 MHz before the light is split into two paths, one for π -polarized light used for Doppler cooling and detection and one for σ -polarized light used for optical pumping. Both these paths contain another AOM in double pass configuration. This setup allows for a high frequency tuning range with little beam pointing instability.

The setups of the other two dipole lasers driving the ${}^2D_{3/2} \rightarrow {}^2P_{1/2}$ and the ${}^2D_{5/2} \rightarrow {}^2P_{3/2}$ transition consist each of an AOM (*Crystal Technologies*³ 3080-124 and 3080-197) in double pass configuration. Their outputs are overlapped and coupled to the same fiber which guides the light to the experiment.

²*Brimrose Corporation of America*, 19 Loveton Circle, Hunt Valley Loveton Center, Baltimore, Maryland 21152-9201, USA

³now: *Gooch & Housego PLC*, Dowlsh Ford, Ilminster TA19 0PF, UK

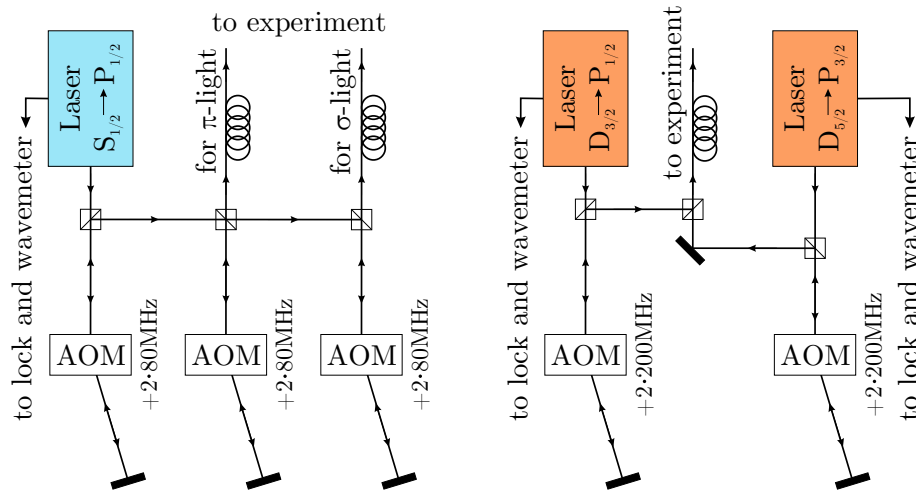


Figure 5.3.: Schematic depiction of the optical setup for the lasers driving dipole transitions. Some of the light of each laser driving the dipole transitions is split-off and sent to the lock and the wavemeter for frequency stabilization. The main light of the laser driving the ${}^2S_{1/2} \rightarrow {}^2P_{1/2}$ transition is sent through an AOM in double pass configuration before being split into two beams which are used for the π - and σ -polarized light at the experiment. In each of these branches, another AOM pulses the light before it is sent via a fiber to the experiment. The other two dipole lasers each have one AOM in double pass configuration. Their outputs are overlapped and sent through the same fiber to the experiment.

5.1.3 Lasers driving quadrupole transitions

When working with optical qubits, the quadrupole transition ${}^2S_{1/2} \leftrightarrow {}^2D_{5/2}$ is used as the qubit transition, see Chapter 2.2. The maximally achievable coherence time of an optical qubit is limited by the linewidth of the laser driving the transition. For example, a 729 nm laser for ${}^{40}\text{Ca}^+$ was locked to a linewidth of about 1 Hz [Chw09] resulting in coherence times of tens of milliseconds [SNM⁺13].

During this PhD thesis, Lukas Postler built the 729 nm laser incorporated in the setup in his Master’s thesis [Pos15]. A brief summary of his work is as follows: the laser is an ECDL with an extended optical resonator (*Toptica* TA pro). The intrinsic linewidth of such an ECDL can be on the order of 1 MHz. Hence, the frequency stabilization has to reduce the linewidth by five or six orders of magnitude to reach the desired 1 Hz linewidth. This is challenging with a single locking stage, and thus, a two-stage approach [LHN⁺07] was pursued for both quadrupole lasers.

The first stage is a PDH lock to a pre-stabilization cavity with medium finesse (MF) of about 10000, which is located on the same cavity spacer as the optical resonators for the dipole lasers (see Figure 5.2), yielding the same FSR of 1.5 GHz. This typically results in a linewidth between 1 and 10 kHz after the first locking stage.

The second stage is another PDH lock in which the feedback acts through a voltage controlled oscillator (VCO) onto an AOM, which locks the first order diffracted light to a high-finesse (HF) cavity from *Stable Laser Systems*⁴. The finesse of the HF cavity is about 250000 with an FSR of 3 GHz. The obtained narrow-linewidth light is then amplified with a tapered amplifier before it is sent to the experiment.

Since the pre-stabilization cavity contains two piezos, which have a non-zero thermal expansion (of first order), its length will thermally drift with respect to the HF cavity, causing their

⁴*Stable Laser Systems*, 4946 63rd Street, Suite B, Boulder, CO 80301, USA

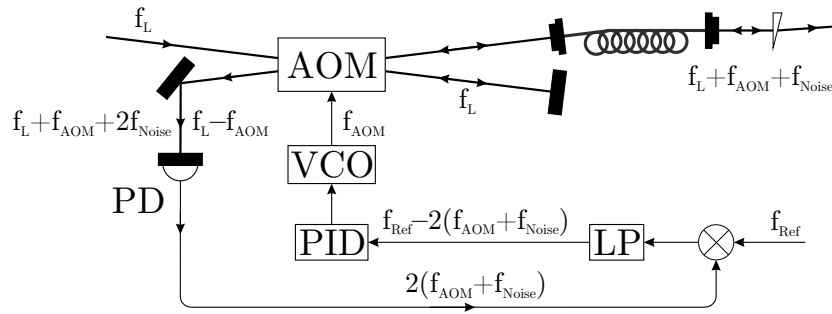


Figure 5.4.: Schematic depiction of fiber noise cancellation setup.

resonance frequencies to drift apart. Due to the limited bandwidth of the VCO driving the AOM, this drift is compensated by feeding back on one of the piezos of the MF cavity with a field programmable gate array (FPGA)-based counter.

In order to measure the linewidth of the laser, beat measurements of the 729 nm laser with the laser from reference [Chw09] were performed. With a finesse of 242742(6) of the 729 nm cavity, a Lorentzian fit of the beat signal of the two 729 nm lasers resulted in a linewidth of 1.58(2) Hz. Additionally, the Allan deviation of the beat signal was calculated and resulted in a lowest Allan deviation of $2.4 \cdot 10^{-15}$ at an averaging time of 0.33 s.

During the course of this thesis, the 674 nm laser was only locked to the MF cavity but not to its HF-cavity. However, since the same lock system is used for both the 729 nm and the 674 nm laser, one can expect similar linewidths.

Transferring this narrow linewidth laser light through a fiber is not trivial since thermal drifts and acoustics couple to the fiber. This changes the refractive index and, therefore, the optical path length of the fiber, which induces phase noise at the output that can be interpreted as frequency broadening caused by the fiber [PHR92]. For QIP with an optical qubit, one has to stabilize the phase at the output of the fiber to avoid decoherence caused by the fiber noise. In a fiber noise cancellation (FNC) setup, one modulates the frequency of an AOM in the beam path such that the phase noise of fiber is compensated [MJYH94].

In the FNC setup, shown in Figure 5.4, the incoming light with frequency f_L is frequency-shifted by f_{AOM} in an AOM before passing through a fiber in which fiber noise f_{Noise} is acquired. A beam sampler reflects a fraction of the light back through the fiber where it acquires another frequency shift of f_{Noise} . This light is then directed at a photodiode (PD). The incoming light that is not deflected by the AOM is sent back to the AOM in which it is frequency-shifted by $-f_{AOM}$ before it interferes with the light coming back from the fiber. The detected beat signal has frequency $2(f_{AOM} + f_{Noise})$ and is mixed down with a reference frequency f_{Ref} and a low-pass (LP) filter to generate an error signal for a PID controller which controls a VCO driving the AOM. This control loop minimizes the error signal $f_{Ref} - 2(f_{AOM} + f_{Noise})$ which is the case when $f_{AOM} + f_{Noise} = f_{Ref}/2$. Therefore, the light at the output of the FNC setup is frequency shifted by $f_{Ref}/2$ compared to its input.

Figure 5.5 depicts the setup used for the 729 nm laser in the experiment. The AOMs used for frequency shifting are *Brimrose* TEM-270-65-729 and TEM-270-65-674, and *Crystal Technologies* 3080-120. A beam sampler couples a fraction of the laser light via a fiber to the wavemeter (WM) and the MF cavity for the first stage of the lock. The main light is frequency shifted by the AOM performing the HF lock and amplified by a tapered amplifier (TA). Some of the light coming out of the TA is split-off for the HF lock. This light has to pass through a frequency shifter which compensates drifts like aging of the HF cavity and a FNC setup before the light can be used for the HF-lock. The main light coming out of the TA passes through another FNC

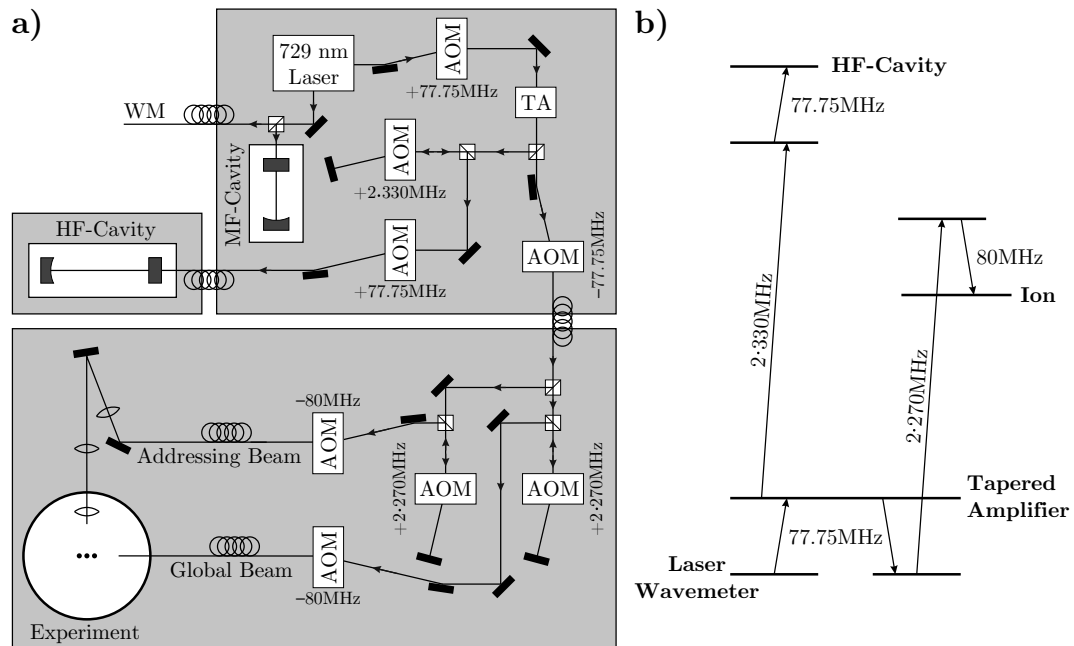


Figure 5.5.: Panel **a** shows the setup of the 729 nm laser. Panel **b** illustrates the frequencies required for the operation of the 729 nm laser in the experiment.

setup before reaching the experimental optical table. There, the light is split into a global and an addressing beam. Each of these two beam paths contains an AOM in double pass and a second one in single pass configuration before their output can be used at the experiment. Figure 5.5 **b** illustrates the frequencies utilized in the 729 nm setup. For the 674 nm, the frequency of the TEM₀₀-mode in the HF-cavity and its relation to the transition frequency in $^{88}\text{Sr}^+$ was not yet obtained. Thus, the optical setup of the 674 nm laser could not yet be set up.

5.1.4 Detection optics

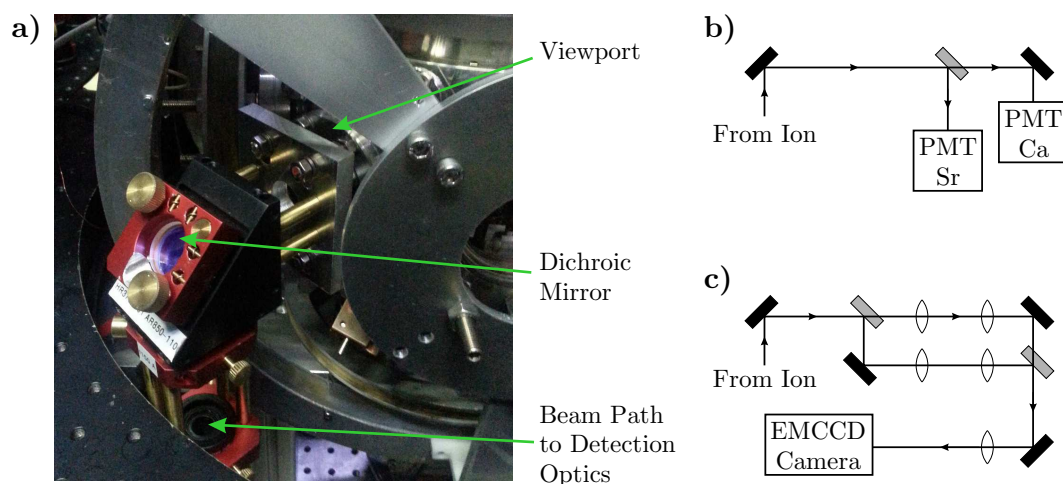


Figure 5.6.: Panel **a** shows the optical setup for addressing and detection near the vacuum chamber. A cage system is attached to the viewport. A dichroic mirror reflects the detection beam downwards while allowing the addressing beam to pass through in the horizontal direction. Panel **b** and **c** depict the setups on the lower level of the optical table used for detection with PMTs **b** and an EMCCD camera **c**.

5.2.1 Electronics for quasi-static signals

The quasi-static signals are signals that do not change during a single experiment and are depicted in the overview of Figure 5.7. They contain for example the RF signal to drive the Paul trap, the piezo voltages setting the transition frequencies in the dipole cavities, or the frequencies for the AOMs switching the dipole lasers. All these signals are controlled via a bus system (Figure 5.8) which was brought to the University of Innsbruck by Florian Schreck [Sch15] and was further improved in Innsbruck.

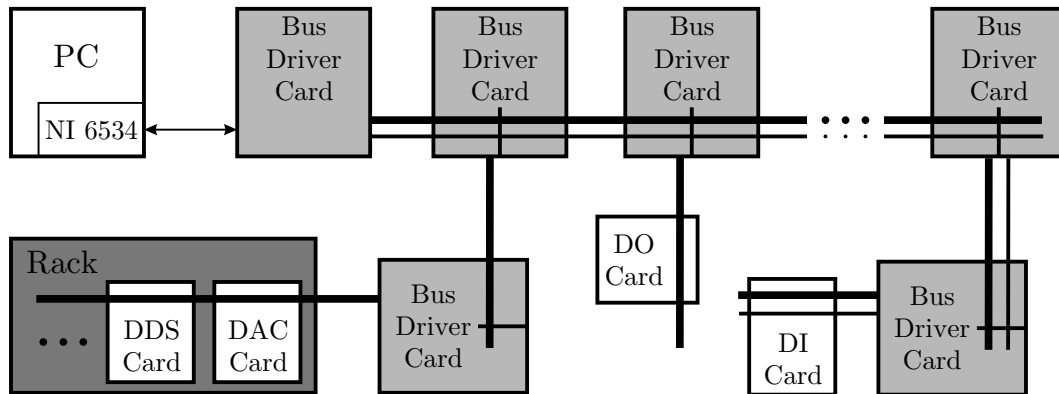


Figure 5.8.: Overview of the bus system. A personal computer (PC) with a National Instruments (NI) 6534 card controls the bus system. Bus driver cards distribute the digital signals of the bus in the lab and thereby refresh the signals and provide galvanic isolation between their input and output. The signals of the bus system typically lead to racks into which one can plug several types of output cards, like DDS cards to generate RF signals or DAC cards to generate analog outputs. But, there is a variety of additional cards that can be controlled via the bus system like digital output (DO) cards and digital input (DI) cards.

The bus has 8 address bits, 16 data bits, and 1 strobe bit, which are sent via a 50 pin ribbon cable, where every second pin is grounded. Additionally, one can add a second ribbon cable for auxiliary signals such as a read/write bit and 3 address signals to increase the address range of the bus system. The ground lines in the ribbon cable cause a considerable capacitance, which limits the transmission length to about 5 m before the signal has to be refreshed to provide a bit error probability below 10^{-9} at a bus timing of $1 \mu\text{s}$. This refreshing is performed by bus driver cards, which provide galvanic isolation between their input and output signals and, thus, also prevent ground loops.

The bus system has output cards for analog voltages, digital voltages, and RF signals. These output cards allow the generation of those signals close to their targets. The RF signals are generated with direct digital synthesizer (DDS) chips, and allow setting an RF signal before a measurement sequence. The signal can be switched on and off via an RF switch during a sequence. The switching of the RF signal can be converted into switching of an optical signal with an AOM in single pass or double pass configuration. The DAC cards are mainly used to control the voltages on the piezos of the cavities of the dipole lasers and, therefore, set the transition frequency of these lasers. The output cards are mounted in rack systems, which additionally support RF amplifiers, sample-and-hold PID controllers, and other cards that are of use in the lab. Furthermore, there is a digital input card that allows reading the state of digital signals. This card is useful to, for example, determine whether all lasers are in lock before starting a measurement.

5.2.2 Electronics for dynamic signals

Dynamic signals (Figure 5.7) are signals which have to change during a single experimental cycle. They contain RF signals to phase-coherently switch the qubit interaction fields, the voltages on the DC segments of the trap to move ions during a measurement cycle, or digital signals to switch the dipole lasers on or off.

The real-time sequencer is the main experiment control device which controls digital outputs and has the ability to change the sequence in dependence of the values of digital inputs. The sequencer, an FPGA-board, was designed by Paul Pham in his Master's thesis [Pha05] and has a timing resolution of 10 ns. It controls a bus system to which one can attach up to 16 DDS boards that Philipp Schindler designed during his diploma thesis [Sch08]. These DDS boards allow phase-coherent frequency switching and amplitude shaping of their outputs.

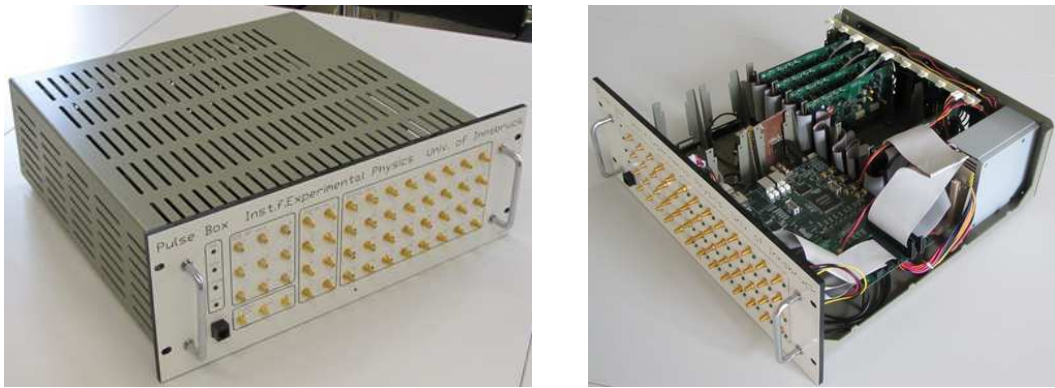


Figure 5.9.: Pictures of the real-time sequencer box.

The sequencer and the "smart" DDS boards are placed inside the sequencer box which was designed during this thesis and is shown in Figure 5.9. Besides the sequencer itself, it can hold up to nine "smart" DDS boards and a phase-locked-loop (PLL) circuit⁷ which allows synchronizing the experiment to a 10 MHz reference clock signal. The PLL generates all frequencies required for the operation of the devices in the sequencer box and the reference frequencies for the DDS boards controlled by the bus system. Hence, expensive commercial signal generators are not necessary for the operation of the experiment. Furthermore, the sequencer controls 32 digital outputs and reacts to 8 digital inputs which are galvanically isolated from each other to prevent ground loops.

The DC voltages for the trap electrodes are supplied by an FPGA-based arbitrary waveform generator designed and built in the Schmidt-Kaler group at the University of Mainz [WZR⁺12]. This arbitrary waveform generator is preprogrammed and triggered by a digital signal from the real-time sequencer to allow movement of ions during a measurement. This functionality enables reconfiguration of the ion string(s) during an experimental cycle.

5.2.3 Electronics developed during this thesis

5.2.3.1 Bus sequencer

For the parts of the experiments, where timing is less crucial, such as Doppler cooling and detection, one can use the real-time bus sequencer shown in Figure 5.10. It was developed

⁷The PLL is home-made and was designed by Gerhard Hendl at the Institute for Quantum Optics and Quantum Information (IQOQI) in Innsbruck, Austria.



Figure 5.10.: Picture of the bus sequencer.

during this thesis to change signals with a $1 \mu\text{s}$ timing resolution on the bus system. During the measurement, it is triggered from the main sequencer via a digital signal. This enables the control of the frequencies of dipole lasers during one measurement. For example, without the bus sequencer, the RF signals driving the AOMs of the dipole lasers are preset before the experiment. In order to switch light on and off, these signals are attenuated with RF switches, which have a typical attenuation is between 30 and 90 dB. With the bus sequencer, one can program the DDS to output frequency 0 Hz. Hence, RF switches are no longer necessary. This will lead to higher attenuation of the light, as the RF signals driving the AOMs are switched off rather than attenuated.

5.2.3.2 Counter to compensate micromotion

In trapped ion quantum computing experiments, PMTs are used to detect the quantum state of an ion by counting the number of detected photons in a given time frame. If the count rate is higher than a threshold, the ion will be in the $|S\rangle$ state, if not, then it will be in the $|D\rangle$ state. Thus, counter cards are an essential part of trapped ion experiments. During the course of this thesis, a counter card was developed. In its first version, the count values were read via the bus system. The new version uses a universal serial bus (USB) connection to transmit the information to a computer for further processing.

Besides working in a continuous operation mode (for loading ions and beam alignment) and a pulse operation mode (for experiments), the counter card supports a third way of operation called differential mode to detect the ion fluorescence even at high background count rates. Its principle is depicted in Figure 5.11. If the repump laser is periodically switched on and off, the fluorescence of the ion will periodically vary as the electron will stay in the $^2D_{3/2}$ state without the repumping light. The variation of the light corresponds to the fluorescence of the ion.

Stray electric fields can shift the ion's position out of the RF null where the ion will undergo oscillations at the trap drive frequencies because of the electric field of the trapping potential in Paul traps (micromotion). The effects of micromotion on QIP and their compensation are discussed in references [Roo00, BMB⁺98b].

One way to compensate micromotion is with the correlation method. A brief explanation is as follows. Under the influence of micromotion, the transition frequency for cooling and detection of an ion is periodically shifted due to the Doppler shift. Therefore, the probability to absorb a photon on such a transition is periodically modulated as well (Figure 5.12). If one assumes that the life time of the excited state of this transition is smaller than the trap drive repetition rate,

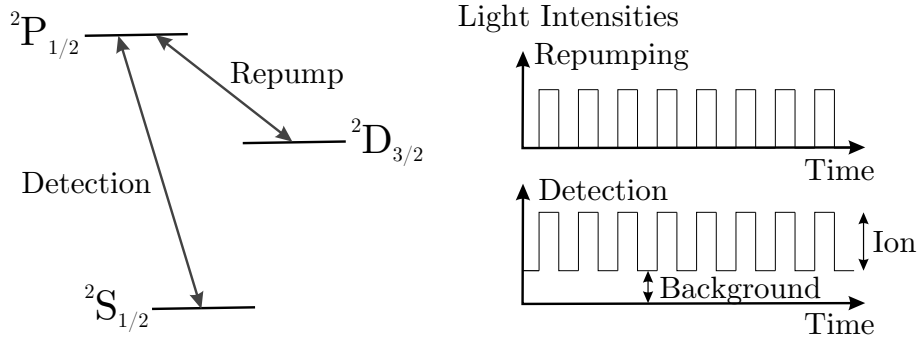


Figure 5.11.: Differential count measurement used when the background light limits the ion detection efficiency.

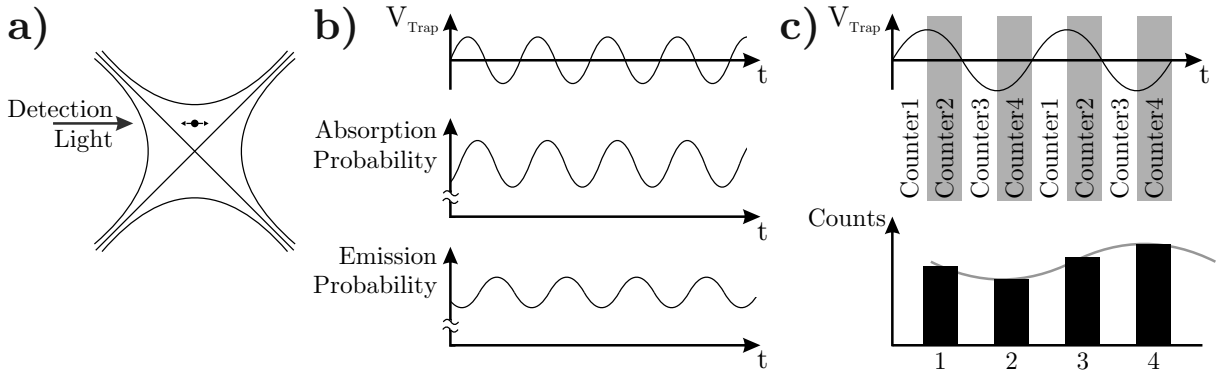


Figure 5.12.: Panel a shows an ion in the quadrupole field of a Paul trap. Detection light interacting with the ion will have a modified absorption and emission probability b due to Doppler shift caused by the micromotion. For the detection, one can generate a histogram c for the photon arrival times with respect to the phase of the trap drive frequency to measure the micromotion.

the photon emission probability on that transition is modulated with the trap drive frequency as well. To detect micromotion, one has to detect this modulation of the emission probability.

By applying the trap drive frequency to the counter card developed during this thesis, an internal PLL multiplies this frequency by four. This allows four counters in the FPGA of the counter card to detect the counts that arrive at phase $0-90^\circ$, $90-180^\circ$, $180-270^\circ$, and $270-360^\circ$ respectively, as illustrated in Figure 5.12 c. After averaging over many counts, one can display a histogram of the phase of the arrived counts with respect to the trap drive. The micromotion is then encoded in the amplitude of the modulation in the histogram. Hence, in order to compensate micromotion, one changes DC compensation voltages and monitors the amplitude of this modulation. By minimizing the amplitude, one minimizes the micromotion. To compensate for micromotion in all directions, one needs incident laser beams with projections on all axes of the trap [Roo00]. The big advantage of this method compared to micromotion compensation with the qubit laser is that one does not need qubit laser light at the trap to perform micromotion compensation. Right after trapping ions for the first time in a trap, it is possible to compensate the micromotion accurately.

6 Experimental results

In this chapter, the cryogenic apparatus is characterized using trapped ions, as also shown in reference [BvMP⁺16].

In the first version of the cryostat, an asymmetric Yedikule trap version 1, as described in Michael Niedermayr's thesis [Nie15], was used and a technical drawing of the trap is depicted in Figure 6.1 a. This trap was able to confine both ion species, $^{40}\text{Ca}^+$ and $^{88}\text{Sr}^+$, and images of the ions can be seen in Figure 6.1 b. In the second version of the cryostat, the trap described in Chapter 4.5 was used. So far, experiments in this setup focused on the characterization of the apparatus using $^{40}\text{Ca}^+$ ions.

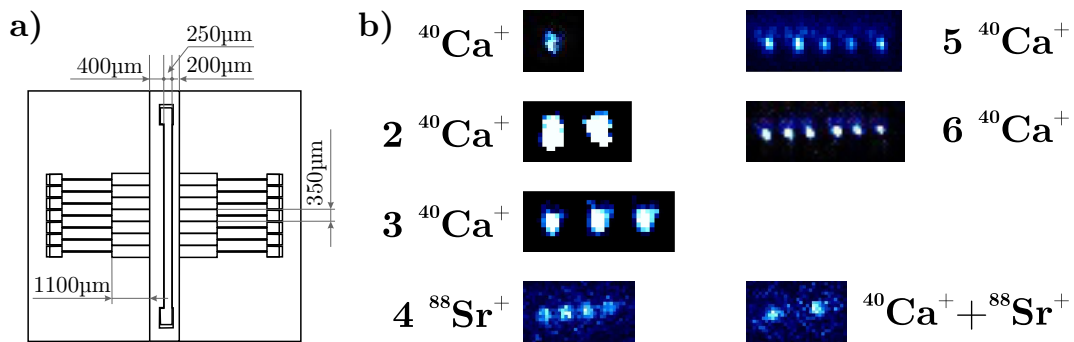


Figure 6.1.: Panel a shows a technical drawing of the Yedikule trap, and panel b illustrates pictures of trapped ions.

The detection optics is characterized using images of an ion on the EMCCD camera, as shown for a $^{40}\text{Ca}^+$ ion in the second version of the cryostat in Figure 6.2. The photon counts of the rows and columns are summed and fitted to a Gaussian distribution. The length scale is calibrated using a two-ion string with a known ion-to-ion distance, yielding a magnification of the imaging system of 15. The Gaussian fits of the photon counts of one ion resulted in $1.84(7) \mu\text{m}$ width and $1.89(11) \mu\text{m}$ height. The details on the characterization of the detection optics can be found in the thesis of Anton Nolf [Nol16].

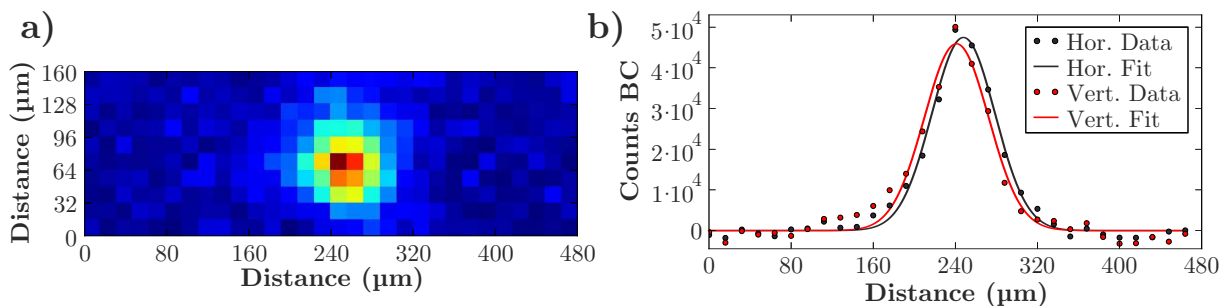


Figure 6.2.: Panel a depicts an image of a $^{40}\text{Ca}^+$ ion on an EMCCD camera. Panel b displays the averaged background corrected (BC) counts of the ion along a horizontal and vertical axis. The counts nicely represent Gaussian fits showing few aberrations in the detection optics.

The experiments described so far have been performed in a continuous way during which the cooling and detection laser driving the $S_{1/2} \leftrightarrow P_{1/2}$ transition and the repumping laser driving the $D_{3/2} \leftrightarrow P_{1/2}$ transition are constantly on. The following experiments are all pulsed which means that during one experimental cycle, the different lasers are switched on and off, as depicted

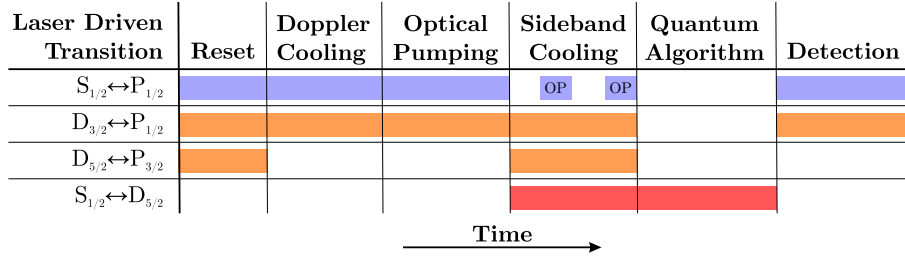


Figure 6.3.: A typical experimental cycle. It consists of resetting and Doppler cooling, followed by optical pumping and sideband cooling. After cooling, the quantum algorithm can be executed which is afterward detected.

in Figure 6.3. Each cycle consists of resetting, Doppler cooling, followed by optical pumping and, if needed, sideband cooling. Optical pumping on the dipole transition takes between 10 and 100 μs , whereas the duration of sideband cooling strongly depends on how many modes have to be cooled. Typical values range from a couple of milliseconds to more than 10 ms. After the ions are cooled and initialized, the quantum algorithm is executed. This can be as simple as a single resonant light pulse to measure Rabi oscillations but can be as complex as Shor's algorithm [MNM⁺16]. After the execution of the algorithm, the states of the ions are detected. The exact detection time depends on the collection efficiency of the detection optics and the fluorescence rate of the ion. For a collection efficiency of about 1 %, as described in Chapter 5.1.4, typical values for the detection with a PMT are less than 3 ms, and up to 10 ms with an EMCCD camera. If the detected number of photons from one ion during the detection time exceeds a threshold value, the ion is detected as in the bright state ($|S\rangle$ also referred to as $|1\rangle$). If the threshold value is not exceeded, the ion is detected as in the dark state ($|D\rangle$ also referred to as $|0\rangle$). State detection is a projective measurement of the σ_z -operator and one gathers only a single bit of information per ion and detection cycle. In order to determine an outcome between 0 and 1, the same cycle is repeated multiple times, typically 100 times, to get statistics.

Prior to benchmarking the trapping performance, one has to perform spectroscopy on the $S \leftrightarrow D$ transition. For this, a light pulse of constant intensity and duration is applied. By varying

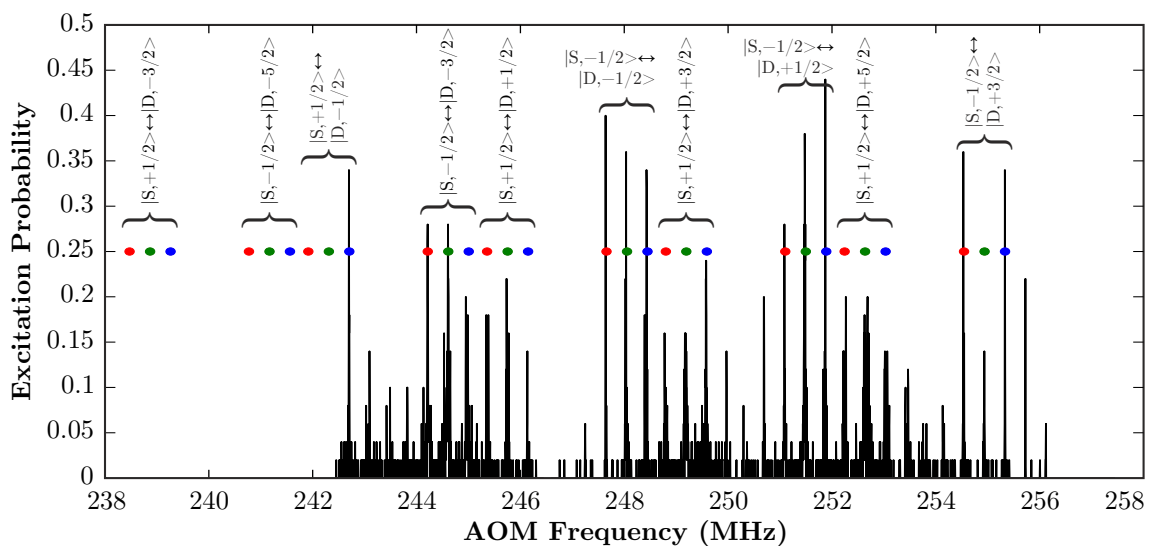


Figure 6.4.: Spectrum of a Doppler cooled $^{40}\text{Ca}^+$ ion without optical pumping using the global beam. The red circles denote red sideband transitions, the green ones carrier transitions, and the blue ones blue sideband transitions.

the light frequency, one obtains a spectrum of the transition. Such a spectrum is illustrated in Figure 6.4 for a Doppler cooled $^{40}\text{Ca}^+$ ion without optical pumping using the global beam. The individual peaks of the spectrum can be assigned to corresponding transitions between Zeeman states of the $S \leftrightarrow D$ transition by varying the magnetic field and tracking their position, as each transition has a unique magnetic field dependence (Eq. 2.2). In Figure 6.4, one can see that each Zeeman transition features three peaks of similar height. The central peak corresponds to the carrier transition and is indicated by a green circle, whereas the red and the blue circles denote the red and blue axial sideband transitions.

Once the transition frequencies are known, one can investigate Rabi oscillations for which the length of the resonant light pulse is varied. The resulting excitation probabilities over the pulse length resemble a cosine (Eq. 2.26). The recorded Rabi flops on the carrier with a sideband cooled $^{40}\text{Ca}^+$ ion using the global beam are shown in Figure 6.5 a. A measurement of the average phonon number \bar{n} , whose measurement will be explained in the next paragraph, resulted in roughly 0.1 phonons along the trap axis, whereas the observed decay corresponds to $\bar{n} \approx 14$. Therefore, one has to assume that the ion was radially at a temperature well above the Doppler cooling limit. It is unclear why Doppler cooling did not work radially and this behavior is currently under investigation at the experiment. The Rabi flops on the blue sideband with a sideband cooled $^{40}\text{Ca}^+$ ion using the global beam are shown in Figure 6.5 b where the mean phonon number was 0.27(3).

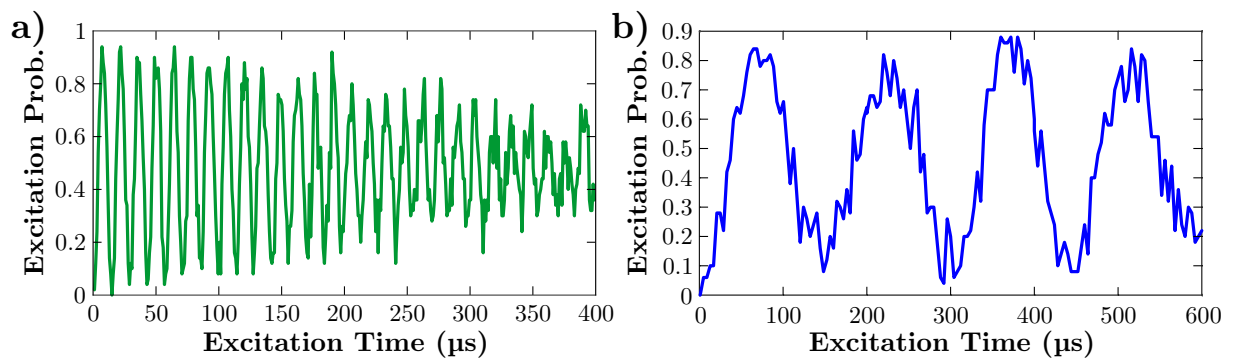


Figure 6.5.: Rabi flops of a sideband cooled $^{40}\text{Ca}^+$ ion using the global beam on **a** the carrier and **b** the blue side band transition.

The heating rate of a trap is a rate of change of motional quanta of a single mode of the secular motion in phonons per second. It is an important quantity as heating rates limit the fidelity of entangling gates as these utilize coupling to motional modes and motional coherence (Chapter 2.6). The heating rate is obtained by measuring the mean phonon number after inducing an idle time between cooling and the analysis pulse. To determine the mean phonon number, one can use the sideband ratio technique described in reference [LBMW03]. A brief description is as follows: the analysis pulse is performed on the red or blue sideband transition yielding the excitation probabilities for both sideband pulses, P_e^{rsb} and P_e^{bsb} . Their ratio is determined by the mean phonon number if the system is in a thermal state

$$R = \frac{P_e^{rsb}}{P_e^{bsb}} = \frac{\bar{n}}{\bar{n} + 1} \quad . \quad (6.1)$$

This equation can be inverted to determine the mean phonon number as $\bar{n} = R/(1-R)$.

The measured heating rate for the axial mode at a frequency of 1.1 MHz of a single $^{40}\text{Ca}^+$ ion is 6.43(27) phonons/s, as shown in Figure 6.6 a. For this measurement, analog output cards of the bus system were used to supply the DC voltages to confine the ion axially. The measurement was repeated with the FPGA-based arbitrary waveform generator developed at

the University of Mainz (see Chapter 5.2.2). The obtained heating rate was $2.14(16)$ phonons/s and is shown in Figure 6.6 b. These results highlight the importance of a low-noise design of the voltage source to minimized technical noise. The measured heating rates are comparable to other experiments with a similar electrode-to-ion distance and secular motion frequency in cryogenic setups [BKR15]. These measurements show that there is little or no influence of the slot on the heating rate of the trap.

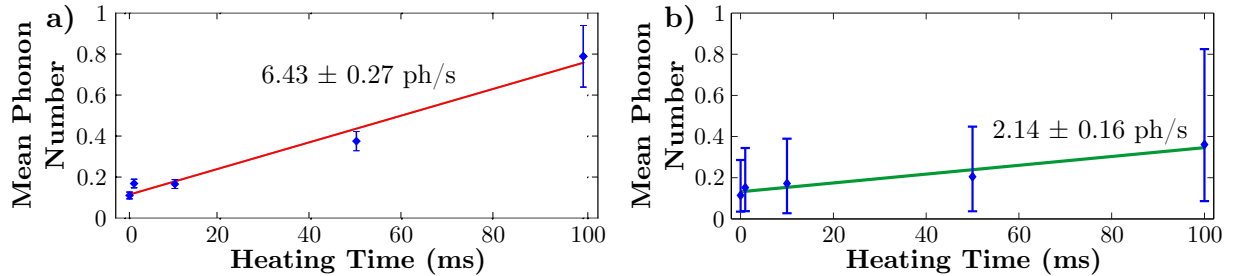


Figure 6.6.: Measured heating rates. Panel a) shows the measurement for which the DC voltages for axial confinement were applied with an analog output card of the bus system. For the measurements of panel b), the FPGA-based arbitrary waveform generator developed at the University of Mainz was used.

To measure the coherence time of the qubit, one usually performs Ramsey spectroscopy [Ram50]. Its principle is illustrated in Figure 6.7. Ramsey experiments consist of two light pulses which each cause a 90° rotation angle on the Bloch sphere and which are separated by the Ramsey time. The first gate operation rotates the Bloch vector into the equatorial plane. During the Ramsey time, external fields (and noise sources) cause phase shifts of the Bloch vector. The phase of the interacting light of the second pulse is varied leading to a sinusoidal variation of the

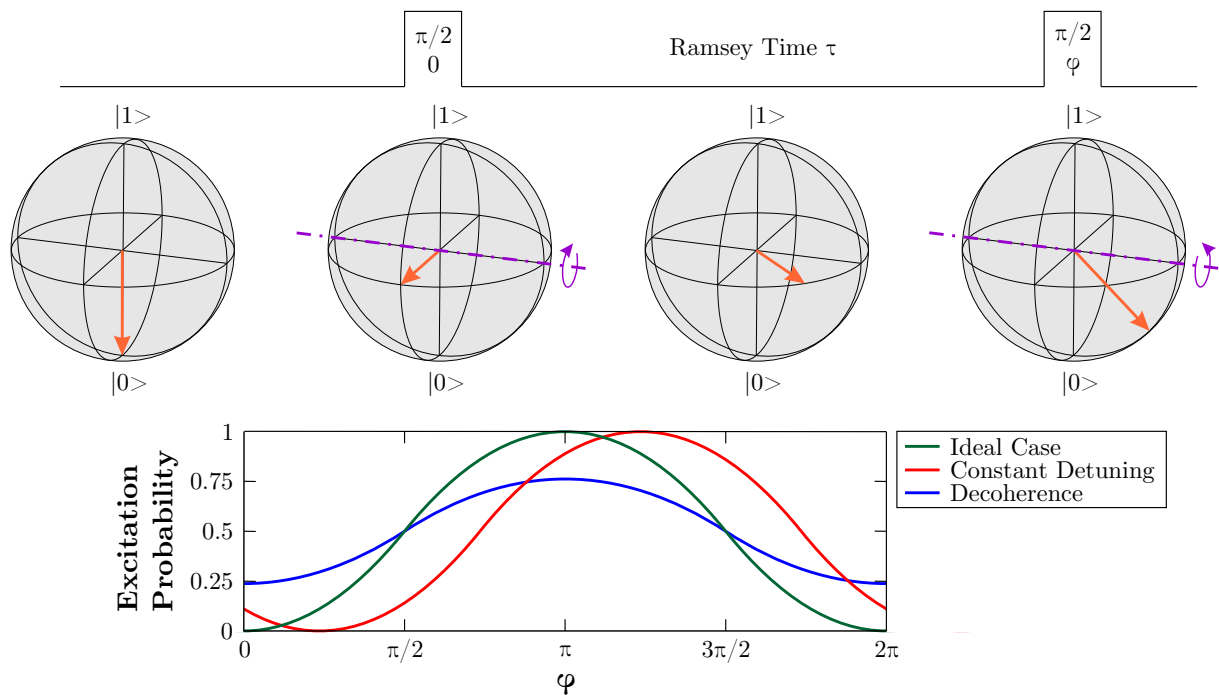


Figure 6.7.: Principle of a Ramsey experiment. First, the state is initialized before the Bloch vector is rotated into the equatorial plane where its phase is influenced by external fields. After the Ramsey time, the Bloch vector is rotated by 90° around a rotation axis. This axis is varied during different experiments to obtain a cosine dependence of excitation probability on the rotation angle of the axis.

excitation probability. A phase offset of this cosine indicates a constant detuning between the driving field and the two-level system. The contrast of the oscillation is called Ramsey contrast and is a measure of the coherence, as decoherence processes reduce the amplitude of the observed cosine.

For the $|S, m_j = 1/2\rangle \leftrightarrow |D, m_j = 1/2\rangle$ transition in a single $^{40}\text{Ca}^+$ ion, the Ramsey measurement resulted in a Gaussian decay of the contrast with a $1/e$ -time of 18.2(8) ms and is shown in Figure 6.8 a. From the high magnetic shielding reported in Chapter 4.11.1 and the narrow-linewidth laser reported in Chapter 5.1.3, one would assume a coherence time closer to the ultimate limit of half the D-state lifetime of $\tau/2 \approx 0.5$ s [Jam98]. But optical qubits are very sensitive to changes of the optical path length, and during the Ramsey measurement, acoustical vibrations coupled into the optical setup outside the vacuum chamber resulting in the observed Gaussian decay of the Ramsey contrast.

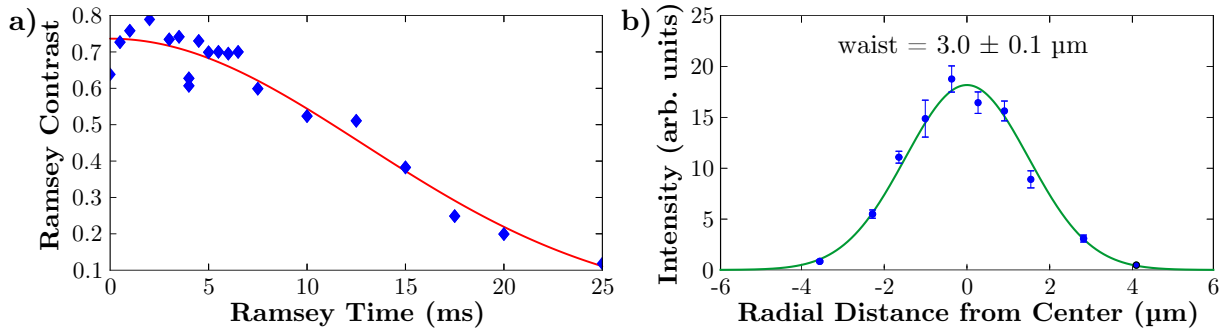


Figure 6.8.: Panel **a** depicts the results of the Ramsey measurements with a single $^{40}\text{Ca}^+$ ion on the $|S, m_j = 1/2\rangle \leftrightarrow |D, m_j = 1/2\rangle$ transition yielding a $1/e$ -time of 18.2(8) ms with a Gaussian fit. Panel **b** shows the results of measurements for which an ion is moved along the trap axis through the addressing beam. The obtained beam waist of the addressing beam was 3.0(1) μm .

The qubit addressing capabilities [NLR⁺99] of the NA=0.23 lens are characterized with a single $^{40}\text{Ca}^+$ ion and a resonant light pulse of constant time and intensity. The ion is moved through the addressing beam along the trap axis by changing the confining DC voltages. The Rabi frequency is proportional to the square root of the intensity [Lou00, Ben08]. Therefore, one obtains knowledge of the light intensity of the addressing beam along the trap axis by measuring the excitation probability along the trap axis. A detailed description of this measurement can be found in the thesis of Anton Nolf [Nol16]. The intensity profile of the beam along the trap axis is depicted in Figure 6.8 b. The observed beam waist of 3.0(1) μm reduces the light intensity to 0.39 % of the peak value at a distance of 5 μm from the peak.

7 Outlook - ideas for improvements and future experiments

This chapter covers ideas to improve the current setup in the lab and ideas for future experiments.

7.1 Higher frequencies of secular motion

A single light pulse from a narrow linewidth laser source will have a continuous spectrum around the center frequency. The spectral width of such a pulse is inversely proportional to the pulse duration. Therefore, the ultimate limit for the speed of single qubit operations with pulsed light from a narrow linewidth laser source is the Fourier width of the used light pulse compared to the frequency spacing to other transitions, as neighboring transitions must not be excited. Hence, higher frequencies of secular motion allow faster single qubit operations.

The resonator described in Chapter 4.9 was designed for high frequencies of secular motion. Anharmonicities of the motion of the stored ions appear for trap stability parameters $q > 0.3$ due to the non-hyperbolic shape of modern traps [GSW97], suggesting a high trap drive frequency which lowers the trap stability parameter q . The losses in the resonator for a constant trap stability parameter scale with the fourth power of the trap drive frequency (Eq. 3.1), suggesting a low trap drive frequency to limit the thermal load on the cryostat. Typical experiments at the University of Innsbruck operate the Paul traps with a trap drive frequency of about 30 MHz resulting in axial modes at 1-1.5 MHz and in radial modes at 3-4 MHz [Har12, Hem14, Nig16]. The resonator built during this thesis operates at 45.4 MHz. Thus, the trap drive frequency is about 50 % higher than of other experiments in Innsbruck, and one can achieve frequencies of secular motion of up to 2 MHz axially and 6 MHz radially with $^{40}\text{Ca}^+$ at the same trap stability parameter q .

Typical magnetic field strengths of the quantization field are 3 Gauss, when working with $^{40}\text{Ca}^+$ ions. For an optical qubit, neighboring transitions have a difference in magnetic field sensitivity of about 1.7 MHz/Gauss (Figure 2.4 b). This results in a frequency splitting of about 5 MHz between neighboring Zeeman transitions for 3 Gauss. Hence, for frequencies of secular motion higher than 2.5 MHz, one has to increase the quantization field strength or otherwise the vibrational modes of two neighboring transitions will spectrally overlap. An overlap would reduce the frequency spacing between vibrational modes which would diminish the effect of increasing the frequencies of secular motion for bigger mode spacing.

One can increase the strength of the magnetic field at the position of the trap to up to 22 Gauss in the current setup without the need for external cooling of the coils. The natural limit to the motional trap frequencies is the frequency spacing to the nearest neighboring transition in the Zeeman manifold. With a quantization field of 15 Gauss, the frequency splitting between neighboring Zeeman transitions would be 25.5 MHz, which is so high that the second-order sidebands of the radial modes at (2.6 MHz =) 12 MHz would not overlap. A disadvantage of such high magnetic field strengths is that the Zeeman splitting also affects the cooling and repumping transitions. The S→P transition in $^{40}\text{Ca}^+$ has a linewidth of about 20 MHz. The Zeeman shifts on that transition in $^{40}\text{Ca}^+$ are between about ± 7 MHz at a magnetic field strength of 3 Gauss. Thus, the Zeeman shifts are smaller than the linewidth of the driven transition. However, the frequency shifts due to a quantization field of 15 Gauss are about ± 37 MHz and therefore bigger than the linewidth. This was anticipated before the optical setup was assembled. Separate frequency shifters for σ - and π -polarized light beams allow accessing each transition individually, and with the setups shown in Figure 5.3, one has enough frequency tuning range to drive each transition on resonance. The remaining problem is the frequency tuning range of

the 270 MHz AOMs in the quadrupole laser setup (Figure 5.5). To access all possible optical qubit transitions, one would require a bandwidth of about 100 MHz which is too much for these AOMs, as they only have 65 MHz bandwidth. Thus, they would have to be driven outside their recommended bandwidth and the feasibility would have to be experimentally confirmed.

Another advantage of the high frequencies of secular motion besides the higher frequency spacing between vibrational modes is that Doppler cooling allows cooling to lower vibrational states for higher frequencies of secular motion. Hence, ground state cooling starts at a lower mean phonon number with higher frequencies of secular motion.

7.2 Stabilizing the interaction field at the position of the ion

In QIP with trapped ions, gate operations can be performed with RF signals and optical signals. In order to perform high fidelity operations, the intensity and phase of the driving field have to be well defined at the ion position. RF signals are guided in coaxial cables and their wavelength is on the order of 1 m (less for hyperfine qubits and more for Zeeman qubits). Therefore, it is not hard to stabilize the field intensity and its phase at the position of the ion [WOC⁺13]. But it is challenging to localize them so that they only interact with a single ion. On the other hand, optical signals are typically guided in air or in fibers and their wavelengths are on the order of 1 μm . In the case of propagation in air, the light intensity at the position of the ion can fluctuate due to turbulence in air. Temperature drifts and acoustic vibrations affect the mirror mounts and, therefore, the optical path length will vary as well as the position and the direction of the beam. In the case of propagation in fibers, temperature and acoustics will change the optical path length as well as change the polarization at the output of the fiber. After passing through a polarizing beam splitter, the change in polarization will be converted to a change in intensity. In general, it is difficult to stabilize the intensity and phase of light fields. But due to the small wavelength, it is not difficult to localize optical signals.

This chapter will describe how one can stabilize the light intensity at the position of the ion and show a way to decrease phase drifts. In both cases, one needs to have an experiment that is mechanically stable as movement leads to phase and intensity changes in the localized light. In the characterization of the cryostat, its movement was analyzed in detail, see Chapter 4.11.2, and the observed vibrations allow further analysis with trapped ions in the cryostat without being limited by the movement of the cryostat.

7.2.1 Stabilizing the intensity of the light

To stabilize the light intensity, one can utilize the following techniques:

1. Continuous wave (CW) intensity stabilization

Although, QIP with trapped ions requires pulsed light, it proved useful to pre-stabilize the light intensity in a continuous way, which can be performed with high precision. For example in gravitational wave detection, high stability of laser intensity in CW mode is required [SKH⁺06] where relative power fluctuations can be below 10^{-7} . This is more than 4 orders of magnitude lower than the intensity stability which is required for gates with 10^{-6} infidelity (see Chapter 2.8.1).

In order to achieve this extremely high stability, they incorporate a ring cavity which filters the spatial mode and reduces high frequency intensity fluctuations, because the cavity output is proportional to the stored light intensity in the cavity which is an average over many round-trips in the cavity. In setups for gravitational wave detection, the actuator to compensate low frequency noise is an AOM which is typically used in trapped ion experiments as well. The main

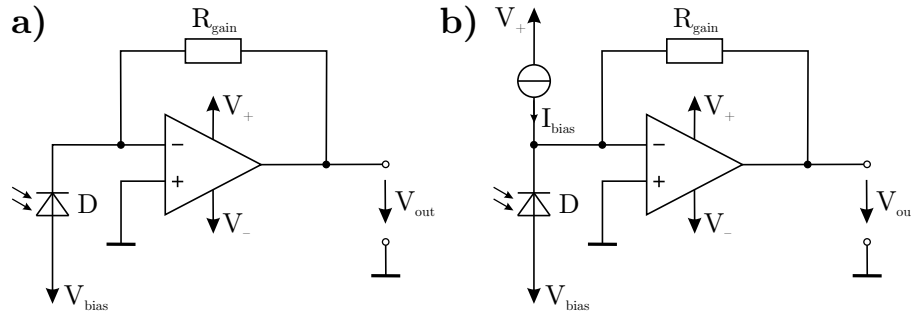


Figure 7.1.: A photodetector circuit without **a** and with **b** a bias current.

difference to trapped ion experiments is the photodetector. Typically, the output of a standard transimpedance amplifier, as depicted in Figure 7.1 a, either saturates at low light intensities (R_{gain} high) or has low sensitivity (R_{gain} low). If the desired light intensity is constant, one can circumvent this problem by subtracting a constant bias current from a precision current source from the photo current, as shown in Figure 7.1 b. The output voltage of the transimpedance amplifier is then proportional to a relative signal allowing for high sensitivity without saturation of the circuit.

2. Pulsed intensity stabilization

Once the light is stabilized in CW with high precision, the next step is to build a pulsed intensity stabilization. There, digital systems with enough resolution are desirable as digital controllers are easier to operate in pulsed mode than analog ones.

In the recent years, a hardware project called Red Pitaya¹ provided a suitable platform for controllers enabling quantum optics experiments. Its hardware is controlled by an FPGA and contains two 14-bit analog-to-digital converters (ADCs) with 125 MSamples/s for analog data acquisition, and two 14-bit DACs with 125 MSamples/s as analog outputs. 14 bits allow a precision of $1/16384$ which should enable intensity stabilization with relative fluctuations smaller than 10^{-3} . As light pulses in trapped ion experiments are on the order of $10 \mu\text{s}$, the high sampling rate of the Red Pitaya allows fast data acquisition which enables the stabilization of the pulse area of individual light pulses.

3. Characterize beam pointing instability

Beam pointing instability is a term for undesired beam displacements in optical setups. It can be caused by thermal effects in crystals (like AOMs), acoustics coupling to mirror mounts, or turbulence in air. When the intensity of the pulsed light is stabilized, one needs to ensure that gate operations are not limited by beam pointing instability. Then, one can perform experiments, which are sensitive to the spatial position of the beam, to detect beam pointing instabilities. Such an experiment could be a $\pi/2$ -pulse with a resonant addressing beam where the position of the addressed ion in the trap is at the steepest slope of the intensity profile of the addressing beam along the trap axis. A drift of the excitation probability in such experiments corresponds to beam pointing instability.

4. Stabilize beam position

If the analysis of the beam pointing instability shows that acoustics are the main source of infidelity, one has to shield the experiment acoustically. In this case, it is important to find a solution for shielding active components like AOMs from acoustics while maintaining sufficient cooling.

¹<http://redpitaya.com>

If the analysis of the beam pointing instability shows that slow thermal drifts limit the experiment, one can mount quadrant photodiodes rigidly to the vacuum chamber, as depicted in Figure 7.2. Since these are mounted such that they do not move (significantly for the required precision) with respect to the trap, one can detect drifts with these diodes. To stabilize the beam position, piezo actuated mirror mounts direct the incident beams to the desired position at the quadrant photodiodes, and by this, aim the beams onto the desired position along the trap axis. Turbulence in air might lead to a beam displacement during the sampling phase of the sample and hold controller, which stabilizes the beam position. Therefore, it is beneficial to perform this stabilization with a digital PI controller with which one can average the beam position over many light pulses and calculate the new actuator positions from these averaged values.

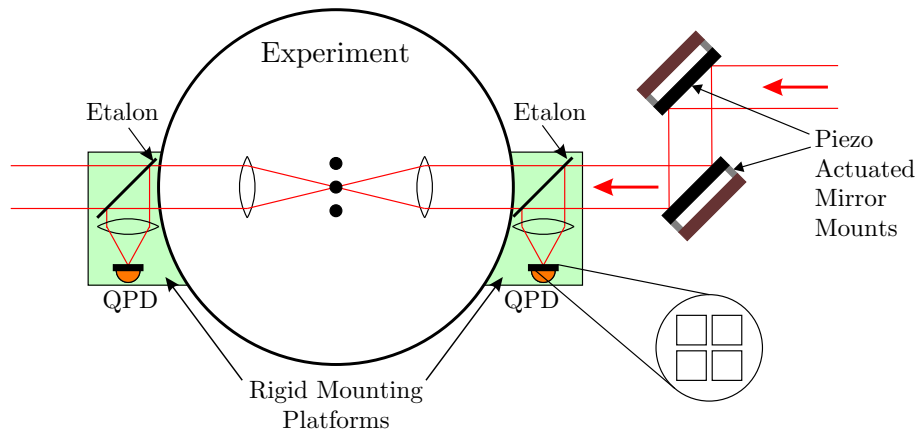


Figure 7.2.: Optical beam path stabilization with quadrant photo diodes (QPDs) and piezo actuated mirror mounts.

7.2.2 Decreasing phase drifts of the light at the position of the ion

The measurements of the vibrations in Chapter 4.11.2 showed that the beam length fluctuations on an optical table over milliseconds are in the percent level of the wavelength of optical qubits (Figure 4.31 b). To avoid decoherence of optical qubits due to this movement, one must try to minimize these vibrations. This can be achieved with a technique that is similar to a fiber noise cancelation (FNC) setup as a FNC setup stabilizes the phase in fibers. After each single pass or double pass setup, one would have to reflect a fraction of the light back and beat it with the light entering this part of the optical setup to stabilize the phase at its output.

However, this cannot be applied to pulsed light in a straightforward way. When the qubit light is switched off, no other light can pass through the setup to stabilize the optical beam length. To stabilize the phase in the setup after the pulsing optics, one needs to add two additional FNC setups per beam to stabilize the phase. The first setup, shown in red in Figure 7.3, stabilizes the phase of the CW light on its way to the experiment. The second FNC setup, shown in blue in Figure 7.3, cancels the phase noise in the fiber. As the pulsed light has to pass through the second FNC setup on its way to the experiment, phase noise of the pulsed light generated in the fiber is canceled as well. Phase stabilization with such a setup causes a frequency shift compared to a setup without the additional FNC setup which needs to be considered. Another way to minimize the effect of acoustics in the fiber on the phase of the light is to use hollow core photonic crystal fibers, which can have a refractive index close to 1. However, phase drifts due to thermal drifts will still be present.

For phase drifts of the setup that pulses the light, there is no easy way to minimize phase

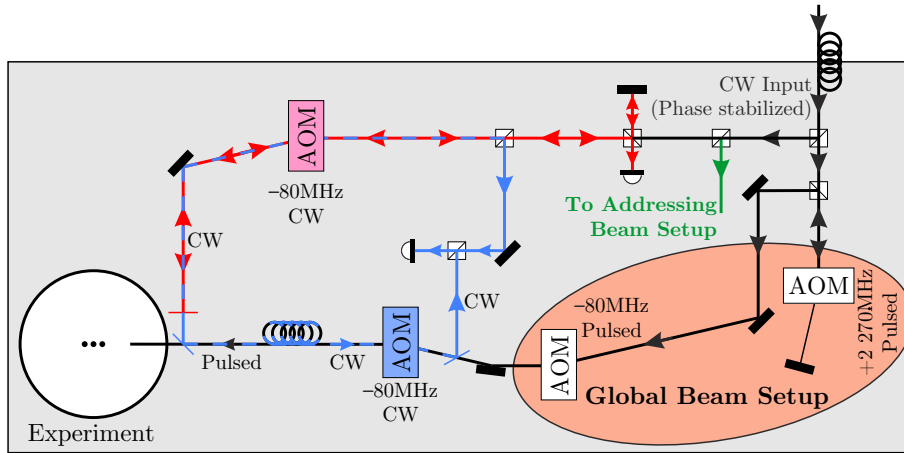


Figure 7.3.: Suggested setup to compensate for phase change induced by the last fiber in front of the chamber in the 729 nm setup of the global beam setup.

drifts due to acoustic or thermal effects. There, one has to make sure that the optical setup is thermally stabilized and acoustically shielded as well as possible.

7.3 Reduce the time of an experimental cycle

As depicted in Figure 6.3, one experimental cycle of a trapped ion quantum computation experiment consists of state reset, Doppler cooling, optical pumping, sideband cooling, the quantum algorithm to execute and measurement. A typical value for the state initialization (cooling and optical pumping) is about 10 ms. Most quantum algorithms are shorter than 1 ms with some exceptions which can last several milliseconds [JLH⁺14]. Detection of multiple ions is performed with an EMCCD camera which requires detection times of 8-10 ms for a collection efficiency of about 1 % and is similar to cooling. In total one experimental cycle lasts about 20 ms of which only 1 ms is used for the quantum algorithm itself. The rest is used for cooling, initialization, and detection. In the following, a couple of suggestions will be made how one can speed up a single measurement to increase the number of measurements that can be performed in a certain period of time.

7.3.1 Implement EIT cooling

One can shorten the time of ground state cooling by using EIT cooling instead of sideband cooling. Since EIT cooling can be performed on a dipole transition, it is faster than sideband cooling on the quadrupole transition. Furthermore, EIT cooling cools multiple modes which means that the modes of a whole frequency range are cooled instead of a single mode.

In the setup depicted in Figure 5.3 a, two double pass setups are placed in series which results in a frequency shift of four times the applied RF signal. The AOMs used in the Ca setup² have a bandwidth of 40 MHz. Thus, it is possible to shift the 397 nm laser light by up to 160 MHz which is sufficient for EIT cooling which is typically performed 80-100 MHz blue of the transition. The AOMs used in the Sr setup³ only have 10 MHz tuning range which is not enough to implement EIT cooling. Hence, EIT cooling of Sr will require changes in the optical setup.

²Brimrose QZF-80-40-397

³Brimrose TEM-80-10-422

7.3.2 Replacing the camera with multiple PMTs

Another part of an experimental cycle that can be shortened is detection. The required time for state detection can be decreased by employing optics with higher collection efficiencies which result in higher count rates. PMTs have lower dark count rates than EMCCD cameras, resulting in typical detection times with $NA \sim 0.2$ detection optics of around 10 ms with an EMCCD camera and less than 1 ms with a PMT.

EMCCD cameras do not allow for time-resolved detection⁴, whereas PMTs produce a digital signal for each detected photon. With time-resolved detection techniques [MSW⁺08, Bur10], one can reduce the detection time even further with PMTs. For example, one problem of high-fidelity state detection of trapped ions is spontaneous decay of the electron in the D-state. With time-resolved detection, one obtains the additional information of the arrival times of the detected photons. If the count rate is low at the beginning of the measurement but high at the end, it is likely that the electron decayed from the D-state to the S-state during the measurement. Thus, the correct state to obtain would be a D-state.

The problem with PMTs is that they are bulky and it is hard to image one ion of a string onto just one PMT. Therefore, PMTs are typically used to detect the collective fluorescence of entire ion chains [SNM⁺13]. Recently, multiple research groups have started to image ion strings onto PMT arrays [DLF⁺16] which brings along two problems. First, the ions in a chain are not equidistant in a normal harmonic potential but the distances between neighboring PMTs in the array are. Therefore, the ion string has to be transferred into an anharmonic potential with equidistant ion spacing for detection. Second, the distances between individual PMTs in a PMT array are on the order of 1 mm. Hence, for ion distances of 4-5 μm , high magnification of greater than 100 is required which usually generates aberrations. These aberrations will then result in optical cross-talk between neighboring PMTs of the PMT array.

One suggestion to circumvent these two problems is to use micro-mirrors onto which the photons emitted by the ions are directed, as depicted in Figure 7.4 a and b. The distance of the micro-mirrors can be adjusted to mimic the ion spacing in the trap. The disadvantage is that this has to be optimized for a certain number of ions. Hence, one will have to split longer ion chains to detected substrings of ions separately with this scheme.

Another idea is to use a fiber array with multimode fibers instead of an array of micro-mirrors [KK09]. The spacing between fibers can be chosen arbitrarily, and the outputs of the fibers can then be directed at separate PMTs. A picture of such a fiber array is shown in Figure 7.4 c.

If it is possible to reliably detect the quantum states of ions in a string in much less than 1 ms, the total number of scattered photons will only be on the order of 1000 to 10000. It is expected to be sufficient to only EIT cool the ion string after detection. This would vastly shorten the duration of one measurement. Cooling and detection might be feasible in less than 1 ms, compared to the current ≈ 20 ms. As typical quantum algorithms have about 1 ms duration, the time of one experimental cycle could be speeded up by a factor of 10 or more.

⁴Streak cameras perform time-resolved detection, but there, the problem is the real-time read-out during one measurement cycle which is required for feed-forward during a measurement cycle, e.g. used in reference [MNM⁺16].

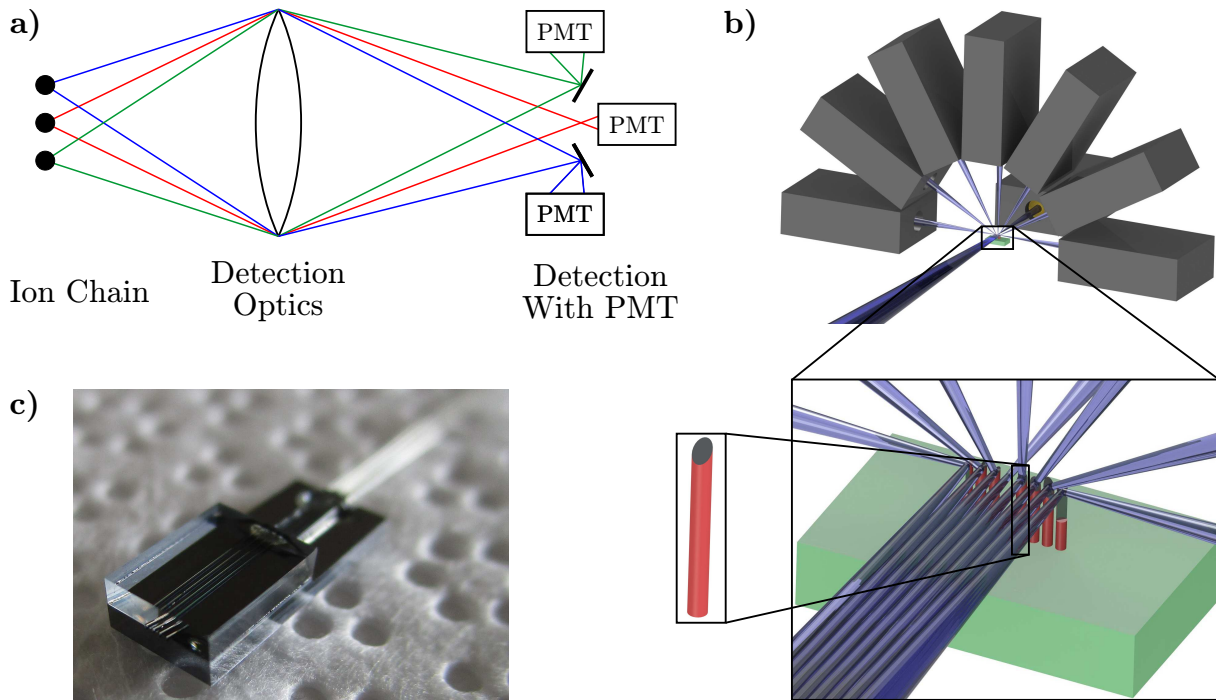


Figure 7.4.: Panel **a** and **b** show how one can detect the state of multiple ions with PMTs. Panel **b**, the detection beam of each ion of an ion string of 8 ions is directed at a micro-mirror which reflects the beams onto dedicated PMTs for each ion. Panel **c** illustrates a picture of a fiber array, which can be used as an alternative to the array of micro-mirrors.

7.3.3 Addressing

Addressing a single ion is performed with a single focused laser beam. In existing experiments, a single ion is addressed by switching the voltage at an electro-optical deflector (EOD) which deflects the beam onto the desired ion [SNM⁺13]. The disadvantages of this addressing scheme are that one can only address one ion at a time and that the voltage change at the EOD takes up to 30 μs for reliable addressing. Hence, if a quantum algorithm contains groups of single qubit operations, one has to add idle times between light pulses for addressing which leads to long idle times in the quantum algorithm. During these wait times, the qubits are subject to decoherence. Hence, faster addressing will lead to less decoherence in quantum algorithms.

One way to speed up addressing is to move the ion string instead of the laser beam. At the University of Mainz, ion movement of 280 μm in 3.6 μs have been demonstrated [WZR⁺12] with the same type of FPGA-based arbitrary waveform generator used in this setup, mentioned in Chapter 5.2.2. Thus, it should be possible to move ion strings tens of μm in less than 3 μs , corresponding to a shortening of the idle time by a factor of (at least) 10.

Another way to speed up addressing is to use an individual laser beam per ion such that multiple ions can be addressed simultaneously. As this requires an optical beam path (with switching capabilities and so on) for each ion, one cannot work with arbitrarily long ion chains, and one has to form substrings of ions. Such a setup was implemented at the University of Maryland [DLF⁺16]. In their setup, they split a continuous wave beam into multiple beams which are modulated in a multi-channel AOM. The output of each channel of the AOM is mapped onto an ion in the trap. This is an elegant solution. However, a disadvantage is that the different channels of the multi-channel AOMs have typically a cross-talk of about 30 dB.

To decrease optical cross-talk between neighboring laser beams in such multi-beam addressing schemes, one can image the light coming from a fiber array onto an ion string, where each

fiber has its individual AOM for phase-coherent switching. Standard single mode fibers have a cladding diameter of $125\ \mu\text{m}$ and $\text{NA}\approx 0.12$. Even if neighboring fibers in a fiber array touch each other, one will need a magnification of $1/25$. In order to maintain a small spot size, one would require $\text{NA}>0.9$ close to the ion string. Since such high NA is typically undesirable, because it restricts other optical access, one has to find fiber arrays with smaller core spacings. Such fiber arrays are commercially available with only $20\ \mu\text{m}$ spacing between neighboring fibers⁵. But these fibers are not single mode for the wavelength regime used in trapped ion experiments, $\sim 700\ \text{nm}$ for the transitions in optical qubits and $\sim 400\ \text{nm}$ for Raman transitions with Zeeman qubits.

It is possible to change the refractive index of glass by locally melting it with an ultra-short light pulse [DMSH96]. This led to new technology which enables "writing" optical waveguides into glass. Such wave guides can be structured arbitrarily. Hence, one can replace a fiber-array, as described in the previous paragraph, with such a wave guide.

Furthermore, one can reverse the idea of detection with micro mirrors by sending multiple light beams at such an array which directs the different light beams onto the respective ions in a Paul trap. In this approach, one can use either a fixed array, similar to the one shown in Figure 7.4, or one can use microelectromechanical systems (MEMS) mirror arrays. A single MEMS mirror has already been used for trapped ion experiments [KKLK07]. MEMS mirror arrays have the advantage of tunability over fixed mirrors, and that one is not limited to one specific number of ions. A fixed array has the advantage that it is easier to manufacture and can have higher mechanical stability. Furthermore, fixed mirrors can be aligned in more than just a straight line. For example, if one wants to address ions in different focal planes, one can add depth to the mirror structure to minimize aberrations.

7.4 Work with Zeeman qubits

The restrictions on phase stability, described in Chapter 2.8.2, show that the phase of the interaction field has to be better stabilized than 10^{-3} of the wavelength at the position of the ion to allow for gate infidelities below 10^{-4} . For optical qubits, the interaction field has a wavelength of about $1\ \mu\text{m}$. To obtain the desired phase stability, the optical path length must not fluctuate by more than $1\ \text{nm}$.

Figure 4.31 b depicts the mean vibrations over a given time interval. At time intervals of about $1\ \text{ms}$, the mean observed peak-to-peak vibrations are about $3\ \text{nm}$. The lengths of the two arms of this interferometer are about a factor of 10 shorter than the optical path length of the $729\ \text{nm}$ laser in the experiment. Hence, it seems that without active path length stabilization, the desired phase stability cannot be reached. As mentioned in Chapter 7.2.2, a continuous phase stabilization is possible, but a pulsed stabilization is technologically challenging.

One way to circumvent the tight restrictions on the optical beam path is to use Zeeman qubits instead of optical qubits. There, the wavelength is about 10^7 times longer. Thus, the maximally allowed beam path fluctuation shifts from $1\ \text{nm}$ to $10\ \text{mm}$.

Besides a lower spatial dependence of the phase of the interaction field, the Zeeman qubit offers independence from the laser driving the transition. The physical limit to the coherence time of the optical qubit is the lifetime of the D-state, $1.2\ \text{s}$ for $^{40}\text{Ca}^+$ [BDL+00] and $0.4\ \text{s}$ for $^{88}\text{Sr}^+$ [LWGS05], whereas Zeeman qubits do not have such a physical limit. Furthermore, RF sources in the frequency regime of the Zeeman qubit transition frequency of about $10\ \text{MHz}$ have much lower linewidth and phase noise as lasers driving quadrupole transitions. Additionally, Zeeman

⁵<http://www.chiralphotonics.com>

qubits do not experience quadrupole shifts [Ita00]. This insensitivity in combination with an improved frequency and phase stability of RF fields over laser fields results in longer coherence times [RSK⁺16]. When storing quantum information, the main contribution to decoherence in Zeeman qubits is magnetic field fluctuations during idle times.

Working with Zeeman qubits instead of optical qubits will require changes in the way gates are performed or changes in the beam geometries. In the current setup, the lenses inside vacuum are used for addressing of individual ions with the quadrupole laser and for detection, see Chapter 4.3. The fluorescence of the ions is reflected to the detection optics on the lower level of the optical table (Figure 5.6) with a dichroic mirror which transmits the light of the quadrupole laser. If one uses Raman transitions to manipulate Zeeman qubits, it will not be possible to use a dichroic mirror to separate the qubit laser light for single ion addressing from fluorescence light from the ions for detection.

There are several ideas how to circumvent this addressing problem. One idea how to address single ions in microwave fields is shown in reference [WOC⁺13], which would require a different electrode structure and would, thus, imply a new trap. Another idea is to use Raman beams which cover the whole ion string. Shuttling of ions into and out of a so called processing zone [KMW02] allows ion movement in a way that only ions which have to interact with the Raman light are in the processing zone. Such an approach will require a lot of ion movement, ion string combination, splitting, and reconfiguration.

Another option for QIP is a hybrid scheme between optical and Zeeman qubit. In this scheme, gates are performed by mapping the Zeeman qubit into an optical qubit with an electron shelving pulse. Since such gates happen on the order of 10 μ s which is faster than acoustics causing spatial decoherence, and faster than possible magnetic field changes in the inner heat shield, see Figure 4.26, the qubits will not be subject to decoherence on such short time scales. Over longer time scales, the mentioned sources of decoherence matter and the quantum information has to be stored in Zeeman qubits by mapping the optical qubit back into the ground state.

If none of the options mentioned above performs well enough for fault-tolerant QC with trapped ions, one will have to adapt the beam geometry. There, one requires high optical access from multiple different directions for addressing and detection with blue laser light. If one has high optical access parallel to the trap surface, one can perform single ion addressing along this direction and use the direction perpendicular to the trap surface for detection, as implemented in reference [DLF⁺16].

7.5 High-fidelity global RF gates

Currently, the lowest infidelity of single qubit gates with trapped ions is performed with global RF gates [HAB⁺14] for which RF signals drive transitions in the ground state of $^{43}\text{Ca}^+$ ions. As mentioned in Chapter 4.10, additional SMT cables are added to apply RF signals to the central electrode. This allows global RF gates in the ground state of the $^{40}\text{Ca}^+$ ions in this setup and one can try to reduce the achievable infidelity with trapped ions even further.

7.6 Measurement of the coherence time

When used as storage for quantum information, optical qubits are subject to decoherence caused by magnetic field fluctuations, laser frequency fluctuations, spontaneous decay, mechanical movement, quadrupole shifts and other higher order shifts. Whereas, qubits in the ground state only

experience decoherence due to magnetic field fluctuations⁶ as mechanical movement can be neglected due to the long wavelength of the interaction field of ground state qubits and frequency sources in the RF regime have sufficiently low bandwidth and low phase noise to not affect the qubit's coherence. Therefore, Zeeman qubits are much better candidates for a quantum memory than optical qubits. In Chapter 4.11.1, the magnetic shielding of the inner heat shield was measured. Along the magnetic field axis, the bound for the attenuation of 50 Hz magnetic fields is 120 dB. Even at a frequency of 1 Hz, the attenuation of 50 Hz magnetic fields along the axis was still 35 dB. Hence, one can expect coherence times longer than 1 s with Zeeman qubits in this setup.

In order to increase the coherence time of a two-level system, one can use a decoherence free subspace [ZR97], in which symmetry properties of a logical qubit consisting of two ions protect against decoherence [MKV⁺09]. The disadvantage of this technique is that it requires the manipulation of logical qubits which is usually laborious. Another way to extend the coherence time is employing spin echo pulses [Hah50] for which the spin of a qubit is repetitively flipped to decouple it from its environment. The magnetic attenuation due to skin effect in the inner heat shield of the cryostat increases exponentially with frequency (Figure 4.26). To decouple the ions from low-frequency noise, a repetition rate of the spin echo pulses has to be a fraction of the coherence time without spin echo pulses which is expected to be longer than 1 s. In combination with high-fidelity RF gates, these spin echo pulses will result in coherence times of minutes or even hours.

Besides efficient quantum storage, one may want to perform quantum algorithms during the expected coherence time of more than 1 s in the future. Although spin echo pulses protect against decoherence, they do not protect against infidelity for example due to not being resonant to the qubit when slow frequency magnetic fields shift the resonant frequency of the two-level system. Such frequency shifts can be caused by the thermal drift of the set point of the current driver of the magnet field coils or changes in earth's magnetic field [Jac91], and their effect can be suppressed by interleaving the quantum measurements with calibration measurements [Chw09]. Another option to suppress such errors during a quantum algorithm is to employ dynamical decoupling [VL98] instead of simple spin echo pulses.

An environmental influence that should not be neglected is people. The vibration measurements of Chapter 4.11.2 have shown that if someone moved in the lab during the measurements, the vibrations amplitudes would be about a factor of 10 higher than if no one moved. If someone carries a magnet and walks by the experiment, the magnetic field change will be too rapid to compensate with interleaved calibration measurements. Given that the experiment is set up right next to a hall way and a public toilet of the university, one must not underestimate the influence of such an environment. A possible solution to decouple the laboratory from the environment is to enclose the room in a ferromagnetic material, as described in reference [Hil70]. This material will strongly attenuate local magnetic fields caused by someone carrying a magnet and it can be used to mechanically decouple the lab from the building such that acoustic noise and other mechanical vibrations created outside of the lab are dampened inside the lab. Ideally, the experimental control computer is not placed inside the lab but outside so that no one has to be present in the lab when the experiments are performed.

To extend the coherence time of an ion species in a multi-species experiment, one can use one species as sensors and sense perturbations in the phase evolution. If the measured perturbations are global, the obtained information from one species can be fed forward onto ions of another species to extend the coherence time of this second species. The expected coherence time of more than 1 s of a Zeeman qubit in the setup built in this thesis should be long enough to obtain information of the phase evolution in one ion species. Since a single magnetic field measurement

⁶ During gate operations on ground state qubits, infidelities can be caused by light shifts, off-resonant excitations, not being resonant to the energy splitting of the two levels.

process will typically take only a fraction of a second, one can only track phase evolutions that are slower than this. Due to the strong attenuation of magnetic field noise for frequencies of more than 3 Hz, this should be fulfilled. Since all Zeeman qubits have the same magnetic field sensitivity, it does not matter whether $^{40}\text{Ca}^+$ ions are used for sensing and the phase evolution of $^{88}\text{Sr}^+$ ions should be extended, or vice versa.

7.7 Suggestions for experimental improvements in future setups

The mount structure of the cryostat (Figure 4.18) holds the inner heat shield only from the top. This is not ideal, as such a single-sided mount represents a cantilever or a pendulum which shows strong resonant behavior. To increase the mechanical stability, one should design mounts which support the inner heat shield from two opposing sides. One idea could be to use spokes which mechanically tighten as the cryostat is cooled down.

One thing that proved impractical during the assembly of the cryostat was the size of the inner heat shield. Modern experiments require control over as many DC segments as possible. In the current design, even the trap, the 21 DC connections, 4 RF connections, 2 lenses, and the resonator in the inner shield barely fit inside the inner heat shield. The size of the inner heat shield is ultimately limited by the size of the vacuum chamber. The chosen CF160 flange of the vacuum chamber resulted in an inner diameter of the inner shield of about 100 mm. Using a CF200 flange would increase the diameter by 40 mm resulting in nearly double the volume in the inner heat shield while maintaining the same height of the inner heat shield.

More volume for the inner heat shield also means that one can design thicker walls than the current 20 mm, which will result in higher attenuation of magnetic field noise. In the design, one has to pay close attention to the weight. A cylindrical inner heat shield with 30 cm outer diameter and 30 cm outer height with 5 cm thick copper walls weighs about 134 kg. Such big weight would have to be lifted with a crane that would have to be installed in the lab. Moreover, ultra-pure aluminum has similar electrical conductivity than ultra-pure copper, and a cylindrical inner heat shield of the same dimensions, but made out of aluminum instead of copper, only weighs about 40 kg. This comes at the expense that aluminum is even softer than copper and, thus, even harder to machine.

If there is enough space for in-vacuum coils, one should try to incorporate superconducting coils into the setup. They stabilize the flux through them resulting in a perfectly stable magnetic field [WLG⁺10]. This will eliminate the dependence on thermal drifts of the set point of the current driver of the coils.

8 Summary

The goal of this thesis was to investigate scalability of trapped ion quantum computation. For this purpose, a new laboratory was set up that contains an ion trap, a laser system for the operation with two ion species ($^{40}\text{Ca}^+$ and $^{88}\text{Sr}^+$), and a new electronic control system.

Scalability dictated the incorporation of a segmented Paul trap, which enables ion movement in a 2D-plane. The integrated planar ion trap was developed at the University of California Berkeley. To provide high optical access, which is required for state manipulation in a single ion of an ion string, the trap contains a slot. The beam geometry was chosen such that all beams, except for a global beam along the trap axis, have to pass through the slot and the high NA beams for addressing and detection are perpendicular to the trap surface.

In order to reduce the heating rate, the trap was placed inside a cryogenic setup. Because of the high magnetic sensitivity of optical qubits, shielding against magnetic field noise is necessary to obtain coherence times on the order of 100 ms. The walls of the inner heat shield are used as magnetic shields exploiting skin effect to repel time varying magnetic fields. The main magnetic field noise in the lab is due to the power lines and thus has a frequency of 50 Hz. For temperatures below the boiling point of liquid nitrogen, the attenuation for 50 Hz magnetic fields exceeded the measurement capabilities of about 60 dB. However, a lower bound for the attenuation could be determined, which yields an attenuation of 120 dB for 50 Hz magnetic signals, when the temperature of the inner heat shield is below 20 K. With this attenuation, the trapped ion qubits are decoupled from ambient alternating magnetic fields which are typically in the low milli-Gauss regime in typical laboratory environments. Slow magnetic field drifts in the bias magnetic field or changes in earth's magnetic field will still affect the qubits inside the inner shield. However in the future, dynamical decoupling sequences with a periodicity faster than the frequencies, that can penetrate the inner shield, will be able to decouple the experiments from these low frequency magnetic field drifts. Additional calibration measurements between quantum information experiments can be introduced to infer the qubit transition frequencies.

To maintain the magnetic shielding while providing high optical access to the ions in the trap, two lenses were placed inside the inner heat shield. Each lens provides a numerical aperture of about 0.2 and requires a hole of only 12 mm diameter in the inner heat shield. During this thesis, cryogenic resonators for the generation of high RF voltages required for the operation of Paul traps were designed and successfully incorporated in the cryogenic setup. An efficient method to match the impedance of such a resonator was developed, which facilitated the operation of the resonator in the inner heat shield.

As the transition wavelengths of optical qubits are about $1\ \mu\text{m}$, these qubits are very sensitive to length changes of the beam path between the laser source and the ions in the trap. Therefore, vibration isolation was incorporated in the cryostat, yielding vibrations of $\pm 20\ \text{nm}$ over 2 s. Further measurements showed that on time scales of typical quantum algorithms (1-3 ms), the vibrations in the optical setup are not limited by movement of the cryostat but by acoustics coupling into the optical assembly outside of it.

In addition to the cryostat, laser setups required for the operation with $^{40}\text{Ca}^+$ and $^{88}\text{Sr}^+$ ions were installed. In combination with the new electronic setup, the setup could be characterized using single $^{40}\text{Ca}^+$ ions. The detection and addressing optics were characterized and Rabi flops were recorded. The measured heating rate of the trap was 2.14(16) phonons/s and the coherence time was measured with Ramsey spectroscopy. The obtained Ramsey contrast displayed a Gaussian decay with a 1/e-time of 18.2(8) ms.

These measurements and the characterization of the magnetic shielding and the vibrations in the system in combination with a segmented surface trap show the potential of this setup to perform high fidelity quantum computation and quantum simulation experiments. Detailed suggestions on how to further improve the setup were given. These suggestions include a setup to stabilize the light intensity and phase during the measurements as well as ideas on how to speed up quantum information processing. Furthermore, ideas for future measurements with this setup were given.

A Appendix

In the appendix, several suggestions to improve trapped ion experiments will be discussed. These ideas are not restricted to cryogenic setups but can be applied to room temperature experiments as well.

A.1 Suggestions for the improvements on magnetic field stability

One of the main sources of decoherence is magnetic field fluctuation. Hence, it is imperative to stabilize the magnetic field as well as possible. In Innsbruck, the newest generation of current drivers for the coils generating the quantization field was developed by Gerhard Hendl and Daniel Nigg and they have a relative stability better than $1 \cdot 10^{-6}$. All components were chosen to be low-noise and have a low sensitivity to temperature changes. Furthermore, the circuits are temperature stabilized and they do not contain a PID controller but only an analog comparator. The output of the controller is a filtered output of the comparator where the filter network behavior defines the behavior of the controller. This circuit design shows higher sensitivity to current fluctuations than a PID controller. However, there are other ways to stabilize the magnetic field with high precision which are presented in this section.

A.1.1 Low-pass filter current through coils for quantization field

Coils used to generate the quantization field in typical trapped ion experiments have a time constant $\tau = L/R$ on the order of 0.1 s, where L is the inductance of the coils and R their DC resistance. In order to measure the current through the coils, a small resistor is placed in series to the coils, see Figure A.1 a. The voltage at the resistor is proportional to the current through the coils and, thus, it can be used as the input of the current controller which sets the input voltage such that voltage at the resistor is constant. Such an RL-system driven by a voltage source is a low-pass filter for the current, and the simulated attenuation of voltage noise on the coil current is shown in Figure A.1 d, where the resistance is 12Ω and the inductance is 1 H ¹. The main source of voltage noise in the stabilization is due to the power lines and, thus, has frequency 50 Hz. In the simulation, one obtains a critical frequency of the RL low-pass filter of about 2 Hz, which results in an attenuation of 50 Hz noise of about 30 dB.

By reducing the cut-off frequency of the low-pass system, one can reach higher attenuation of current noise at frequencies of 50 Hz and higher. As depicted in Figure A.1 b, one can place a second coil in series to the first coil. This second coil does not have to be located close to the experiment. As non-magnetic materials are only required close to the experiment, one can use a ferromagnetic core which allows a much higher inductance at the same volume and the same ohmic resistance of the coil than a coil with a non-magnetic core. Values for such a coil can be 100 H and 5Ω . Simulations, which are depicted in Figure A.1 d, show that such a second coil reduces the cut-off frequency by about two orders of magnitude. The attenuation of 50 Hz voltage noise on the current in the coils is then about 70 dB.

In order to increase the attenuation of 50 Hz noise even further, one can build an LC low-pass filter, shown in Figure A.1 c. As the inductance of the LC filter, one can use the same coil as in the previous consideration with the coil in series to the Helmholtz coils. The capacitor for this filter has to be high quality and it will be difficult to get high quality capacitors with a

¹ 1 H and 12Ω are approximately the values of the Helmholtz coils design in this thesis, see Chapter 4.4.1.

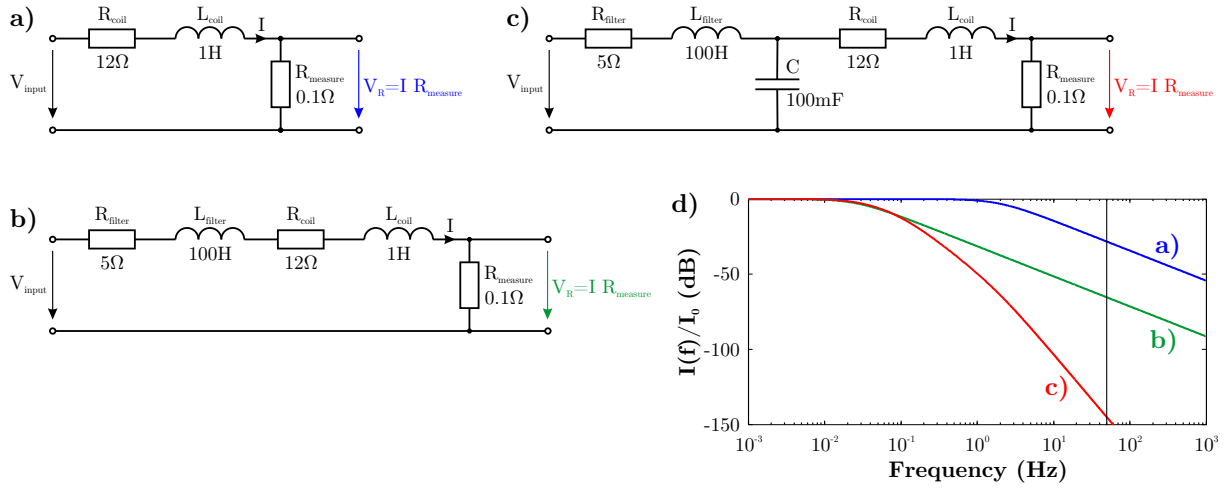


Figure A.1.: Circuits of the coils generating the magnetic field for the experiment with a resistor for current measurement **a**, with an additional coil in series **b**, and with an LC-filter in series **c**. Panel **d** displays the frequency dependence of the current through the field coils on an input voltage noise for the three circuits.

capacitance greater than 1 F which can withstand a voltage of more than 24 V that is caused by a current of 2 A through the $12\ \Omega$ resistance of the Helmholtz coils. However, capacitors of about 100 mF with a maximum voltage of 25 V are readily available. For such a circuit, the attenuation of 50 Hz voltage noise on the current in the coils is higher than 140 dB, as displayed in Figure A.1 d.

There is a limit for the filtering of voltage noise on the current in the field coils, though. If the system of coils and capacitors becomes too slow, the current controller will no longer be able to regulate the current accurately and start to oscillate.

A.1.2 Passively stabilize the magnetic field with copper

Besides low-pass filtering the current in the coils, one can low-pass filter the magnetic field as well. In the setup designed in this thesis, this is already done by using the inner heat shield as a shield against alternating magnetic fields, see Chapter 4.4.2. However, in room temperature setups, the ion trap is generally not surrounded by thick walls of highly conducting metal. In such setups, one could think of making the coil former of a thick, highly conducting material, such as copper.

The skin depth of 50 Hz in copper at room temperature is 9.22 mm which suggests thick copper formers for high attenuation of 50 Hz noise. If the field lines of the coils have to pass through 2 cm of copper, the field will be attenuated by ~ 10 dB. However, if one is only interested in coherence times of a couple of milliseconds, the walls of the former do not have to be several centimeters thick. The skin depth of 1 kHz in copper at room temperature is only 2.06 mm. Hence, if the field lines of the coils have to pass through 1 cm of copper, the field will be attenuated by 42 dB.

A.2 Shield against EM noise with a conductor around the trap

Typical secular motion frequencies in trapped ion QC experiments are between 10 kHz and 10 MHz. In this frequency regime, there are many noise sources in quantum optics labs, e.g. switching power supplies or DC-to-DC converters. This electromagnetic (EM) noise can impact

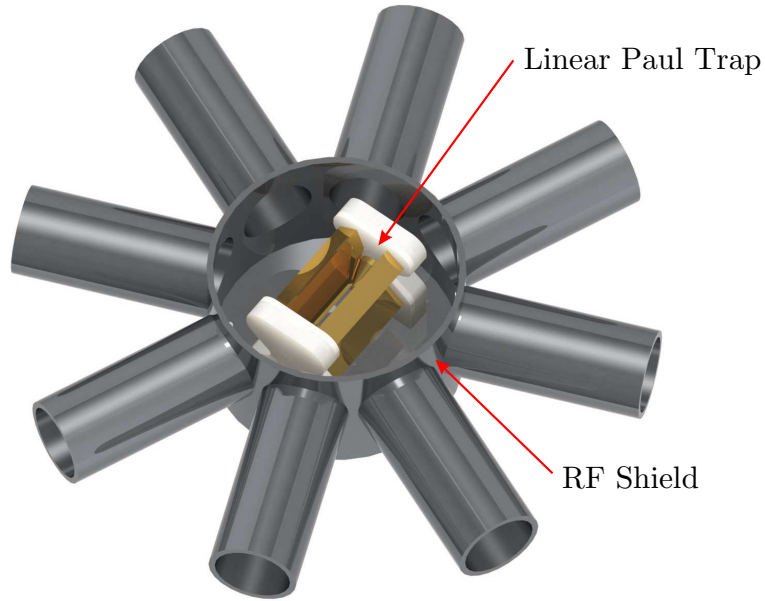


Figure A.2.: Cutaway view of an RF shield surrounding a linear Paul trap.

the heating rate of the trap by generating phonons in the ion crystals. EM waves in this regime are only weakly attenuated by walls of buildings². Hence, even if one bans all switching power supplies and DC-to-DC converters from the lab, another lab close by might cause enough noise to impact the heating rate of the trap. For low heating rates, it is, thus, necessary to shield the experiment against EM noise at the secular motion frequencies.

One way to shield the experiment against EM noise is to surround the whole vacuum chamber containing the experiment with a conductor. For example, the skin depth of 100 kHz in aluminum is about $270 \mu\text{m}$. If one places an aluminum box with 1 cm thick walls around the experiment, the 1 cm aluminum will result in about 320 dB attenuation of 100 kHz EM noise. Mu-metal shields instead of aluminum shields result in similar attenuation but shield against low frequencies EM noise of about 50 Hz as well [Mon11, Hem14]. The disadvantage is that mu-metal is expensive and heavy.

In cryogenic setups, the ion traps are placed in heat shields. These heat shields are made of a material which has high thermal conductivity and, thus, high electrical conductivity (Wiedemann-Franz law [FW53]). Therefore, the heat shields attenuate EM noise in the frequency regime between 10 kHz and 10 MHz very efficiently and no additional shielding is necessary in cryogenic setups.

If one tries to avoid building bulky metal shields around the experiment while still shielding the experiment against EM noise, one can surround only the ion trap in the vacuum chamber with a highly conducting shield. For example, an aluminum shield with 2 mm thick walls results in an attenuation of about 65 dB for 100 kHz EM noise, or about 200 dB for 1 MHz EM noise. A cutaway view of a linear Paul trap in such an aluminum shield is shown in Figure A.2. The attenuation of a conducting cylinder is proportional to $\exp(-\alpha \frac{z}{r})$, Eq. 4.5, where α is a prefactor, z is the length of the cylinder, and r its radius. Hence, in order to maintain high shielding against EM noise and to not restrict optical access, one can attach tubes to the holes in the shield, as illustrated in Figure A.2. The exact geometry of the shield is a trade-off between shielding against EM noise, optical access, and big cross-sections for efficient vacuum pumping.

² An example for this is the reception of amplitude modulation (AM) in the basement of houses with no frequency-modulation (FM) reception, as the frequency range of 10 kHz to 10 MHz contains all AM radio frequencies.

Once the experiment is shielded against radiated EM noise, one has to make sure that EM noise cannot reach the ion trap through wires inside the shield which would then transmit the noise to the experiment. This can be achieved by placing filters close to the shielding. Ideally, one will place filter stages inside as well as outside the shield.

A.3 RF voltage stabilization

When performing entangling gates with radial modes of secular motion, thermal drifts of the secular motion frequency lead to infidelity. These drifts can be caused by a change of the RF amplitude of the RF source, by a change of the gain of the RF amplifier, and by geometry changes in the resonator due to thermal expansion. An RF pick up, as described in Chapter 3.1.1.3, can be used to monitor the voltage at the trap as well as to stabilize the voltage at the trap³.

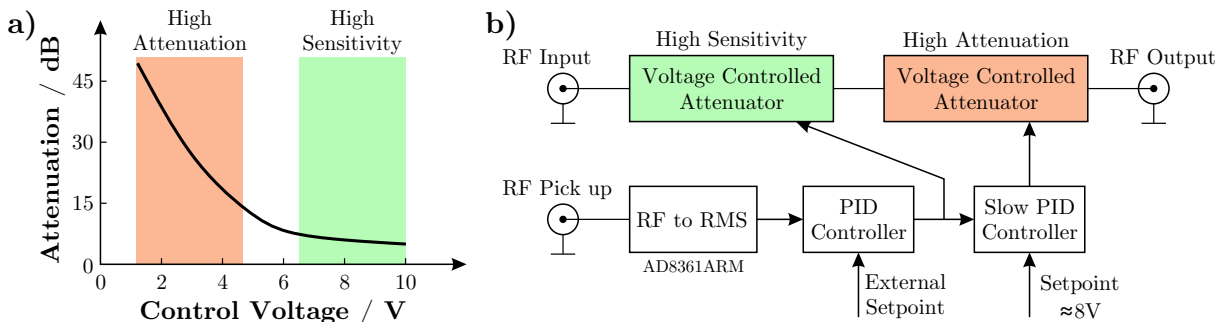


Figure A.3.: Panel a depicts a typical attenuation curve of a voltage controlled attenuator. Panel b shows a two-stage RF stabilization scheme. A fast PID controller with high sensitivity adjusts the RF voltage accurately, and a second slow PID controller makes sure that the fast PID runs in the high sensitivity regime of the voltage controlled attenuator.

The feedback on the RF amplitude can either be performed with an analog multiplexer, as demonstrated in reference [JWCR⁺16], or with a voltage controlled attenuator (VCA), as presented in the following. A typical transfer function of a VCA, illustrated in Figure A.3 a, shows a high attenuation region, in which a couple of volts change in the control voltage will lead to a change of tens of dB of attenuation, and a high sensitivity region, in which a couple of volts change in the control voltage will lead to a change of less than 1 dB of attenuation. Operation in the high attenuation region of a VCA results in a high tuning range, which is useful if someone wants to have the capability to change the set point of the PID controller by an order of magnitude or more. In the high sensitivity region, a VCA is more responsive than an analog multiplexer which allows more precise tuning. This comes at the price of a low tuning range of less than 1 dB.

To combine a high tuning range with a high sensitivity, one can choose the circuit depicted in Figure A.3 b which contains two VCAs. The RF pick up is converted to a DC voltage proportional to its amplitude. This voltage is used as the input of a fast PID controller, which has a set point that can be adjusted externally. The PID controller is operated such that its output voltage is in the high sensitivity region of the VCA that it is controlling. This results in a precise feedback on the amplitude of the RF voltage. The same output voltage of the fast PID controller is also fed into a slow PID controller which operates a second VCA in the high attenuation region and makes sure that the fast PID controller is operated in the center of the high sensitivity region.

³Since such a stabilization only regulates the voltage at the trap but the secular motion frequencies depend on electric field strength, a dependence on the trap temperature will remain, as thermal expansion changes the trap geometry.

In Innsbruck, Gerhard Hendl built a prototype with such a circuit and Cornelius Hempel tested this prototype in an experiment which had a previous RF stabilization so that the new stabilization could be compared to the old one. In order to measure the changes in the secular motion frequency, Cornelius performed motional Ramsey experiments. The principle of these measurements is illustrated in Figure A.4 a and b. Similar to normal Ramsey experiments, one starts with a $\pi/2$ -pulse on the carrier for these measurements. To map the electronic superposition to a motional superposition a π -pulse on the blue side band transition is performed. During the following idle time⁴, fluctuations in the secular motion frequency cause phase changes which can be detected with another π -pulse on the blue side band transition followed by another $\pi/2$ -pulse on the carrier. The phase of the last pulse is varied to obtain the typical dependence of the Ramsey signal on this phase. A measured phase shift of this Ramsey signal compared to an ideal Ramsey signal can be used in combination with the idle time to derive the drift of the secular motion frequency.

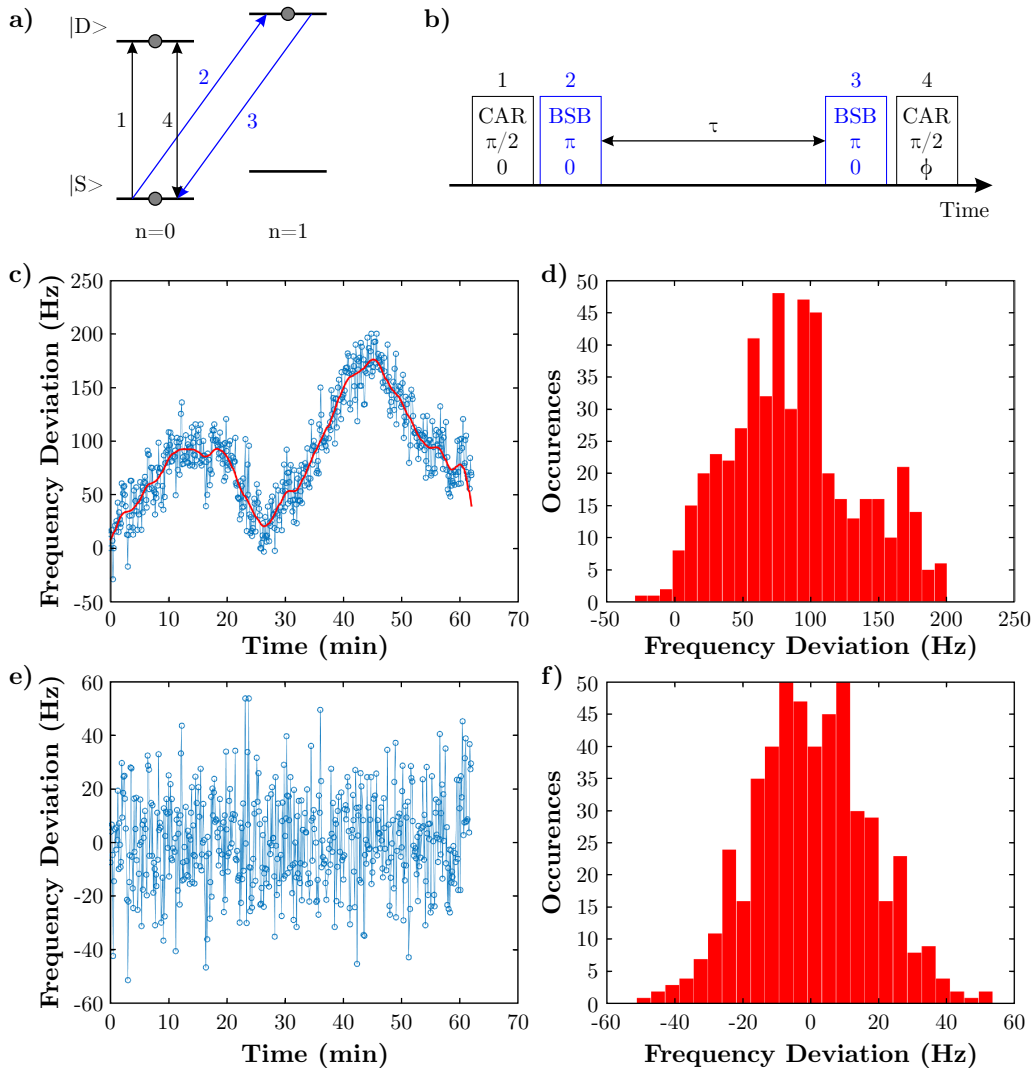


Figure A.4.: Motional Ramsey experiment. Panel a and b depict the principle of a motional Ramsey experiment. Panel c shows the drift of the radial secular motion frequency over the course of an hour measured with a Ramsey time of 1 ms. Panel d illustrates a histogram of this measurements resulting in a standard deviation of 46.7 Hz. Panel e and f show the same measurements as in Panel c and d but where the thermal drift is subtracted. This results in a standard deviation in the histogram of 17.3 Hz.

⁴In Cornelius' experiments, the Ramsey (idle) time was 1 ms.

The results of such motional Ramsey experiments over the course of one hour are shown in Figure A.4 c. A histogram of the frequency deviations is shown in Figure A.4 d and resulted in a standard deviation of 46.7 Hz for a Gaussian fit. Although all parts of the circuit are temperature stabilized, there is still a thermal drift of up to 200 Hz in these measurements. The reason for this is that the pick up used in the experiment takes 0.5 W out of the experiment's resonator when terminated with 50 Ω . This is too much power for the RF-to-RMS conversion circuit which has a maximum input power of 10 mW. Therefore, a 20 dB attenuator is placed in series to the pick up to reduce the input power at the RF-to-RMS circuit. Unfortunately, this attenuator is not thermally stabilized. Thus, one observes a drift in dependence of the lab temperature. When the drift is subtracted (Figure A.4 e), the histogram shows a standard deviation of only 17.3 Hz (Figure A.4 f). This is an improvement of more than a factor of 10 compared to the old stabilization even without fine tuning of the PID parameters.

At cryogenic temperatures, the thermal expansion coefficients of most materials approach zero [Eki06], see Figure 4.11 a. Hence, cryogenic resonators and traps are less dependent on thermal drifts than room temperature setups, and it is easier to control their secular motion frequencies accurately.

B Construction manual of the cryostat

B.1 Assembly of the inner heat shield including the trap

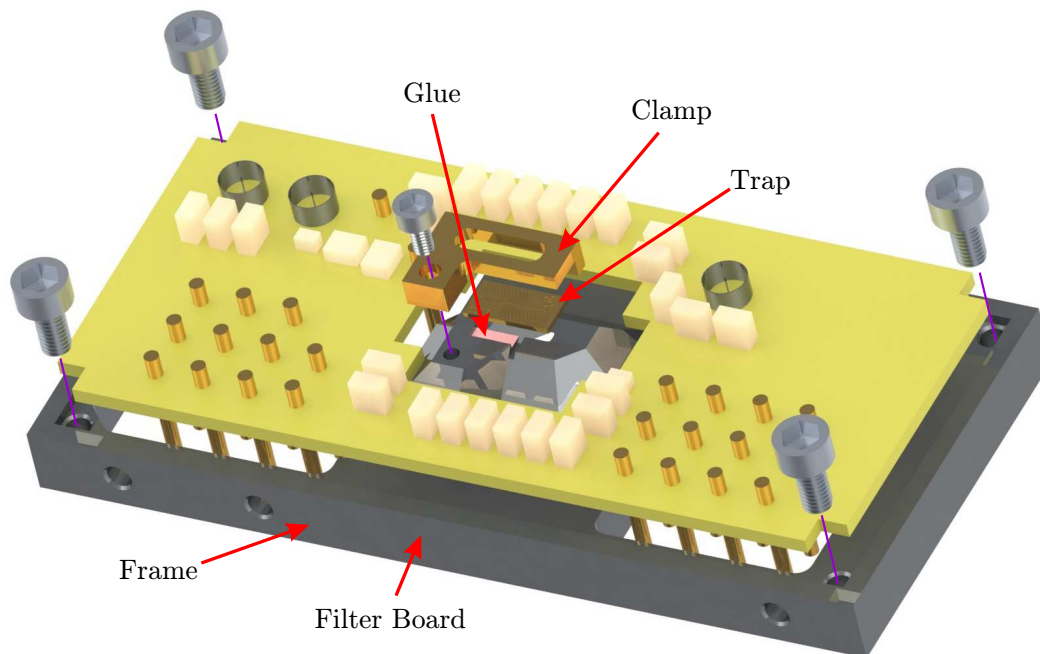


Figure B.1.: At first, the filter board is screwed to the frame with M3 screws. Then, the trap is glued to the frame (on the surface of the frame indicated in red) before the trap's segments is bonded to the filter board. After the bonding, the clamp is screwed to the frame with an M2 screw.

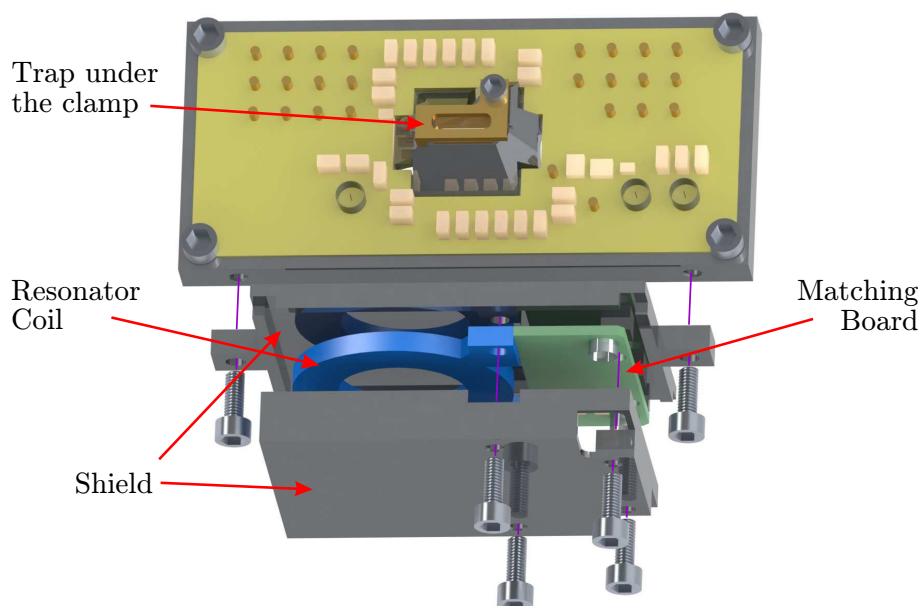


Figure B.2.: The resonator in its shield is attached to the frame, which holds the trap, with M3 screws. Then, it can be electrically connected to the filter board and thereby to the trap.

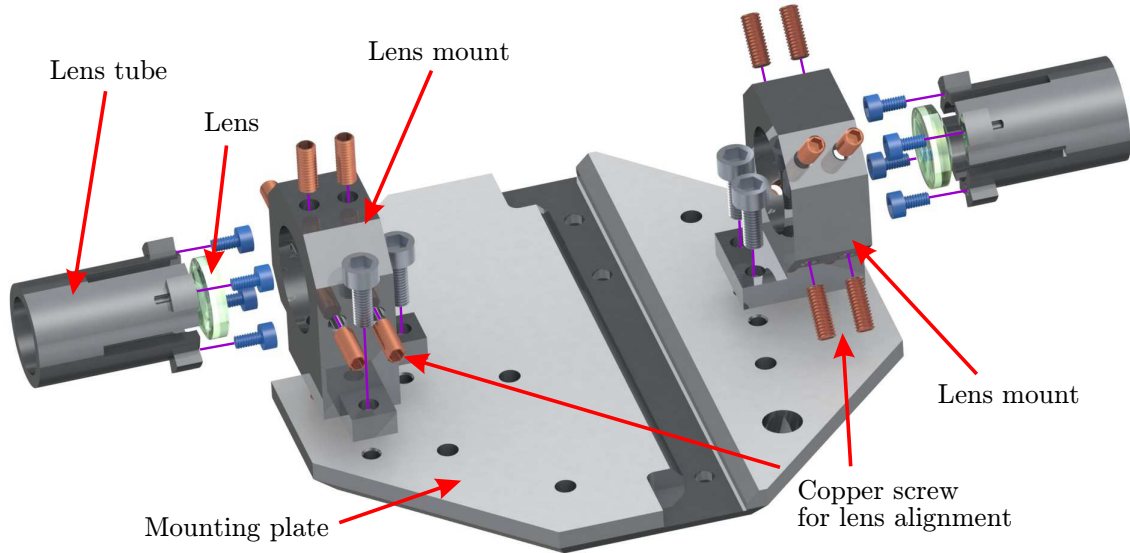


Figure B.3.: The aspheric lenses are mounted in the lens tubes and held by M2 Teflon screws. The lens tubes are placed in the lens mounts which are attached to the mounting plate. By placing optical targets in the center, where the trap will be mounted, and sending laser beams through the lenses, one can minimize the aberrations by aligning the focal points of the lenses with the aid of the head-less copper screws in the lens mounts onto the targets.

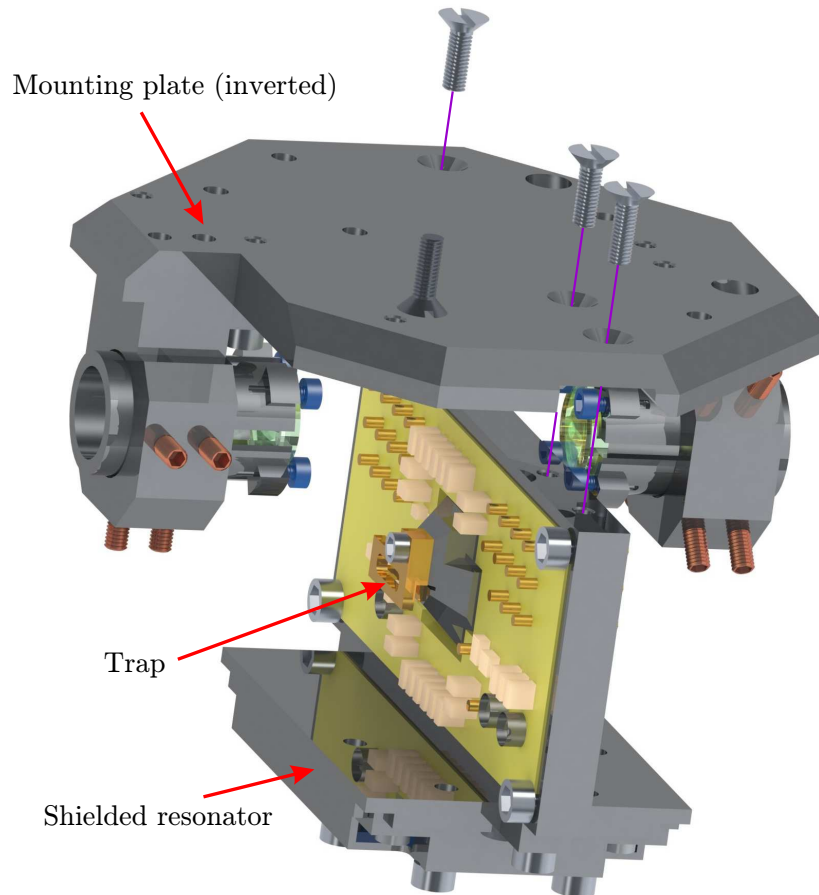


Figure B.4.: After the lens alignment, the trap with its resonator can be attached to the mounting plate of the inner heat shield.

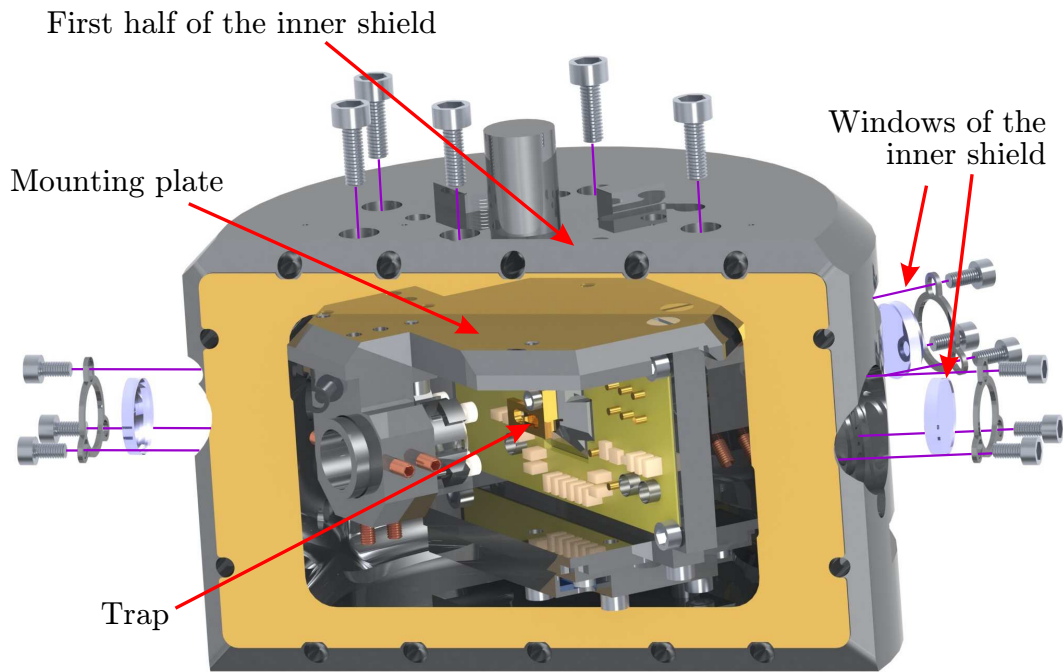


Figure B.5.: The assembled trap on the mounting plate is placed in the first half of the inner shield where it is held by M4 screws. During this step, the wiring for the DC segments has to be attached to the filter board (not depicted). Then, the five windows of the first half of the inner shield are attached.

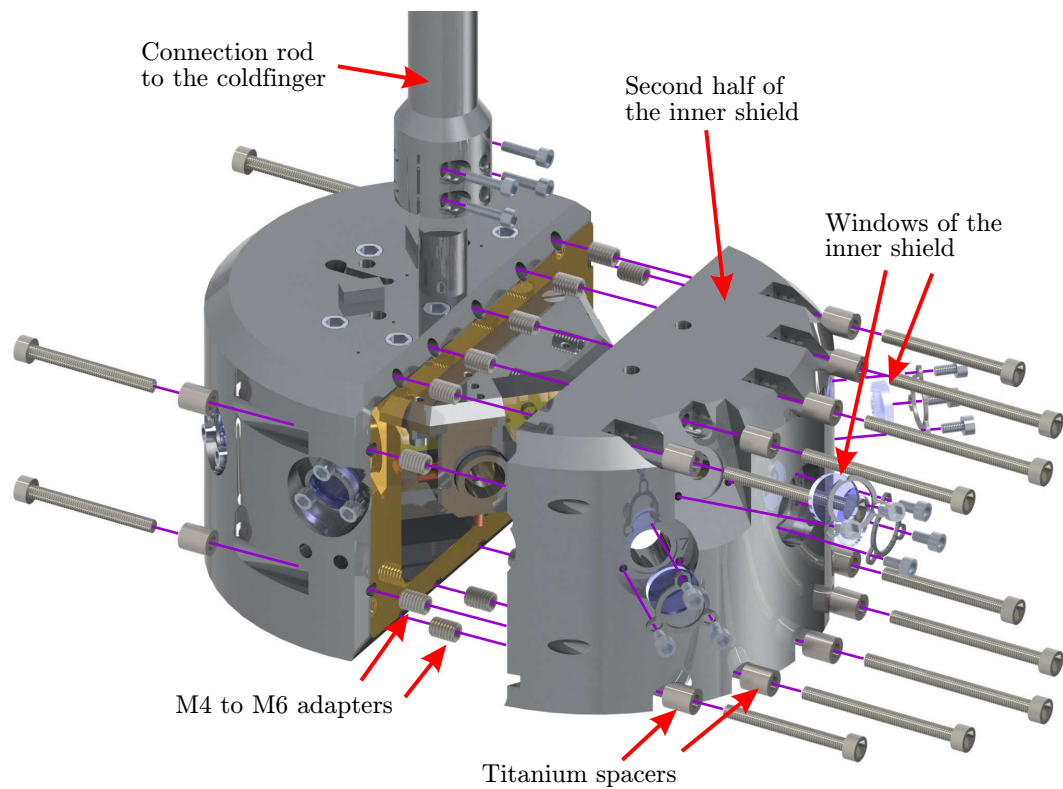


Figure B.6.: After the second half is attached with the aid of M4 screws, M4-to-M6 adapters and titanium spacers, the remaining four windows are mounted as well as the connection rod to the coldfinger.

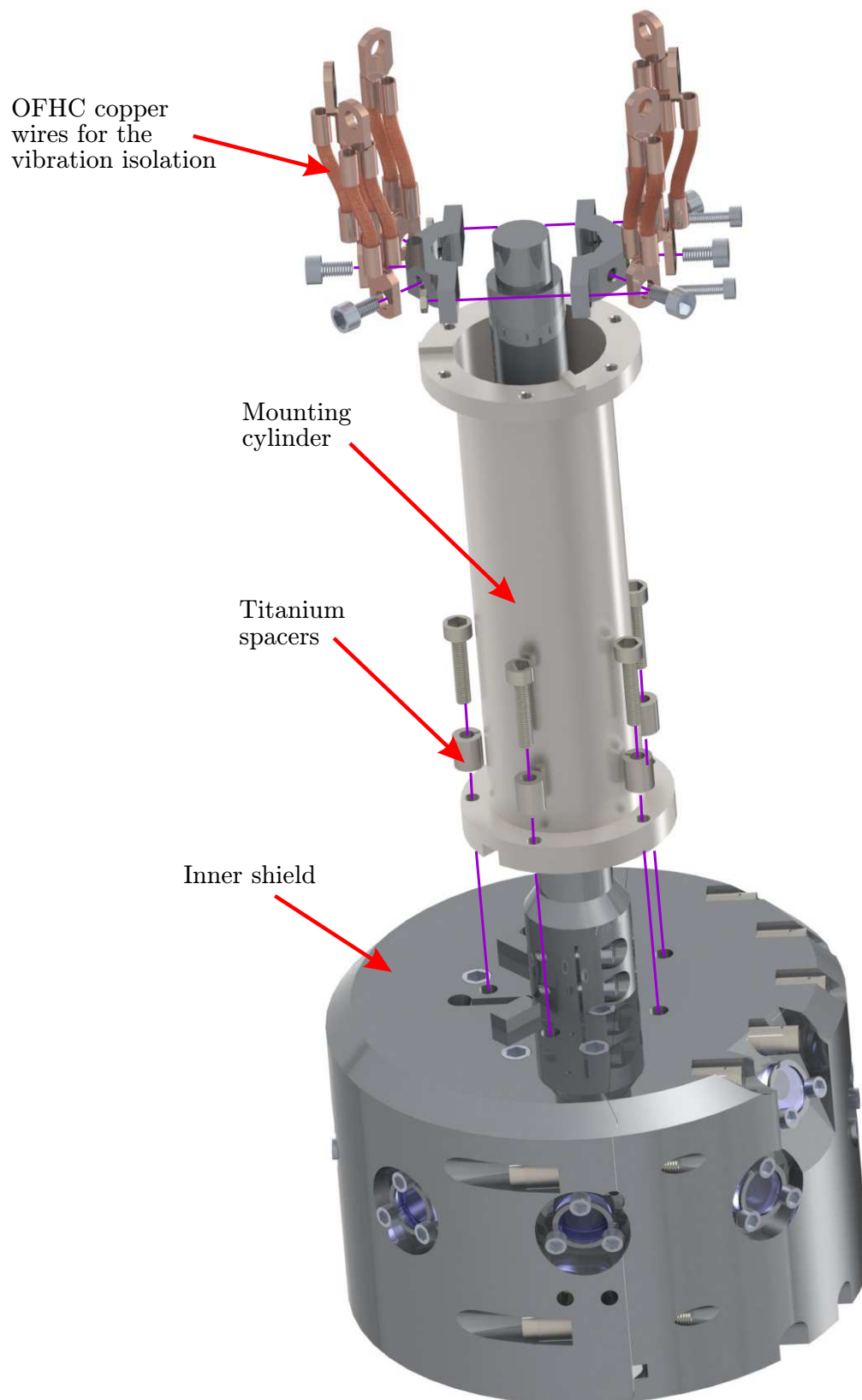


Figure B.7.: The wiring has to be thermally anchored to the connection rod of the coldfinger (not depicted), before the mounting cylinder is attached to inner shield. Then, the vibration isolation of the inner heat shield with the OFHC copper wires is attached to the connection rod

B.2 Assembly of the vacuum chamber and outer heat shield

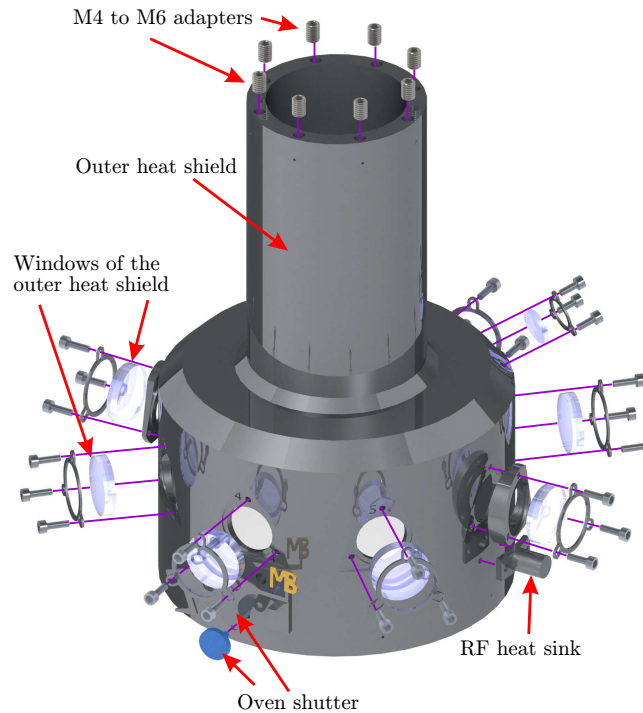


Figure B.8.: The outer heat shield contains nine windows. Two of these windows are mounted with special adapters so that reflections are reflected sideways instead of straight back. The oven shutter, which can be opened or closed with a wobble stick from outside vacuum, is mounted with a Teflon screw.

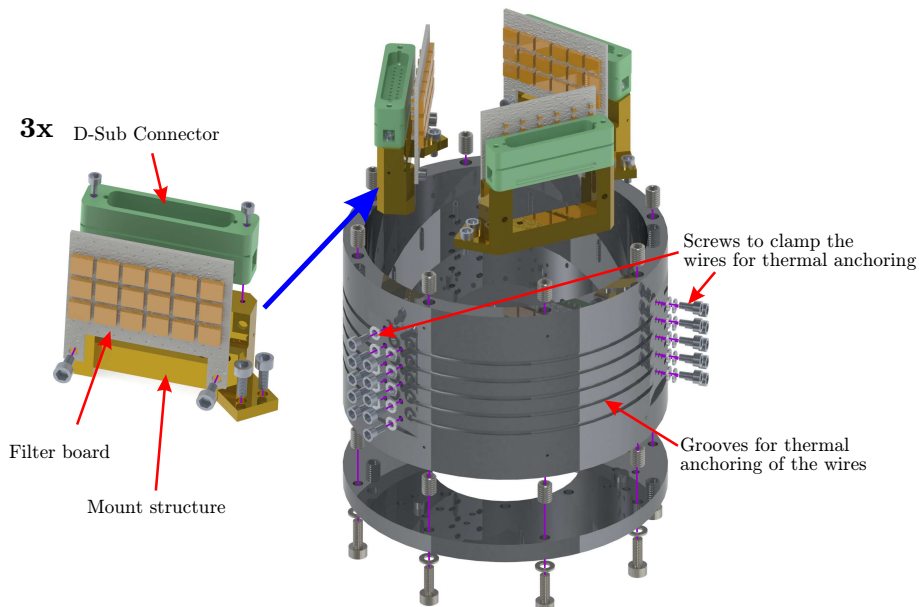


Figure B.9.: The three filter boards can be connected to wiring of the inner heat shield via D Sub 25 connectors. For the wiring from the outer heat shield to the feedthroughs, the cables (not depicted here) are stuck through holes in a cylindrical part of the outer heat shield. The cables are guided in grooves and clamped by M3 screws for efficient thermal anchoring.

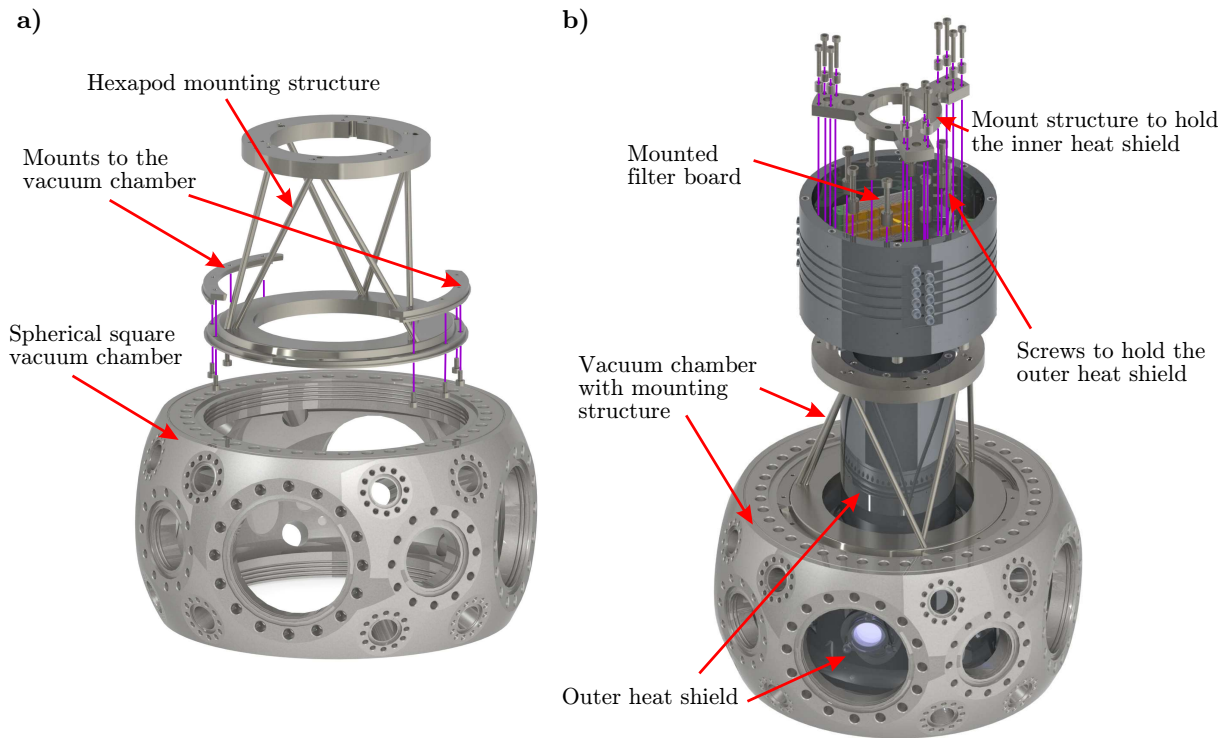


Figure B.10.: Panel **a** shows the Kimball Physics Spherical Square vacuum chamber with Groove Grabbers which hold the hexapod structure. Panel **b** depicts how the filter boards and outer heat shield are attached to the hexapod structure.

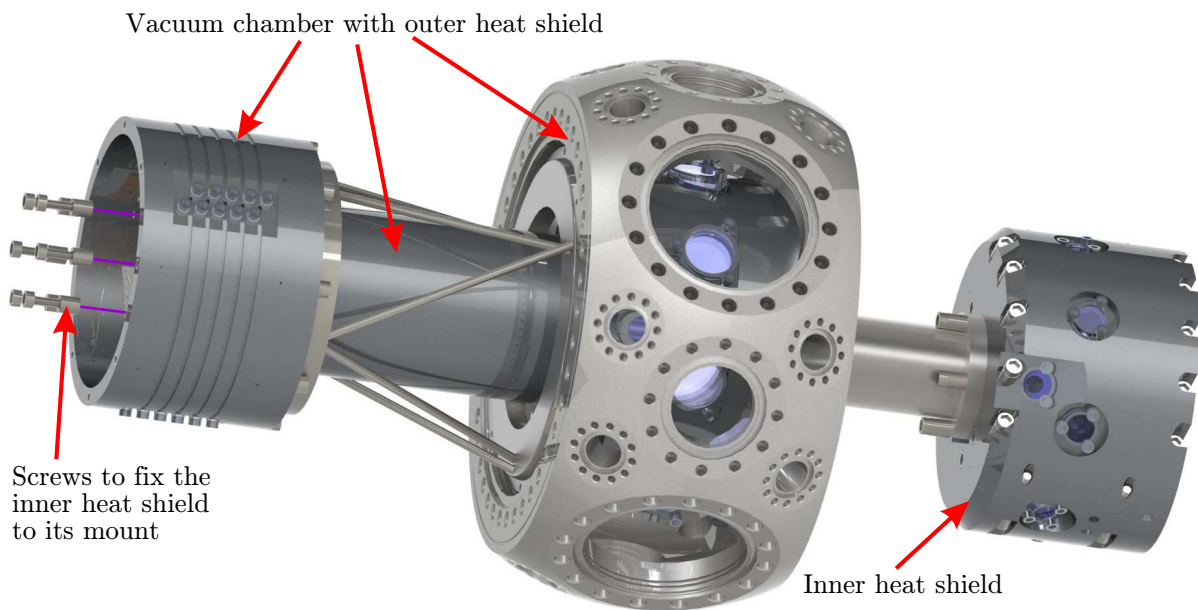


Figure B.11.: The inner heat shield is moved into the outer shield from below and fixed with screws to its mounting structure.

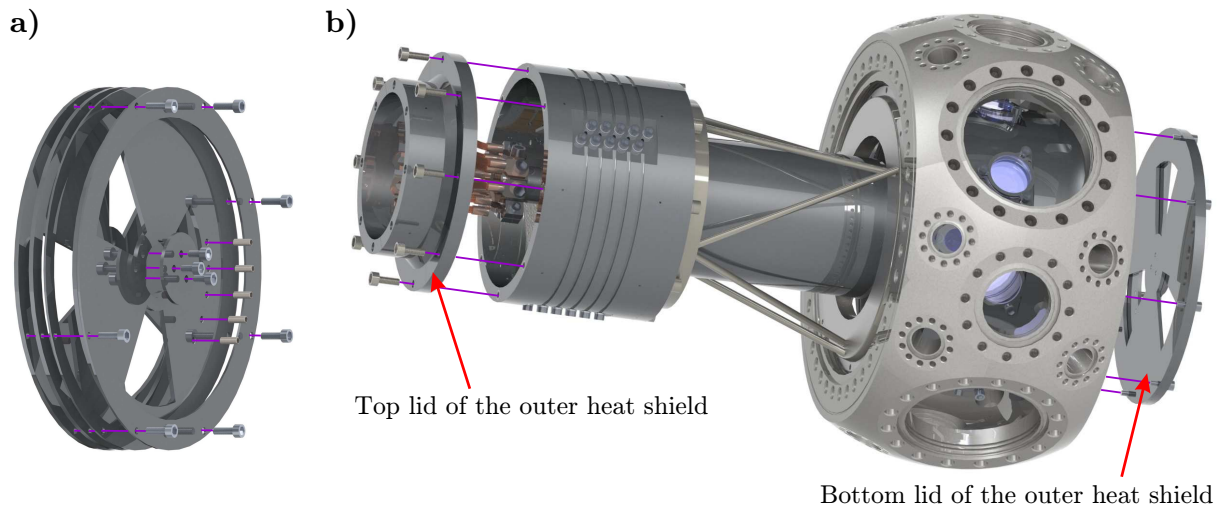


Figure B.12.: Panel a shows the assembly of the bottom lid of the outer heat shield. Panel b depicts how both the top and the bottom lid are attached to the outer heat shield.

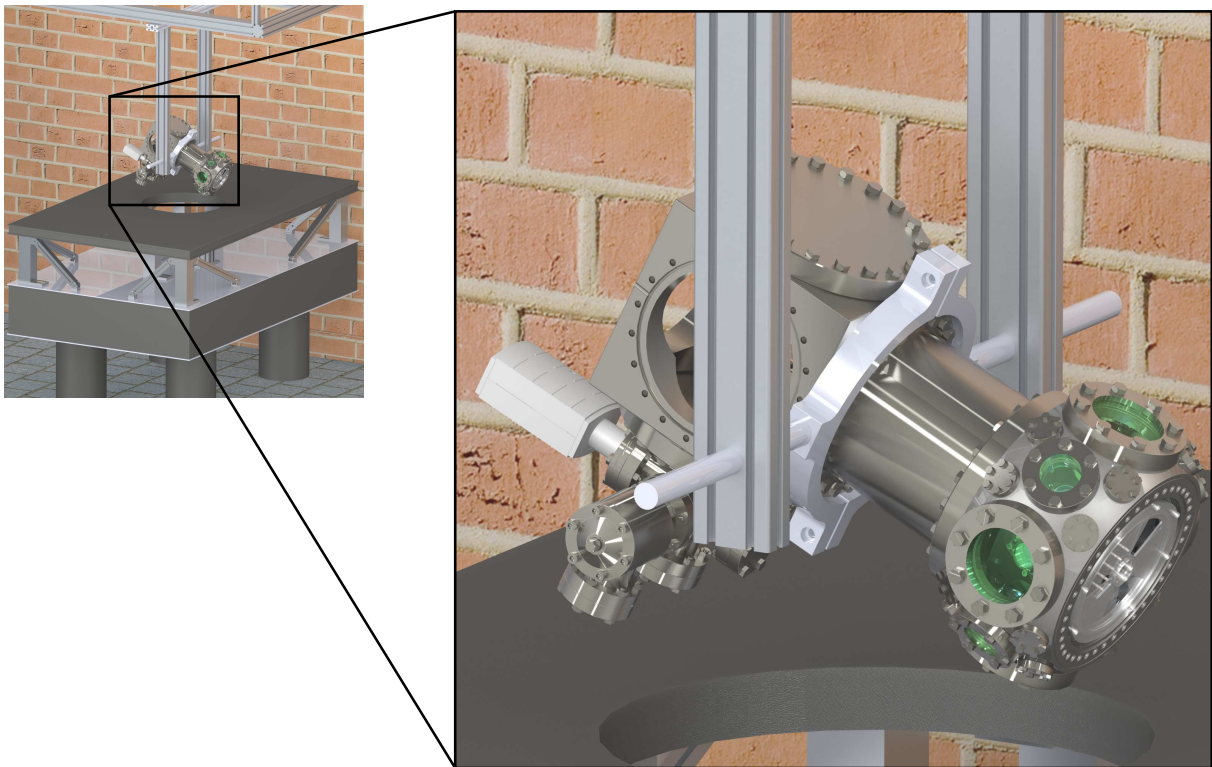


Figure B.13.: Typically, the outer and the inner heat shield are mounted in the vacuum chamber when it is tilted horizontally so that one can access it from above and below.

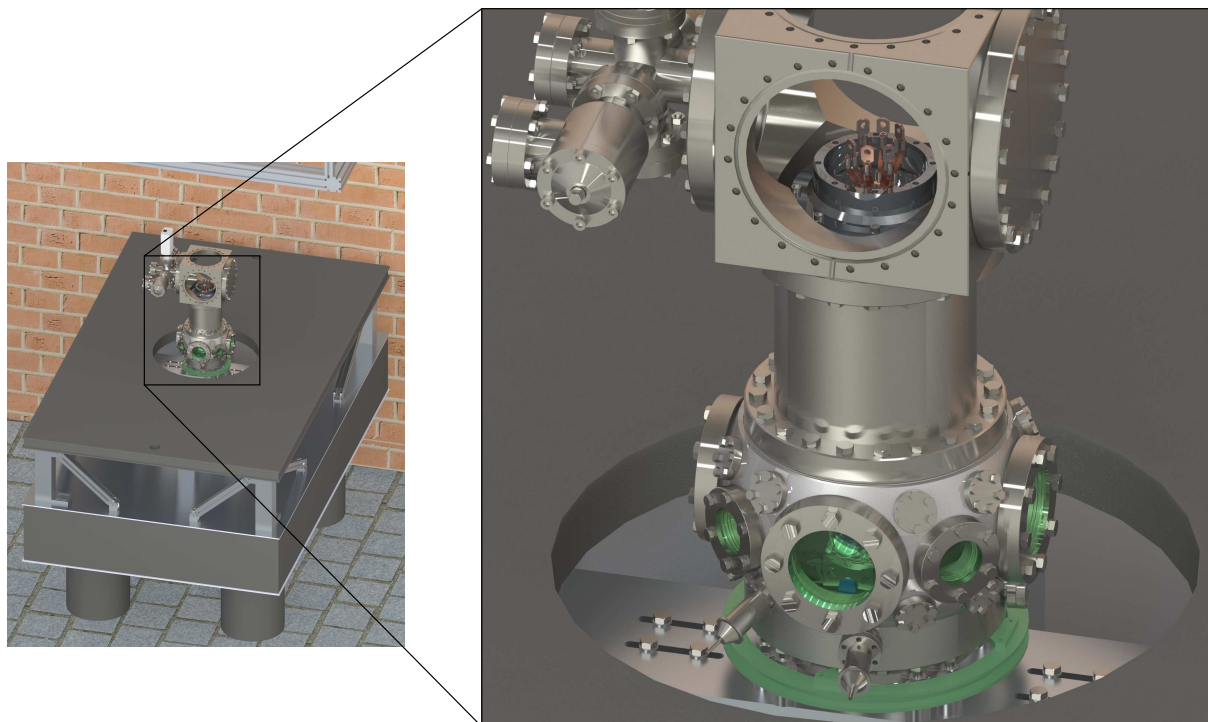


Figure B.14.: After the bottom flange and the bottom coil are attached, the vacuum chamber can be fixed to the optical table.

B.3 Assembly of the flow cryostat and the oven mount

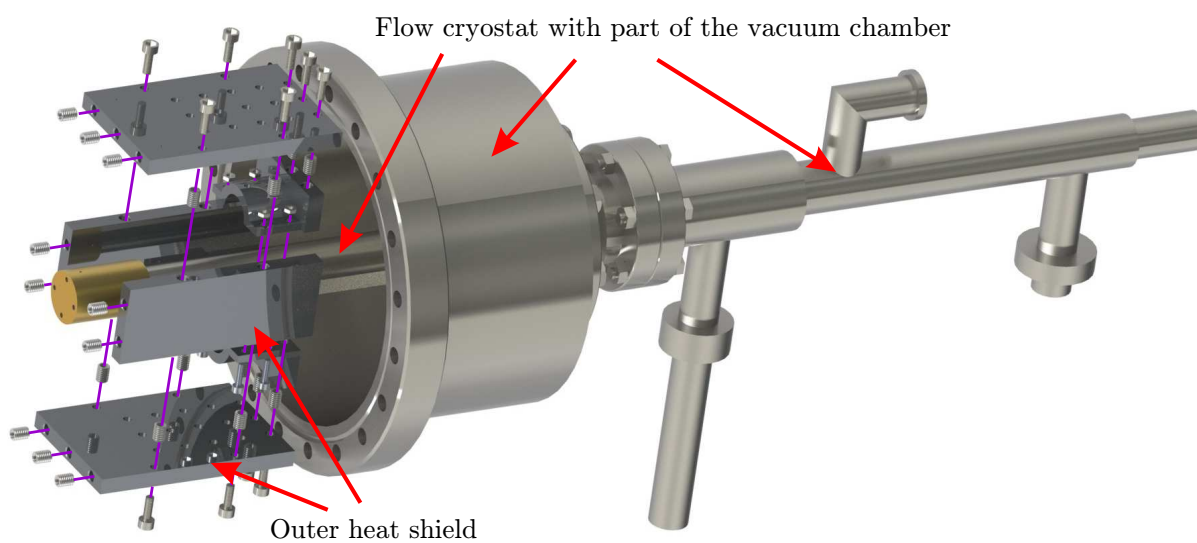


Figure B.15.: The heat shield near the flow cryostat has to be mounted when the cryostat is attached to the top flanges. The height, at which it is attached, can be varied to optimize cooling power for the outer heat shield.

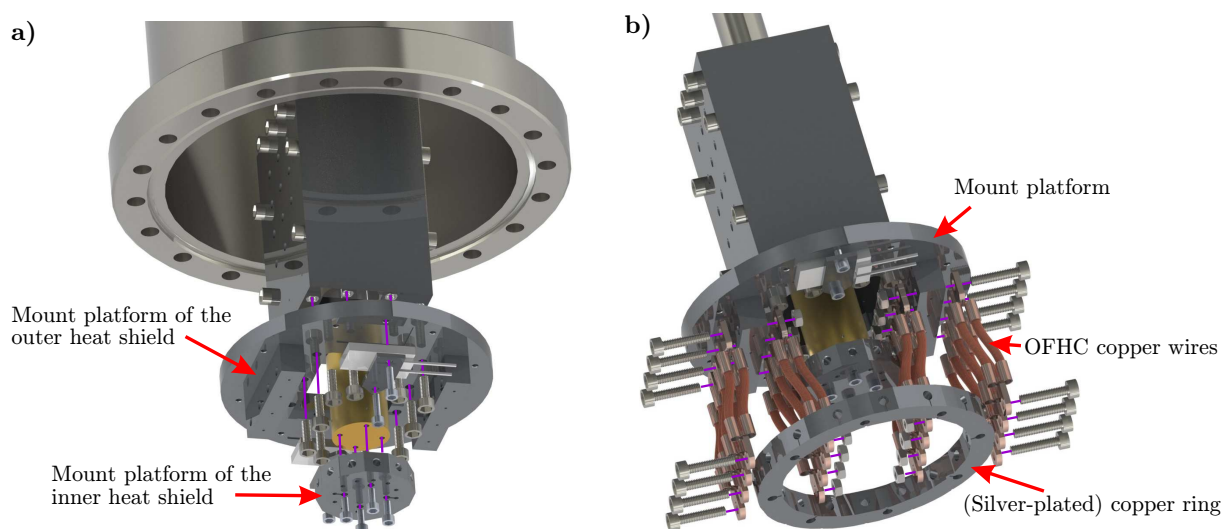


Figure B.16.: Panel a shows how the mount platforms for the vibration isolation of the inner and the outer heat shield are attached. Panel b depicts how the OFHC copper wires are mounted for the vibration isolation of the outer heat shield.

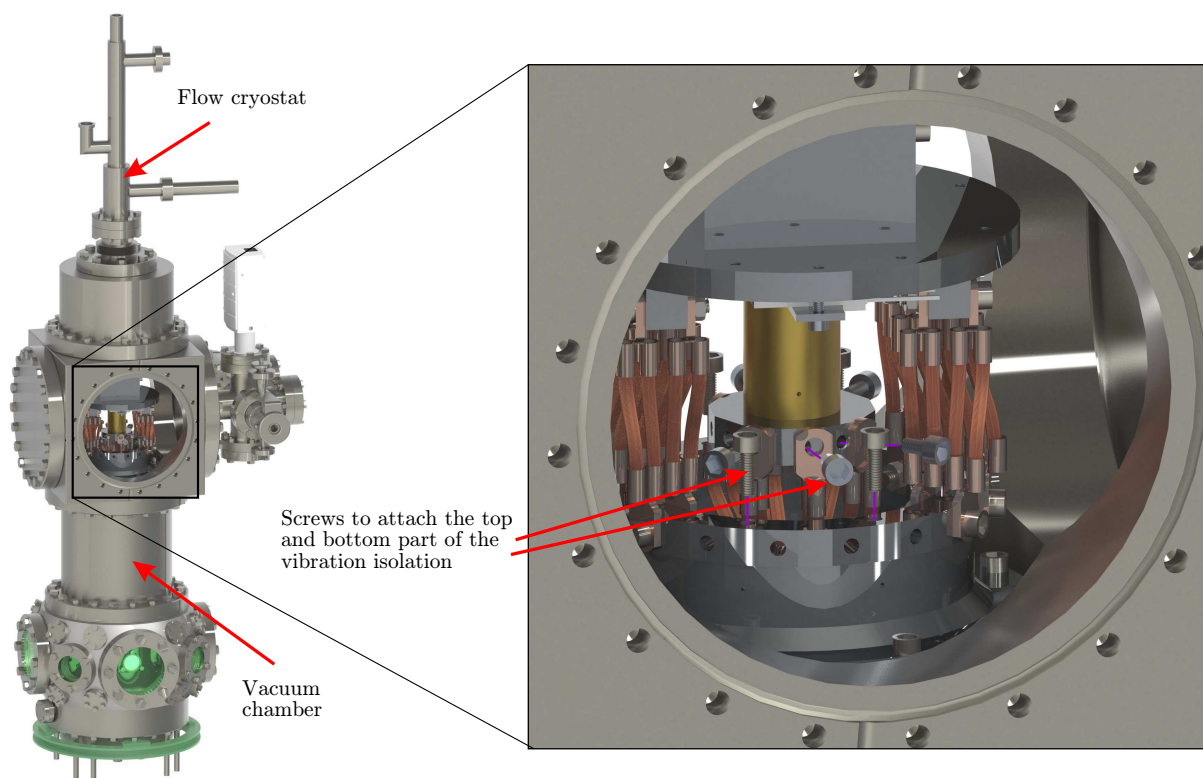


Figure B.17.: The flow cryostat is inserted into the vacuum chamber from above. After the flow cryostat is attached, the coldfinger can be connected to the rest of the cryostat in the vacuum chamber.

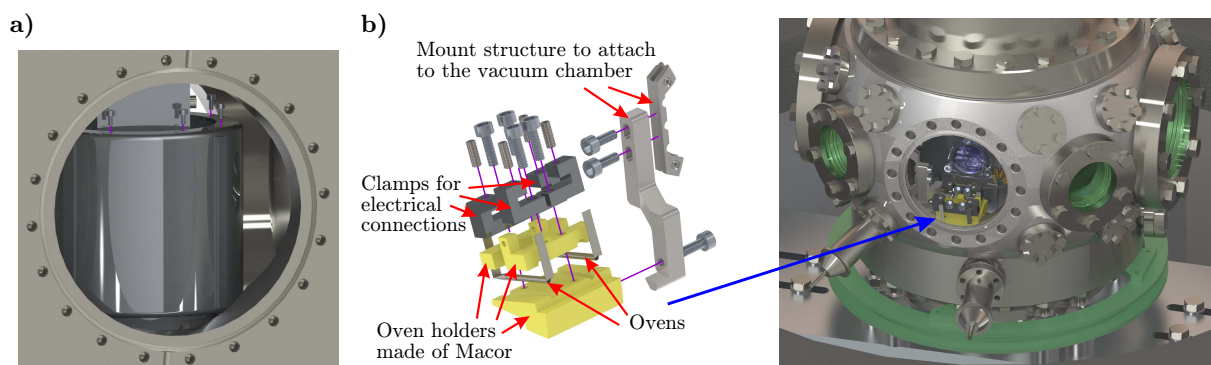


Figure B.18.: Panel a shows how the shield is placed around the vibration isolation in the top part of the vacuum chamber. Panel b depicts the oven mount and where it is mounted in the vacuum chamber.

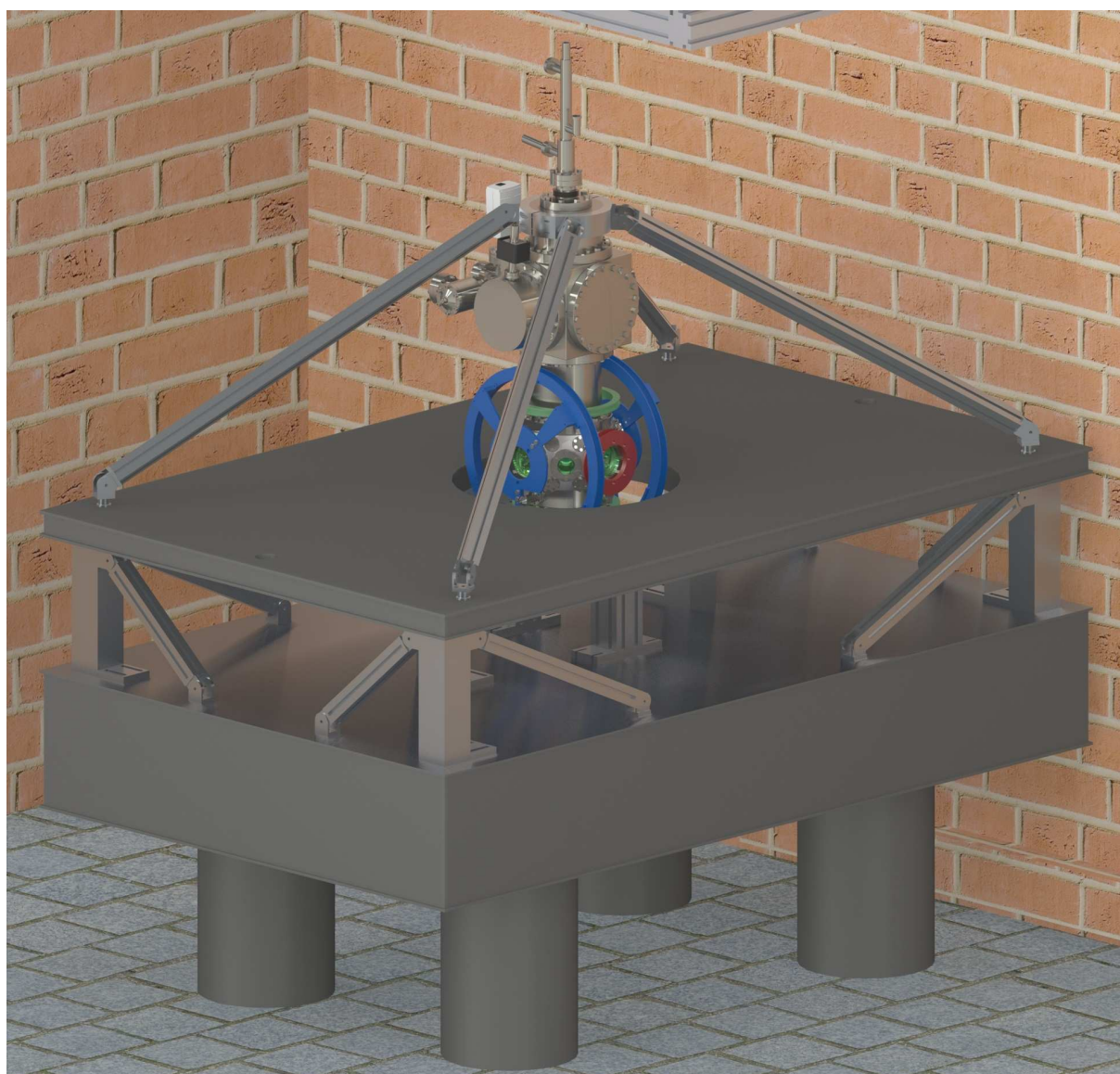


Figure B.19.: The vacuum chamber with the flow cryostat mounted on the optical table in the laboratory.

C Journal publications

Cryogenic setup for trapped ion quantum computing

M.F. Brandl, M.W. van Mourik, L. Postler, A. Nolf, K. Lakhmanskiy, R.R. Paiva, S. Möller, N. Daniilidis, H. Häffner, V. Kaushal, T. Ruster, C. Warschburger, H. Kaufmann, U.G. Poschinger, F. Schmidt-Kaler, P. Schindler, T. Monz, R. Blatt
Rev. Sci. Instrum. **87**, 113103 (2016)

Cryogenic resonator design for trapped ion experiments in Paul traps

M.F. Brandl, P. Schindler, T. Monz, R. Blatt
Appl. Phys. B **122**, 157 (2016)

Realization of a scalable Shor algorithm

T. Monz, D. Nigg, E.A. Martinez, M.F. Brandl, P. Schindler, R. Rines, S.X. Wang, I.L. Chuang, R. Blatt
Science **351**, 1068 (2016)

A quantum information processor with trapped ions

P. Schindler, D. Nigg, T. Monz, J.T. Barreiro, E. Martinez, S.X. Wang, S. Quint, M.F. Brandl, V. Nebendahl, C.F. Roos, M. Chwalla, M. Hennrich, R. Blatt
New. J. Phys. **15**, 123012 (2013)

Undoing a quantum measurement

P. Schindler, T. Monz, D. Nigg, J.T. Barreiro, E.A. Martinez, M.F. Brandl, M. Chwalla, M. Hennrich, R. Blatt
Phys. Rev. Lett. **110**, 070403 (2013)

Bibliography

- [ABH⁺06] M. ACTON, K.-A. BRICKMAN, P. HALJAN, P. LEE, L. DESLAURIERS, C. MONROE. *Near-perfect Simultaneous Measurement of a Qubit Register*. Quantum Info. Comput. **6**, 6 (2006), 465–482
- [ALS⁺16] J. ALONSO, F. LEUPOLD, Z. SOLÉR, M. FADEL, M. MARINELLI, B. KEITCH, V. NEGNEVITSKY, J. HOME. *Generation of large coherent states by bang-bang control of a trapped-ion oscillator*. Nature Communications **7** (2016), 11243
- [AMRS01] F. ALIMENTI, P. MEZZANOTTE, L. ROSELLI, R. SORRENTINO. *Modeling and characterization of the bonding-wire interconnection*. Microwave Theory and Techniques, IEEE Transactions on **49**, 1 (2001), 142–150
- [ASA⁺09] P. B. ANTOHI, D. SCHUSTER, G. M. AKSELROD, J. LABAZIEWICZ, Y. GE, Z. LIN, W. S. BAKR, I. L. CHUANG. *Cryogenic ion trapping systems with surface-electrode traps*. Review of Scientific Instruments **80**, 1 013103
- [Bac78] J. BACKUS. *Can Programming Be Liberated from the Von Neumann Style?: A Functional Style and Its Algebra of Programs*. Commun. ACM **21**, 8 (1978), 613–641
- [Bal96] N. H. BALSHAW. *Practical Cryogenics: An Introduction to Laboratory Cryogenics* (Oxford Instruments (UK), Scientific Research Division) (1996). ISBN 978-0952759409
- [BBC⁺93] C. BENNETT, G. BRASSARD, C. CRÉPEAU, R. JOZSA, A. PERES, W. WOOTTERS. *Teleporting an unknown quantum state via dual classical and Einstein-Podolsky-Rosen channels*. Phys. Rev. Lett. **70** (1993), 1895–1899
- [BBC⁺95] A. BARENCO, C. BENNETT, R. CLEVE, D. DIVINCENZO, N. MARGOLUS, P. SHOR, T. SLEATOR, J. SMOLIN, H. WEINFURTER. *Elementary gates for quantum computation*. Phys. Rev. A **52** (1995), 3457–3467
- [BC97] B. BUSHAW, B. CANNON. *Diode laser based resonance ionization mass spectrometric measurement of strontium-90*. Spectrochimica Acta Part B: Atomic Spectroscopy **52**, 12 (1997), 1839–1854
- [BDL⁺00] P. A. BARTON, C. J. S. DONALD, D. M. LUCAS, D. A. STEVENS, A. M. STEANE, D. N. STACEY. *Measurement of the lifetime of the $3d^2D_{5/2}$ state in $^{40}\text{Ca}^+$* . Phys. Rev. A **62** (2000), 032503
- [BDS⁺03] M. D. BARRETT, B. DEMARCO, T. SCHAEZT, V. MEYER, D. LEIBFRIED, J. BRITTON, J. CHIAVERINI, W. M. ITANO, B. JELENKOVIĆ, J. D. JOST, C. LANGER, T. ROSEN BAND, D. J. WINELAND. *Sympathetic cooling of $^9\text{Be}^+$ and $^{24}\text{Mg}^+$ for quantum logic*. Phys. Rev. A **68** (2003), 042302
- [Ben08] J. BENHELM. *Precision Spectroscopy and quantum information processing with trapped calcium ions*. Ph.D. thesis, Universität Innsbruck (2008)
- [BGL⁺12] R. BOWLER, J. GAEBLER, Y. LIN, T. R. TAN, D. HANNEKE, J. D. JOST, J. P. HOME, D. LEIBFRIED, D. J. WINELAND. *Coherent Diabatic Ion Transport and Separation in a Multizone Trap Array*. Phys. Rev. Lett. **109** (2012), 080502
- [BHI⁺91] J. J. BOLLINGER, D. J. HEIZEN, W. M. ITANO, S. L. GILBERT, D. J. WINELAND. *A 303-MHz frequency standard based on trapped Be^+ ions*. IEEE Transactions on Instrumentation and Measurement **40**, 2 (1991), 126–128
- [BHIW86] J. BERGQUIST, R. G. HULET, W. M. ITANO, D. WINELAND. *Observation of Quantum Jumps in a Single Atom*. Phys. Rev. Lett. **57** (1986), 1699–1702
- [BHK⁺15] G. P. BARWOOD, G. HUANG, S. A. KING, H. A. KLEIN, P. GILL. *Frequency noise processes in a strontium ion optical clock*. Journal of Physics B: Atomic, Molecular and Optical Physics **48**, 3 (2015), 035401
- [BHL⁺16] C. J. BALLANCE, T. P. HARTY, N. M. LINKE, M. A. SEPIOL, D. M. LUCAS. *High-Fidelity Quantum Logic Gates Using Trapped-Ion Hyperfine Qubits*. Phys. Rev. Lett. **117** (2016), 060504
- [BKRB08] J. BENHELM, G. KIRCHMAIR, C. ROOS, R. BLATT. *Towards fault-tolerant quantum computing with trapped ions*. Nature Physics **4** (2008), 463–466

- [BKRB15] M. BROWNNUTT, M. KUMPH, P. RABL, R. BLATT. *Ion-trap measurements of electric-field noise near surfaces*. Rev. Mod. Phys. **87** (2015), 1419–1482
- [Bla10] R. BLAKESTAD. *Transport of Trapped-Ion Qubits within a Scalable Quantum Processor*. Ph.D. thesis, University of Colorado (2010)
- [BLMW04] B. B. BLINOV, D. LEIBFRIED, C. MONROE, D. J. WINELAND. *Quantum Computing with Trapped Ion Hyperfine Qubits*. Quantum Information Processing **3**, 1 (2004), 45–59
- [BLW⁺07] M. BROWNNUTT, V. LETCHUMANAN, G. WILPERS, R. THOMPSON, P. GILL, A. SINCLAIR. *Controlled photoionization loading of 88Sr⁺ for precision ion-trap experiments*. Applied Physics B **87**, 3 (2007), 411–415
- [BMB⁺98a] D. J. BERKELAND, J. D. MILLER, J. C. BERGQUIST, W. M. ITANO, D. J. WINELAND. *Laser-Cooled Mercury Ion Frequency Standard*. Phys. Rev. Lett. **80** (1998), 2089–2092
- [BMB⁺98b] D. J. BERKELAND, J. D. MILLER, J. C. BERGQUIST, W. M. ITANO, D. J. WINELAND. *Minimization of ion micromotion in a Paul trap*. Journal of Applied Physics **83**, 10 (1998), 5025–5033
- [BOC⁺11] K. BROWN, C. OSPELKAUS, Y. COLOMBE, A. WILSON, D. LEIBFRIED, D. WINELAND. *Coupled quantized mechanical oscillators*. Nature **471** (2011), 196–199
- [BOV⁺11] R. B. BLAKESTAD, C. OSPELKAUS, A. P. VANDEVENDER, J. H. WESENBERG, M. J. BIERCUK, D. LEIBFRIED, D. J. WINELAND. *Near-ground-state transport of trapped-ion qubits through a multidimensional array*. Phys. Rev. A **84** (2011), 032314
- [BSF⁺01] S. S. BABUA, M. L. SANTELLAA, Z. FENGB, B. W. RIEMERC, J. W. COHRON. *Empirical model of effects of pressure and temperature on electrical contact resistance of metals*. Science and Technology of Welding and Joining **6** (2001), 126–132
- [BSMB16] M. BRANDL, P. SCHINDLER, T. MONZ, R. BLATT. *Cryogenic resonator design for trapped ion experiments in Paul traps*. Applied Physics B **122**, 6 (2016), 1–9
- [Bur10] A. H. BURRELL. *High Fidelity Readout of Trapped Ion Qubits*. Ph.D. thesis, Department of Physics, University of Oxford (2010)
- [BvMP⁺16] M. BRANDL, M. VAN MOURIK, L. POSTLER, A. NOLF, K. LAKHMANSKIY, R. PAIVA, S. MÖLLER, N. DANILIDIS, H. HÄFFNER, V. KAUSHAL, T. RUSTER, C. WARSCHBURGER, H. KAUFMANN, U. POSCHINGER, F. SCHMIDT-KALER, P. SCHINDLER, T. MONZ, R. BLATT. *Cryogenic setup for trapped ion quantum computing*. Review of Scientific Instruments **87**, 11 113103
- [BWC⁺11] K. R. BROWN, A. C. WILSON, Y. COLOMBE, C. OSPELKAUS, A. M. MEIER, E. KNILL, D. LEIBFRIED, D. J. WINELAND. *Single-qubit-gate error below 10⁻⁴ in a trapped ion*. Phys. Rev. A **84** (2011), 030303
- [CBK⁺09] M. CHWALLA, J. BENHELM, K. KIM, G. KIRCHMAIR, T. MONZ, M. RIEBE, P. SCHINDLER, A. S. VILLAR, W. HÄNSEL, C. F. ROOS, R. BLATT, M. ABGRALL, G. SANTARELLI, G. D. ROVERA, P. LAURENT. *Absolute Frequency Measurement of the ⁴⁰Ca⁺ 4s ²S_{1/2} – 3d ²D_{5/2} Clock Transition*. Phys. Rev. Lett. **102** (2009), 023002
- [CC88] M. CAFFAREL, P. CLAVERIE. *Development of a pure diffusion quantum Monte Carlo method using a full generalized Feynman-Kac formula. I. Formalism*. The Journal of Chemical Physics **88**, 2 (1988), 1088–1099
- [CDM⁺14] T. CHOI, S. DEBNATH, T. A. MANNING, C. FIGGATT, Z.-X. GONG, L.-M. DUAN, C. MONROE. *Optimal Quantum Control of Multimode Couplings between Trapped Ion Qubits for Scalable Entanglement*. Phys. Rev. Lett. **112** (2014), 190502
- [Che98] W.-K. CHEN. *Passive and Active Filters: Theory and Implementations* (John Wiley & Sons) (1998). ISBN 9780471823520
- [Chw09] M. CHWALLA. *Precision spectroscopy with ⁴⁰Ca⁺ ions in a Paul trap*. Ph.D. thesis, Universität Innsbruck (2009)
- [CLCH⁺16] I. D. CONWAY LAMB, J. I. COLLESS, J. M. HORNIBROOK, S. J. PAUKA, S. J. WADDY, M. K. FRECHTLING, D. J. REILLY. *An FPGA-based instrumentation platform for use at deep cryogenic temperatures*. Review of Scientific Instruments **87**, 1 014701

- [CM99] J. R. CLAYCOMB, J. H. MILLER. *Superconducting magnetic shields for SQUID applications*. Review of Scientific Instruments **70**, 12 (1999), 4562–4568
- [CS96] A. R. CALDERBANK, P. W. SHOR. *Good quantum error-correcting codes exist*. Phys. Rev. A **54** (1996), 1098–1105
- [CS14] J. CHIAVERINI, J. M. SAGE. *Insensitivity of the rate of ion motional heating to trap-electrode material over a large temperature range*. Phys. Rev. A **89** (2014), 012318
- [CSW⁺14] Y. COLOMBE, D. H. SLICHTER, A. C. WILSON, D. LEIBFRIED, D. J. WINELAND. *Single-mode optical fiber for high-power, low-loss UV transmission*. Opt. Express **22**, 16 (2014), 19783–19793
- [CTDL99] C. COHEN-TANNOUJJI, B. DIU, F. LALOË. *Quantenmechanik* (Walter De Gruyter Inc.) (1999). ISBN 3-11-016459-0
- [CZ95] J. I. CIRAC, P. ZOLLER. *Quantum Computations with Cold Trapped Ions*. Phys. Rev. Lett. **74** (1995), 4091–4094
- [CZ00] J. CIRAC, P. ZOLLER. *A scalable quantum computer with ions in an array of microtraps*. Nature **404** (2000), 579–581
- [Day] C. DAY. *Basics and applications of cryopumps*. CERN summer school, <http://cds.cern.ch/record/1047069/files/p241.pdf> - visited on July 14, 2016
- [Deu89] D. DEUTSCH. *Quantum Computational Networks*. Proceedings of the Royal Society of London A: Mathematical, Physical and Engineering Sciences **425**, 1868 (1989), 73–90
- [DGTH13] N. DANILIDIS, D. J. GORMAN, L. TIAN, H. HÄFFNER. *Quantum information processing with trapped electrons and superconducting electronics*. New Journal of Physics **15**, 7 (2013), 073017
- [DHH⁺98] M. DIEDERICH, H. HÄFFNER, N. HERMANSPAHN, M. IMMEL, H. KLUGE, R. LEY, R. MANN, W. QUINT, S. STAHL, G. WERTH. *Observing a single hydrogen-like ion in a Penning trap at $T = 4$ K*. Hyperfine Interactions **115**, 1 (1998), 185–192
- [DHK⁺83] R. W. P. DREVER, J. L. HALL, F. V. KOWALSKI, J. HOUGH, G. M. FORD, A. J. MUNLEY, H. WARD. *Laser phase and frequency stabilization using an optical resonator*. Applied Physics B **31** (1983), 97–105
- [DI00] D. DIVINCENZO, IBM. *The Physical Implementation of Quantum Computation* (2000). arXiv:quant-ph/0002077
- [DLF⁺16] S. DEBNATH, N. M. LINKE, C. FIGGATT, K. A. LANDSMAN, K. WRIGHT, C. MONROE. *Demonstration of a programmable quantum computer module*. Nature **536** (2016), 63–66
- [DMGR⁺16] D. DE MOTTE, A. R. GROUNDS, M. REHÁK, A. RODRIGUEZ BLANCO, B. LEKITSCH, G. S. GIRI, P. NEILINGER, G. OELSNER, E. IL'ICHEV, M. GRAJCAR, W. K. HENSINGER. *Experimental system design for the integration of trapped-ion and superconducting qubit systems*. Quantum Information Processing **15**, 12 (2016), 5385–5414
- [DMSH96] K. M. DAVIS, K. MIURA, N. SUGIMOTO, K. HIRAO. *Writing waveguides in glass with a femtosecond laser*. Opt. Lett. **21**, 21 (1996), 1729–1731
- [DW14] K. M. S. DAVE WECKER. *LIQUi>: A Software Design Architecture and Domain-Specific Language for Quantum Computing* (2014)
- [Ear42] S. EARNSHAW. *On the Nature of the Molecular Forces which Regulate the Constitution of the Luminiferous Ether*. Trans. Camb. Phil. Soc. **7** (1842), 97–112
- [Eki06] J. EKIN. *Experimental Techniques for Low-Temperature Measurements: Cryostat Design, Material Properties and Superconductor Critical-Current Testing* (Oxford University Press), 1st ed. (2006). ISBN 9780198570547
- [ELH⁺14] E. S. ENDRES, O. LAKHMANSKAYA, D. HAUSER, S. E. HUBER, T. BEST, S. S. KUMAR, M. PROBST, R. WESTER. *Upper Limits to the Reaction Rate Coefficients of C_n^+ and C_nH^+ ($n = 2, 4, 6$) with Molecular Hydrogen*. The Journal of Physical Chemistry A **118**, 33 (2014), 6705–6710. PMID: 25058339
- [EPR35] A. EINSTEIN, B. PODOLSKY, N. ROSEN. *Can Quantum-Mechanical Description of Physical Reality Be Considered Complete?* Phys. Rev. **47** (1935), 777–780

- [ESG⁺00] D. G. ENZER, M. M. SCHAUER, J. J. GOMEZ, M. S. GULLEY, M. H. HOLZSCHEITER, P. G. KWIAT, S. K. LAMOREAUX, C. G. PETERSON, V. D. SANDBERG, D. TUPA, A. G. WHITE, R. J. HUGHES, D. F. V. JAMES. *Observation of Power-Law Scaling for Phase Transitions in Linear Trapped Ion Crystals*. Phys. Rev. Lett. **85** (2000), 2466–2469
- [Fey82] R. FEYNMAN. *Simulating physics with computers*. International Journal of Theoretical Physics **21**, 6 (1982), 467–488
- [FM63] J. FILE, R. G. MILLS. *Observation of Persistent Current in a Superconducting Solenoid*. Phys. Rev. Lett. **10** (1963), 93–96
- [FSLC97] P. FISK, M. SELLARS, M. LAWN, G. COLES. *Accurate measurement of the 12.6 GHz "clock" transition in trapped $^{171}\text{Yb}^+$ ions*. IEEE Transactions on Ultrasonics, Ferroelectrics, and Frequency Control **44**, 2 (1997), 344–354
- [FW53] R. FRANZ, G. WIEDEMANN. *Über die Wärme-Leitungsfähigkeit der Metalle*. Annalen der Physik **165**, 8 (1853), 497–531
- [GB15] T. J. GREEN, M. J. BIERCUK. *Phase-Modulated Decoupling and Error Suppression in Qubit-Oscillator Systems*. Phys. Rev. Lett. **114** (2015), 120502
- [Ger15] L. GERSTER. *Spectral Filtering and laser diode injection for multi-qubit trapped ion gates*. Master's thesis, ETH Zürich (2015)
- [GHZ07] D. GREENBERGER, M. HORNE, A. ZEILINGER. *Going Beyond Bell's Theorem* (2007). arXiv:0712.0921
- [GKMR99] G. GRANDI, M. KAZIMIERCZUK, A. MASSARINI, U. REGGIANI. *Stray capacitances of single-layer solenoid air-core inductors*. Industry Applications, IEEE Transactions on **35**, 5 (1999), 1162–1168
- [GKZ⁺10] R. GERRITSMA, G. KIRCHMAIR, F. ZÄHRINGER, E. SOLANO, R. BLATT, C. ROOS. *Quantum simulation of the Dirac equation*. Nature **463** (2010), 68–71
- [Gla63] R. J. GLAUBER. *The Quantum Theory of Optical Coherence*. Phys. Rev. **130** (1963), 2529–2539
- [GNK⁺12] D. GANDOLFI, M. NIEDERMAYR, M. KUMPH, M. BROWNNUTT, R. BLATT. *Compact radio-frequency resonator for cryogenic ion traps*. Review of Scientific Instruments **83**, 8 084705
- [GRB⁺01] S. GULDE, D. ROTTER, P. BARTON, F. SCHMIDT-KALER, R. BLATT, W. HOGERVORST. *Simple and efficient photo-ionization loading of ions for precision ion-trapping experiments*. Applied Physics B **73** (2001), 861–863
- [Gro97] L. GROVER. *Quantum Mechanics Helps in Searching for a Needle in a Haystack*. Phys. Rev. Lett. **79** (1997), 325–328
- [GSW97] T. GUDJONS, P. SEIBERT, G. WERTH. *Influence of anharmonicities of a Paul trap potential on the motion of stored ions*. Applied Physics B **65**, 1 (1997), 57–62
- [Gul03] S. T. GULDE. *Experimental Realization of Quantum Gates and Deutsch-Josza Algorithm with Trapped $^{40}\text{Ca}^+$ Ions*. Ph.D. thesis, University of Innsbruck (2003)
- [HAB⁺14] T. P. HARTY, D. T. C. ALLCOCK, C. J. BALLANCE, L. GUIDONI, H. A. JANACEK, N. M. LINKE, D. N. STACEY, D. M. LUCAS. *High-Fidelity Preparation, Gates, Memory, and Readout of a Trapped-Ion Quantum Bit*. Phys. Rev. Lett. **113** (2014), 220501
- [Hah50] E. L. HAHN. *Spin Echoes*. Phys. Rev. **80** (1950), 580–594
- [Ham70] W. HAMILTON. *Superconducting shielding*. Rev. Phys. Appl. (Paris) **5**, 1 (1970), 41–48
- [Har12] M. J. HARLANDER. *Architecture for a scalable ion-trap quantum computer*. Ph.D. thesis, University of Innsbruck (2012)
- [Har13] T. HARTY. *High-Fidelity Microwave-Driven Quantum Logic in Intermediate-Field $^{43}\text{Ca}^+$* . Ph.D. thesis, Department of Physics, University of Oxford (2013)
- [HBHB10] M. HARLANDER, M. BROWNNUTT, W. HÄNSEL, R. BLATT. *Trapped-ion probing of light-induced charging effects on dielectrics*. New Journal of Physics **12**, 9 (2010), 093035

- [Hem14] C. HEMPEL. *Digital quantum simulation, Schrödinger cat state spectroscopy and setting up a linear ion trap*. Ph.D. thesis, Universität Innsbruck (2014)
- [Hil70] A. HILDEBRANDT. *Shielding with superconductors in small magnetic fields*. *Revue de Physique Appliquée* **5**, 1 (1970), 49–52
- [HLB⁺11] M. HARLANDER, R. LECHNER, M. BROWNNUTT, R. BLATT, W. HÄNSEL. *Trapped-ion antennae for the transmission of quantum information*. *Nature* **471** (2011), 200–203
- [Hom13] J. HOME. *Quantum science and metrology with mixed-species ion chains* (2013). arXiv:1306.5950
- [HSL⁺16] N. HUNTEMANN, C. SANNER, B. LIPPHARDT, C. TAMM, E. PEIK. *Single-Ion Atomic Clock with 3×10^{-18} Systematic Uncertainty*. *Phys. Rev. Lett.* **116** (2016), 063001
- [HVZM11] C. HAMACHER, Z. VRANESIC, S. ZAKY, N. MANJIKIAN. *Computer Organization and Embedded Systems* (McGraw-Hill Education), 6th ed. (2011). ISBN 0073380652
- [IBB⁺07] W. M. ITANO, J. C. BERGQUIST, A. BRUSCH, S. A. DIDDAMS, T. M. FORTIER, T. P. HEAVNER, L. HOLLBERG, D. B. HUME, S. R. JEFFERTS, L. LORINI, T. E. PARKER, T. ROSEN BAND, J. E. STALNAKER. *Optical frequency standards based on mercury and aluminum ions*. *Proc. SPIE* **6673** (2007), 667303–667303–11
- [Ita00] W. ITANO. *External-Field Shifts of the $^{199}\text{Hg}^+$ Optical Frequency Standard*. *Journal of Research of the National Institute of Standards and Technology* **105**, 6 (2000), 829–837
- [Jac91] J. A. JACOBS. *Geomagnetism, Volume 4* (Academic Press) (1991). ISBN 0123786746
- [Jam98] D. F. V. JAMES. *Quantum dynamics of cold trapped ions with application to quantum computation*. *Applied Physics B* **66**, 2 (1998), 181–190
- [JLH⁺14] P. JURCEVIC, B. P. LANYON, P. HAUKE, C. HEMPEL, P. ZOLLER, R. BLATT, C. F. ROOS. *Quasi-particle engineering and entanglement propagation in a quantum many-body system*. *Nature* **511** (2014), 202–205
- [JMBW95] S. R. JEFFERTS, C. MONROE, E. W. BELL, D. J. WINELAND. *Coaxial-resonator-driven rf (Paul) trap for strong confinement*. *Phys. Rev. A* **51** (1995), 3112–3116
- [JVMF⁺12] N. JONES, R. VAN METER, A. FOWLER, P. MCMAHON, J. KIM, T. LADD, Y. YAMAMOTO. *Layered Architecture for Quantum Computing*. *Phys. Rev. X* **2** (2012), 031007
- [JW06] F. JELEZKO, J. WRACHTRUP. *Single defect centres in diamond: A review*. *Physica Status Solidi (a)* **203**, 13 (2006), 3207–3225
- [JWCR⁺16] K. G. JOHNSON, J. D. WONG-CAMPOS, A. RESTELLI, K. A. LANDSMAN, B. NEYENHUIS, J. MIZRAHI, C. MONROE. *Active stabilization of ion trap radiofrequency potentials*. *Review of Scientific Instruments* **87**, 5 053110
- [KAN⁺14] S. KOTLER, N. AKERMAN, N. NAVON, Y. GLICKMAN, R. OZERI. *Measurement of the magnetic interaction between two bound electrons of two separate ions*. *Nature* **510** (2014), 376–380
- [Kaz09] M. K. KAZIMIERCZUK. *High-Frequency Magnetic Components* (John Wiley & Sons) (2009). ISBN 9780470714539
- [KBB11] M. KUMPH, M. BROWNNUTT, R. BLATT. *Two-dimensional arrays of radio-frequency ion traps with addressable interactions*. *New Journal of Physics* **13**, 7 (2011), 073043
- [KK09] J. KIM, C. KIM. *Integrated Optical Approach to Trapped Ion Quantum Computation*. *Quantum Info. Comput.* **9**, 3 (2009), 181–202
- [KKA12] P. KAMBY, A. KNOTT, M. A. E. ANDERSEN. *Printed Circuit Board Integrated Toroidal Radio Frequency Inductors*. In *Proceedings of the 38th Annual Conference of the IEEE Industrial Electronics Society*, 680–684 (IEEE) (2012)
- [KKLK07] C. KIM, C. KNOERNSCHILD, B. LIU, J. KIM. *Design and Characterization of MEMS Micromirrors for Ion-Trap Quantum Computation*. *IEEE Journal of Selected Topics in Quantum Electronics* **13**, 2 (2007), 322–329

- [KKM⁺00] D. KIELPINSKI, B. E. KING, C. J. MYATT, C. A. SACKETT, Q. A. TURCHETTE, W. M. ITANO, C. MONROE, D. J. WINELAND, W. H. ZUREK. *Sympathetic cooling of trapped ions for quantum logic*. Phys. Rev. A **61** (2000), 032310
- [KMW02] D. KIELPINSKI, C. MONROE, D. J. WINELAND. *Architecture for a large-scale ion-trap quantum computer*. Nature **417** (2002), 709–711
- [Kum15] M. KUMPH. *2D Arrays of Ion Traps for Large Scale Integration of Quantum Information Processors*. Ph.D. thesis, Universität Innsbruck (2015)
- [KYG⁺07] J. KOCH, T. M. YU, J. GAMBETTA, A. A. HOUCK, D. I. SCHUSTER, J. MAJER, A. BLAIS, M. H. DEVORET, S. M. GIRVIN, R. J. SCHOELKOPF. *Charge-insensitive qubit design derived from the Cooper pair box*. Phys. Rev. A **76** (2007), 042319
- [LBB⁺86] D. J. LARSON, J. C. BERGQUIST, J. J. BOLLINGER, W. M. ITANO, D. J. WINELAND. *Sympathetic cooling of trapped ions: A laser-cooled two-species nonneutral ion plasma*. Phys. Rev. Lett. **57** (1986), 70–73
- [LBC⁺12] E. LUCERO, R. BARENS, Y. CHEN, J. KELLY, M. MARIANTONI, A. MEGRANT, P. O'MALLEY, D. SANK, A. VAINSENER, J. WENNER, T. WHITE, Y. YIN, A. N. CLELAND, J. MARTINIS. *Computing prime factors with a Josephson phase qubit quantum processor*. Nature Physics **8** (2012), 719–723
- [LBMW03] D. LEIBFRIED, R. BLATT, C. MONROE, D. WINELAND. *Quantum dynamics of single trapped ions*. Rev. Mod. Phys. **75** (2003), 281–324
- [LDM⁺03] D. LEIBFRIED, B. DEMARCO, V. MEYER, D. LUCAS, M. BARRETT, J. BRITTON, W. M. ITANO, B. JELENKOVIĆ, C. LANGER, T. ROSEN BAND, D. J. WINELAND. *Experimental demonstration of a robust, high-fidelity geometric two ion-qubit phase gate*. Nature **422** (2003), 412–415
- [Lec16] R. LECHNER. *Multi-mode cooling techniques for trapped ions*. Ph.D. thesis, Universität Innsbruck (2016)
- [LGA⁺08] J. LABAZIEWICZ, Y. GE, P. ANTOHI, D. LEIBRANDT, K. R. BROWN, I. L. CHUANG. *Suppression of Heating Rates in Cryogenic Surface-Electrode Ion Traps*. Phys. Rev. Lett. **100** (2008), 013001
- [LHN⁺07] A. D. LUDLOW, X. HUANG, M. NOTCUTT, T. ZANON-WILLETTE, S. M. FOREMAN, M. M. BOYD, S. BLATT, J. YE. *Compact, thermal-noise-limited optical cavity for diode laser stabilization at 1×10^{-15}* . Opt. Lett. **32**, 6 (2007), 641–643
- [LHN⁺11] B. P. LANYON, C. HEMPEL, D. NIGG, M. MÜLLER, R. GERRITSMAN, F. ZÄHRINGER, P. SCHINDLER, J. T. BARREIRO, M. RAMBACH, G. KIRCHMAIR, M. HENNRICH, P. ZOLLER, R. BLATT, C. F. ROOS. *Universal Digital Quantum Simulation with Trapped Ions*. Science **334**, 6052 (2011), 57–61
- [LMM⁺15] A. LAUCHT, J. T. MUHONEN, F. A. MOHIYADDIN, R. KALRA, J. P. DEHOLLAIN, S. FREER, F. E. HUDSON, M. VELDHORST, R. RAHMAN, G. KLIMECK, K. M. ITOH, D. N. JAMIESON, J. C. MCCALLUM, A. S. DZURAK, A. MORELLO. *Electrically controlling single-spin qubits in a continuous microwave field*. Science Advances **1**, 3
- [LMN08] A. LITA, A. MILLER, S. NAM. *Counting near-infrared single-photons with 95% efficiency*. Opt. Express **16**, 5 (2008), 3032–3040
- [LOJ⁺05] C. LANGER, R. OZERI, J. D. JOST, J. CHIAVERINI, B. DEMARCO, A. BEN-KISH, R. B. BLAKESTAD, J. BRITTON, D. B. HUME, W. M. ITANO, D. LEIBFRIED, R. REICHLER, T. ROSEN BAND, T. SCHAETZ, P. O. SCHMIDT, D. J. WINELAND. *Long-Lived Qubit Memory Using Atomic Ions*. Phys. Rev. Lett. **95** (2005), 060502
- [Lou00] R. LOUDON. *The Quantum Theory of Light* (Oxford University Press) (2000). ISBN 0198501765
- [LRH⁺04] D. M. LUCAS, A. RAMOS, J. P. HOME, M. J. McDONNELL, S. NAKAYAMA, J.-P. STACEY, S. C. WEBSTER, D. N. STACEY, A. M. STEANE. *Isotope-selective photoionization for calcium ion trapping*. Phys. Rev. A **69** (2004), 012711
- [LWGS05] V. LETCHUMANAN, M. A. WILSON, P. GILL, A. G. SINCLAIR. *Lifetime measurement of the metastable $4d^2 D_{5/2}$ state in $^{88}\text{Sr}^+$ using a single trapped ion*. Phys. Rev. A **72** (2005), 012509
- [MEK00] G. MORIGI, J. ESCHNER, C. KEITEL. *Ground State Laser Cooling Using Electromagnetically Induced Transparency*. Phys. Rev. Lett. **85** (2000), 4458–4461

- [MGW05] F. G. MAJOR, V. N. GHEORGHE, G. WERTH. *Charged Particle Traps* (Springer Berlin Heidelberg) (2005). ISBN 978-3-540-22043-5
- [MHB⁺03] H. S. MARGOLIS, G. HUANG, G. P. BARWOOD, S. N. LEA, H. A. KLEIN, W. R. C. ROWLEY, P. GILL, R. S. WINDELER. *Absolute frequency measurement of the 674-nm $^{88}\text{Sr}^+$ clock transition using a femtosecond optical frequency comb*. Phys. Rev. A **67** (2003), 032501
- [MHS⁺11] D. L. MOEHRING, C. HIGHSTRETE, D. STICK, K. M. FORTIER, R. HALTLI, C. TIGGES, M. G. BLAIN. *Design, fabrication and experimental demonstration of junction surface ion traps*. New Journal of Physics **13**, 7 (2011), 075018
- [MJYH94] L. MA, P. JUNGNER, J. YE, J. HALL. *Delivering the same optical frequency at two places: accurate cancellation of phase noise introduced by an optical fiber or other time-varying path*. Opt. Lett. **19**, 21 (1994), 1777–1779
- [MK13] C. MONROE, J. KIM. *Scaling the Ion Trap Quantum Processor*. Science **339**, 6124 (2013), 1164–1169
- [MKV⁺09] T. MONZ, K. KIM, A. S. VILLAR, P. SCHINDLER, M. CHWALLA, M. RIEBE, C. F. ROOS, H. HÄFFNER, W. HÄNSEL, M. HENNRICH, R. BLATT. *Realization of Universal Ion-Trap Quantum Computation with Decoherence-Free Qubits*. Phys. Rev. Lett. **103** (2009), 200503
- [MLX⁺15] K. M. MALLER, M. T. LICHTMAN, T. XIA, Y. SUN, M. J. PIOTROWICZ, A. W. CARR, L. ISENHOWER, M. SAFFMAN. *Rydberg-blockade controlled-not gate and entanglement in a two-dimensional array of neutral-atom qubits*. Phys. Rev. A **92** (2015), 022336
- [MMK⁺95] C. MONROE, D. M. MEEKHOF, B. E. KING, S. R. JEFFERTS, W. M. ITANO, D. J. WINELAND, P. GOULD. *Resolved-Sideband Raman Cooling of a Bound Atom to the 3D Zero-Point Energy*. Phys. Rev. Lett. **75** (1995), 4011–4014
- [MMN⁺16] E. MARTINEZ, T. MONZ, D. NIGG, P. SCHINDLER, R. BLATT. *Compiling quantum algorithms for architectures with multi-qubit gates*. New Journal of Physics **18**, 6 (2016), 063029
- [MNM⁺16] T. MONZ, D. NIGG, E. A. MARTINEZ, M. F. BRANDL, P. SCHINDLER, R. RINES, S. X. WANG, I. L. CHUANG, R. BLATT. *Realization of a scalable Shor algorithm*. Science **351** (2016), 1068–1070
- [MO33] W. MEISSNER, R. OCHSENFELD. *Ein neuer Effekt bei Eintritt der Supraleitfähigkeit*. Naturwissenschaften **21**, 44 (1933), 787–788
- [Moh99] S. S. MOHAN. *The design, modeling and optimization of on-chip inductor and transformer circuits*. Ph.D. thesis, Stanford University (1999)
- [Mon11] T. MONZ. *Quantum information processing beyond ten ion-qubits*. Ph.D. thesis, Universität Innsbruck (2011)
- [Moo65] G. MOORE. *Cramming More Components onto Integrated Circuits*. Electronics **38** (1965), 114–117
- [Moo75] G. MOORE. *Progress in Digital Integrated Electronics*. In *IEDM Tech. Digest*, 11–13 (1975)
- [MRR⁺53] N. METROPOLIS, A. ROSENBLUTH, M. ROSENBLUTH, A. TELLER, E. TELLER. *Equation of State Calculations by Fast Computing Machines*. The Journal of Chemical Physics **21**, 6 (1953), 1087–1092
- [MS59] W. MACALPINE, R. SCHILDKNECHT. *Coaxial resonators with helical inner conductor*. Proc. of the IRE **47** (1959), 2099–2105
- [MSB⁺11] T. MONZ, P. SCHINDLER, J. T. BARREIRO, M. CHWALLA, D. NIGG, W. A. COISH, M. HARLANDER, W. HÄNSEL, M. HENNRICH, R. BLATT. *14-Qubit Entanglement: Creation and Coherence*. Phys. Rev. Lett. **106** (2011), 130506
- [MSW⁺08] A. H. MYERSON, D. J. SZWER, S. C. WEBSTER, D. T. C. ALLCOCK, M. J. CURTIS, G. IMREH, J. A. SHERMAN, D. N. STACEY, A. M. STEANE, D. M. LUCAS. *High-Fidelity Readout of Trapped-Ion Qubits*. Phys. Rev. Lett. **100** (2008), 200502
- [MTC⁺05] T. METODI, D. THAKER, A. CROSS, F. CHONG, I. CHUANG. *A Quantum Logic Array Microarchitecture: Scalable Quantum Data Movement and Computation*. In *Proceedings of the 38th Annual IEEE/ACM International Symposium on Microarchitecture*, MICRO 38, 305–318 (IEEE Computer Society, Washington, DC, USA) (2005). ISBN 0-7695-2440-0

- [MWY⁺11] M. MARIANTONI, H. WANG, T. YAMAMOTO, M. NEELEY, R. C. BIALCZAK, Y. CHEN, M. LENANDER, E. LUCERO, A. D. O'CONNELL, D. SANK, M. WEIDES, J. WENNER, Y. YIN, J. ZHAO, A. N. KOROTKOV, A. N. CLELAND, J. M. MARTINIS. *Implementing the Quantum von Neumann Architecture with Superconducting Circuits*. Science **334**, 6052 (2011), 61–65
- [NBE⁺98] H. NÄGERL, W. BECHTER, J. ESCHNER, F. SCHMIDT-KALER, R. BLATT. *Ion strings for quantum gates*. Applied Physics B **66**, 5 (1998), 603–608
- [NC11] M. A. NIELSEN, I. L. CHUANG. *Quantum Computation and Quantum Information* (Cambridge University Press) (2011). ISBN 1107002176
- [Neu45] J. V. NEUMANN. *First Draft of a Report on the EDVAC*. Tech. rep., Stanford University (1945)
- [NHR09] V. NEBENDAHL, H. HÄFFNER, C. F. ROOS. *Optimal control of entangling operations for trapped-ion quantum computing*. Phys. Rev. A **79** (2009), 012312
- [Nie15] M. NIEDERMAYR. *Cryogenic surface ion traps*. Ph.D. thesis, University of Innsbruck (2015)
- [Nig16] D. NIGG. *Towards fault tolerant quantum computation*. Ph.D. thesis, Universität Innsbruck (2016)
- [NLK⁺14] M. NIEDERMAYR, K. LAKHMANSKIY, M. KUMPH, S. PARTEL, J. EDLINGER, M. BROWNNUTT, R. BLATT. *Cryogenic surface ion trap based on intrinsic silicon*. New Journal of Physics **16**, 11 (2014), 113068
- [NLR⁺99] H. C. NÄGERL, D. LEIBFRIED, H. ROHDE, G. THALHAMMER, J. ESCHNER, F. SCHMIDT-KALER, R. BLATT. *Laser addressing of individual ions in a linear ion trap*. Phys. Rev. A **60** (1999), 145–148
- [NMM⁺14] D. NIGG, M. MÜLLER, E. MARTINEZ, P. SCHINDLER, M. HENNRICH, T. MONZ, M. A. MARTINDELGADO, R. BLATT. *Quantum computations on a topologically encoded qubit*. Science **345** (2014), 302–305
- [Nol16] A. NOLF. *Einzelionenadressierung und -Abbildung*. Master's thesis, Universität Innsbruck (2016)
- [NSD86] W. NAGOURNEY, J. SANDBERG, H. DEHMELT. *Shelved optical electron amplifier: Observation of quantum jumps*. Phys. Rev. Lett. **56** (1986), 2797–2799
- [ODH06] D. K. L. OI, S. J. DEVITT, L. C. L. HOLLENBERG. *Scalable error correction in distributed ion trap computers*. Phys. Rev. A **74** (2006), 052313
- [OIB⁺07] R. OZERI, W. M. ITANO, R. B. BLAKESTAD, J. BRITTON, J. CHIAVERINI, J. D. JOST, C. LANGER, D. LEIBFRIED, R. REICHLE, S. SEIDELIN, J. H. WESENBERG, D. J. WINELAND. *Errors in trapped-ion quantum gates due to spontaneous photon scattering*. Phys. Rev. A **75** (2007), 042329
- [OWC⁺11] C. OSPELKAUS, U. WARRING, Y. COLOMBE, K. R. BROWN, J. M. AMINI, D. LEIBFRIED, D. J. WINELAND. *Microwave quantum logic gates for trapped ions*. Nature **476** (2011), 181–184
- [Oze11] R. OZERI. *The trapped-ion qubit tool box*. Contemporary Physics **52**, 6 (2011), 531–550
- [Pau90] W. PAUL. *Electromagnetic traps for charged and neutral particles*. Review of Modern Physics **62** (1990), 531–540
- [PBIW96] M. E. POITZSCH, J. C. BERGQUIST, W. M. ITANO, D. J. WINELAND. *Cryogenic linear ion trap for accurate spectroscopy*. Review of Scientific Instruments **67**, 1 (1996), 129–134
- [PC04] D. PORRAS, J. I. CIRAC. *Effective Quantum Spin Systems with Trapped Ions*. Phys. Rev. Lett. **92** (2004), 207901
- [Pen36] F. M. PENNING. *Die Glimmentladung bei niedrigem Druck zwischen koaxialen Zylindern in einem axialen Magnetfeld*. Physica **3** (1936), 873–894
- [Pha05] P. PHAM. *A general purpose pulse sequencer for quantum computing*. Master's thesis, Massachusetts Institute of Technology (2005)
- [PHR92] Y. PANG, J. HAMILTON, J. RICHARD. *Frequency noise induced by fiber perturbations in a fiber-linked stabilized laser*. Appl. Opt. **31**, 36 (1992), 7532–7534
- [Pie54] J. R. PIERCE. *Theory and Design of Electron Beams* (D. Van Nostrand Co., Inc.; 2nd edition) (1954). ISBN 1124091300

- [PMZ⁺95] A. S. PARKINS, P. MARTE, P. ZOLLER, O. CARNAL, H. J. KIMBLE. *Quantum-state mapping between multilevel atoms and cavity light fields*. Phys. Rev. A **51** (1995), 1578–1596
- [PMZK93] A. S. PARKINS, P. MARTE, P. ZOLLER, H. J. KIMBLE. *Synthesis of arbitrary quantum states via adiabatic transfer of Zeeman coherence*. Phys. Rev. Lett. **71** (1993), 3095–3098
- [Pob92] F. POBELL. *Matter and methods at low temperatures* (Springer) (1992). ISBN 3-540-53751-1
- [POF58] W. PAUL, O. OSBERGHAUS, E. FISCHER. *Ein Ionenkäfig*. Forschungsberichte des Wirtschafts- und Verkehrsministeriums NRW **415** (1958), 1–42
- [Pos15] L. POSTLER. *Ein schmalbandiges Halbleiter-Lasersystem für Quanteninformationsverarbeitung und Spektroskopie*. Master's thesis, Universität Innsbruck (2015)
- [Poz11] D. M. POZAR. *Microwave Engineering* (John Wiley & Sons) (2011). ISBN 9780470631553
- [Ram50] N. RAMSEY. *A Molecular Beam Resonance Method with Separated Oscillating Fields*. Phys. Rev. **78** (1950), 695–699
- [RBKD⁺02] M. A. ROWE, A. BEN-KISH, B. DEMARCO, D. LEIBFRIED, V. MEYER, J. BEALL, J. BRITTON, J. HUGHES, W. M. ITANO, B. JELENKOVIĆ, C. LANGER, T. ROSENAND, D. J. WINELAND. *Transport of Quantum States and Separation of Ions in a Dual RF Ion Trap*. Quantum Info. Comput. **2**, 4 (2002), 257–271
- [RGL⁺14] P. RICHERME, Z. X. GONG, A. LEE, C. SENKO, J. SMITH, M. FOSS-FEIG, S. MICHALAKIS, A. V. GORSHKOV, C. MONROE. *Non-local propagation of correlations in quantum systems with long-range interactions*. Nature **511** (2014), 198–201
- [Rie05] M. RIEBE. *Preparation of Entangled States and Quantum Teleportation with Atomic Qubits*. Ph.D. thesis, Universität Innsbruck (2005)
- [RLM⁺00] C. F. ROOS, D. LEIBFRIED, A. MUNDT, F. SCHMIDT-KALER, J. ESCHNER, R. BLATT. *Experimental Demonstration of Ground State Laser Cooling with Electromagnetically Induced Transparency*. Phys. Rev. Lett. **85** (2000), 5547–5550
- [Roo00] C. F. ROOS. *Controlling the quantum state of trapped ions*. Ph.D. thesis, University of Innsbruck (2000)
- [RSK⁺16] T. RUSTER, C. SCHMIEGELOW, H. KAUFMANN, C. WARSCHBURGER, F. SCHMIDT-KALER, U. POSCHINGER. *A long-lived Zeeman trapped-ion qubit*. Applied Physics B **122**, 10 (2016), 254
- [RSS⁺13] P. RICHERME, C. SENKO, J. SMITH, A. LEE, S. KORENBLIT, C. MONROE. *Experimental performance of a quantum simulator: Optimizing adiabatic evolution and identifying many-body ground states*. Phys. Rev. A **88** (2013), 012334
- [RWK⁺14] T. RUSTER, C. WARSCHBURGER, H. KAUFMANN, C. T. SCHMIEGELOW, A. WALTHER, M. HETRICH, A. PFISTER, V. KAUSHAL, F. SCHMIDT-KALER, U. G. POSCHINGER. *Experimental realization of fast ion separation in segmented Paul traps*. Phys. Rev. A **90** (2014), 033410
- [RZR⁺99] C. ROOS, T. ZEIGER, H. ROHDE, H. C. NÄGERL, J. ESCHNER, D. LEIBFRIED, F. SCHMIDT-KALER, R. BLATT. *Quantum State Engineering on an Optical Transition and Decoherence in a Paul Trap*. Phys. Rev. Lett. **83** (1999), 4713–4716
- [SBL⁺05] T. SCHAEZT, M. D. BARRETT, D. LEIBFRIED, J. BRITTON, J. CHIAVERINI, W. M. ITANO, J. D. JOST, E. KNILL, C. LANGER, D. J. WINELAND. *Enhanced Quantum State Detection Efficiency through Quantum Information Processing*. Phys. Rev. Lett. **94** (2005), 010501
- [SBM⁺11] P. SCHINDLER, J. BARREIRO, T. MONZ, V. NEBENDAHL, D. NIGG, M. CHWALLA, M. HENNRICH, R. BLATT. *Experimental Repetitive Quantum Error Correction*. Science **332** (2011), 1059–1061
- [Sch93] J. P. SCHIFFER. *Phase transitions in anisotropically confined ionic crystals*. Phys. Rev. Lett. **70** (1993), 818–821
- [Sch08] P. SCHINDLER. *Frequency synthesis and pulse shaping for quantum information processing with trapped ions*. Master's thesis, Universität Innsbruck (2008)
- [Sch15] F. SCHRECK. *Control System* (2015). <http://www.strontiumbec.com/> visited on March 2, 2016

- [SCR⁺06] S. SEIDELIN, J. CHIAVERINI, R. REICHLER, J. J. BOLLINGER, D. LEIBFRIED, J. BRITTON, J. H. WESENBERG, R. B. BLAKESTAD, R. J. EPSTEIN, D. B. HUME, W. M. ITANO, J. D. JOST, C. LANGER, R. OZERI, N. SHIGA, D. J. WINELAND. *Microfabricated Surface-Electrode Ion Trap for Scalable Quantum Information Processing*. Phys. Rev. Lett. **96** (2006), 253003
- [SCS⁺12] A. STUTE, B. CASABONE, P. SCHINDLER, T. MONZ, P. O. SCHMIDT, B. BRANDSTÄTTER, T. E. NORTHUP, R. BLATT. *Tunable ion-photon entanglement in an optical cavity*. Nature **485** (2012), 482–485
- [SDH66] W. SACHTLER, G. DORGELO, A. HOLSCHER. *The work function of gold*. Surface Science **5**, 2 (1966), 221 – 229
- [Shi00] S. SHIVA. *Computer Organization, Design, and Architecture, Fourth Edition* (Taylor & Francis) (2000). ISBN 9780203908594
- [Sho97] P. W. SHOR. *Polynomial-Time Algorithms for Prime Factorization and Discrete Logarithms on a Quantum Computer*. SIAM J. Comput. **26**, 5 (1997), 1484–1509
- [SKH⁺06] F. SEIFERT, P. KWEE, M. HEURS, B. WILLKE, K. DANZMANN. *Laser power stabilization for second-generation gravitational wave detectors*. Opt. Lett. **31**, 13 (2006), 2000–2002
- [SM99] A. SØRENSEN, K. MØLMER. *Quantum Computation with Ions in Thermal Motion*. Phys. Rev. Lett. **82** (1999), 1971–1974
- [SMDB07] A. D. SHINER, A. A. MADEJ, P. DUBÉ, J. E. BERNARD. *Absolute optical frequency measurement of saturated absorption lines in Rb near 422 nm*. Applied Physics B **89** (2007), 595–601
- [SNBT86] T. SAUTER, W. NEUHAUSER, R. BLATT, P. TOSCHEK. *Observation of Quantum Jumps*. Phys. Rev. Lett. **57** (1986), 1696–1698
- [SNM⁺13] P. SCHINDLER, D. NIGG, T. MONZ, J. BARREIRO, E. MARTINEZ, S. WANG, S. QUINT, M. BRANDL, V. NEBENDAHL, C. ROOS, M. CHWALLA, M. HENNRICH, R. BLATT. *A quantum information processor with trapped ions*. New Journal of Physics **15**, 12 (2013), 123012
- [SSWH12] J. SIVERNS, L. SIMKINS, S. WEIDT, W. HENSINGER. *On the application of radio frequency voltages to ion traps via helical resonators*. Applied Physics B **107**, 4 (2012), 921–934
- [Ste96] A. M. STEANE. *Error Correcting Codes in Quantum Theory*. Phys. Rev. Lett. **77** (1996), 793–797
- [Ste07] A. STEANE. *How to Build a 300 Bit, 1 Giga-operation Quantum Computer*. Quantum Info. Comput. **7**, 3 (2007), 171–183
- [Stu12] A. STUTE. *A light-matter quantum interface: ion-photon entanglement and state mapping*. Ph.D. thesis, Universität Innsbruck (2012)
- [SVW⁺12] M. SCHWARZ, O. O. VERSOLATO, A. WINDBERGER, F. R. BRUNNER, T. BALLANCE, S. N. EBERLE, J. ULLRICH, P. O. SCHMIDT, A. K. HANSEN, A. D. GINGELL, M. DREWSEN, J. R. C. LÓPEZ-URRUTIA. *Cryogenic linear Paul trap for cold highly charged ion experiments*. Review of Scientific Instruments **83**, 083115
- [SZM93] M. SKAKALA, V. ZRUBEC, J. MANKA. *Active compensation for ambient magnetic noise in the unshielded environment*. Measurement Science and Technology **4**, 4 (1993), 468
- [TAA⁺10] J. C. TARTER, A. AGRAWAL, R. ACKERMANN, P. BACKUS, S. K. BLAIR, M. T. BRADFORD, G. R. HARP, J. JORDAN, T. KILSDONK, K. E. SMOLEK, J. RICHARDS, J. ROSS, G. S. SHOSTAK, D. VAKOCH. *SETI turns 50: five decades of progress in the search for extraterrestrial intelligence*. Proc. SPIE **7819** (2010), 781902–781902–13
- [Tan05] A. TANENBAUM. *Structured Computer Organization* (Pearson), 5th ed. (2005). ISBN 0131485210
- [TGL⁺15] T. TAN, J. GAEBLER, Y. LIN, Y. WAN, R. BOWLER, D. LEIBFRIED, D. J. WINELAND. *Multi-element logic gates for trapped-ion qubits*. Nature **528** (2015), 380–383
- [TKK⁺00] Q. A. TURCHETTE, KIELPINSKI, B. E. KING, D. LEIBFRIED, D. M. MEEKHOF, C. J. MYATT, M. A. ROWE, C. A. SACKETT, C. S. WOOD, W. M. ITANO, C. MONROE, D. J. WINELAND. *Heating of trapped ions from the quantum ground state*. Phys. Rev. A **61** (2000), 063418
- [TL08] P. TIPLER, R. LLEWELLYN. *Modern Physics* (Clancy Marshall), 5th ed. (2008). ISBN 0-7167-7550-6

- [TP10] F. TEYSSANDIER, D. PRÊLE. *Commercially Available Capacitors at Cryogenic Temperatures*. In *Ninth International Workshop on Low Temperature Electronics - WOLTE9* (Guaruja, Brazil) (2010)
- [TPR⁺03] G. TOMMASEO, T. PFEIL, G. REVALDE, G. WERTH, P. INDELICATO, J. DESCLAUX. *The g -factor in the ground state of Ca^+* . The European Physical Journal D **25** (2003), 113–121
- [TRF⁺11] M. J. THORPE, L. RIPPE, T. M. FORTIER, M. S. KIRCHNER, T. ROSEN BAND. *Frequency stabilization to 6×10^{-16} via spectral-hole burning*. Nature Photonics **5** (2011), 688–693
- [Tro59] H. TROTTER. *On the product of semi-groups of operators*. Proc. Amer. Math. Soc. **10** (1959), 545–551
- [TSH⁺05] T. TOMARU, T. SUZUKI, T. HARUYAMA, T. SHINTOMI, N. SATO, A. YAMAMOTO, Y. IKUSHIMA, R. LI, T. AKUTSU, T. UCHIYAMA, S. MIYOKI. *Vibration-Free Pulse Tube Cryocooler System for Gravitational Wave Detectors, Part I: Vibration-Reduction Method and Measurement*. In *Cyrocoolers*, 695–702 (Springer US) (2005). ISBN 978-0-387-23901-9
- [Uhr07] G. UHRIG. *Keeping a Quantum Bit Alive by Optimized π -Pulse Sequences*. Phys. Rev. Lett. **98** (2007), 100504
- [VCA⁺10] A. P. VANDEVENDER, Y. COLOMBE, J. AMINI, D. LEIBFRIED, D. J. WINELAND. *Efficient Fiber Optic Detection of Trapped Ion Fluorescence*. Phys. Rev. Lett. **105** (2010), 023001
- [VKGS⁺13] J. VOIGT, S. KNAPPE-GRÜNEBERG, A. SCHNABEL, R. KÖRBER, M. BURGHOFF. *Active compensation for ambient magnetic noise in the unshielded environment*. Metrology and Measurement Systems **20** (2013), 239–248
- [VL98] L. VIOLA, S. LLOYD. *Dynamical suppression of decoherence in two-state quantum systems*. Phys. Rev. A **58** (1998), 2733–2744
- [VMH13] R. VAN METER, C. HORSMAN. *A Blueprint for Building a Quantum Computer*. Commun. ACM **56**, 10 (2013), 84–93
- [VMI05] R. VAN METER, K. ITOH. *Fast quantum modular exponentiation*. Phys. Rev. A **71** (2005), 052320
- [VMI06] R. VAN METER III. *Architecture of a Quantum Multicomputer Optimized for Shor’s Factoring Algorithm*. Ph.D. thesis, Keio University (2006)
- [VW94] W. VOGEL, D. WELSCH. *Lectures on Quantum Optics* (Wiley-VCH) (1994)
- [VWB⁺13] G. VITTORINI, K. WRIGHT, K. R. BROWN, A. W. HARTER, S. C. DORET. *Modular cryostat for ion trapping with surface-electrode ion traps*. Review of Scientific Instruments **84**, 4 043112
- [VYH⁺15] M. VELDHORST, C. YANG, J. HWANG, W. HUANG, J. DEHOLLAIN, J. MUHONEN, S. SIMMONS, A. LAUCHT, F. HUDSON, K. ITOH, A. MORELLO, A. DZURAK. *A two-qubit logic gate in silicon*. Nature **526** (2015), 410–414
- [Wal16] M. WALDROP. *The chips are down for Moore’s law*. Nature **530** (2016), 144–147
- [WAMS12] J. B. WÜBBENA, S. AMAIRI, O. MANDEL, P. O. SCHMIDT. *Sympathetic cooling of mixed-species two-ion crystals for precision spectroscopy*. Phys. Rev. A **85** (2012), 043412
- [Wan12] S. X. WANG. *Quantum Gates, Sensors, and Systems with Trapped Ions*. Ph.D. thesis, Massachusetts Institute of Technology (2012)
- [WAW88] M. WUTZ, H. ADAM, W. WALCHER. *Theorie und Praxis der Vakuumtechnik* (Friedr. Vieweg & Sohn, Braunschweig / Wiesbaden) (1988). ISBN 3-528-24884-X
- [WBB⁺03] D. J. WINELAND, M. BARRETT, J. BRITTON, J. CHIAVERINI, B. DEMARCO, W. M. ITANO, B. JELLENKOVIĆ, C. LANGER, D. LEIBFRIED, V. MEYER, T. ROSEN BAND, T. SCHÄTZ. *Quantum information processing with trapped ions*. Philosophical Transactions of the Royal Society of London A: Mathematical, Physical and Engineering Sciences **361**, 1808 (2003), 1349–1361
- [WGM09] G. WERTH, V. N. GHEORGHE, F. G. MAJOR. *Charged Particle Traps II* (Springer Berlin Heidelberg) (2009). ISBN 978-3-642-26042-1
- [WLG⁺10] S. X. WANG, J. LABAZIEWICZ, Y. GE, R. SHEWMON, I. L. CHUANG. *Demonstration of a quantum logic gate in a cryogenic surface-electrode ion trap*. Phys. Rev. A **81** (2010), 062332

- [WMI⁺98] D. J. WINELAND, C. MONROE, W. M. ITANO, D. LEIBFRIED, B. E. KING, D. M. MEEKHOF. *Experimental Issues in Coherent Quantum-State Manipulation of Trapped Atomic Ions*. J. Res. Natl. Inst. Stand. Technol. **103**, 3 (1998), 259–328
- [WOC⁺13] U. WARRING, C. OSPELKAUS, Y. COLOMBE, R. JÖRDENS, D. LEIBFRIED, D. J. WINELAND. *Individual-Ion Addressing with Microwave Field Gradients*. Phys. Rev. Lett. **110** (2013), 173002
- [WZ82] W. WOOTTERS, W. ZUREK. *A single quantum cannot be cloned*. Nature **299** (1982), 802
- [WZR⁺12] A. WALTHER, F. ZIESEL, T. RUSTER, S. T. DAWKINS, K. OTT, M. HETTRICH, K. SINGER, F. SCHMIDT-KALER, U. POSCHINGER. *Controlling Fast Transport of Cold Trapped Ions*. Phys. Rev. Lett. **109** (2012), 080501
- [Zie12] F. ZIESEL. *Quantum State Manipulation and Dynamics in Micro Ion Traps*. Ph.D. thesis, Universität Ulm (2012)
- [ZMD06] S.-L. ZHU, C. MONROE, L.-M. DUAN. *Trapped Ion Quantum Computation with Transverse Phonon Modes*. Phys. Rev. Lett. **97** (2006), 050505
- [ZR97] P. ZANARDI, M. RASETTI. *Noiseless Quantum Codes*. Phys. Rev. Lett. **79** (1997), 3306–3309

Danksagung

Hiermit möchte ich mich bei allen, die zu dieser Arbeit beigetragen haben herzlich bedanken. Im Speziellen geht mein Dank an Rainer Blatt unter dessen Führung ich mein Doktorat machen durfte.

Während meiner Forschungszeit in Innsbruck hatte ich das Vergnügen mit vielen interessanten Menschen zusammenzuarbeiten. Es war eine Bereicherung mit allen Leuten des SQIP-Teams über Quantenphysik, Laboraufbauten und die weitere Entwicklung unseres Experimentes zu diskutieren. Besonders hervorheben möchte ich die Zusammenarbeit mit Lukas Postler, Martin van Mourik und Philipp Schindler. Ohne diese Leute würde das Experiment heute nicht so gut laufen, wie es läuft.

Aber ich möchte mich natürlich auch bei den anderen Mitgliedern der Arbeitsgruppe für die Zusammenarbeit über die Jahre bedanken. Zum Beispiel habe ich von Michael Niedermayr viel über Kryostaten und deren Integration in ein Ionenfallenexperiment lernen können. Muir Kumph hat mir viel über RF-Schwingkreise beigebracht und hat mich auf die Publikation mit den PCB-Spulen aufmerksam gemacht, aus der dann eine meiner zwei Erstautorpublikationen entstanden ist. Aus den Diskussionen mit Yves Colombe bei uns im Büro habe ich viel über Quantenphysik aber auch Physik im Allgemeinen gelernt.

Da ein Doktorat nicht zu hundert Prozent aus Forschen besteht, möchte ich mich auch herzlich bei den Leuten bedanken, die unsere Forschung durch ihre Arbeit erst möglich machen. Das betrifft Patricia Moser und Renate Rupprechter für die administrativen Tätigkeiten und Wolfgang Kratz, Wolfgang Kuen und Michael Hofer für die Unterstützung in der Elektronikwerkstatt auf der Uni. Besonderer Dank geht an Gerhard Hendl vom IQOQI, der mit mir gemeinsam einige nützliche Schaltungen für die Arbeitsgruppe entwickelt hat und mir immer bei Elektronikproblemen zur Seite gestanden hat. Wenn man ein Labor neu aufbaut und dabei einen hochkomplizierten Kryostaten baut, ist die tatkräftige Unterstützung einer mechanischen Werkstatt notwendig. Deshalb möchte ich mich herzlich bei Armin Sailer, Helmut Jordan, Anton Schönherr, Armin Hofmeister, Christoph Wegscheider, Stefan Haslwanter und Andreas Strasser für die Zusammenarbeit bedanken.

Abschließend möchte ich mich bei meiner Familie bedanken, die mich stets auf dem Weg, den ich für richtig hielt, unterstützt hat. Und ganz besonders danke ich Simone für ihre Geduld und Unterstützung auf diesem langen Weg.